

DOT/FAA/AR-02/114

Office of Aviation Research  
Washington, D.C. 20591

# Fundamental Studies: Inspection Properties for Engine Titanium Alloys

December 2002

Final Report

This document is available to the U.S. public  
through the National Technical Information  
Service (NTIS), Springfield, Virginia 22161.



U.S. Department of Transportation  
Federal Aviation Administration

**DISTRIBUTION STATEMENT A**  
Approved for Public Release  
Distribution Unlimited

20030319 025

## **NOTICE**

This document is disseminated under the sponsorship of the U.S. Department of Transportation in the interest of information exchange. The United States Government assumes no liability for the contents or use thereof. The United States Government does not endorse products or manufacturers. Trade or manufacturer's names appear herein solely because they are considered essential to the objective of this report. This document does not constitute FAA certification policy. Consult your local FAA aircraft certification office as to its use.

This report is available at the Federal Aviation Administration William J. Hughes Technical Center's Full-Text Technical Reports page: [actlibrary.tc.faa.gov](http://actlibrary.tc.faa.gov) in Adobe Acrobat portable document format (PDF).

**Technical Report Documentation Page**

1. Report No.  DOT/FAA/AR-02/114	2. Government Accession No.	3. Recipient's Catalog No.	
4. Title and Subtitle  <b>FUNDAMENTAL STUDIES: INSPECTION PROPERTIES FOR ENGINE TITANIUM ALLOYS</b>		5. Report Date  <b>December 2002</b>	
7. Author(s)  F.J. Margetan <sup>1</sup> , M. Gigliotti <sup>2</sup> , L. Brashe <sup>1</sup> and W. Leach <sup>2</sup> (with important input from all members of the research team)		6. Performing Organization Code	
<sup>1</sup> Iowa State University Center for NDE Ames, IA 50011	<sup>2</sup> General Electric Aircraft Engines Cincinnati, Ohio	8. Performing Organization Report No.	
12. Sponsoring Agency Name and Address  U.S. Department of Transportation Federal Aviation Administration Office of Aviation Research Washington, DC 20591		10. Work Unit No. (TRAIS)	
		11. Contract or Grant No.	
13. Type of Report and Period Covered  <b>Final Report</b>		14. Sponsoring Agency Code  <b>ANE-110</b>	
15. Supplementary Notes  The FAA William J. Hughes Technical Center Program Managers were Dr. Christopher Smith and Mr. Bruce Fenton.			
16. Abstract  Titanium alloys are widely used in critical rotating components for jet engine applications. Because of the important role they play in overall flight safety, it is important that the components be free of defects which can lead to failure. In light of this requirement, titanium components are typically inspected several times during the production process. One of the methods used is ultrasonic inspection. However, titanium is an ultrasonically noisy material which can lead to false indications or missed flaws. In an effort to understand the relationship between microstructure and detectability, the Engine Titanium Consortium completed an extensive study of the fundamental properties of titanium materials. This study focused on Ti-6Al-4V and Ti-17 (Ti-5 wt.% Al-2 wt.% Sn-2 wt.% Zr-4 wt.% Cr-4 wt.% Mo), two common alloys used in jet engine applications. The results of this work provided needed data and samples to other technical tasks in the Engine Titanium Consortium. A summary of the findings is provided in this document.			
17. Key Words  Ultrasonic inspection, Titanium properties, Critical rotating components, Jet engine		18. Distribution Statement  This document is available to the public through the National Technical Information Service (NTIS) Springfield, Virginia 22161.	
19. Security Classif. (of this report)  Unclassified	20. Security Classif. (of this page)  Unclassified	21. No. of Pages  158	22. Price

## ACKNOWLEDGEMENT

The authors would like to acknowledge the Federal Aviation Administration for the support in funding this project. Further thanks go to Al Broz, Michael Borfitz, and Chris Smith for their guidance during the project.

### Research Team:

#### Iowa State University:

Lisa Brasche  
Scot Goetsch  
Kim Han  
Frank Margetan  
Seth Meyer  
Paul Panetta  
R. Bruce Thompson  
Isaac Yalda

#### General Electric Aircraft Engines:

Mike Keller  
Rich Klassen  
Robert Gilmore  
Mike Gigliotti  
William Leach  
Lee Perocchi

#### Pratt & Whitney:

Bob Goodwin  
Kevin Smith  
Dave Raulerson  
Jeff Umbach

#### Honeywell Engines:

Lloyd Schaeffer  
Janet Wade

## TABLE OF CONTENTS

	Page
<b>EXECUTIVE SUMMARY</b>	<b>xiii</b>
1. INTRODUCTION	1
2. BACKGROUND	3
3. OBJECTIVES	4
4. APPROACH	4
5. RESULTS	5
5.1 Effect of Hard Alpha Composition on Inspectability	5
5.1.1 Introduction	5
5.1.2 Preparation of Synthetic Hard Alpha Samples	6
5.1.3 Detection of Synthetic Hard Alpha Inclusions	21
5.1.4 Estimation of Ultrasonic Reflectance and S/N of Ti-N Inclusions in Ti Alloys	23
5.1.5 Summary of the Effect of Hard Alpha Composition on Inspectability	27
5.2 Elastic Constant Determination for a Common Ti Engine Alloy	27
5.2.1 Introduction	27
5.2.2 Preparation of the Enlarged Grain Plate	30
5.2.3 Ultrasonic Velocity Measurements	31
5.2.4 Summary	36
5.3 Ultrasonic Properties of Ti-17 and Ti 6-4 Alloys	36
5.3.1 Introduction	36
5.3.2 Specimen Descriptions	37
5.3.3 Sound Speed Measurements	43
5.3.4 Summary of Velocity Measurements	46
5.3.5 Longitudinal Wave Attenuation Measurements	47

5.3.6	Dependence of Deduced Attenuation on Details of the Measurement Method	60
5.3.7	Beam Disruption, Wave front Distortion, and Beam Steering: Implications for Signal Reduction	77
5.3.8	Attenuation Summary	93
5.3.9	Longitudinal Wave Backscattered Noise Measurements	96
5.3.10	Summary of Backscattered Noise FOM Results	103
5.3.11	Characteristics of Fixed-Time and Gated-Peak Noise Distributions	105
5.3.12	Noise Distribution Summary: Implications for Inspections	111
6.	SUMMARY AND CONCLUSIONS	112
7.	REFERENCES	115

## APPENDICES

A—Ultrasonic Test Specimens

B—Development, Testing, and Use of Backscattered Noise Models

## LIST OF FIGURES

Figure		Page
1	Three-Dimensional Reconstruction of Optical Micrographs for a Typical Hard Alpha Defect	1
2	Task Relationships for the ETC Program	2
3	Ternary Ti-N-O Phase Diagram, Locating Analyzed Synthetic Hard Alpha Compositions	9
4	Microstructure of Powder Metallurgy Composition Ti- 4.55 at% N- 7.48 at% O, PB16	10
5	Microstructure of an 0.8-mm-Diameter Inclusion of Ti- 5.30 at% N- 0.97 at% O, HIPped in Ti 6-4 at 900°C, 105 MPa, for 4 Hours	12
6	Microstructure of 1.9-mm-Diameter, 1.9-mm-Long Pin of Ti- 5.28 at% N- 0.67 at% O, HIPped in Ti 6-4 at 900°C, 105 MPa, 4 Hours (RAM 1237 Seed)	13
7	Microstructure of 1.9-mm-Diameter, 1.9-mm-Long Pin of Ti- 8.36 at% N- 0.66 at% O, HIPped in Ti 6-4 at 900°C, 105 MPa, 4 Hours (RAM 1234 Seed)	13
8	Microstructure of 1.9-mm-Diameter, 1.9-mm-Long Pin of Ti- 10.90 at% N- 0.81 at% O, HIPped in Ti 6-4 at 900°C, 105 MPa, 4 Hours (RAM 1229 Seed)	14
9	Microstructure of 1.9-mm-Diameter, 1.9-mm-Long Inclusion of Ti- 17.46 at% N-1.21 at% O, HIPped in Ti 6-4 At 900°C, 105 MPa, 4 Hours (RAM 1228 Seed)	14
10	Microstructural Features Developed During the Diffusion Bonding Process	15
11	Scanning Electron Micrographs of Bond Lines in Samples 17H1, 17H2, and 17H3	17
12	Experimental Setup for Ultrasonic C-Scans of Ti-17 Blocks 17H1, 17H2, and 17H3	17
13	Comparison of C-Scan Amplitude and Time-of-Flight Methods	18
14	Time-of-Flight Images for Three Diffusion-Bonded Ti-17 Samples: Images for Parent Material (Top Row) and Diffusion Bond Zone (Bottom Row)	19
15	Time-of-Flight Data for Three Ti-17 Samples: Histograms for Parent Material (Top Row) and Diffusion Bond (Bottom Row)	19
16	Three-Dimensional Representation of TOF Scan Data for Ti-17 Sample 17H1	20
17	Acoustic Image of Synthetic Hard Alpha Inclusions in Block 90-PMA	21
18	Acoustic Image of Arc-Melted Synthetic Hard Alpha Inclusions in Block 93-1	22

19	Measured Longitudinal Velocity of Synthetic Hard Alpha Material Versus Oxygen and Nitrogen	23
20	Calculated Longitudinal Velocity of Ti-N Compositions Versus at% N	24
21	Calculated Longitudinal Wave Reflectance as a Function of Nitrogen Content for Ti-N Inclusions in Pure Ti and in Ti 6-4	25
22	Measured Signal-to-Noise Ratio of Synthetic Hard Alpha Inclusions in Block 90-PMA Versus Sound Velocity	26
23	Typical Ti 6-4 Billet Microstructure	29
24	Backscattered Electron Image (Top) and SEM Orientation Image (Bottom) of Ti 6-4 Billet	29
25	Macrostructure of the Ti 6-4 Enlarged Grain Plate in Which Large Grains Were Grown	30
26	Microstructure of One Colony in the Enlarged Grain Plate	31
27	Two Methods Used to Image Macrograins in the Enlarged Grain Plate: Surface Waves (Top) and Longitudinal Waves (Bottom)	32
28	Ultrasonic Images of the Enlarged Grain Plate Obtained Using Longitudinal Waves (Upper Two Images) and Surface Waves (Lower Two Images)	32
29	EBSP Icosohedral Image (Left) and Vector Normal Image (Right) of the Macrograin With the Lowest Measured Sound Velocity	33
30	EBSP Icosohedral Image (Left) and Vector Normal Image (Right) of the Macrograin With the Highest Measured Sound Velocity	34
31	Sound Velocity Anisotropy of Pure (Close Packed) Ti and Ti 6-4	34
32	Summary of Shear Wave Velocity Measurements on Single Macrograins of Ti 6-4	35
33	Ultrasonic Impedance (Velocity Times Density) of Ti 6-4 and Ti-N Alloys	36
34	Sources for the 14 Billet and Forging Specimens Designated A-N	38
35	Numbering Scheme Used to Label the Faces (Sound Entry Surfaces) of a Rectangular Coupon	39
36	(a) Schematic Drawing of a Typical Specimen, Showing the Location of the Wedge Removed for Metallography and (b) Sectioning of the Wedge Into Five Pieces	40
37	(a) Microstructure and (b) Macrostructure of a Typical Ti-17 Billet Specimen	41

38	(a) Microstructure and (b) Macrostructure of a Typical Ti 6-4 Billet Specimen	41
39	Typical Relationship Between Macrograin (or Flow Line) Orientations and the Directional Dependence of L-Wave Attenuation and Backscattered Noise	42
40	Sound Paths for L-Wave Ultrasonic Velocity Measurements	43
41	Measured L-Wave Speeds for Billet and Forging Specimens A-N	44
42	Dependence of L-Wave Velocity on Position	45
43	Identical Defects at Different Depths Give Rise to Echoes of Different Strengths, Partially as a Result of Material Attenuation	47
44	Examples of Beam Distortion Effects in Engine Titanium Alloys	50
45	Inspection Geometry and Ray Paths for the Three Attenuation Measurement Procedures	52
46	Resemblance of Columnar Microstructure (Left) and Back-Surface Echo Amplitude Pattern (Right) in Ti-17 Billet Specimen C1	55
47	Use of the BS Echo Method to Measure Attenuation in the Ti 6-4 Enlarged Grain Plate	56
48	Measured Attenuation of Ti-17 Billet Specimen L Using the BS Method	58
49	Measured Attenuations of Specimens A-N at 5 and 10 MHz, as Deduced By Comparing BS Echoes in Titanium and FQ Blocks	59
50	BS Echo Attenuation for Six Coupons From a Ti 6-4 Billet, as Measured Using Two Probes: 10-MHz, 0.25" Planar and 5-MHz, 0.75", F=6" Focused on the Back Surface	60
51	Effects of Beam Misalignment on the Measured BS Attenuation of Ti-17 Billet Specimen P for Radial Propagation	62
52	Attenuation of Ti-17 Billet Specimen P (Axial Propagation) as Deduced From Back-Surface Echoes at ISU and GEAE	63
53	Average BS Attenuation of the Ti 6-4 Enlarged Grain Plate as Measured Using Three 15-MHz Broadband Transducers	64
54	Effect of Beam Size on Attenuation of Back-Surface Echoes	65
55	Effect of Water Path Choice on Measured BS Attenuation Using a Focused Transducer	65
56	Average Attenuations of Ti-17 Billet Specimen P	66

57	Measured Fluctuations of Back-Surface Echoes for Axial Propagation in a Ti-17 Billet Specimen	67
58	Through-Transmission C-Scan Amplitude Images of the Beam From a 10-MHz, 0.25"-Diameter Planar Probe After Passage Through 3" Thick Blocks of Ti-17 (Billet Specimen L) and Fused Quartz	70
59	C-Scan Images of Through-Transmitted Phase at 9.2 MHz for the Inspection Described in Figure 58	71
60	Comparison of Measured TTE Attenuation and Average BS Attenuation for Radial and Axial Propagation in Ti-17 Billet Specimen L	71
61	C-Scan Images of Peak-to-Peak Voltage for Planar-Probe (Upper Row) and Focused-Probe (Lower Row) Scans of Flat-Bottomed Hole Arrays in Nickel and Ti-17 Billet Specimen L	74
62	(a) Average Attenuation of Ti-17 Billet Specimen L as Deduced by Analyzing FBH Echoes Using a D=2", F=16" Focused Transducer and (b) Comparison of Average Attenuation Values Deduced Using the BS, FBH, and TTE Methods With Planar (Flat) and Focused Probes	75
63	Values of the Fraction $F$ for Beams Transmitted Through a 3" Fused-Quartz Block and Ti-17 Billet Specimen L	80
64	A Downward Propagating Wave front From A Planar Transducer Becomes Deformed When it Enters a Metal Specimen Having Different Sound Velocities in Three Regions	81
65	(a) C-Scan Image of the Measured Back-Surface Echo Amplitude for a Scan of the Enlarged Grain Block Using a 15 MHz, 0.5", F/7 Transducer and (b) Measured Attenuation at 10.2 MHz as a Function of Position for the Scan Line Indicated at Left	82
66	The Ray Model for Back-Surface Echo Response	83
67	Use of the Ray Model to Predict Back-Surface Attenuation in the Enlarged Grain Block	84
68	Comparison of Measured (Left) and Predicted (Right) BS Attenuations for the Enlarged Grain Block	85
69	Average Attenuation of Back-Surface Echoes for Normal-Incidence and Optimized-Angle Scans of Ti-17 Billet Specimen P Using Focused (Left) and Planar (Right) Probes	88
70	Two Methods of Varying the Metal Travel Distance Used for Attenuation Measurements	91

71	Effect of Metal Travel Distance on Measured Attenuation	92
72	C-Scan Image of Gated-Peak Noise Showing the Noise Banding Pattern of a 6" Diameter Ti 6-4 Billet	96
73	Typical Dependence of Grain Noise on Depth in a Focused Probe Inspection of a Billet When no Distance-Amplitude Correction is Used (Left) and When a Distance-Amplitude Correction Based on the Strength of a FHB Echo is Used (Right)	97
74	Inspection Setup for Acquiring Reference and Noise A-Scans	98
75	Absolute rms Noise Levels Measured for Radial, Axial, and Hoop Propagation in Ti 6-4 Billet Specimen H	100
76	Frequency-Dependent FOM Values Deduced for Radial and Axial Propagation in Ti 6-4 Billet Specimen H	101
77	FOM Values Deduced for a Ti 6-4 Billet Specimen Using Both 5- and 15-MHz Focused Probes	102
78	Measured FOM Values at 5-MHz for 14 Specimens, Deduced by Analyzing Backscattered Noise A-Scans Acquired With a 5-MHz, F/8 Transducer	103
79	Dependence of Noise on Radial Depth at High- and Low-Noise Sites on a 6" Diameter Ti 6-4 Billet (CBS Billet Coupons)	105
80	RF Noise Voltage Distributions for Backscattered Noise From the Focal Zone of a 5-MHz, 3/4", F=6" Transducer	107
81	Gated-Peak Noise Distributions for Three Time Gates Having Different Durations but the Same Center Time	107
82	Relationship Between Gated-Peak Noise and rms Noise in 5-MHz Focused Inspections	108
83	Value of the Shape Parameter M Obtained by Fitting a K-Distribution to the Measured RF Noise Voltage Distribution $p(v)$ Near the Focal Zone	110
84	Noise Distribution Shape Parameters for 15-MHz Focused-Probe Inspections of the P and N Halves of Ti 6-4 Forging Specimen G as Functions of the Noise Arrival Time	111

## LIST OF TABLES

Table		Page
1	List of Blocks Containing SHA Defects Constructed During FAA-ETC Phase I and/or Used for Data Acquisition in the Course of the Program	8
2	Chemical Analysis of Synthetic Hard Alpha Material	8
3	Measured Sound Velocity of Ti Alloys and Synthetic Hard Alpha Material	11
4	Diffusion Bond Attachment Steps and Evaluation Techniques	16
5	Measured Signal-to-Noise Ratio From Ti-N-O Inclusions in Ti 6-4	22
6	Calculated Sound Velocity of Ti-N Compositions	23
7	Calculated Reflectance of Titanium-Nitrogen Alloys	25
8	Measured Longitudinal Wave Speeds for Specimens A-N	44
9	Contributing Factors for Sound Attenuation in Titanium Alloys	50
10	Attenuation Measurement Methods	52
11	Inspection Parameters for the Measurement of Back-Surface Attenuation in Specimen L, a 3" Cube Cut From the Outer Portion of a Ti-17 Billet	57
12	Flat-Bottomed Hole Attenuation Specimens	73
13	Attenuation Coefficients of Ti 6-4 Specimens Deduced by Analyzing FBH and Back-Surface Echoes	76
14	Angle Adjustment Statistics (in Water) for the Beam Tilt Study	87
15	Percentage Reduction in Apparent Ti-17 Back-Surface Attenuation Achieved by Adjusting Probe Tilt Angles	88
16	Percentage Reduction in the 5- and 10-MHz Spectral Components of the Fused-Quartz, Back-Surface Echo Resulting From Tilting the Transducer Away From Normal Incidence	89
17	Typical Setup and Analysis Parameters for Noise-FOM Measurement	99
18	Probability Distributions of Two Noise Attributes of Interest	106
19	Variability of Measured Ultrasonic Properties in Coupons A-N	114

## EXECUTIVE SUMMARY

This report describes the results of the Fundamental Studies task within the Federal Aviation Administration (FAA) Engine Titanium Consortium (ETC), Phase I program. The objective of the ETC was to provide the FAA and industry with reliable, cost-effective new methods and improvements in mature methods for detecting cracks, inclusions, and imperfections in premium rotor-grade titanium alloys. The Fundamental Studies task supported the ETC inspection system development and validation by developing and fabricating representative samples and providing accurate material characterization data.

Sections 1 and 2 discuss the background that established the requirements for this program. In the fall of 1989, the FAA formed the Titanium Rotating Components Review Team (TRCRT) in response to the fatal Sioux City, Iowa, accident earlier that year. The National Transportation Safety Board reported that the accident was caused by the fatigue fracture failure of a titanium rotating component initiated at an alloy melt-related anomaly (hard alpha inclusion). This accident highlighted the role rotating components play in flight safety and the importance that they be free of anomalies that can lead to a failure. The TRCRT report included recommendations for improvements in the capability to detect subsurface anomalies in the absence of a crack or void as well improvements in the ability to detect the resulting cracks in service.

Sections 3 and 4 develop the objectives and experimental approach of the task. The fact that the microstructure of titanium alloys is ultrasonically noisy has lead to false indications or missed anomalies in production. Therefore, the study attempted to develop an improved understanding of the relationship between microstructure and detectability. The goal was to improve the current inspection practices on the shop floor by gaining insight into how the fundamental properties are likely to affect a given inspection. This task was also intended to aid in the development and testing of computer models of ultrasonic inspection processes being pursued under other ETC Phase I tasks. The approach was organized into two major components: specimen fabrication and ultrasonic property measurements.

Section 5 reports the results of the effect of hard alpha composition on inspectability, the elastic constant determination for a common titanium engine alloy, and the ultrasonic properties of Ti-17 and Ti-64 alloys.

Section 6 features key accomplishments and findings.

Appendix A provides a listing of all the ultrasonic test specimens that were fabricated.

Appendix B provides a description of the development, testing, and use of backscattered noise models.

## 1. INTRODUCTION.

Titanium alloys are widely used in applications that require high strength at intermediate temperatures, good creep properties, and lightweight. Titanium alloys are used in engine components in both commercial and military aviation. Much of the demand for these alloys emanates from safety critical areas such as jet engine components. The criticality of these components requires that they be free of defects, such as inclusions, cracks, and imperfections that could lead to failure. Because failure of these components can contribute to catastrophic failure of the plane, it is imperative that inspections are performed and that the inspections are reliable.

One possible cause of failure in titanium alloys is the occurrence of hard alpha defects that are caused by nitrogen and/or oxygen impurities in the metal. Hard alpha inclusions, also known as high interstitial defects (HID), are localized regions that are contaminated by oxygen and/or nitrogen impurities, which cause a region of substantially higher hardness than the surrounding material. These brittle regions then act as stress concentrators in the material and can be a source of crack initiation that eventually leads to failure. The defects are irregularly shaped and cover a wide range of sizes. Figure 1 shows a typical hard alpha defect as reconstructed using a series of optical micrographs. The hard alpha defects are often associated with cracks and voids, which may be detected using present ultrasonic and eddy-current procedures. Subsurface hard alpha defects that are found in production are almost always associated with cracks or voids. These hard alpha regions, being more brittle than nominal material, generally crack prior to the surrounding material, thereby acting as origins for fatigue crack growth.

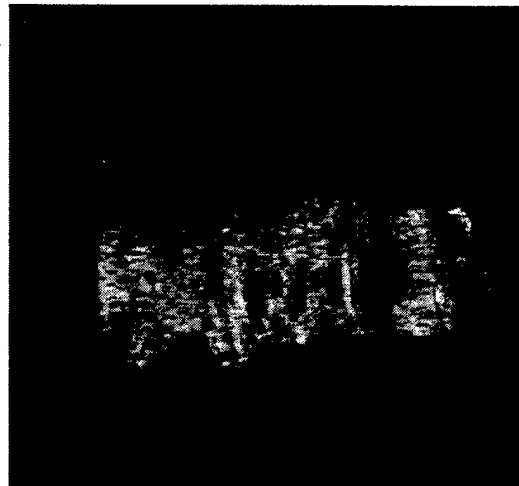


FIGURE 1. THREE-DIMENSIONAL RECONSTRUCTION OF OPTICAL MICROGRAPHS FOR A TYPICAL HARD ALPHA DEFECT

In the fall of 1989, the U.S. Congress convened a series of hearings that resulted in an amendment to the Federal Aviation Act of 1958 and established the Catastrophic Failure Prevention Act. Also in the fall of 1989, the Federal Aviation Administration (FAA) formed the Titanium Rotating Components Review Team (TRCRT), which was chartered to review the design, manufacturing, inspection, and life management procedures of titanium rotating

components and to make recommendations for improvement of their structural integrity. To accomplish this mission, the TRCRT interviewed over 20 organizations and facilities to assess industry practices in the design and manufacturing phases of the life cycle of titanium components. The results of this review were released in report form on December 14, 1990, and presented in an industrial forum in 1991. According to the report, hard alpha was involved in the Sioux City, Iowa crash of July 1989. The TRCRT report is comprehensive in its evaluation of the titanium industry and concludes that cost-effective safety improvements are possible. The report also included recommendations for improvements in the capability to detect subsurface hard alpha in the absence of a crack or void as well as improvements in the ability to detect the resulting cracks in service.

To address the safety critical issues involved with engine inspection, particularly of titanium components, the FAA-Center for Aviation Systems Reliability (CASR) staff worked with the FAA and the three major U.S. engine manufacturers to form a consortium of university research staff and engine manufacturers to work with titanium producers and airline personnel to tackle this problem. The consortium was established in an initial meeting at the FAA William J. Hughes Technical Center in June 1992. The consortium includes Iowa State University, AlliedSignal Engine Division, General Electric Aircraft Engines, and Pratt & Whitney. In response to inspection recommendations included in the TRCRT report, the Engine Titanium Consortium (ETC) began technical work in 1993. The objective of the consortium was to provide the FAA and the manufacturers with reliable and cost-effective new methods, and/or improvements in mature methods, for detecting cracks, inclusions, and imperfections in titanium.

The ETC Phase I program was organized as four major tasks with interdependencies as shown in figure 2. A key component of effective inspection system development and validation includes the provision of representative samples and accurate materials characterization data. Because of the infrequent occurrence of natural hard alpha defects, a crucial contribution of this task is the development and subsequent utilization of metallurgical processes to produce simulated hard alpha. Additional samples for measuring sensitivity improvements of the systems being developed include flat bottom holes and notch samples in both titanium and aluminum.

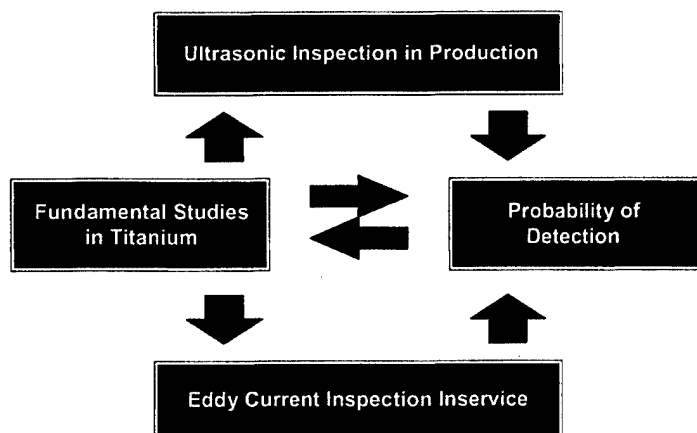


FIGURE 2. TASK RELATIONSHIPS FOR THE ETC PROGRAM  
(The fundamental studies effort supported the material property and sample needs for the program.)

A critical aspect of inspection system development is the effect of material variability on detectability. Materials characterization measurements included ultrasonic amplitude response, velocity, attenuation, and backscattered grain noise. These measurements were made as a function of position to track microstructural variations that occur within regions in a billet (near-surface, midradius, center), from billet-to-billet, and within forgings. Microstructural and macrostructural studies were completed to allow correlation with material property measurements. Details of the sample preparation methods are included in respective sections below.

## 2. BACKGROUND.

Our ability to detect hard alpha inclusions depends primarily on (1) the relative ultrasonic impedances of hard alpha material and unflawed host metal and (2) the crystalline microstructure of the host. The first determines the size of an ultrasonic echo from a hard alpha defect, and the second determines the size of competing noise echoes scattered from grain boundaries. Titanium alloys representative of those used in the manufacture of aircraft engines were identified for this study and appropriate amounts of the material procured. The materials chosen include Ti 6-4 and Ti-17, which provide examples of alpha stabilized and beta stabilized alpha-beta alloys respectively. Material procured from participants and from their suppliers was used to prepare samples with known defect conditions. The parent materials were also studied to provide baseline information on nondestructive evaluation (NDE) characteristics. The various sample types included the following:

- Flat bottom holes (FBH) of different sizes were drilled into flat and cylindrical machined samples. These represent the "ideal" air-backed defect and provide a quantifiable target to demonstrate increased detection sensitivity.
- Synthetic hard alpha defects (SHA) were produced in cylindrical rods of different diameters. The rods were then sliced into appropriate lengths, placed in titanium blocks and hipped. These provide a simulation of hard alpha defects for use in quantitative studies of detectability without the presence of cracking or voiding.
- Surface discontinuities: Surface defects were studied using specimens currently available from the participating companies and on loan from the Air Force. The samples were produced by notching the specimens, initiating cracks from the notches, machining off the notches, and then stressing to propagate the cracks to the length/depth desired.
- Subsurface hard alpha defects: Subsurface hard alpha defects were created using SHA seeds representing typical hard alpha defects. The seeds were positioned in bars of Ti 6-4 that were then machined to provide fatigue specimens with seeds at known depths. The intent was to provide a more realistic situation whereby cracking propagates from a defect through a peened surface, rather than the traditional approach of crack growth followed by peening.

Details of the samples, including their descriptions and serial numbers, are included in appendix A.

### 3. OBJECTIVES.

- To measure and document those properties of hard alpha material and the host alloys (Ti-17, Ti 6-4), which strongly affect the detectability of hard alpha defects in billets and forgings.
- To provide special-purpose specimens and property data in support of other related ETC tasks.

For hard alpha material, the relevant properties are the density and the speeds of longitudinal and shear sound waves, all of which are functions of the nitrogen contamination level. For the host alloy, the pertinent properties are the density, speeds of sound, ultrasonic attenuation, and microstructural figure-of-merit (FOM). The latter is a measure of the inherent noise-generating capacity of the alloy. Both the attenuation and FOM are strongly dependent on frequency, and their values were measured at typical inspection frequencies (5-15 MHz).

There were two motivations of the ETC fundamental studies efforts:

- To improve current inspection practices on the shop floor. By gaining insight into how the fundamental properties of titanium are likely to affect a given inspection, recommendations can be made on more optimal choices of inspection parameters (probe selection, wave type, incident angle, water path, gain setting, etc.)
- To aid in the development and testing of computer models of ultrasonic inspection processes being pursued under other ETC tasks. Those models are designed to predict such things as incident pressure fields within billets, echoes from hypothetical defects, properties of the backscattered noise, and signal-to-noise (S/N) ratios. If the models are shown to make accurate predictions, they could be of significant help in optimizing inspections and estimating detection reliability. The material properties are necessary inputs for the models. Property values for specific specimens will be provided for inclusion in detailed model testing and to build a database of representative property values for more general use.

### 4. APPROACH.

The research program included two major components: specimen fabrication and ultrasonic property measurements. The fabricated specimens fall into three classes:

- Hard alpha batch specimens
- Coupons cut from representative Ti 6-4 and Ti-17 billets and forgings
- Special-purpose specimens

Several batches of synthetic hard alpha material with varying levels of nitrogen contamination were produced. Some of the material was machined into centimeter-sized cubes for density and sound speed measurements and some was machined into small spheres or cylinders for insertion as synthetic defects in special-purpose specimens.

Several dozen coupons of unflawed metal alloy, typically 3" cubes, were cut from representative Ti-17 and Ti 6-4 billets and forgings for use in property measurements. The ultrasonic properties, particularly the attenuations and noise FOM values, proved to be quite sensitive to details of the microstructure, which, in turn, were determined by the processing history (e.g., heat treatment, mechanical working). In addition to specimen-to-specimen differences arising from processing differences, ultrasonic properties were observed to vary with position within a given specimen. Thus when surveying the properties of Ti-17 and Ti 6-4 alloys, it was prudent to select a representative sample of specimens and to cut multiple coupons from each. Property measurements were generally made in three independent directions; namely, the radial, axial, and hoop direction of the original billet or forging from which the coupon was obtained.

To support other ETC tasks, a number of special-purpose specimens were fabricated and included the following:

- Rectangular defect blocks containing arrays of small FBHs or SHA defects
- Enlarged grain block
- Probability of detection (PoD) random defect block billet
- Eddy-current specimens

For the most part, measurements on the special-purpose specimens were made under other ETC tasks and are not described in this report. The only notable exception is the enlarged grain block (EGB), a 1/4" thick plate of unflawed Ti 6-4 material that was heat treated to produce very large macrograins. With this specimen, property measurements could be made within single macrograins, allowing the elastic constants of generic Ti 6-4 material to be determined. This information then allows one to compare hypothetical grain boundary echoes with those from hard alpha defects. All measurements and analyses using the EGB are reported herein.

## 5. RESULTS.

### 5.1 EFFECT OF HARD ALPHA COMPOSITION ON INSPECTABILITY.

#### 5.1.1 Introduction.

Detecting hard alpha inclusions in titanium rotating aircraft engine parts is difficult because they are only slightly different in composition from the surrounding titanium, and show little detectable response when interrogated with sensor energies such as x-rays or ultrasound. They are much more difficult to detect than open metal flaws (such as cracks and voids) that have the same size, shape and orientation. However, detection difficulties notwithstanding, critically sized flaws must be detected because their presence can significantly degrade the material performance, under cyclic stress and temperature [1, 2, and 3].

Hard alpha occurs when nitrogen and/or oxygen stabilize the alpha phase in titanium [4, 5, and 6]. For increasing weight percent nitrogen, the ultrasonic velocity, density, hardness, and brittleness of a hard alpha inclusion also increase proportionally. The increase in the hardness and brittleness of an included flaw potentially increases the risk of material failure. For inclusions containing from 3.5 wt.% N to 14.8 wt.% N, hardnesses were measured from

Rockwell C 50 to 80, compared to Rockwell C 32 to 36 for the base Ti-6Al-4V (Ti 6-4) material. Fortunately, this increase in risk is balanced by increases in ultrasonic reflectance and therefore detectability. This section reports on work that is directed toward determining the physical nature of the hard alpha inclusion. The role composition plays in determining an inclusion's ultrasonic reflectance is a key relationship required in understanding the detectability of hard alpha. In addition, this section tabulates fundamental hard alpha property data that is necessary to provide risk assessments for engine fleet management.

In order to determine the detectability of hard alpha inclusions, it was necessary to develop methods to make unvoided and uncracked synthetic hard alpha inclusions of known composition, to measure their composition and physical properties, and to incorporate them into calibration blocks fabricated from aircraft engine titanium alloys. Once these blocks were fabricated, the ultrasonic detectability of the inclusions could be determined from C-Scan images and from other ultrasonic data. In the following sections each of these steps will be reported in brief but comprehensive detail.

Nondestructive inspection of titanium parts includes ultrasonic techniques to find hard alpha [7 and 8]. Extensive work has related microstructure of the titanium matrix alloy to the ultrasonic noise produced by that microstructure [9, 10, 11, and 12]. This is very important because the ultrasonic detection of any discontinuity or flaw is usually dependent on the amplitude of the signal reflected by the discontinuity being greater than the signals reflected by the microstructure of the host material. In the case of very fine-grained materials, the ultrasonic noise is of sufficiently low amplitude that the electronic noise from the amplifiers usually establishes the lower limit for detection. For relatively large grain materials, such as titanium, the lower limit for signal detection is usually established by the unwanted ultrasonic echoes from the microstructure, i.e., the ultrasonic noise. For either situation, the signal-to-noise ratio (S/N), the ratio of the flaw amplitude to the noise amplitude) defines the capability of an inspection method to detect a flaw, and the PoD for a flaw producing that reflected signal amplitude.

### 5.1.2 Preparation of Synthetic Hard alpha Samples.

#### 5.1.2.1 Preparation of Titanium-Nitrogen-Oxygen Alloys: Synthetic Hard Alpha Inclusions.

Titanium-nitrogen samples were prepared by three techniques: (1) hot isostatic press (HIP) consolidation of blended titanium and titanium nitride powders; (2) arc melting of titanium sponge in a nitrogen-containing atmosphere; and (3) arc melting of sponge titanium plus titanium nitride powder. Each technique produced titanium-nitrogen alloys containing a certain amount of oxygen carried in with the constituent raw materials.

1. HIP consolidation of titanium powder blends. Five compositions were prepared by mixing 16 g samples of powder. The powders used were Baker Ti powder, Lot 512350, and CERAC TiN, Lot 2332. The five nominal compositions prepared were 12.8; 6.8; 4.7; 3.5; and 1.8 wt.% (33.3; 20.0; 14.3; 11.1; 5.9 atomic %) nitrogen. The powders were blended by rolling in jars for 20 hours. The powders were HIPped at 1400°C, 210 MPa for 3 hours. The container used to hold the powder during the HIP process was made from a drilled rod of Ti 6-4.

2. Vacuum arc melting of titanium sponge in a nitrogen-containing atmosphere. Two alloy compositions were made by melting titanium sponge in a nitrogen atmosphere. First, 333 g of titanium sponge was arc-melted in a static environment of argon-15 volume% nitrogen. The metal was melted into a small cylindrical button, about 75 mm (3 in.) in diameter. The alloy was melted three times in the argon-nitrogen atmosphere. Then, the ingot was melted three times in an argon atmosphere (no nitrogen) to homogenize the composition. The metal was weighed before and after every melting step, with the weight change assumed to be due to nitrogen uptake. The ingot was then HIPped at 1300°C, 210 MPa for 3 hours. Two ingots were made in this manner; one was estimated to contain 5.1 wt.% nitrogen, the other 4.4 wt.% nitrogen. These nitrogenated ingots were cut into pieces and were melted with titanium sponge to produce two further ingots, with target compositions 2.5 and 1.5 wt.% (8.1 and 5.0 at%), based on the assumed compositions of the nitrogenated ingot. These ingots were melted in an argon atmosphere three times each, with the ingot flipped each time. The ingots were then HIPped at 1300°C, 210 MPa for 3 hours.
3. Vacuum arc melting of sponge titanium plus titanium nitride powder. This method appears to be the most effective and most reproducible process for manufacturing synthetic hard alpha samples. During ETC Phase I, approximately 20 compositions were prepared by electron beam melting a mixture of titanium sponge and titanium nitride powder (Alfa, Lot 082782) in an argon atmosphere. The ingots were melted three times, flipping the ingot over after each melt. After melting, the ingots were HIPped at 1300°C, 210 MPa for 3 hours. The target compositions were 7 wt.% (20.5 at%), 5 wt.% (15.3 at%), 3.5 wt.% (11.0 at%) and 2.0 wt.% (6.5 at%) nitrogen, and heat weights were calculated assuming the TiN powder was stoichiometric, i.e., contained 22.63 wt.% (50 at%) nitrogen.

Having determined the most reliable and reproducible method for making synthetic hard alpha material, (method 3, above) this method was then used to produce SHA defects (seeds) for insertion into Ti-alloy blocks. Two arc-melting furnaces were used to produce the SHA material, denoted RAM and VAM, respectively. Individual heats of SHA material were identified by the furnace descriptor and a four-digit code number, such as RAM1237. The SHA material itself was used to produce the inclusion blocks listed in table 1 and a small number of additional blocks used for sectioning and analysis.

#### 5.1.2.2 Chemical Analyses.

The oxygen and nitrogen analyses listed in table 2 are for samples made by the three methods described above. Nitrogen was determined by acid dissolution and titration, and oxygen by using a LECO TC-136 oxygen/nitrogen analysis machine (LECO, 3000 Lakeview Ave., St. Joseph, MI 49085-2396).

TABLE 1. LIST OF BLOCKS CONTAINING SHA DEFECTS CONSTRUCTED DURING FAA-ETC PHASE I AND/OR USED FOR DATA ACQUISITION IN THE COURSE OF THE PROGRAM

Block Name/Serial No.	Defect Description	Seed Composition (wt.% N) and Furnace Heat No.
Ti 6-4 Block S940119-1.6N	90° Cylindrical Seeds	1.6%N-RAM1237
Ti 6-4 Block S940128-2.6N	90° Cylindrical Seeds	2.6%N-RAM1234
Ti 6-4 Block S940217-5.9N	90° Cylindrical Seeds	5.9%N-RAM1228
Ti 6-4 Block SA940314-5.2N	45° Cylindrical Seeds	5.2%N-RAM1227
Ti 6-4 Block SA940512-2.8N	45° Cylindrical Seeds	2.8%N-RAM1232
Ti 6-4 Block SA940513-1.5N	45° Cylindrical Seeds	1.5%N-RAM1235
Ti-17 Block SA941201-2.8N	45° Cylindrical Seeds	2.8%N-RAM1232
Ti-17 Block S941202-2.8N	90° Cylindrical Seeds	2.8%N-RAM1232
Ti-17 Block S950316-1.5N	90° Cylindrical Seeds	1.5%N-RAM1235
Ti-17 Block SA950317-5.2N	45° Cylindrical Seeds	5.2%N-RAM1227
Ti-17 Block S950320-5.2N	90° Cylindrical Seeds	5.2%N-RAM1227
Ti-17 Block SA950321-1.5N	45° Cylindrical Seeds	1.5%N-RAM1235
Ti 6-4 Block R062697-Sphere	Spherical Seeds, 5 sizes	5.9%N, 4.8%N, 3.8%N, 3.1%N, 2.5%N (various)
Ti 6-4 Random 10" Billet Block	Several dozen cylindrical and/ or spherical seeds with randomized sizes, depths, and orientations	2.7%N, 4.5%N, 5.9%N, 20.0%N (various heats)

TABLE 2. CHEMICAL ANALYSIS OF SYNTHETIC HARD ALPHA MATERIAL

Serial No.	Preparation Method	Nominal wt.% (at%) N	Measured wt.% (at%) N	Measured wt.% (at%) O
Ti	Baker Powder	0.0	Not measured	2.787 (7.90)
TiN	Alfa 082782	22.6 (50.0)	16.22 (39.50)	0.586 (1.25)
PB2	Powder Blend	12.8 (33.3)	10.73 (28.35)	1.733 (4.01)
PB4	Powder Blend	6.8 (20.0)	5.91 (17.02)	2.227 (5.62)
PB6	Powder Blend	4.7 (14.3)	4.06 (12.11)	2.427 (6.34)
PB8	Powder Blend	3.5 (11.1)	3.11 (9.46)	2.487 (6.62)
PB16	Powder Blend	1.8 (5.9)	1.45 (4.55)	2.720 (7.48)
VAM 1224	Arc melt in Ar-N <sub>2</sub>	2.5 (8.1)	2.72 (8.66)	0.39 (1.09)
VAM 1202	Arc melt in Ar-N <sub>2</sub>	1.5 (5.0)	1.62 (5.30)	0.34 (0.97)
RAM 1228	Arc melt TiN + Ti	7.0 (20.5)	5.88 (17.46)	0.465 (1.21)
RAM 1229	Arc melt TiN + Ti	5.0 (15.3)	3.48 (10.90)	0.296 (0.81)
RAM 1234	Arc melt TiN + Ti	3.5 (11.0)	2.61 (8.36)	0.234 (0.66)
RAM 1237	Arc melt TiN + Ti	2.0 (6.5)	1.61 (5.28)	0.233 (0.67)

The Ti-N samples made from powder blends have high levels of oxygen. The oxygen in these Ti-TiN powder blends appears to be supplied chiefly by the Ti powder. The analyzed nitrogen levels of the powder blends are systematically below the nominal levels. The nitrogen levels are consistent with the CERAC TiN powder having an actual composition of 43 at% N (Ti-N<sub>0.75</sub>). The Ti-N alloys made by melting in a nitrogen atmosphere have a slightly higher nitrogen content than that predicted from weight change—likely resulting from titanium metal evaporating during the melting step, since all weight changes were assumed to be due to nitrogen uptake.

The nitrogen contents of the alloys made by melting TiN plus Ti sponge are lower than nominal. The analyzed values are consistent with the nitrogen content of the TiN used. This TiN, Alfa lot 082782, was analyzed and found to contain 39.5 at% N.

Figure 3 displays the ternary Ti-N-O phase diagram on which solvus lines at 1300° and 1400°C are formed both by extensions from the binary phase diagrams [4] and also from experimental data in which the  $\beta$  phase extends out to about 7.7 percent N and 6.7 percent O at 1400°C [13]. Using the phase fields drawn from extensions from the binary diagrams, the powder blend alloys PB8, PB6, and PB4 would be in a single-phase  $\alpha$  field at 1400°C HIP temperature; and PB2 would be in the TiN field at 1400°C HIP. Based on the binary Ti-N diagram, the PB2 composition should transform from a nitrogen-lean TiN to  $\alpha$  + Ti<sub>2</sub>N on cooling. The experimentally determined  $\alpha$ + $\beta$  phase field would contain the PB16 composition. Metallography of PB16, figure 4, reveals a fine grain structure with a small amount of a second phase, which is consistent with this composition being in the two-phase field but near the boundary with the all- $\alpha$  field. The higher nitrogen composition powder metallurgy alloys appear to be single phase.

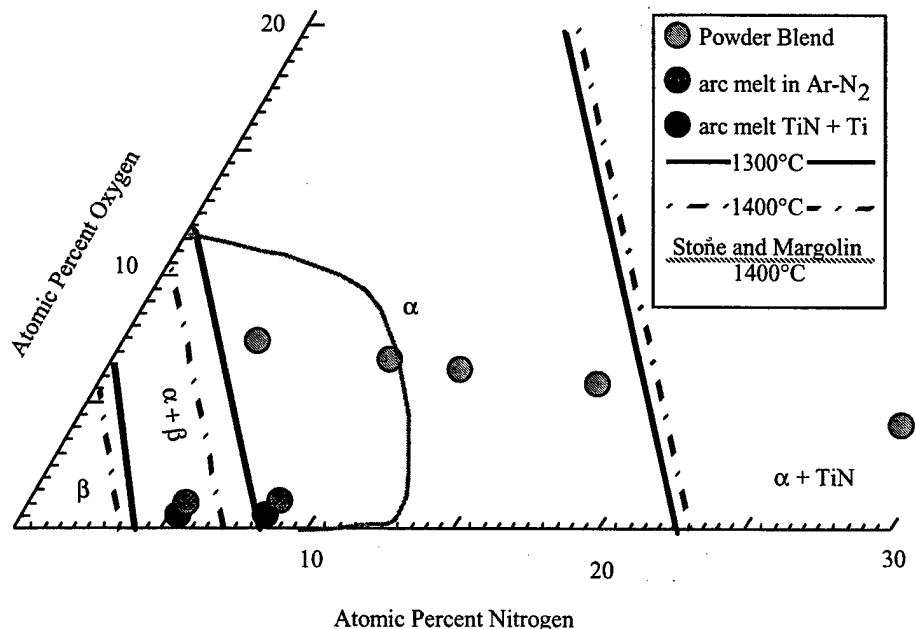


FIGURE 3. TERNARY Ti-N-O PHASE DIAGRAM, LOCATING ANALYZED SYNTHETIC HARD ALPHA COMPOSITIONS

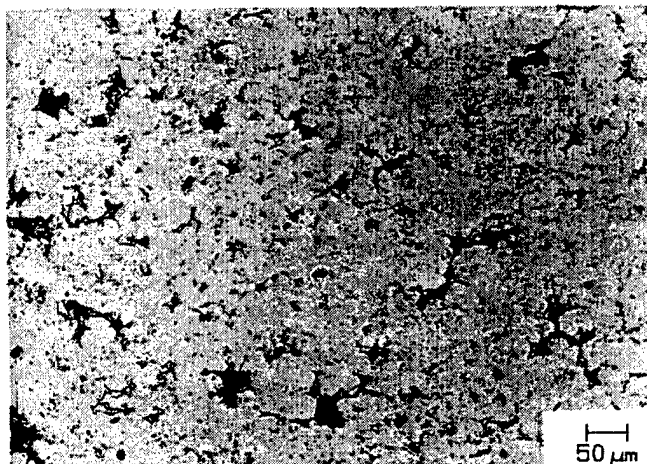


FIGURE 4. MICROSTRUCTURE OF POWDER METALLURGY COMPOSITION  
Ti- 4.55 at% N- 7.48 at% O, PB16

The low nitrogen ingot melting compositions, VAM 1202 and RAM 1237 would lie well into the  $\alpha + \beta$  field at 1300°C HIP temperature. VAM 1224 and RAM 1228 would lie near the border of the  $\alpha + \beta$  and the all- $\alpha$  fields. RAM 1229 and RAM 1234 would be in an all- $\alpha$  field, see table 2.

#### 5.1.2.3 Sound Velocity Measurements.

Longitudinal and shear wave velocities were measured in the Ti-N-O materials. For the powder metallurgy alloys, the velocity was measured on slices of the HIPped alloys. For the arc-melted compositions, the velocities were measured on small rectangular parallelepipeds, about 1 cm (0.4 in.) on an edge. Additionally, velocities were measured in Ti 6-4 and Ti-17 alloys. Separate broadband ultrasonic transducers were used to produce longitudinal and shear wave pulses in the sample materials.

The electronic apparatus for transmitting and receiving the ultrasonic pulses was a 250-MHz bandwidth CAUM-3000 ultrasonic system developed at General Electric (GE). The pulse travel times were measured with a Tektronix 7864 dual-beam oscilloscope containing a 7A26 vertical amplifier, a 7B85 delaying time base, a 7B80 delayed time base, and a 7D15 counter-timer. The counter-timer was set to average 1000 ultrasonic pulse travel times and then to display the averaged time. Warmed up and stabilized, this combined system produced delay-time measurements with a jitter of less than 0.3 ns.

An alternative method for time measurement used a Tektronix 2445 analog oscilloscope. The time base settings were selected such that the delay time between pulses was reported to  $\pm 5.0$  ns. This system was used for the thicker samples, i.e., for the longer travel times.

The samples measured in this work were nominally 6.35 to 12.7 mm (1/4 to 1/2 in.) in thickness, and the precision in thickness measurement was typically to  $\pm 2.5$   $\mu$ m. The resulting precision was no worse than  $\pm 0.03\%$  of the sample thickness. Depending on the sample thickness and the propagation mode being measured, the ultrasonic round trip travel times between adjacent echoes in the samples were approximately 2.0 to 4.0  $\mu$ s for longitudinal waves and 4.0 to 8.0  $\mu$ s

for shear waves. The delay time between two successive time-domain echoes was determined by the pulse superposition method [14]. In this method one determines the time shift that must be applied to the second echo to bring it into approximate coincidence with the first echo. The leading edge and the phase of the second echo is brought in with that of the first echo. Therefore, for the material being measured, the method effectively leads to an averaged value of the group and phase velocities. Depending on which oscilloscope assembly was used, the delay times were measured to precisions of  $\pm 1$  or  $\pm 5$  Ns. Since the lower precision system was used only for the thicker samples, the overall precision for all the velocity measurements (twice thickness divided by time) is no worse than  $\pm 0.1\%$  of the reported value. The sound velocity results are listed in table 3.

TABLE 3. MEASURED SOUND VELOCITY OF Ti ALLOYS AND SYNTHETIC HARD ALPHA MATERIAL

Serial No.	Measured N, at%	Measured O, at%	Longitudinal Velocity m/s	Shear Velocity m/s
PB2	28.35	4.01	7,902	4,350
PB4	17.02	5.62	7,470	4,210
PB6	12.11	6.34	7,110	3,930
PB8	9.46	6.62	7,030	3,780
PB16	4.55	7.48	6,560	3,490
VAM 1224	8.66	1.09	6,568	
VAM 1202	5.30	0.97	6,442	
RAM 1229	10.90	0.81	6,713	
RAM 1234	8.36	0.66	6,543(6,534 <sup>a</sup> )	(3,510 <sup>a</sup> )
RAM 1237	5.28	0.67	6,349(6,333 <sup>a</sup> )	(3,340 <sup>a</sup> )
Ti 6-4			6,175	3,151
Ti-17			6,055	3,110

<sup>a</sup>ISU results averaged over propagation direction.

Velocity measurements using the pulse superposition method were also performed at Iowa State University (ISU) on two of the specimens, RAM 1234 and RAM 1237 [15]. The sound speed was found to depend slightly on the direction of propagation through the specimen, with a typical difference of 0.5% between the high- and low-speed directions. Sound speeds measured at ISU, and averaged over direction, differed by about 0.2% from those reported by GE.

#### 5.1.2.4 Incorporation of Ti-N-O Seeds in Ti 6-4 Blocks.

Seeds made from the Ti-N-O alloys were placed as inclusions within Ti 6-4 blocks to enable study of ultrasonic reflectance and detectability as a function of seed composition. All of the calibration blocks containing arc-melted Ti-N-O alloy inclusions were produced essentially in the same way. The procedure was to place cylindrical or spherical inclusions into holes drilled into a face of a Ti 6-4 block, usually 51 to 53 mm thick. This face was then covered with a mating plate of Ti 6-4, 25 to 26 mm thick. The assembly was clamped in position in a vacuum

chamber and the edges of the mating interface were electron beam welded all around leaving only the interior unbonded. The interior interface between the cover plate and the block was then diffusion bonded using a HIP apparatus. The most successful HIP conditions for Ti 6-4 were 3 hours at 954°C and 105 MPa or 954°C and 210 MPa. These were selected to assure good bonding, to minimize nitrogen diffusion out of the inclusion, and to minimize changes in the phase volume and microstructure of the Ti 6-4 host. Ti-17 was bonded at the same pressures and times but at 900°C because of the lower  $\alpha - \beta$  transition for that alloy.

The cylindrical inclusions, small Ti-N-O cylinders with lengths approximately equal to their diameter, were produced by traveling wire electro-discharge-machining (EDM) followed by etching in a solution of 30% nitric acid and 10% hydrofluoric acid. Figure 5 illustrates the transverse microstructure of an 0.8-mm-diameter (0.032-in.) cylinder of VAM 1202 HIPped in Ti 6-4 at 900°C, 105 MPa. The noncircular cross section is due to a small protuberance where the EDM cut began and ended, and the facetting is due to etching. Both metallographic observations of the original inclusion and subsequent ultrasonic tests of the HIPped blocks verified that none of the inclusions appeared to be cracked.

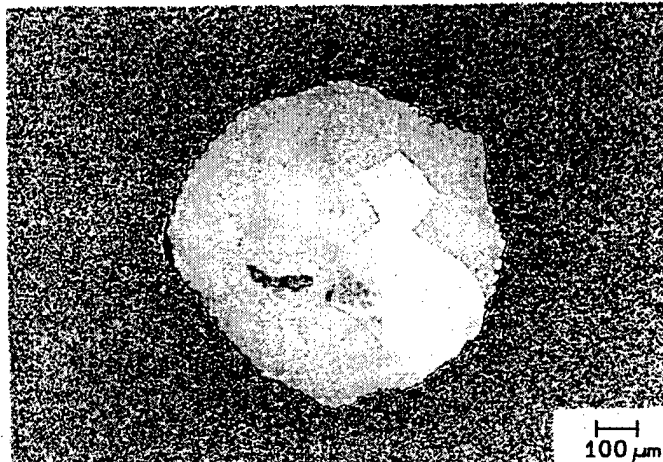


FIGURE 5. MICROSTRUCTURE OF AN 0.8-mm-DIAMETER INCLUSION OF Ti- 5.30 at% N- 0.97 at% O, HIPPED IN Ti 6-4 AT 900°C, 105 MPa, FOR 4 HOURS

One set of Ti 6-4 blocks, S/N 93-1, 93-2, 93-3, 93-4, containing inclusions from arc-melted Ti-TiN compositions had face dimensions 50 by 50 mm (2 in.). One inclusion each of RAM 1237, RAM 1234, RAM 1229, and RAM 1228 was placed in each block in a square array. The inclusions were cylindrical in shape, 1.9 mm diameter and 1.9 mm long (0.075 in.), and the cavity was slightly larger, 2 mm (0.078 in.). The blocks were 25 mm (1 in.) thick, and the cover plates were 13 mm (0.5 in.) thick. The blocks were HIPped at 900°C, 105 MPa.

The inclusions within one of these blocks are illustrated in figures 6 through 9. After ultrasonic inspections of block 93-1, the block was cut into fourths, each piece containing one inclusion. Each piece was then polished to the midplane ( $r-z$ ) of the inclusions. With reference to the figures, each inclusion is oriented with the cylindrical axis horizontal; and the bond line in the Ti 6-4 host is vertical, along the right face of the inclusion. The low nitrogen compositions,

RAM 1237 and RAM 1234, are essentially single phase; however, both exhibit plate-like etching traces of a transformed beta microstructure, consistent with these chemistries containing  $\beta$  phase during the 1300°C HIP of the Ti-N-O ingot. The high nitrogen compositions, RAM 1229 and RAM 1228, are two-phase, probably as a consequence of the peritectic solidification reaction, where TiN is the first phase to freeze and converts to  $\alpha$ -Ti by the peritectic reaction  $L + TiN \rightarrow \alpha-Ti$ . Incompletely reacted TiN, or its transformation products, might be this second phase. The interface between the inclusions and Ti 6-4 is slightly irregular; this results from the inclusions being cleaned by chemical etching prior to HIP bonding. Inclusions from RAM 1237, RAM 1234, and RAM 1229 are uncracked on polishing. There are some cracks on the polished face of the RAM 1228 inclusion, the highest nitrogen composition, but this result is ambiguous; the cracks are very tight, do not effect the shape of grain boundaries, and are located along the edges of the inclusion, suggesting that these cracks might be due to the mechanical action during polishing or relief of residual stress. What is significant to later discussions on detectability is that the seeds with the three lowest nitrogen compositions are not cracked.

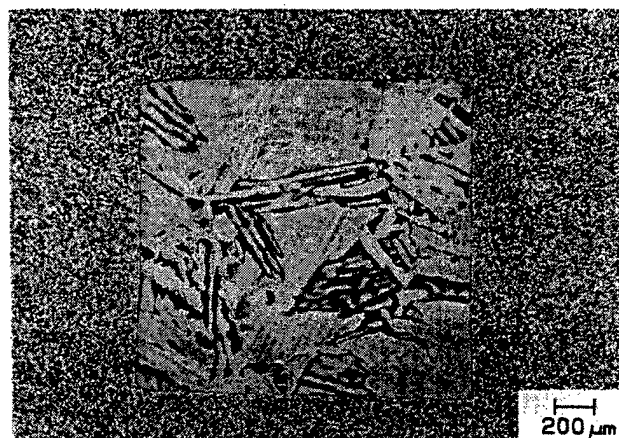


FIGURE 6. MICROSTRUCTURE OF 1.9-mm-DIAMETER, 1.9-mm LONG PIN OF Ti- 5.28 at% N- 0.67 at% O, HIPPED IN Ti 6-4 AT 900°C, 105 MPa, 4 HOURS (RAM 1237 SEED)

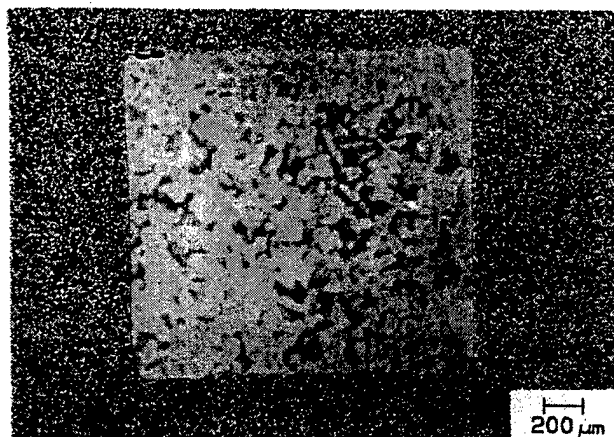


FIGURE 7. MICROSTRUCTURE OF 1.9-mm-DIAMETER, 1.9-mm-LONG PIN OF Ti- 8.36 at% N- 0.66 at% O, HIPPED IN Ti 6-4 AT 900°C, 105 MPa, 4 HOURS (RAM 1234 SEED)

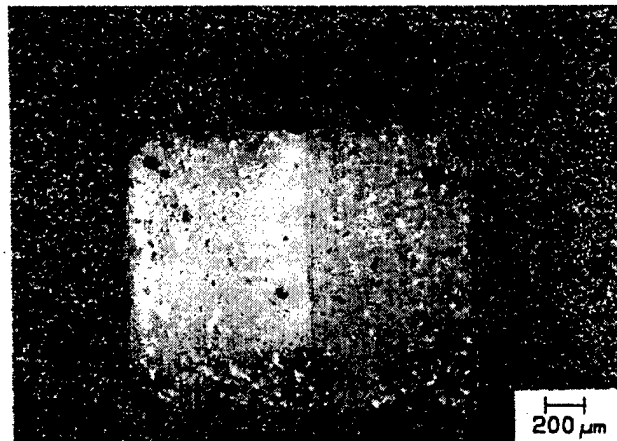


FIGURE 8. MICROSTRUCTURE OF 1.9-mm-DIAMETER, 1.9-mm-LONG PIN OF  
Ti- 10.90 at% N- 0.81 at% O, HIPPED IN Ti 6-4 AT 900°C, 105 MPa, 4 HOURS  
(RAM 1229 SEED)

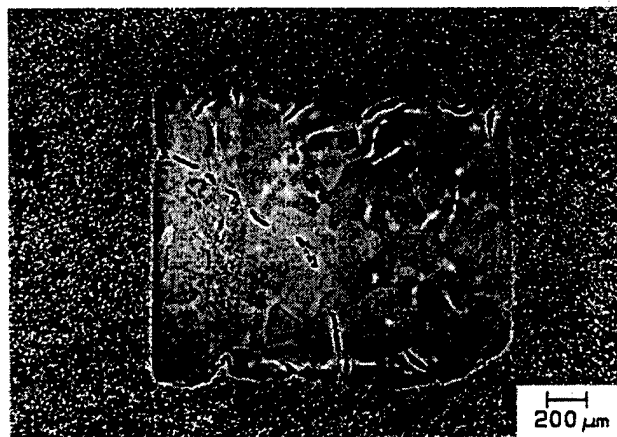


FIGURE 9. MICROSTRUCTURE OF 1.9-mm-DIAMETER, 1.9-mm-LONG INCLUSION OF  
Ti- 17.46 at% N- 1.21 at% O, HIPPED IN Ti 6-4 AT 900°C, 105 MPa, 4 HOURS  
(RAM 1228 SEED)

#### 5.1.2.5 Evaluation of the Diffusion Bond Quality in Titanium SHA Specimens.

During the diffusion bond process, parts are heated to about one half the absolute melting point, pressed together at a stress below the macroscopic yield stress, and these conditions are maintained for a specified time. Bonding proceeds through three steps:

- Local yielding of contact points upon initial application of stress
- Creep deformation on the bonding plane to yield discontinuous voids
- Closure of voids by vacancy diffusion

At the end of this process, the material is considered bonded. However, the bond plane consists of a planar array of grain boundaries between grains from opposite sides of the bond plane. This planar array may have only a fraction of the strength of the base materials. Additional thermal

exposure can permit the planar array of grain boundaries to breakup (as grains assume more equilibrium shapes and individual grain boundaries move off the bond plane) to yield a material with mechanical properties equivalent to base metal.

The ultrasonic methods that characterize diffusion bonds and distinguish between planar bonded structures and more mature structures achieved after appropriate thermal exposure will now be discussed. An ideal NDE methodology for diffusion bonds would characterize the state of the bonding region at all points in the bonding process through the point at which the bond is considered metallurgically sound. The term, metallurgically sound, will be used to denote the condition where the component material is fully attached, with no voids, cracks, or pores; and the grains in the bond region have achieved an equilibrium geometric structure, i.e., the grains at the bond region have migrated across the bond line, and the bonding plane is not metallographically apparent. This represents a return of the bonded component to an unperturbed parent material state. Figure 10 shows schematically the material features at points in the process of diffusion bonding two pieces of similar material.

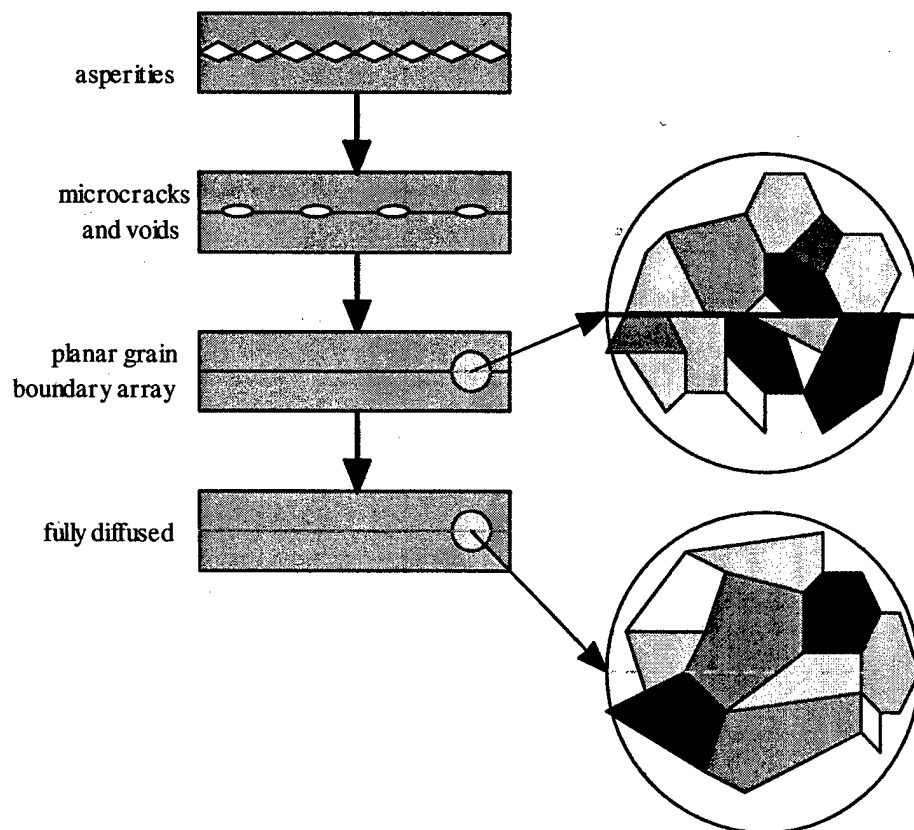


FIGURE 10. MICROSTRUCTURAL FEATURES DEVELOPED DURING THE DIFFUSION BONDING PROCESS

The structural features present on the bond line during the initial stages of diffusion bonding constitute continuous cracks, pores, and voids. There has been steady progress in NDE techniques for diffusion bonds. For the above-cited structural features that strongly reflect ultrasound, the methods to deduce void number, size, or area fraction from the analysis of the

amplitude of reflected ultrasonic signals are now established [16, 17, 18, 19, and 20]. To date, it is possible to identify the strong reflectors at the bond line (microcracks and voids) by such techniques as ultrasonic amplitude C-scan. At the diffusion bond process point where the strong reflectors at the bond line have disappeared, the grain boundaries have not moved off the bond line. This resulting planar grain boundary array is undesirable since it will not be as mechanically strong as a fully diffused bond and does not represent a return to the parent material state. The lack of strong reflectors in the planar grain boundary array makes conventional C-scan an inappropriate technique. Ojard, Buck, and Rehbein [20] may have observed such conditions; they characterized material for which C-scan imaging showed no strong reflectors, and yet the mechanical properties of the bond were weaker than those of the base metal. Thus C-scan amplitude imaging was not capable of identifying planar grain boundary arrays in material substantially absent of voids.

The following describes work that uses time-of-flight (TOF) imaging to examine bonding in the last two stages listed in table 4. Images and statistics support this technique as a viable means of evaluating such bonds.

TABLE 4. DIFFUSION BOND ATTACHMENT STEPS AND EVALUATION TECHNIQUES

Attachment Steps	Evaluation Technique
Unbonded	Pulse-Echo, C-scan
Asperities	Pulse-Echo, C-scan
Microcracks/Voids	C-scan
Attached Planar Grain Boundary Array	TOF Imaging
Fully diffused and random bond	TOF Imaging

A parametric study of diffusion bonding by HIP was carried out on blocks of Ti-17. Parameters for HIP bonding include pressure, temperature, and time. For purposes of this study, constant pressure was maintained while temperatures and times were varied. Three samples (designated 17H1, 17H2, and 17H3) were created, each being 1.5" high with the diffusion bond located 0.5" below one surface. All samples were hipped at 103 MPa pressure. Sample 17H1 was heated for 2 hours at 865°C followed by 4 hours at 800°C. Both of these temperatures are below the beta transus temperature of Ti-17, about 880°C. Sample 17H2 was heated at 910°C for 2 hours followed by 4 hours at 800°C and sample 17H3 was heated for 4 hours at 800°C. Scanning electron micrographs of these samples are presented in figure 11. The line of the diffusion bond is vertical at about the center of each sample. Note that samples 17H1 and 17H3 exhibit a bond line with a planar grain boundary array. Sample 17H2 most closely resembles the random nature of grains seen in the parent material.

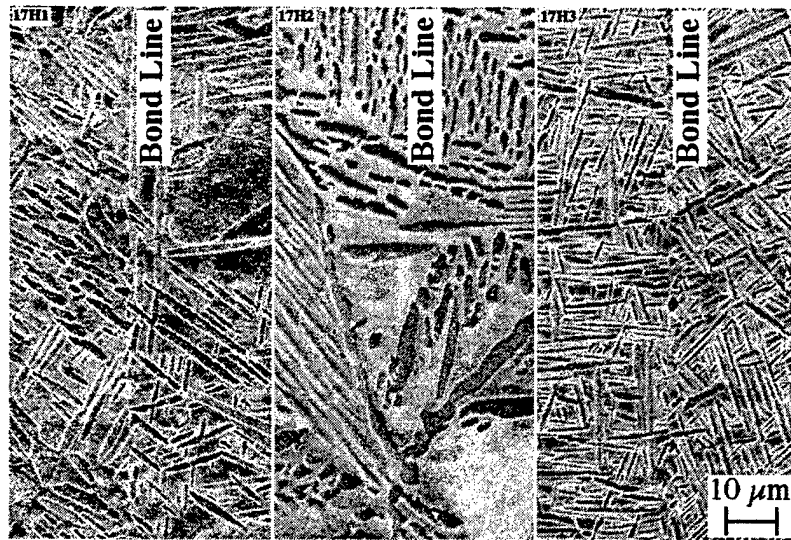


FIGURE 11. SCANNING ELECTRON MICROGRAPHS OF BOND LINES IN SAMPLES 17H1, 17H2, AND 17H3

The blocks were first examined using ultrasonic C-scan (amplitude) imaging. For each block, two scans were performed: one of the diffusion bond region and one of the parent materials to serve as a reference. Figure 12 shows the experimental setup for the two scans; the instrument settings were not modified between scans; the blocks were merely turned upside down.

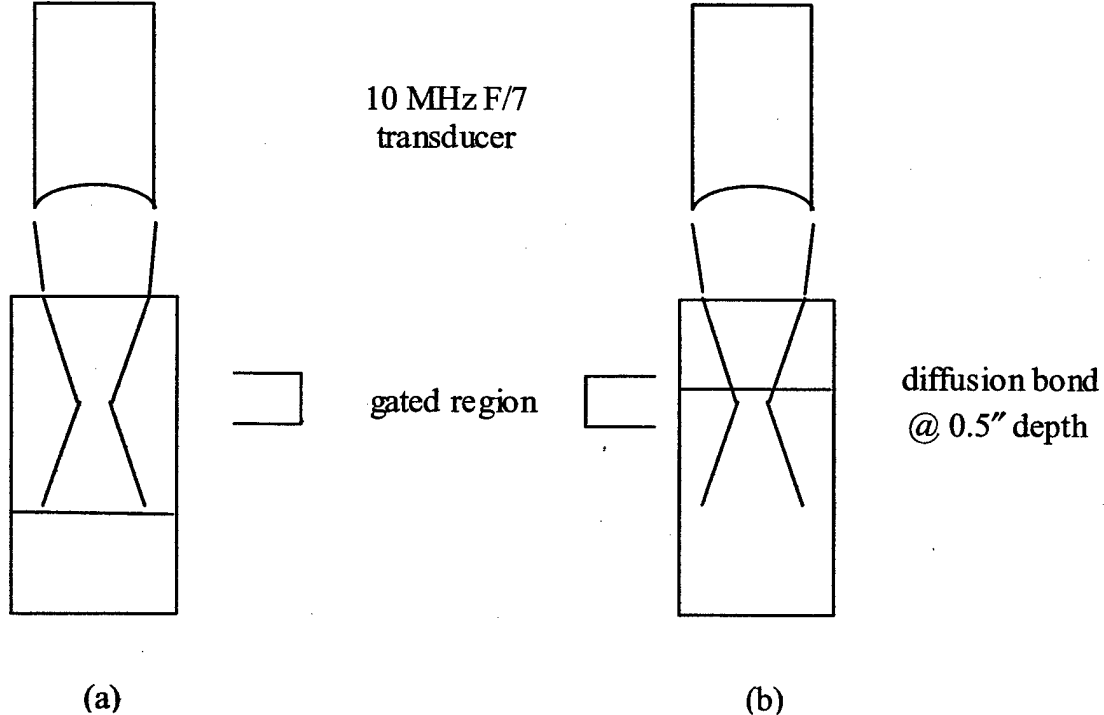


FIGURE 12. EXPERIMENTAL SETUP FOR ULTRASONIC C-SCANS OF Ti-17 BLOCKS 17H1, 17H2, AND 17H3

With reference to figure 11, the micrographs clearly show a variation in the microstructure of the diffusion bonds. C-scan images of the ultrasonic amplitude from the bonded region and their histograms, however, showed little difference between the diffusion bond and the parent material. The histograms for the diffusion bonds in samples 17H1 and 17H3 did show differences from their parent material but not enough to be statistically significant. C-scan amplitude images were not able to show clear differences among these samples.

TOF imaging was then carried out on the three blocks. Figure 13 illustrates the conceptual difference between C-scan and TOF imaging. In the traditional C-scan method, the peak signal amplitude is recorded at each transducer position. In the TOF method, the time at which the peak amplitude signal is recorded at each position. TOF data can be measured from any constant reference point—the figure shows this as the transducer main bang. The measurements on the Ti-17 blocks used the smooth front entry surface of the sample for the constant reference point.

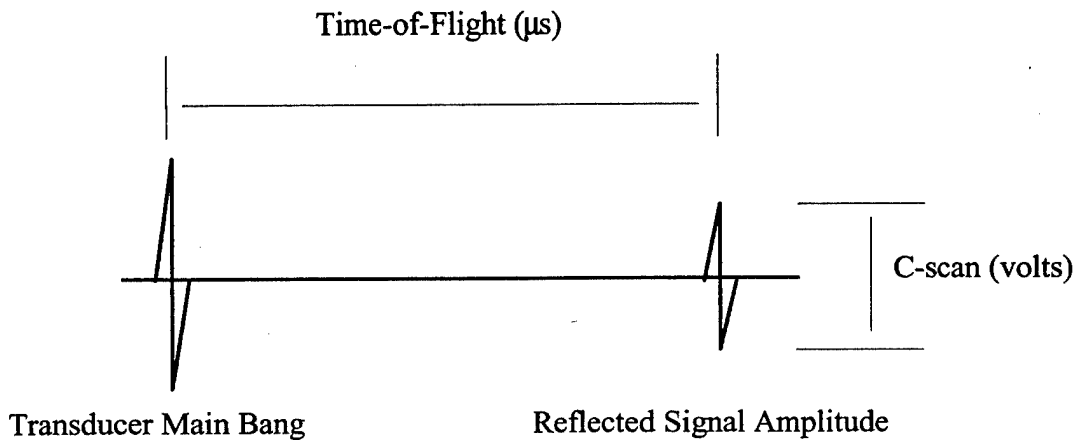


FIGURE 13. COMPARISON OF C-SCAN AMPLITUDE AND TIME-OF-FLIGHT METHODS

TOF data were acquired in the same fashion as for the C-scan amplitude data; in fact the instrument recorded both types of data at the same time. Figure 14 shows the TOF data in image form and figure 15 shows the data in histogram fashion. Alternatively, TOF data can be presented as a three-dimensional (3D) image. Figure 16 shows 3-D representations of the TOF data for two of the blocks.

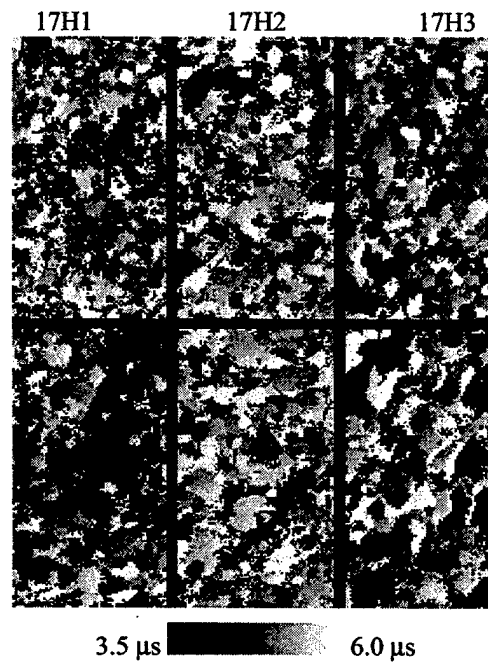


FIGURE 14. TIME-OF-FLIGHT IMAGES FOR THREE DIFFUSION-BONDED Ti-17 SAMPLES: IMAGES FOR PARENT MATERIAL (TOP ROW) AND DIFFUSION BOND ZONE (BOTTOM ROW)

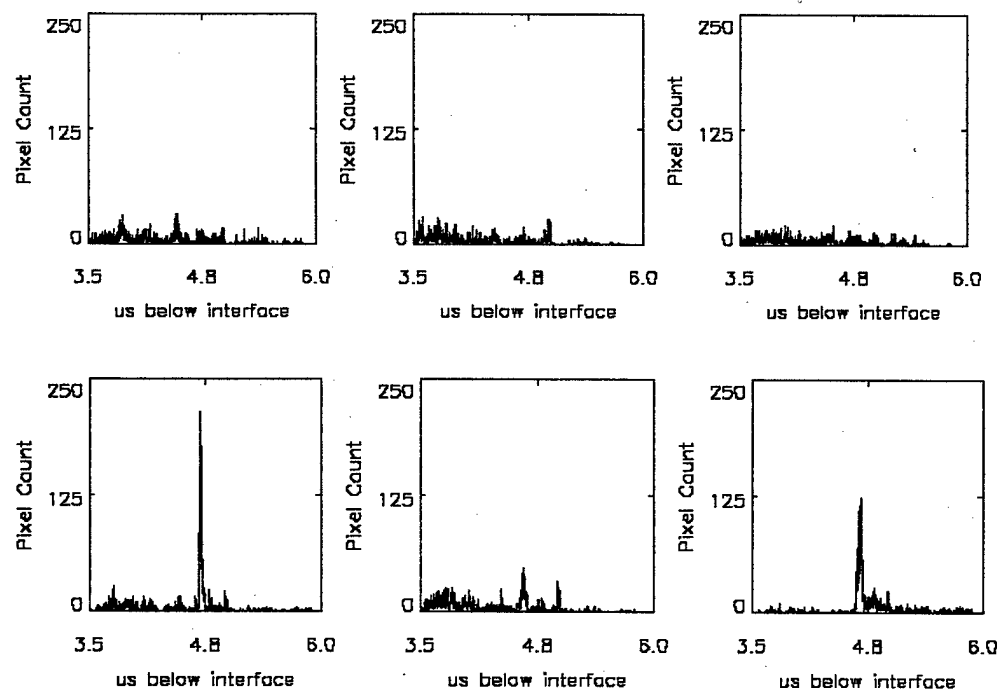


FIGURE 15. TIME-OF-FLIGHT DATA FOR THREE Ti-17 SAMPLES: HISTOGRAMS FOR PARENT MATERIAL (TOP ROW) AND DIFFUSION BOND (BOTTOM ROW)  
(From left to right, specimens are 17H1, 17H2, and 17H3.)

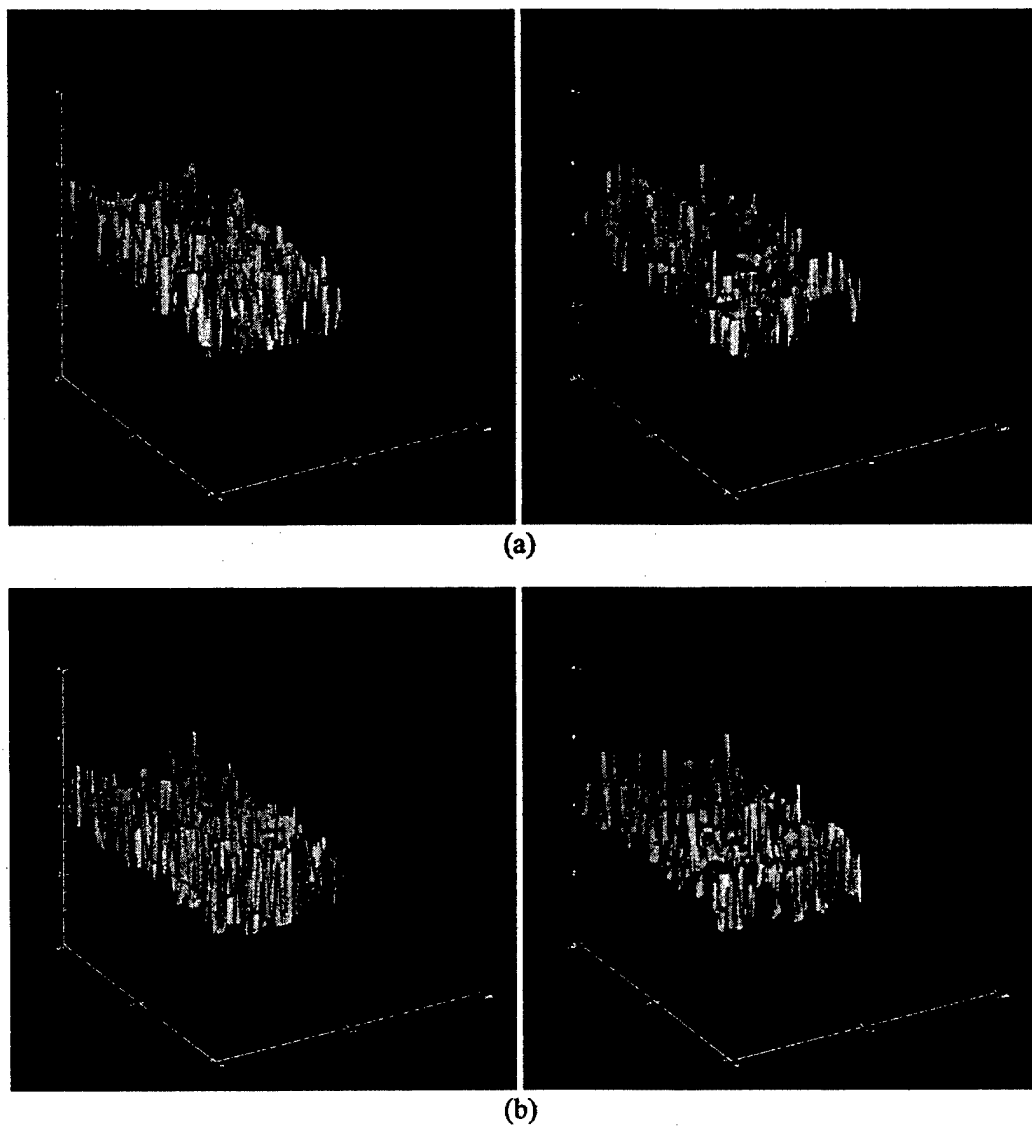


FIGURE 16. THREE-DIMENSIONAL REPRESENTATION OF TOF SCAN DATA FOR Ti-17 SAMPLE 17H1 (a) PARENT MATERIAL (LEFT) AND DIFFUSION BOND (RIGHT)—INDICATIVE OF A POOR BOND; Ti-17 SAMPLE 17H2 (b) PARENT MATERIAL (LEFT) AND DIFFUSION BOND (RIGHT)—INDICATIVE OF A GOOD BOND

The TOF data for the parent material in each sample shows a random, almost uniform distribution in time of the peak reflectors from the gated region. This would represent an underlying grain structure with no preferred orientation. The bond zone in sample 17H2, in which the diffusion bond was most similar to the parent material by microscopy, also shows TOF behavior—in the image and in the histogram—very similar to that of the parent material. This would be expected since the underlying structure/orientation of the grains at the diffusion bond closely resembles that of unperturbed parent material. On the other hand, samples 17H1 and 17H3 show a concentration of peak echoes at a particular time as seen in the images and the histogram. This time corresponds to the depth below the interface of the diffusion bond.

Since C-scan amplitude imaging records echoes from grain boundaries in both the parent material and the diffusion bond, there is nothing to distinguish one from the other when all strong reflectors (voids, cracks, etc.) have closed or migrated away. The TOF data show that, in samples having a planar grain boundary array at the diffusion bond, a predominant number of the ultrasonic reflections come from grain boundaries at the interface. Once the grains have migrated across this diffusion bond—as in the case of sample 17H2—the distribution of reflection times more closely approaches the random distribution of the parent material.

### 5.1.3 Detection of Synthetic Hard Alpha Inclusions.

Figures 17 and 18 show 15-MHz F/7.0 C-scan images of the flaws in blocks 90-PMA and 93-1. For each of these images, the blocks were immersed in water, and the ultrasonic transducer was focused beneath the flat entry surface at the depth of the flaws. The -6 dB beam diameter produced a resolution size of 0.71 mm (0.028 in.) that is substantially smaller than the 9.5 mm (0.375 in.) inclusions in 90-PMA or the 2 mm (0.078 in.) inclusions in 93-1.

Figure 17 is the acoustic image of the powder metallurgy inclusions in block 90-PMA. With reference to this figure, there are 13 inclusions in 5 rows—alternating 3 inclusions/row and 2 inclusions/row. The inclusions are, from the top of the image, row 1: PB2, PB16, and PB4; row 2: PB8 and PB2; row 3: PB4, PB16, and PB6; row 4: PB6 and PB4; and row 5: PB8, PB2, and PB16. The C-scan displays not only the HIPped powder, but also the Ti-6-4 jacket in which it was HIPped. The reflection from the Ti 6-4 jacket is likely due to its having picked up a small amount of nitrogen and oxygen during the 1400°C powder HIP.

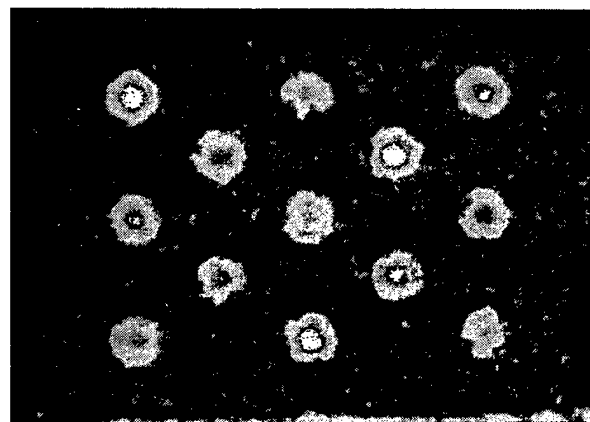


FIGURE 17. ACOUSTIC IMAGE OF SYNTHETIC HARD ALPHA INCLUSIONS IN BLOCK 90-PMA

Figure 18 is the acoustic image of the four arc-melted inclusions in block 93-1. The top row of two seeds are (left to right): RAM 1234 and RAM 1229; the bottom row—RAM 1237 and RAM 1228. After these images were made, sections of the block containing one inclusion each were polished to the midsection of the seeds to yield the metallographic sections shown earlier in figures 6 through 9. The inclusions shown in figures 6 through 8 were not cracked. Thus, uncracked synthetic hard alpha cylinders, with compositions as low as 1.61 wt.% N and 0.23 wt.% O (5.28 at% N and 0.67 at% O), can be imaged ultrasonically.

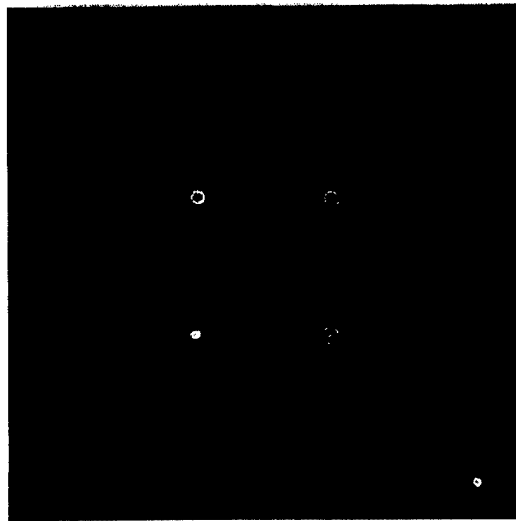


FIGURE 18. ACOUSTIC IMAGE OF ARC-MELTED SYNTHETIC HARD ALPHA INCLUSIONS IN BLOCK 93-1

A signal-to-noise ratio was measured as the amplitude of the reflection from an inclusion divided by the average amplitude of the background noise. Table 5 lists the S/N from the inclusions within the blocks 90-PMA and 93-1.

TABLE 5. MEASURED SIGNAL-TO-NOISE RATIO FROM Ti-N-O INCLUSIONS IN Ti 6-4

Block Serial No.	Inclusion	at% N	at% O	Signal to Noise
90-PMA	PB2	28.35	4.01	17.5
90-PMA	PB4	17.02	5.62	11.5
90-PMA	PB6	12.11	6.34	8
90-PMA	PB8	9.46	6.62	6.5
90-PMA	PB16	4.55	7.48	4
93-1	RAM 1228	17.46	1.21	17.4
93-1	RAM 1229	10.90	0.81	10.1
93-1	RAM 1234	8.36	0.66	8.5
93-1	RAM 1237	5.28	0.67	5.7

With reference to table 5, for the block containing the powder metallurgy inclusions, 90-PMA, the signal-to-noise ratio was measured looking downward onto the top of the inclusions, such that their cross section was a circle. The inclusions were located 25 mm (1 in.) below the surface.

For block 93-1, containing the arc-melted Ti-TiN inclusions, the signal-to-noise ratio was measured looking in from the side of the block toward the radial direction of the inclusion, after the block had been cut into quarters, each containing one inclusion. The signal-to-noise ratio was determined from the reflections from the front of each flaw. The inclusions were located about 7.3 mm (0.3 in.) below the surface. It was found that the Ti 6-4 block had different

acoustic behavior in the two directions 90° apart looking radially onto the inclusions. One direction had a higher level of background noise than the other, most likely due to forging texture in the Ti 6-4 block. Table 5 lists the signal-to-noise ratio for this highest-noise direction.

#### 5.1.4 Estimation of Ultrasonic Reflectance and S/N of Ti-N Inclusions in Ti Alloys.

In order to understand the effect that nitrogen has on the sample velocities, it is necessary to separate the sound velocity increase caused by oxygen from the increase caused by nitrogen. The measured sound velocities listed in table 6 are plotted in figure 19. A linear regression fits the longitudinal velocity,  $C_L$ , data to a curve of the form:

$$C_L = 6002.2 + 61.86 \cdot (\text{at\% N}) + 54.31 \cdot (\text{at\% O}) \text{ m/s}$$

TABLE 6. CALCULATED SOUND VELOCITY OF Ti-N COMPOSITIONS

Serial No.	Measured at% N	Measured at% O	Measured $C_L$ , m/s	$C_L$ , Calculated for 0% O, m/s
PB2	28.35	4.01	7902	7700
PB4	17.02	5.62	7470	7187
PB6	12.11	6.34	7110	6791
PB8	9.46	6.62	7030	6697
PB16	4.55	7.48	6560	6184
1224	8.66	1.09	6568	6513
1202	5.30	0.97	6442	6393
1229	10.90	0.81	6713	6669
1234	8.36	0.66	6543	6510
1237	5.28	0.67	6349	6312

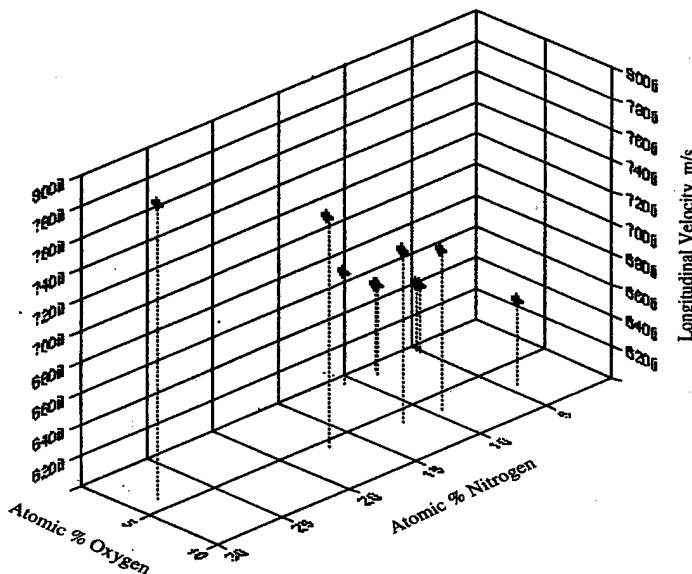


FIGURE 19. MEASURED LONGITUDINAL VELOCITY OF SYNTHETIC HARD ALPHA MATERIAL VERSUS OXYGEN AND NITROGEN

This oxygen dependence is consistent with sound velocity data for titanium-oxygen alloys measured by Hsu and Conrad [21]. Their data can be fit to the equation  $C_l = 6053.6 + 55.39 \cdot (\text{at\% O}) \text{ m/s}$ , for the oxygen contents through 2.6 at%. The effect of oxygen on the sound velocities of the Ti-N-O alloys can be removed by reducing the measured sound velocity of each composition by  $54.31 \cdot (\text{at\% O}) \text{ m/s}$ . This has been done in table 6 and figure 20.

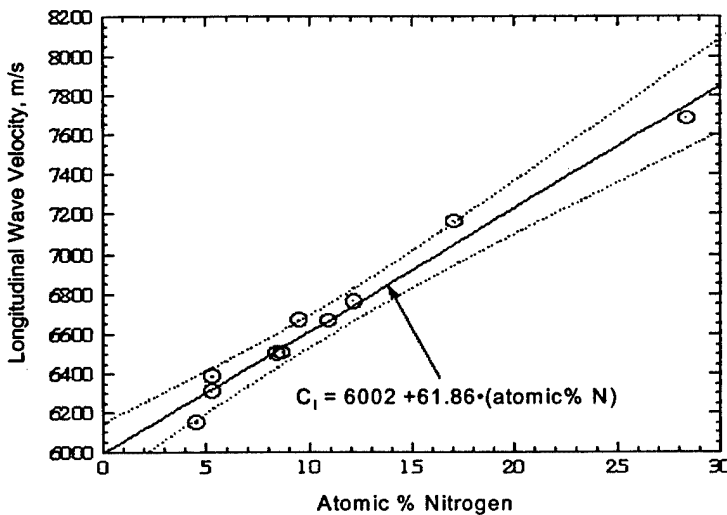


FIGURE 20. CALCULATED LONGITUDINAL VELOCITY OF Ti-N COMPOSITIONS VERSUS at% N

Titanium-nitrogen alloys have a hexagonal crystal structure. Their lattice parameters,  $a$  and  $c$ , have been compiled by Murray [4]. These were fit to linear equations:

$$a = 0.2951 + 9.738 \times 10^{-5} \cdot (\text{at\% N}) \text{ nm}$$

$$c = 0.4657 + 5.344 \times 10^{-4} \cdot (\text{at\% N}) \text{ nm}$$

The theoretical density of titanium-nitrogen alloys was calculated by dividing the atomic mass within a unit cell (six titanium atoms plus the interstitial nitrogen) by the volume of a unit cell calculated from the above lattice parameter fit. The theoretical density of titanium-nitrogen alloys calculated in this manner can be fit to the equation:

$$\rho = 4490.9 + 5.03 \cdot (\text{at\% N}) - 0.01 \cdot (\text{at\% N})^2 \text{ kg/m}^3$$

The analysis of the sound velocities of the Ti-N alloys and the calculation of the theoretical density of Ti-N alloys as functions of composition now permit calculation of ultrasonic reflectance. The reflectance  $R$  of a Ti-N inclusion within a Ti alloy matrix is defined as normalized difference in the product of the speed of sound,  $C_l$ , and density,  $\rho$ ,

$$R = \frac{\rho_i C_i - \rho_m C_m}{\rho_i C_i + \rho_m C_m}$$

where subscripts *i* and *m* refer to the inclusion and the matrix alloy respectively. The reflectance of longitudinal sound waves on hard alpha inclusions can now be calculated as a function of nitrogen content, as shown in table 7 and figure 21.

TABLE 7. CALCULATED REFLECTANCE OF TITANIUM-NITROGEN ALLOYS

Atomic % N	Weight % N	Reflectance of Ti(N) in Ti	Reflectance of Ti(N) in Ti 6-4
0	0	0	
2	0.59	0.011	0.007
4	1.2	0.022	0.018
6	1.8	0.032	0.029
8	2.5	0.043	0.039
10	3.1	0.053	0.049
12	3.8	0.063	0.059
14	4.5	0.073	0.069
16	5.3	0.082	0.079
18	6.0	0.092	0.088
20	6.8	0.101	0.097
22	7.6	0.110	0.107
24	8.5	0.119	0.115
26	9.3	0.128	0.124

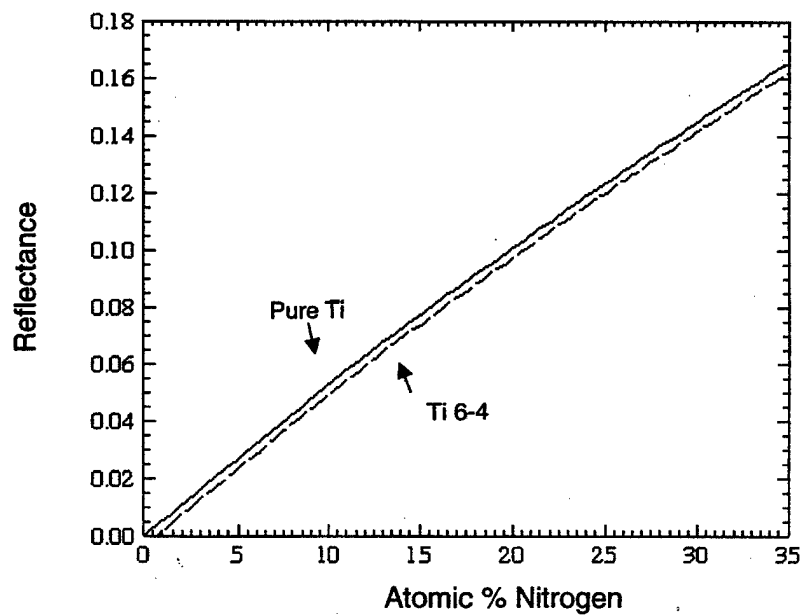


FIGURE 21. CALCULATED LONGITUDINAL WAVE REFLECTANCE AS A FUNCTION OF NITROGEN CONTENT FOR Ti-N INCLUSIONS IN PURE Ti AND Ti 6-4

For a Ti 6-4 matrix, the measured longitudinal velocity value, 6175 m/s, was used, and the density was taken as 4461 kg/m<sup>3</sup>. These values of reflectance show clearly the difficulties of detection. For example, a 16 at% nitrogen inclusion in Ti 6-4 has a calculated reflectance of about 0.079, i.e., less than 1/12 the reflectance of an open crack.

The fractional change in sound velocity from nitrogen and oxygen additions is much greater than the fractional change in density. For a 1 at% addition, nitrogen increases the speed of sound 1.03%, and oxygen increases the speed of sound 0.90%. The density change is much less. For a 1 at% addition, nitrogen increases the theoretical density by only 0.1%. The change in density with oxygen additions was measured by Hsu and Conrad [21] and can be fit to

$$\rho = 4494.5 + 11.74 \cdot (\text{at\% O}) \text{ kg/m}^3$$

Thus, oxygen increases the density by 0.3% for a 1 at% addition.

Figure 22 displays the measured signal-to-noise ratio of the inclusions in block 90-PMA plotted against the sound velocity measured in the alloys that were used as inclusions. This figure illustrates the strong relationship between the physical property, sound velocity, and the detectability of the synthetic inclusion. The signal-to-noise ratio monotonically increases with the sound velocity of the inclusion. The ratio extrapolates to zero at about the velocity of the Ti 6-4 host (~6175 m/s).

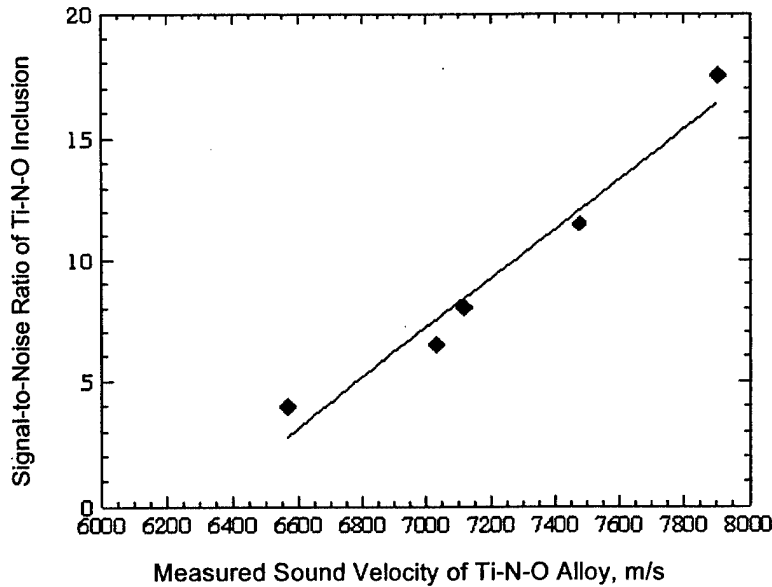


FIGURE 22. MEASURED SIGNAL-TO-NOISE RATIO OF SYNTHETIC HARD ALPHA INCLUSIONS IN BLOCK 90-PMA VERSUS SOUND VELOCITY

### 5.1.5 Summary of the Effect of Hard Alpha Composition on Inspectability.

- Hard alpha, Ti-N-O alloys, can be synthesized by both powder metallurgical and arc-melting techniques. Arc-melting mixtures of TiN and Ti sponge has proven to be the most reproducible method for producing synthetic hard alpha of known composition. These Ti-N-O alloys can be produced without cracks and are suitable for both direct ultrasonic property measurements and for incorporation as inclusions into titanium alloy blocks for detectability studies.
- Ultrasonic longitudinal and shear wave velocities were measured over a range of nitrogen and oxygen contents. Velocity increases caused by the interstitials were tabulated, and ultrasonic reflectances were calculated for synthetic hard alpha inclusions in Ti and Ti 6-4 host metal.
- Hard alpha inclusions within Ti 6-4 and Ti-17 blocks were synthesized via HIP-bonding Ti-N-O seeds into the blocks. Subsequent ultrasonic measurements on the blocks show no evidence of cracking in these inclusions.
- Uncracked synthetic hard alpha inclusions with compositions as low as 1.5wt.% N can be imaged and detected with ultrasonic C-scans. These inclusions have the lowest reflectance of the seeded inclusions and therefore the lowest detectability.
- Ultrasonic signal-to-noise ratios for the synthetic inclusions have been measured and related to the physical property differences between the Ti 6-4 host block and the Ti-N-O alloy inclusion.
- TOF imaging has been shown to be capable of assessing the grain boundary structure of diffusion bonds. Both TOF image and statistical methods can be used to examine ultrasonic data to make a determination of bond quality. An overall preferred NDE methodology for diffusion bonds would include C-scan amplitude imaging for the initial steps in the diffusion bond press and TOF techniques for the final steps in the process.

## 5.2 ELASTIC CONSTANT DETERMINATION FOR A COMMON Ti ENGINE ALLOY.

### 5.2.1 Introduction.

Pure titanium is allotropic. At temperatures below 882°C (1620°F), it has a hexagonal close-packed crystal structure—usually called alpha; and at temperatures above 882°C (1620°F), its stable crystal structure is body-centered cubic phase—usually called beta. Titanium alloys used in structural applications usually contain both alpha and beta phases, which has been achieved by adding certain elements such as Al or Sn to stabilize alpha and elements such as V or Mo to stabilize beta.

For the widely used titanium based alloy Ti- 6wt.%Al- 4wt.%V, Ti 6-4, the room temperature microstructure is mostly alpha phase with a small amount of beta. At elevated temperatures, the volume fraction beta present in the structure increases, and the volume fraction of alpha phase

decreases. The temperature at which the last amount of alpha phase is transformed to beta is termed the "beta transus." The beta transus of Ti 6-4 is about 1030°C (1890°F).

The microstructure of a titanium alloy is determined by the forming process and heat treatments to which the alloy is subjected. Typically, billets are first processed above the beta transus temperature and subsequently below the beta transus temperature. The prior beta grain size and shape can have a strong influence on the low-temperature structure. The crystallographic orientation of the alpha phase has a relationship to that of the beta grain in which it is growing, such that the close-packed direction and plane in the alpha phase are parallel to that direction and plane in the beta grain. This relationship, called Burgers relationship, is expressed crystallographically as

$$[111]\{110\}_{\text{bcc}} // [10\cdot0]\{0001\}_{\text{hcp}}$$

Because of the symmetry of the cubic and hexagonal phases, there can be three alpha orientations within a prior beta grain.

At high cooling rates and in worked structures, alpha phase can nucleate throughout a beta grain in all three orientations, and a basket weave structure of three interpenetrating orientations is formed.

For lower cooling rates, such as those found in billet manufacture, alpha phase nucleates at prior beta boundaries or at only one or two places within a prior beta grain. The alpha phase grows as a colony of parallel plates in the beta grain. These colonies of alpha plates, all having identical crystallographic orientation, interact with a sound wave as if they were a single grain. Thus, for purposes of describing the interaction of a titanium alloy with sound, the grain size is not the size of an individual alpha particle, but the size of the alpha colony.

This behavior was illustrated in work performed at General Electric Aircraft Engines (GEAE) prior to the ETC contract, where the colony structure of Ti 6-4 billet was characterized. Figure 23 is an optical micrograph of a Ti 6-4 billet. The microstructure consists of alpha plates about 10  $\mu\text{m}$  wide and about 100  $\mu\text{m}$  long. With reference to this figure alone, the alpha grain size could be said to have dimensions between 10 and 100  $\mu\text{m}$ . For comparison the wavelength of longitudinal sound at the typical 5-MHz inspection frequency is 1200  $\mu\text{m}$ . When the billet is characterized by electron backscatter diffraction, the alpha plates are shown to be parts of much larger colonies. Figure 24 shows a scanning electron micrograph and the accompanying electron beam backscatter pattern (EBSP) icosohedral image. In the icosohedral image, the orientation of the axis of hexagonal symmetry (c axis) with respect to the plane of the specimen is represented by the colors shown in the accompanying icosohedron. Regions with similar grain orientation are assigned a common color that provides an assessment of texture effects within the sampled microstructure. Figure 24 illustrates that large regions share a common c-axis declination, and thus a common acoustic behavior.

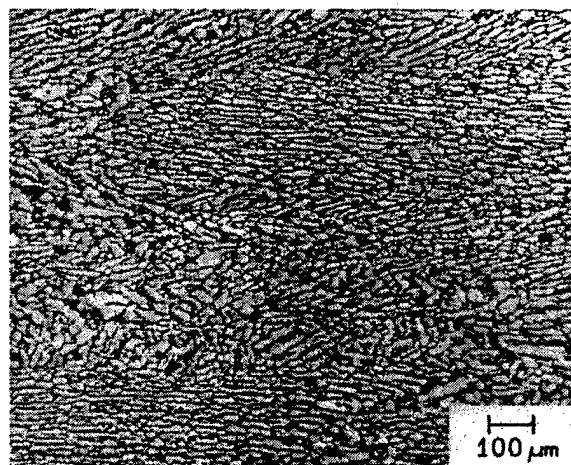
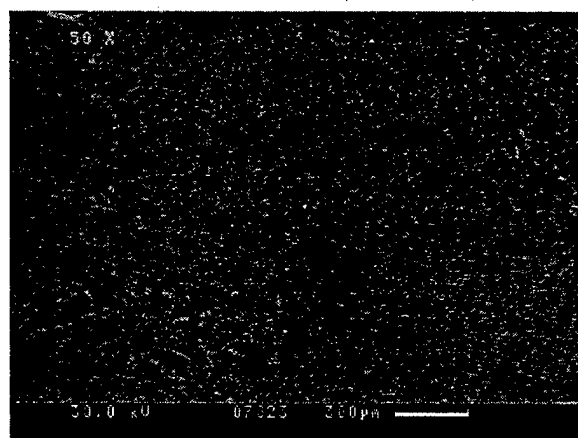


FIGURE 23. TYPICAL Ti 6-4 BILLET MICROSTRUCTURE



Backscattered Electron Image



Icosohedral Image



FIGURE 24. BACKSCATTERED ELECTRON IMAGE (TOP) AND SEM ORIENTATION IMAGE (BOTTOM) OF Ti 6-4 BILLET

The scattering of sound at colony-to-colony boundaries is proportional to the normalized difference in velocity. Thus, an effort was made to measure the minimum and maximum velocities in Ti 6-4. The minimum and maximum velocities for pure titanium are 6003 m/s and 6332 m/s, respectively [22]. The corresponding velocity values are not known for Ti 6-4.

### 5.2.2 Preparation of the Enlarged Grain Plate.

In an effort to measure the velocity spread for alloyed titanium, namely Ti 6-4, a plate, 6.35 mm (0.25") thick, with colonies extending through the plate thickness was prepared by a beta anneal and slow cooling as follows. A plate section was machined from a Ti 6-4 forged ring. The plate sample dimensions were 35 by 105 by 6.35 mm (1.5" by 4.5" by 0.25"). The plate surface was ground plane and parallel  $\pm 0.025$  mm ( $\pm 0.001$ "). The plate was encapsulated in a fused silica ampoule with a partial pressure of argon. The ampoule was heat treated at 1150°C (2102°F) for 2 hours and slow cooled to 100°C (212°F) at 1°C/h (1.8°F/h).

The resulting sample had very large prior beta grains, containing some alpha colonies that extended through the entire thickness. Beta grain boundaries could be seen clearly on the sample surface due to thermal etching, i.e., the slight differences in surface height due to differences in local vapor pressure brought about by differences in surface free energy as a function of grain orientation. The sample macrostructure is shown in figure 25.



FIGURE 25. MACROSTRUCTURE OF THE Ti 6-4 ENLARGED GRAIN PLATE IN WHICH LARGE GRAINS WERE GROWN

The microstructure of the sample contained very coarse alpha plates with a discontinuous beta phase. Figure 26 illustrates this microstructure in a colony that extended through the full thickness of the sample.

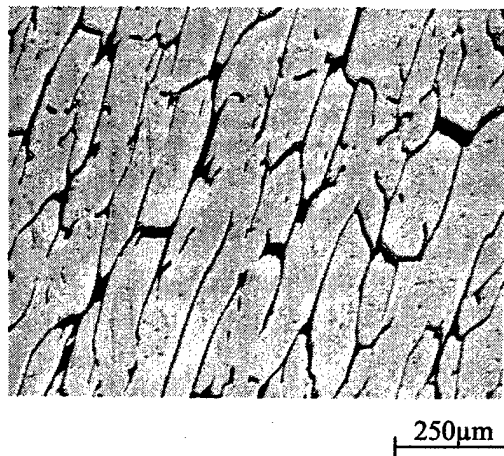


FIGURE 26. MICROSTRUCTURE OF ONE COLONY IN THE ENLARGED GRAIN PLATE

### 5.2.3 Ultrasonic Velocity Measurements.

Two ultrasonic scanning techniques were used to study velocity variations within the enlarged grain plate:

- Surface wave imaging
- Longitudinal-wave pulse/echo imaging

The signals used by the two methods are illustrated in figure 27. For the surface wave measurement a highly focused transducer was used with the water path chosen to focus the beam just below the surface. Some of the sonic rays strike the metal surface at the proper angle to excite surface waves. As these rays propagate along the metal surface, they radiate energy back into the water and a portion of that energy returns to the transducer at the proper angle to produce a coherent output signal. If the speed of surface wave propagation is independent of direction along the metal surface (within the beam spot), the amplitude of the surface wave signal will be large. This would be the case for a large single macrograin of Ti 6-4 which had its hexagonal symmetry axis perpendicular to the surface. On the other hand, if the wave speed varies with lateral direction, the amplitude of the surface wave signal will be reduced. That would be the case, for example, for a single macrograin whose symmetry axis lay in the plane of the surface. Thus, by gating the surface wave echo and displaying its amplitude as a function of position, one can image the macrostructure.

Surface wave measurements were made using a 50 MHz, 0.25" diameter transducer, which had a 0.2" focal length in water. The water path was set to about 0.060" less than the focal length, producing a beam entry circle of about 0.050" on the surface. The resulting surface wave amplitude images are shown in the lower two panels of figure 28. Both sides of the specimen were imaged, and the lower image has been inverted to correct for the flipping of the specimen between scans. A region having a uniform amplitude that is the same from both sides is a candidate for a single macrograin, which spans the full thickness of the plate.

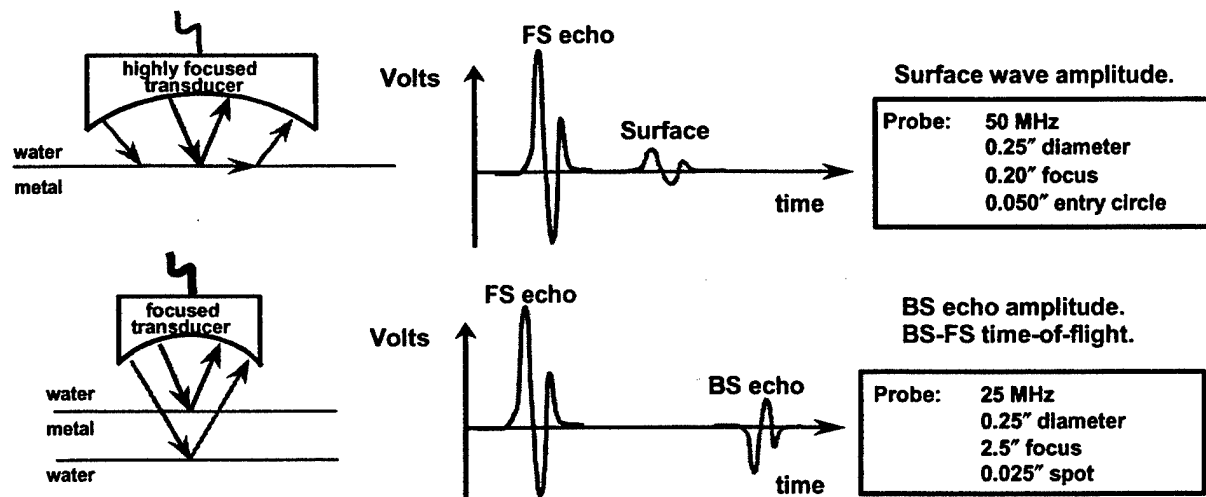


FIGURE 27. TWO METHODS USED TO IMAGE MACROGRAINS IN THE ENLARGED GRAIN PLATE: SURFACE WAVES (TOP) AND LONGITUDINAL WAVES (BOTTOM)

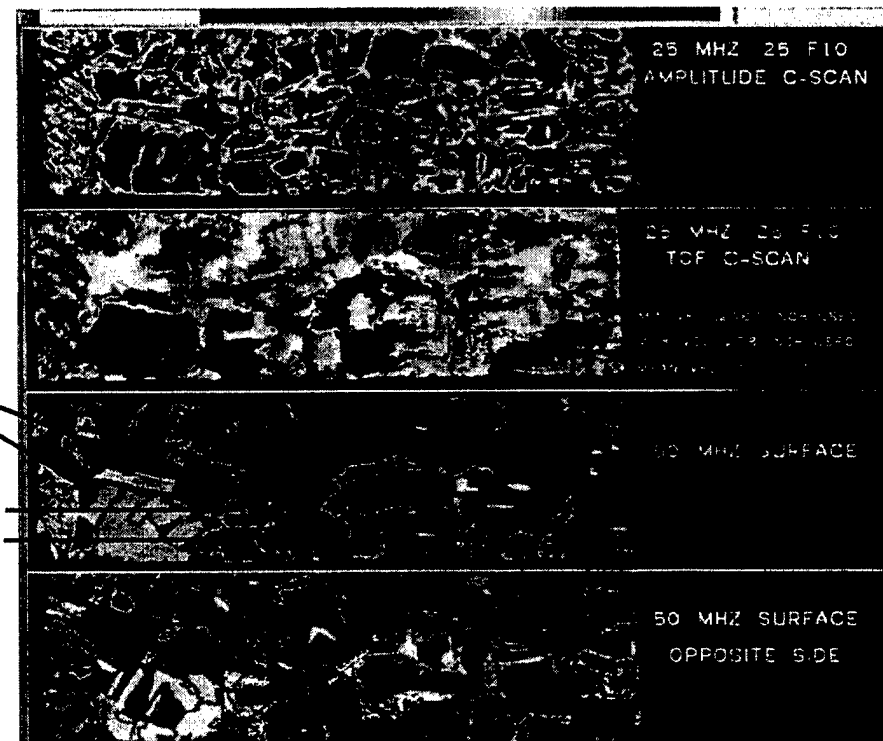


FIGURE 28. ULTRASONIC IMAGES OF THE ENLARGED GRAIN PLATE OBTAINED USING LONGITUDINAL WAVES (UPPER TWO IMAGES) AND SURFACE WAVES (LOWER TWO IMAGES) (White/red coloration indicates a high value of amplitude or time of flight; blue/violet indicates a low value.)

A longitudinal wave imaging method was also used. A 25-MHz, 0.25" diameter transducer having a 2.5" focal length was employed, and the water path was chosen to focus the beam near the mid-plane of the plate. Distinct echoes from the front and back surfaces of the plate were

seen and used to construct two images: one based on the amplitude of the back-surface echo (back-wall echo); and one based on the TOF between the front-surface and back-surface echoes. A single macrograin which spans the thickness of the plate would appear in the images as a region having a uniform back surface amplitude and uniform TOF.

Two regions, where the velocity was estimated to be highest and lowest, were selected for more detailed characterization. These regions are designated H1 and L1, respectively, in figure 28. The crystallographic orientations of the regions were determined by electron backscatter diffraction. The orientation in the region of lowest sound velocity (L1) had the c axis parallel to the plane of the plate; the crystallographic orientation in the region of highest sound velocity (H1) had the c axis perpendicular to the plane of the plate as described below.

Figure 29 displays an icosohedral image and a vector normal image of the region of lowest sound velocity. The image is of a 10.2-mm-square region, and orientations were measured in 0.2-mm steps. A vector normal image displays the declination of the c-axis relative to the plane of the sample as a shade of grey, going from black (c axis in the plane of the sample) to white (c axis normal to plane of the sample). Figure 29 illustrates that there is a large triangular-shaped grain, of about 5-mm sides, in the center of the image, whose vector normal shading is black; thus, the c axis is in the plane of the sample.

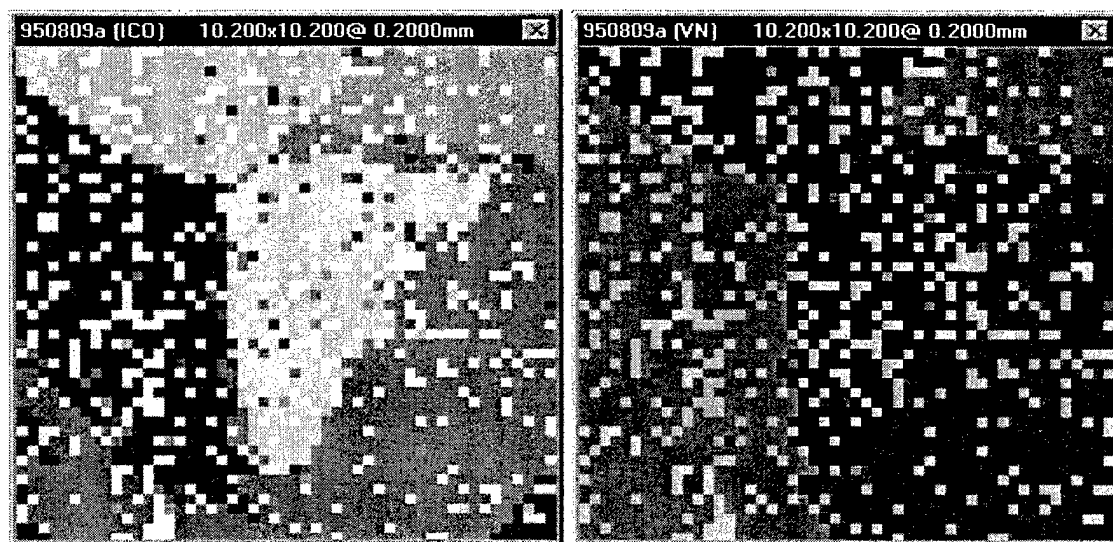


FIGURE 29. EBSP ICOSOHEDRAL IMAGE (LEFT) AND VECTOR NORMAL IMAGE (RIGHT) OF THE MACROGRAIN WITH THE LOWEST MEASURED SOUND VELOCITY (C axis in plane of plate)

Figure 30 displays an icosohedral image and a vector normal image of the region of highest sound velocity. Again the image is of a 10.2-mm-square region, and orientations were measured in 0.2-mm steps. Figure 30 illustrates that there is a large triangular grain, of about 7-mm sides, in the center of the image, whose vector normal shading is white; thus, the c axis is perpendicular to the plane of the sample.

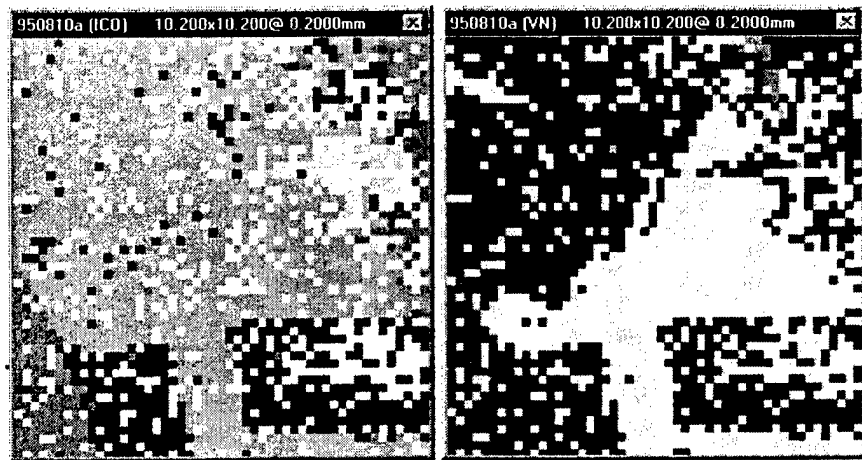


FIGURE 30. EBSP ICOSOHEDRAL IMAGE (LEFT) AND VECTOR NORMAL IMAGE (RIGHT) OF THE MACROGRAIN WITH THE HIGHEST MEASURED SOUND VELOCITY (C axis normal to plane of plate)

Based on these EBSP results, which identified grains with c axes parallel and perpendicular to the plane of the sample, longitudinal sound velocities were measured with a contact transducer at the two locations. The local thickness of the plate was measured at the position of the alpha colonies. Sound velocity was then determined by using a 20-MHz, 3-mm (1/8") diameter transducer and measuring sound wave traverse times on an oscilloscope.

The velocity through the grain whose c axis lies in the plane of the plate (perpendicular to the direction of sound propagation) was measured as 6063 m/s. The velocity through the grain whose c axis lies perpendicular to the plane of the plate (parallel to the direction of sound propagation) was measured as 6712 m/s. These results are displayed in a bar graph (figure 31), which illustrates that the degree of anisotropy in sound velocity is higher for Ti 6-4 than for pure Ti. The minimum velocity is about the same, but the maximum velocity is higher for Ti 6-4 than for pure Ti.

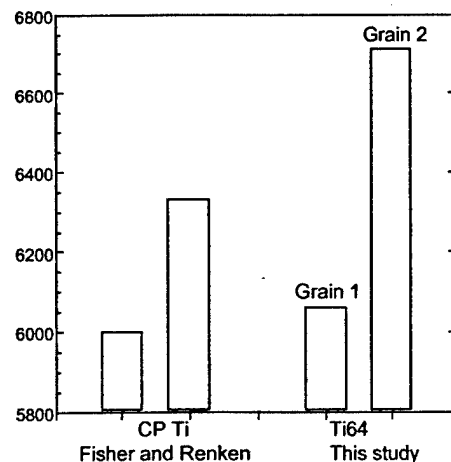


FIGURE 31. SOUND VELOCITY ANISOTROPY OF PURE (CLOSE PACKED) Ti AND Ti 6-4

Shear wave velocity measurements were also performed on apparent single macrograins of Ti 6-4. A 5-MHz, 0.25-in.-diameter contact, shear-wave transducer was used. The regions designated H1 and L1 in figure 28 were found to be too small to produce reliable velocity measurements with this transducer. Thus, the measurements were made in the nearby larger regions (designated as H2 and L2 in figure 28) which appeared to have similar image characteristics. The results of the shear wave velocity measurements are summarized in figure 32. A 20% variation in shear wave speed was observed, depending on the propagation and polarization directions relative to the hexagonal crystal lattice.

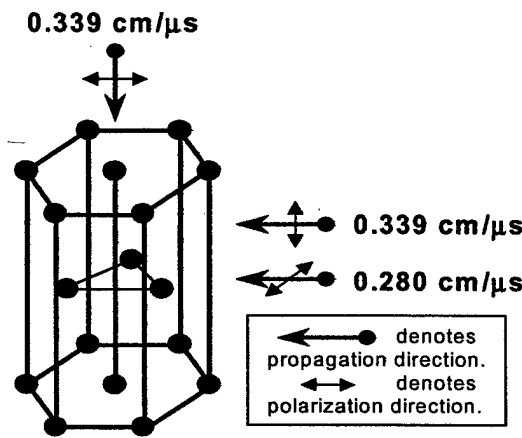


FIGURE 32. SUMMARY OF SHEAR WAVE VELOCITY MEASUREMENTS ON SINGLE MACROGRAINS OF Ti 6-4 (Results depend on the orientation of the sonic beam relative to the hexagonal crystal lattice.)

Since detection of hard alpha by ultrasound depends on reflectance (difference in the normalized product of density and sound velocity), the increased anisotropy of sound velocity in Ti 6-4 acts to make detection of uncracked low-nitrogen inclusions more difficult. Adjacent Ti 6-4 grains of maximum difference in sound velocity can reflect sound to the same degree as that of a low-nitrogen inclusion. This is illustrated in figure 33 where the product of density and longitudinal velocity is plotted versus nitrogen content. The impedance spread on this plot is superimposed, resulting from the minimum and maximum velocities of Ti 6-4. This plot would suggest that uncracked hard alpha with compositions less than about 3 wt.% N might not be detectable if present in a region of large alpha colonies.

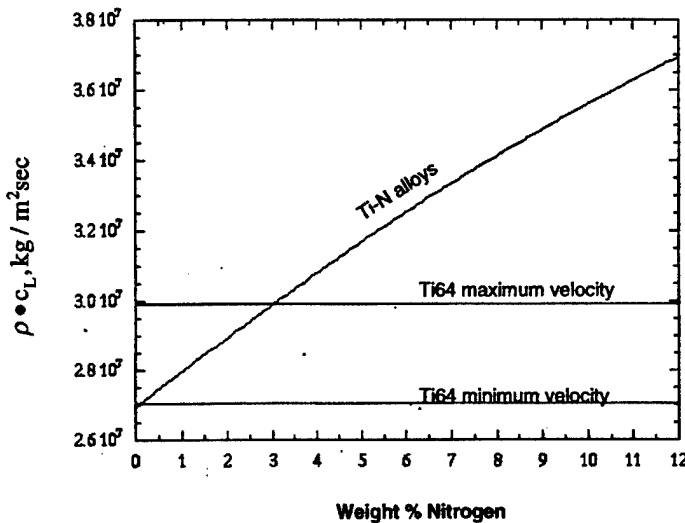


FIGURE 33. ULTRASONIC IMPEDANCE (VELOCITY TIMES DENSITY) OF Ti 6-4 AND Ti-N ALLOYS

#### 5.2.4 Summary.

The following conclusions were reached using the enlarged grain plate:

- Sound velocity and crystallographic orientations were measured in large alpha colonies in alloy Ti 6-4. The minimum longitudinal sound velocity was measured for a grain whose hexagonal c axis was perpendicular to the direction of sound propagation. The maximum longitudinal sound velocity was measured for a grain whose hexagonal c axis was parallel to the direction of sound propagation.
- The measured degree of anisotropy in longitudinal sound velocity in Ti 6-4 is about 10%, i.e., about twice that reported for pure Ti. The measured anisotropy in shear sound velocity in Ti 6-4 is about 20%.
- Uncracked hard alpha with compositions less than about 3 wt.% N might not be detectable if present in a region of large alpha colonies because of insufficient differences in reflectance.

### 5.3 ULTRASONIC PROPERTIES OF Ti-17 AND Ti 6-4 ALLOYS.

#### 5.3.1 Introduction.

As indicated in section 2, the ability to detect hard alpha inclusions depends primarily on the relative ultrasonic impedances of hard alpha material and unflawed host metal and the crystalline microstructure of the host. The first determines the size of an ultrasonic echo from a hard alpha defect (signal response), and the second determines the size of competing noise echoes scattered from grain boundaries (material noise). Understanding the relationship of the signal and noise response provides the necessary input to probability of detection studies and to inspection development efforts underway in other areas of the ETC program. The ultrasonic properties of

Ti-17 and Ti 6-4 were surveyed with details provided here. Measured quantities were the ultrasonic velocity, attenuation, and backscattered noise figure-of-merit (FOM). The latter is a frequency-dependent measure of the noise-generating capacity of the microstructure.

There is a natural order for carrying out the property measurements, namely: velocity first, attenuation second, and noise FOM third. Velocity measurements can be made in a straightforward manner without any a priori knowledge of the specimen. Measurement is made of the specimen thickness and the round-trip time required for an ultrasonic pulse to travel through it to calculate the velocity. Attenuation measurements are made by comparing reflected or through-transmitted signals from a titanium specimen to similar signals in a low-attenuation reference block (fused quartz or powdered metal). Such measurements require knowledge of density and velocity, since these determine the transmission and reflection coefficients at the boundaries of the specimen. In addition, accurate attenuation measurements that attempt to account for the effects of diffraction (beam spreading and focusing) require knowledge of the velocity, since it controls the rate of diffraction. As will become evident later, the model-based measurement of the noise FOM requires knowledge of both the velocity and attenuation. In presenting the results, this natural sequence of measurement will also be followed, discussing velocities, attenuations, and noise FOMs in that order. The primary interest is in the immersion inspection of titanium billets at normal incidence, where longitudinal waves (L-waves) are the principal inspection mode. Thus, the property measurements described in this report are limited to the L-wave case.

The bulk of the property measurements were made at two sites: the Center for NDE at Iowa State University in Ames and GEAE in Cincinnati. Although there was considerable collaboration between the two sites, the measurement philosophies were somewhat different. Motivated in part by the need to acquire accurate frequency-dependent inputs for computer models, the Ames group focused on the careful, systematic measurement of attenuation-vs-frequency and FOM-vs-frequency curves in a representative set of 14 specimens. In these specimens, properties were measured in the radial, axial, and hoop directions using a fixed set of transducers and measurement geometries. As will be described later, broadband ultrasonic pulses were used, and Fast Fourier Transform (FFT) methods were applied to deduce attenuation and FOM values over a range of frequencies within the bandwidth of the pulse. After the initial survey of 14 specimens, follow-up studies were performed on a limited number of additional specimens to address additional questions. The Cincinnati group was primarily motivated by the desire to understand the effect of titanium properties on typical industrial inspections, which generally rely on signal amplitude analyses not requiring FFT computations. Their emphasis was on rapidly surveying a large number of specimens to discover the important general trends and their likely consequences for practical inspections. Although FFT analyses were used by the Cincinnati group for some attenuation studies, amplitude analysis was usually the tool of choice.

### 5.3.2 Specimen Descriptions.

A complete listing of the specimens fabricated for the property survey task is provided in appendix A. The specimens are generally large coupons cut from billets and forgings, and the terms "specimens" and "coupons" are used interchangeably when referring to them. Since some representative source materials were easier to obtain than others, the coupons became available for study at different times. A set of fourteen coupons from three billets and two forgings

became available early in the program. These are identified in figure 34 and designated by the letters A through N with their official serial numbers included in appendix A. For these 14 specimens, velocity, attenuation, and noise FOM measurements were measured in a uniform and systematic manner using a common set of ultrasonic transducers.

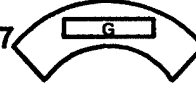
Label	Material	Source	Size (inches)	Location
A, B, C	Ti-17	9" Billet	$(1.5)^3$	
D, E, F	Ti 6-4	Forged Disk	$(6)^3$	
G	Ti 6-4	Forged Disk	$1.5 \times 11 \times 7$	
H, I, J, K	Ti 6-4	9.25" Billet	$(3)^3$	
L, M, N	Ti-17	7" Billet	$(3)^3$	

FIGURE 34. SOURCES FOR THE 14 BILLET AND FORGING SPECIMENS  
DESIGNATED A-N

All of the coupons for material property measurements were rectangular prisms, in most cases approximately cubic in shape. The billets and forgings, which were the sources of the coupons, all had shapes that were cylindrically symmetric, and the coupons were cut to preserve this symmetry as much as possible. Thus, each flat face of a coupon had a normal vector which approximately pointed in either the radial, axial, or hoop direction of the billet or forging. For measurements at ISU, the six primary faces of each specimen were numbered in the manner shown in figure 35: three mutually orthogonal sides were numbered 1, 2, and 3 and the three opposite sides were then numbered 4, 5, and 6, respectively. Relative to the original billet or forging, the directions of the inward normal vectors to sides 1, 2, and 3 were approximately:

- Side 1: radial (i.e., radially inward)
- Side 2: axial (i.e., parallel to the axis of rotational symmetry)
- Side 3: transverse or "hoop" (i.e., tangent to the circumference)

An alternative numbering scheme was generally used at GEAE in which sides 1-6 were designated as R-1, A-1, T-1, R-2, A-2, and T-2, respectively.

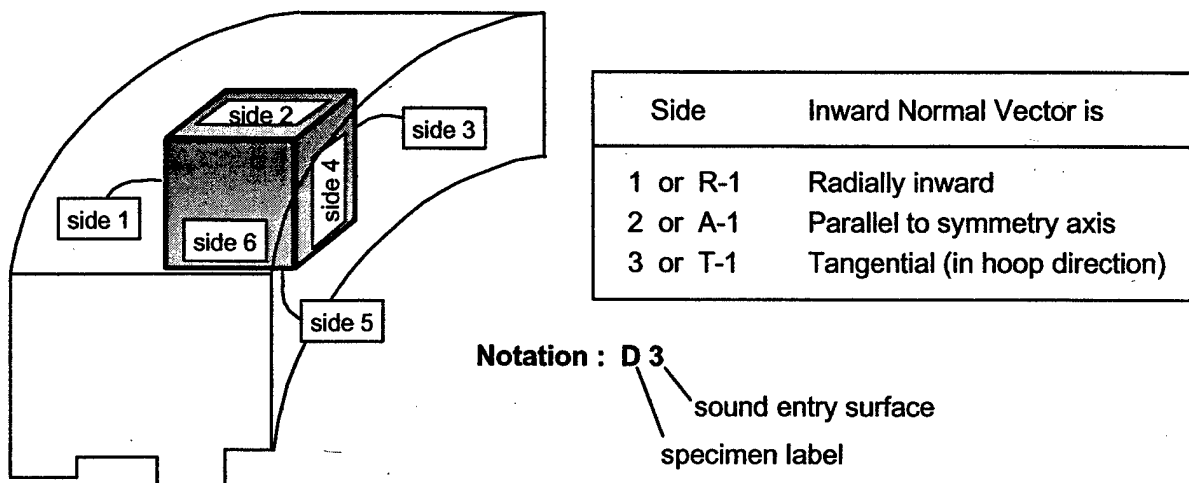


FIGURE 35. NUMBERING SCHEME USED TO LABEL THE FACES  
(SOUND ENTRY SURFACES) OF A RECTANGULAR COUPON  
(The scheme is illustrated for forging specimen D.)

In most cases when a specimen was studied, separate normal-incidence measurements were made for sound propagation in the radial, axial, and hoop directions, with sides 1, 2, and 3 serving as the sound entry surfaces. For specimens A-N, there were two notable exceptions. Specimen G was a 1.5" thick plate containing 64 flat-bottomed holes (FBHs) that had been drilled in the "radial" direction for PoD studies. For this specimen, measurements were only made for radial propagation, and these were carried out in the regions between the FBHs. The backscattered noise level in specimen G was observed to vary noticeably with position, and separate noise and attenuation measurements were made on two halves of the specimen: the half containing the engraved serial number was designated GP, and the opposite half was designated GN. The other measurement exception occurred for forging specimens D-F. These were rather large coupons, approximately 6" cubes, and the noise measurements effectively surveyed only about the first two inches of depth. Thus for specimens D-F additional noise measurements were made using side 4 as the entry surface (radially outward propagation). This allowed us to determine the noise FOM on both the OD and ID regions of these coupons. For all other specimens, the volume surveyed during FOM measurement was centered near the mid-plane of the specimen.

Microstructures were generally documented by cutting small coupons from each rectangular specimen and then polishing, etching, and photographing the coupons. The usual procedure is summarized in figure 36. From one edge of the specimen, a thin triangular prism was removed with its long dimension approximately aligned with the radial direction. This prism was then cut into five sections, and one surface of each section was polished and etched.

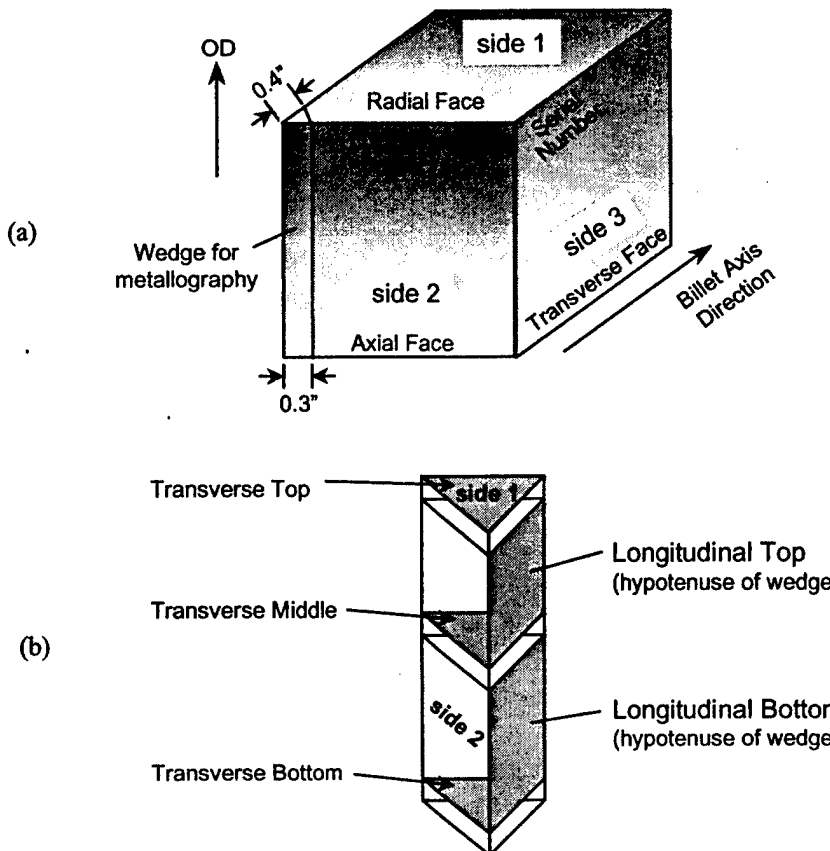


FIGURE 36. (a) SCHEMATIC DRAWING OF A TYPICAL SPECIMEN, SHOWING THE LOCATION OF THE WEDGE REMOVED FOR METALLOGRAPHY AND (b) SECTIONING OF THE WEDGE INTO FIVE PIECES (The shading indicates the area on each piece that was polished, etched, and photographed.)

Low-magnification and high-magnification photographs were taken of the polished surfaces to reveal the coarse-scale and fine-scale microstructures, respectively. The term macrostructure is generally used when referring to the coarse structure whose features typically have dimensions of a few millimeters. Notice that the three polished surfaces labeled transverse top, middle, and bottom in figure 36 are each parallel to side 1 of the specimen; their photos consequently reveal the microstructure as viewed with a radially inward line of sight. On the other hand, the surfaces labeled longitudinal top and bottom are not parallel to either side 2 or to side 3; the viewing direction is perpendicular to the billet radius but partly along both the axial and hoop directions.

Representative examples of the Ti-17 and Ti 6-4 billet microstructures are shown in figures 37 and 38, respectively. For a Ti-17 billet specimen the high-magnification photograph (figure 37(a)) reveals needle-shaped alpha-phase (hexagonal) crystallites with diameters of a few microns and lengths up to several hundred microns. Within small local regions, the long dimensions of the needles tend to be partially aligned. On a larger scale (figure 37(b)), one can observe macrograins that tend to be elongated in the direction parallel to the billet axis. The high-magnification photograph of the Ti 6-4 billet specimen reveals alpha crystallites that are somewhat rounder in appearance (figure 38(a)), but the macrograins (figure 38(b)) have the same general axial elongation seen for Ti-17.

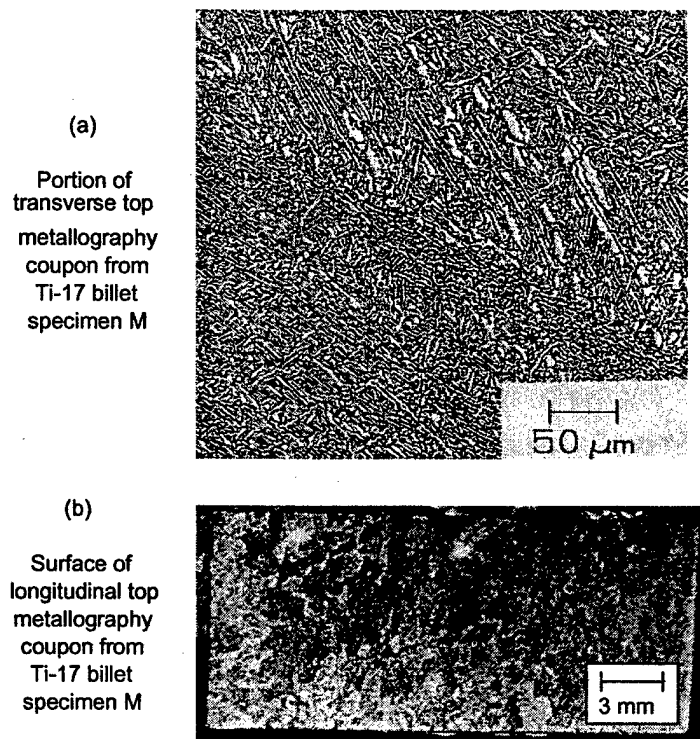


FIGURE 37. (a) MICROSTRUCTURE AND (b) MACROSTRUCTURE OF A TYPICAL Ti-17 BILLET SPECIMEN

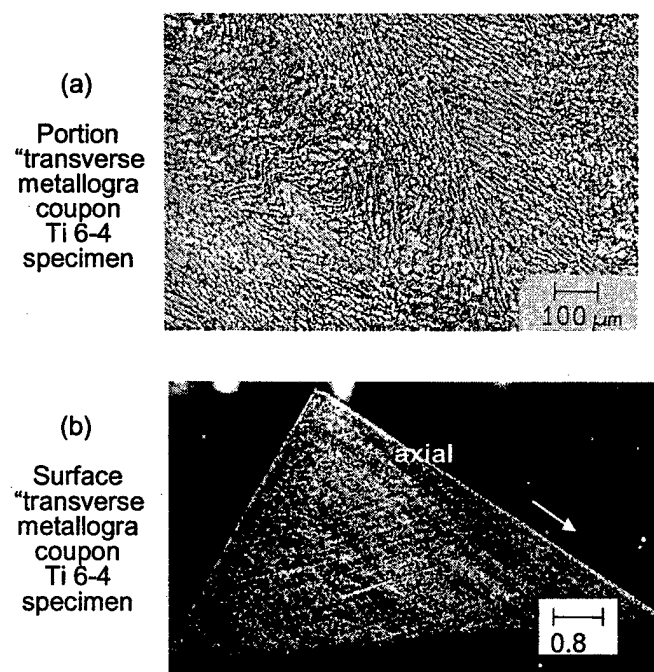
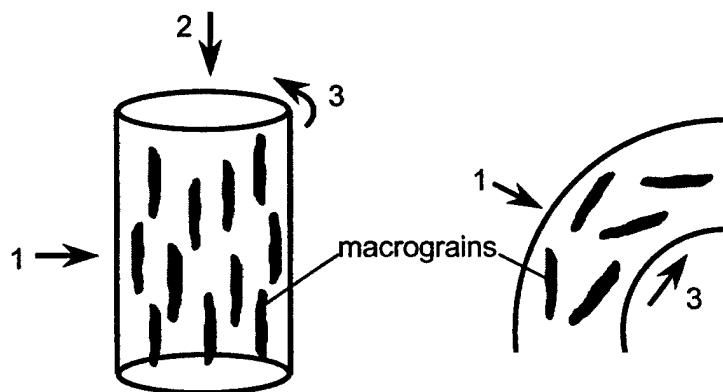


FIGURE 38. (a) MICROSTRUCTURE AND (b) MACROSTRUCTURE OF A TYPICAL Ti 6-4 BILLET SPECIMEN

For either alloy, the macrograins are believed to arise from prior beta grains, i.e., regions that were cubic crystallites during a prior high-temperature phase of the billet's processing history. It is believed that the atomic plane axes for the prior beta grain determined a set of allowed crystalline orientations for the fine-scale structure that subsequently developed when the metal was cooled. Thus, the microstructure remembers the macrostructure from which it develops, resulting in a localized texture that varies from one macrograin to the next. It is likely that for any given macrograin, the speed of sound depends on the direction of sound propagation relative to the principal axes of the original cubic crystal structure. Since different macrograins presumably have different orientations for their principal axes, the speed of sound in a given propagation direction is likely to vary from one macrograin to the next. This influences the ultrasonic grain noise, which arises from the scattering of sound at grain and macrograin boundaries, and also affects attenuation measurements, as will be discussed later. In surveying the specimen properties, a general relationship was observed between macrograin shapes and the directional dependence of noise and attenuation. Those relationships are summarized in figure 39. Note that the measured attenuation tends to be highest when the propagating sound beam approaches the elongated macrograins head on. However, the backscattered noise level is largest when the macrograins are ensonified from the side.



For billets: tend to be aligned with billet axis.

For forgings: tend to be partially aligned with hoop direction.

	Measured Attenuation		Measured Grain Noise	
	lowest	highest	lowest	highest
Billets	1 or 3	2	2	1 or 3
Forgings	1 or 2	3	3	1 or 2

FIGURE 39. TYPICAL RELATIONSHIP BETWEEN MACROGRAIN (OR FLOW LINE) ORIENTATIONS AND THE DIRECTIONAL DEPENDENCE OF L-WAVE ATTENUATION AND BACKSCATTERED NOISE

### 5.3.3 Sound Speed Measurements.

Longitudinal wave velocities were measured using the simple pulse/echo, normal-incidence, immersion geometry shown in figure 40. Velocities were determined by measuring the time shifts needed to overlap the front-surface (FS) and the first few back-surface (BS) echoes. Due to attenuation and beam diffraction, the shapes of these echoes usually differed slightly from one another (after accounting for the phase reversal between FS and BS echoes). Thus, in practice, the time delays were measured between a specific feature of each echo, namely the first zero-crossing point before the dominant peak. At ISU, the pulse/echo time-of-flight measurements were generally made using a 0.25" diameter, 10-MHz broadband planar transducer. Follow-up measurements on selected specimens using 5-MHz transducers were found to yield nearly identical results. In addition to the transducer, the measurement equipment consisted of a Panametrics 5052PR pulser/receiver and a LeCroy 9400A digitizing oscilloscope with a 100-MHz sampling rate. With this equipment, time-of-flight measurements at a fixed specimen location were typically reproducible to within a few nanoseconds.

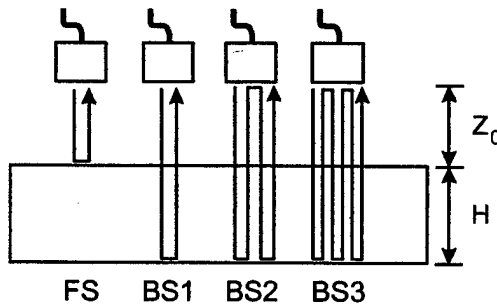


FIGURE 40. SOUND PATHS FOR L-WAVE ULTRASONIC VELOCITY MEASUREMENTS

The specimen thickness in the sound propagation direction must be known to calculate the sonic wave speed. It was typically found that the thickness in a given direction varied slightly (by up to 2 mils in the largest specimens), depending on the location of the measurement. It was generally chosen to measure the thickness very near the middle of each specimen (i.e., between central points on opposing faces) and to make an ultrasonic velocity measurement at that single location. Because of the presence of the flat-bottomed holes, specimen G was treated somewhat differently. For that plate, the thickness and time-of-flight measurements were made at 10 locations around the periphery away from the FBH sites.

The measured L-wave speeds of specimens A through N are listed in table 8 and summarized graphically in figure 41. The measurements were made with the transducer centered over the entry surface (except for specimen G) and were reproducible to within 0.1%. In repeated trials using different investigators, there would generally be slight differences in probe positioning and normalization leading to minor (< 0.1%) differences in the deduced wave speeds. It was noted that each tabulated value is actually an average velocity for sonic pulse travel over several inches; thus, grain-to-grain velocity differences like those seen in the enlarged grain block are largely averaged in these measurements. Notice that for a fixed metal alloy (Ti-17 or Ti 6-4), all of the measured velocities fall within a very narrow band.

TABLE 8. MEASURED LONGITUDINAL WAVE SPEEDS FOR SPECIMENS A-N (In most cases, measurements were repeated using different transducers and the average value is listed.)

Specimen	Source Material	Side 1 (Radial)		Side 2 (Axial)		Side 3 (Hoop)	
		cm/ $\mu$ s	inch/ $\mu$ s	cm/ $\mu$ s	inch/ $\mu$ s	cm/ $\mu$ s	inch/ $\mu$ s
A	Ti-17 Billet (9")	0.6067	0.2389	0.6004	0.2364	0.6038	0.2377
B	Ti-17 Billet (9")	0.6064	0.2387	0.6040	0.2378	0.6057	0.2385
C	Ti-17 Billet (9")	0.6052	0.2383	0.6004	0.2364	0.6041	0.2378
D	Ti 6-4 Forging	0.6230	0.2453	0.6178	0.2432	0.6225	0.2451
E	Ti 6-4 Forging	0.6224	0.2450	0.6177	0.2432	0.6229	0.2452
F	Ti 6-4 Forging	0.6229	0.2452	0.6171	0.2430	0.6243	0.2458
G	Ti 6-4 Forging	0.6193	0.2438				
H	Ti 6-4 Billet (9.25")	0.6200	0.2441	0.6223	0.2450	0.6207	0.2444
I	Ti 6-4 Billet (9.25")	0.6208	0.2444	0.6199	0.2441	0.6199	0.2441
J	Ti 6-4 Billet (9.25")	0.6217	0.2448	0.6208	0.2444	0.6196	0.2439
K	Ti 6-4 Billet (9.25")	0.6170	0.2429	0.6201	0.2441	0.6219	0.2448
L	Ti-17 Billet (7")	0.6067	0.2389	0.6004	0.2364	0.6049	0.2381
M	Ti-17 Billet (7")	0.6065	0.2388	0.6005	0.2364	0.6050	0.2382
N	Ti-17 Billet (7")	0.6061	0.2386	0.6016	0.2369	0.6051	0.2382

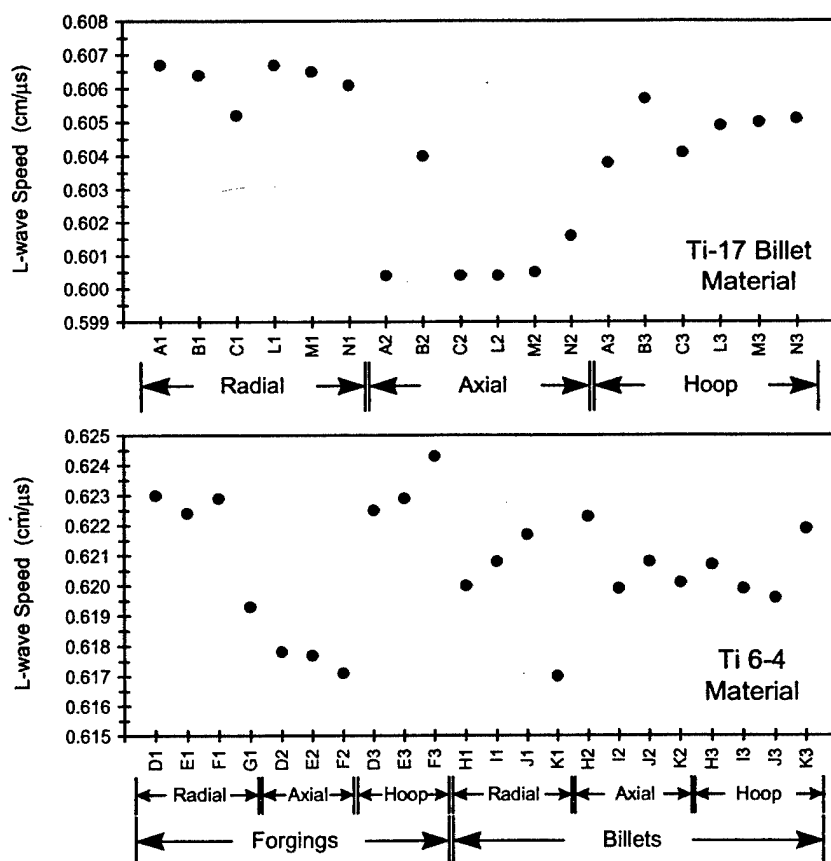


FIGURE 41. MEASURED L-WAVE SPEEDS FOR BILLET AND FORGING SPECIMENS A-N

As illustrated in figure 42, the measurements reveal minor but systematic variations of L-wave velocity with position for a fixed inspection direction. For thicker coupons, the positional variations of velocity are partially averaged out by the long sound travel path, making trends harder to discern. The dependence of velocity on position is most clearly seen when measurements are made on a series of relatively thin coupons removed from adjacent sites. For example, figure 42(d) displays the dependence of radial speed on depth in one Ti 6-4 billet that was examined after the A-N study was completed. In this case, coupons were removed at three depths from two sites on the billet, one where the OD noise level was high and one where it was low. Measured velocities for radial sound propagation are shown for these six coupons and an interesting systematic variation is seen. A similar variation with depth was seen when Ti-17 billet coupons A-C were examined (figure 42(a)), although for that case it is not known whether the coupons were removed from a high- or low-noise site.

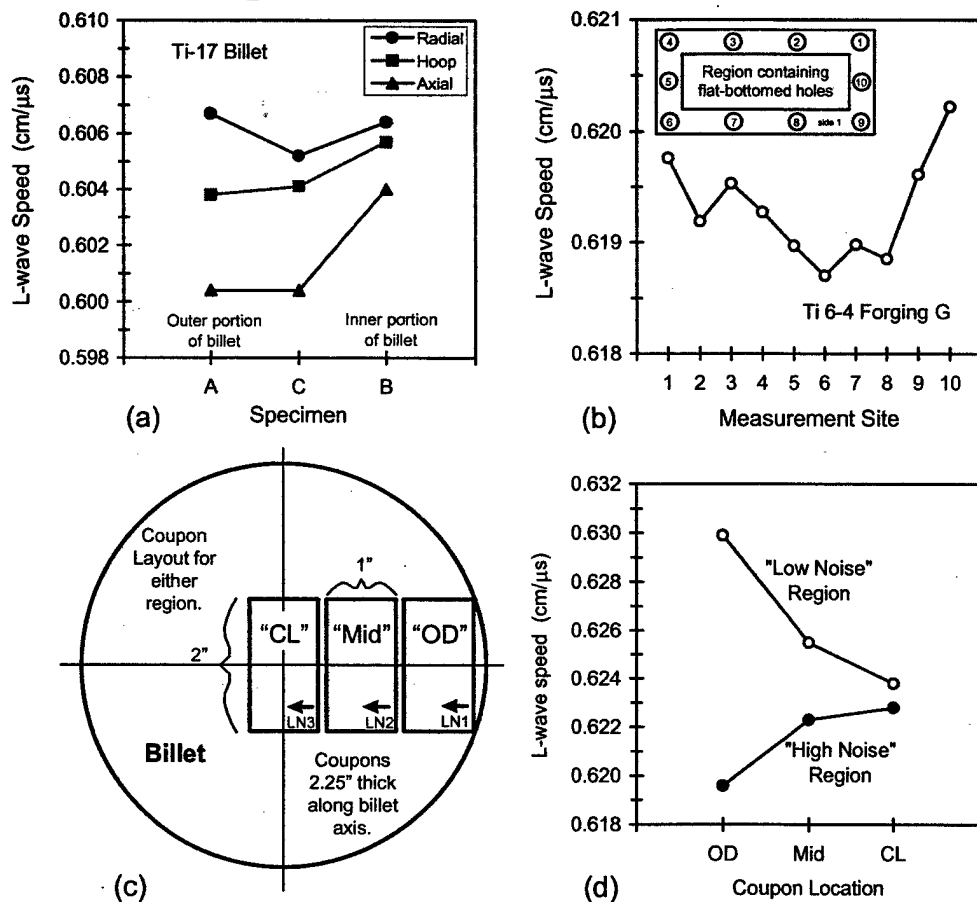


FIGURE 42. DEPENDENCE OF L-WAVE VELOCITY ON POSITION (a) DEPTH DEPENDENCE IN A 9" DIAMETER Ti-17 BILLET, (b) DEPENDENCE OF RADIAL VELOCITY ON POSITION AT 10 POINTS ON THE PERIPHERY OF Ti 6-4 FORGING SPECIMEN G, (c) COUPON LOCATIONS IN A 6" DIAMETER Ti 6-4 BILLET. THREE COUPONS EACH WERE REMOVED FROM SITES DISPLAYING HIGH AND LOW BACKSCATTERED NOISE LEVELS, AND (d) DEPTH DEPENDENCE OF RADIAL VELOCITY IN THE Ti 6-4 BILLET (c).

### 5.3.4 Summary of Velocity Measurements.

The following points can be made to summarize the L-wave velocity findings:

- Overall, on a percentage basis, the velocity variations were quite small when compared to the variations seen in attenuation and backscattered noise levels. For coupons A-N, all measured Ti-17 velocities were within 0.7% of 0.604 cm/μs, and all Ti 6-4 velocities were within 0.7% of 0.621 cm/μs. A somewhat wider range of speeds was seen when thinner specimens were cut from high- and low-noise regions of a 6" diameter Ti 6-4 billet.
- When measurements were made on the same specimen using both 5- and 10-MHz transducers, very little difference (typically ~ 0.1%) was seen in the deduced sound speeds. Moreover, such differences due to frequency were much smaller than specimen-to-specimen differences or than the dependence of velocity on propagation direction in a given specimen.
- For the Ti-17 billet specimens (A-C and L-M) and the Ti 6-4 forging specimens (D-F), a systematic dependence of velocity was observed on the direction of sound propagation: the axial velocity in each specimen tended to be about 1% lower than the radial or hoop velocity, and the latter two velocities were about equal. No systematic trend was seen for Ti 6-4 billet specimens H-K.
- Clear departures from rotational symmetry were observed in billet properties. The billets themselves are cylinders, so their shapes possess full rotational symmetry about the central axis. If billet properties were also rotationally symmetric, then measurements through corresponding sides of specimens H and J should produce identical results, as would corresponding measurements in I and K or L and M. In addition, measurements through sides 1 and 3 of a centerline specimen (I, K, N) should be equal, since both propagation directions are in fact radial for such a specimen. Departures from symmetry of as much as 0.8% in velocity were seen (e.g., for radial and hoop propagation in specimen K). This is not surprising since C-scans of backscattered noise in billets show similar asymmetries: the noise banding patterns are not rotationally symmetric.
- For the Ti-17 billet specimens (A-C and L-M), there was a systematic relationship between velocity and depth: the radial and hoop velocities were approximately independent of depth, and the axial velocity tended to increase as one approached the billet center. Later measurements using small Ti 6-4 billet coupons also revealed a dependence on depth but with a more complicated pattern: whether a given velocity increased or decreased with depth depended on the lateral position (axial and hoop coordinates). This is likely to be the general case for all billets, since all display some degree of noise banding.

In summary, it was known from the enlarged grain block study that there is a substantial (> 10%) dependence of sound speed on propagation direction within a given macrograin. However, such differences tend to average out when the beam traverses many macrograins with partially randomized orientations. As a consequence, average L-wave velocities for billet and forging

specimens over travel paths of several inches usually vary only modestly (i.e., by 1% or less) on specimen or inspection direction for a given alloy type. Since the measured sound speeds are not isotropic, the macrograin orientations within a given coupon are not completely randomized, and the directional dependence of measured velocities provides insight to the preferred crystalline orientations. For example, the fact that the sound velocity is slowest for axial propagation in Ti-17 billet specimens A-C (figure 42(a)) indicates that the alpha-phase crystallites there are more likely to have their symmetry axes aligned normal to the billet axis than along it. Even though the average sound speed differences along different sonic ray paths are small for billet and forging material, those velocity differences can cause significant distortions of propagating ultrasonic beams. As will be discussed in the next section, this can have a large impact on the sizes and fluctuations of ultrasonic echoes from surfaces and defects.

### 5.3.5 Longitudinal Wave Attenuation Measurements.

Ultrasonic attenuation is used to describe the loss of strength of a sound wave as it propagates through a distance and the associated reduction in the amplitude of an ultrasonic signal. Suppose, for example, that a component with a flat entry surface has several identical defects located at different depths, as illustrated in figure 43. Using any given transducer and a fixed gain setting, the echoes from these defects will generally be different. In fine-grained metals, these differences arise from two principal effects:

- Diffraction, which encompasses both beam-focusing and beam-spreading effects and acts to redistribute the energy carried by the beam.
- Attenuation resulting from the absorption and scattering of sound which acts to remove energy from the forward-propagating beam.

Thus, attenuation describes the loss of signal due to increased travel path, after accounting for diffraction.

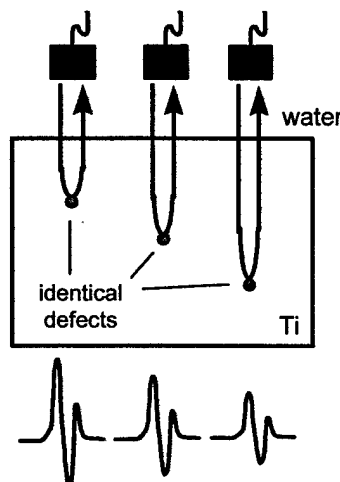


FIGURE 43. IDENTICAL DEFECTS AT DIFFERENT DEPTHS GIVE RISE TO ECHOES OF DIFFERENT STRENGTHS, PARTIALLY AS A RESULT OF MATERIAL ATTENUATION

The symbol  $\alpha$  to represent the ultrasonic attenuation coefficient will be used. It is a frequency-dependent quantity which generally increases with frequency ( $f$ ), and our goal is to measure it at typical inspection frequencies, i.e., within the range from about 2 to 15 MHz. Two sets of units, Nepers/cm and dB/inch, are commonly used when quoting attenuation values and both will be used. They are related by:

- 1 Neper/cm = 22.06 dB/inch
- 1 dB/inch = 0.0453 Nepers/cm

A bit later, the precise operational definition of  $\alpha$ , on which our measurement procedures are based, will be given. For now, a common sense definition will do. If a specimen has a measured attenuation of say 2 dB/inch (at an inspection frequency of interest), then the echo from a reflector 3" deep would be reduced by  $(2)(3\text{"})(2 \text{ dB/inch})=12 \text{ dB}$  when compared to an echo from a similar reflector in an ideal nonattenuating specimen having the same density and sound speed. More generally, if Neper/cm units are used and if the round trip sonic travel distance is  $z$ , then the amplitude of an ultrasonic signal is reduced by a factor of  $\exp(-\alpha z)$  relative to the nonattenuated case.

There are two principal motivations for studying attenuation. First, to test computer models of ultrasonic inspection processes which predict such things as defect echoes, backscattered grain noise characteristics, signal-to-noise ratios, and probability-of-detection curves. Attenuation is one of the inputs to these models, and hence, it must be known before model predictions can be made for comparison with experiment. Secondly, different billets with different processing histories likely have different attenuations, and knowledge of those differences can be used to improve inspections. For example, a common practice prior to billet inspection is to use a calibration standard containing FBHs to make initial equipment settings. An inspector may set the amplification level such that an echo from a #2 FBH in the standard occupies 80% of the screen height on his monitor. The supposition is that a #2 FBH at the same depth in the billet to be inspected would also give rise to an 80% echo. This will not be the case if the attenuations of the billet and calibration standard differ appreciably. However, if the relative attenuations of the two billets have been measured, then appropriate gain adjustments could be made to insure that similar defects in the two billets return echoes of similar amplitude. How important are such adjustments in practice? How can they best be implemented? An understanding of signal attenuation in engine alloys can help to answer such questions and hopefully lead to improved inspection practices.

Earlier it was stated that for fine-grained metals, echoes from identical defects at different depths would generally differ due to the effects of both diffraction and attenuation. In many instances, the effects of diffraction dominate. For example, a deep defect that happens to be located near the focal plane of a focused transducer can return a much larger echo than a similar defect at a shallower depth. Thus when making attenuation measurements it is very important to remove that fraction of the signal loss (or gain) that arises from anticipated beam spreading or focusing effects. A simple way of doing this, pioneered by Robert Gilmore at GE Corporate Research and Development Center (CR&D), is to use a low-attenuation reference specimen with about the same thickness and sound speed as the titanium specimen under study [23]. The attenuation of titanium is then deduced by comparing the relative sizes of corresponding ultrasonic signals in

the two specimens. Since the rate of beam diffraction depends on sound velocity (about equal in the titanium and reference blocks), diffraction effects will largely cancel in the measurement. As will be discussed later, the cancellation can be made more exact by small adjustments in the water paths.

Such methods of accounting for beam diffraction during  $\alpha$  measurement assume that the beam is well behaved, i.e., that the beam profile resembles that seen in a fine-grained material of similar sound speed. As we shall demonstrate, this is not the case in engine titanium alloys. Indeed, the local microstructure can cause significant distortions of the beam which vary from location-to-location in the specimen. These distortions affect our measurements in two ways:

- They can cause a shift in the average strength of an ultrasonic signal of interest (e.g., a back-surface echo); and
- They can lead to sizable fluctuations about that average during a scanning experiment.

Thus both the average value and uncertainty of the measured attenuation can be affected by beam distortions. When making attenuation measurements, the aforementioned reference block technique will be used to correct for the effects of beam diffraction in well-behaved material. Unfortunately, there are no models currently available which can be used to make similar corrections for the average effects of beam distortion. In a fine-grained metal where the microstructure is small compared to the ultrasonic wavelength, the measured attenuation simply describes the loss of energy by a sonic beam as it propagates. In engine titanium, however, the measured attenuation values will reflect the combined effects of both energy loss and beam distortion.

Five effects have been identified as, having microstructural origins, which can contribute to the measured attenuation in engine titanium specimens. These are listed in the table 9. The first two effects describe the actual loss of energy from the beam, while the last three essentially describe how the remaining energy is redistributed within the propagating sonic pulse. Figure 44 provides visual evidence for the existence of beam distortion effects in engine titanium alloys. For figure 44(a) and (b), a 10-MHz, 0.25" diameter planar probe was used to ensonify, in turn, 3" thick blocks of fused quartz (FQ) and Ti-17 billet material (axial propagation in specimen L). The through-transmitted beam emerging from the back of each specimen was then "mapped" using a small, planar point probe, having a diameter of about 0.5 mm. Fourier transforms of the received signals were computed so that the individual spectral components of the emerging beam could be displayed.

In figure 44(a), the amplitudes at 9.2 MHz of the through-transmitted ultrasonic signals are compared after adjustments for the differing interface losses, essentially providing a comparison of the emerging pressure amplitude fields for the two beams. The beam emerging from FQ has the expected circularly-symmetric profile, while that from Ti-17 is clearly distorted and displays a fragmentation of the beam intensity profile into several hot spots. Distortions in phase also occur, as documented in figure 44(b). There, the C-scan images essentially display the relative phases of the pressure oscillations in the emerging beams at 9.2 MHz. For FQ, the points of equal phase in the scanning plane of the receiver are concentric circles, indicating that the three-

dimensional wave fronts resemble the smooth, nearly spherical surfaces expected in the far field of an ideal piston probe. For Ti-17, however, the equal-phase lines are decidedly noncircular, indicating that the microstructure has caused the wave fronts to wrinkle. Other examples of measured amplitude and phase profiles in Ti 6-4 and Ti-17 alloys can be found in publications by Panetta, et al. [24 and 25].

TABLE 9. CONTRIBUTING FACTORS FOR SOUND ATTENUATION IN TITANIUM ALLOYS

Effect	Meaning
Scattering	Reflection of sound at grain boundaries into nonforward directions.
Absorption	Transfer of sound energy into heat and mechanical work.
Beam Steering	Movement of the beam's center of intensity away from the path it would normally follow (in fine-grained, homogeneous material).
Beam Disruption (Amplitude Distortion)	Distortions in the normal shape of the beam intensity pattern, including, in some cases, the splitting of the beam into two or more high-intensity lobes.
Wave Front Distortion (Phase Aberrations)	Bending or wrinkling of the constant-phase wave fronts away from the simply-curved shapes they would normally have.

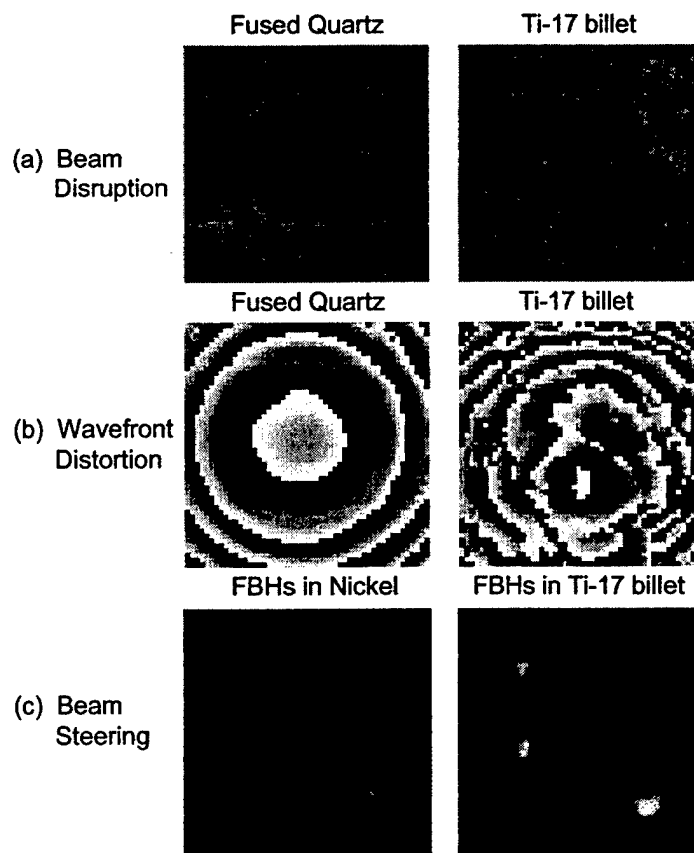


FIGURE 44. EXAMPLES OF BEAM DISTORTION EFFECTS IN ENGINE TITANIUM ALLOYS

In addition to distorting the amplitude and phase profiles of a sonic beam, the titanium microstructure can cause the center of intensity to be steered away from its expected path. This effect is demonstrated in figure 44(c). A 10-MHz 1/4" planar probe was used to scan 3 by 3 arrays of #1 FBHs located about 2.75" deep in two blocks: one fabricated from powdered nickel alloy and one from Ti-17 billet material (specimen L, axial propagation). In each case, the FBHs were arranged in a uniform lattice having a 0.5" by 0.5" step size. The C-scan images display the peak-to-peak amplitudes seen within a 2-microsecond-wide time gate centered at the expected arrival time for FBH echoes. As expected, the C-scan map of the fine-grained nickel specimen contains nine equally spaced FBH images with nearly identical peak amplitudes. This is not the case for the Ti-17 specimen, however. Although the holes are regularly spaced, their images are not. This indicated that the local microstructure above each hole is acting to steer the beam slightly and that the net shift in beam direction is different at each location.

For the most part, the common practice of measuring attenuation by analyzing ultrasonic echoes from some type of reflector such as a large flat surface or a small FBH will be followed. The size of such an echo will depend upon the details of the incident pressure field (both amplitude and phase) that is brought to bear on the reflector. Since all five of the effects in table 9 describe alterations in the pressure field, they all contribute to measured attenuation. In situations where the first two effects dominate, one expects the attenuation to be approximately independent of details of the procedure used to measure it. Unfortunately in engine titanium alloys, this turns out not to be the case, and the combined contribution of the beam distortion effects can be as large or larger than the contribution from energy loss. As a consequence, as will be shown, different methods of measuring the attenuation can give different numerical values. Moreover, even if a single-measurement method is used (say using back-surface echoes) but one switches from a planar to a focused transducer, the deduced attenuation can change. Thus, it is important to keep in mind that an apparent or effective attenuation is being determined, whose value is somewhat tied to the type of signal being studied and, to a lesser extent, to details of the measurement procedure. Thus, for example, an attenuation value appropriate for describing the decay with depth of backscattered grain noise may not be appropriate for describing the decay with depth of a back-surface echo or a flaw echo. This unfortunate circumstance is a consequence of the complex nature of the interaction between sound and titanium microstructure.

### 5.3.5.1 Attenuation Measurement Methods.

The attenuation of an engine alloy specimen can be measured in a variety of ways and beam distortion phenomena will affect each measurement method differently. In the present work, the three methods indicated in figure 45 were used. In each case, the attenuation of a titanium specimen was deduced by comparing sonic signals observed in titanium to similar signals observed in a reference block with negligible attenuation. The signal attributes compared in each method are listed in table 10.

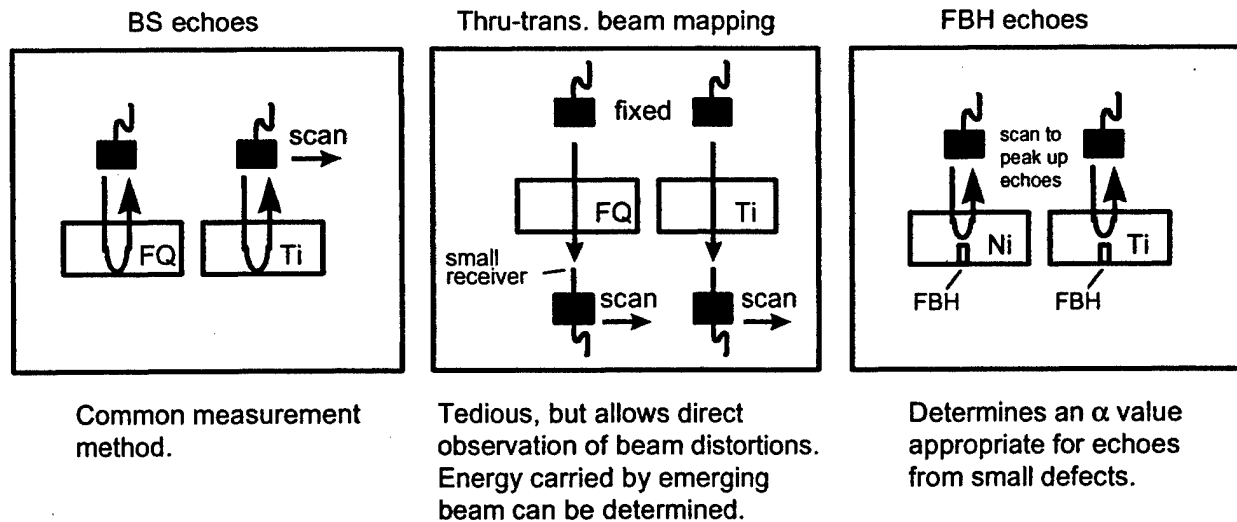


FIGURE 45. INSPECTION GEOMETRY AND RAY PATHS FOR THE THREE ATTENUATION MEASUREMENT PROCEDURES

TABLE 10. ATTENUATION MEASUREMENT METHODS

Method	Shorthand	Signal Attribute Examined
1	BS	Voltages or spectral amplitudes of back-surface echoes
2	TTE	The energy in a through-transmitted beam as mapped with a focused or point receiver i.e., the square of the transmitted voltage or spectral amplitude integrated over the cross section of the emerging beam.
3	FBH	Voltages or spectral amplitudes of echoes from FBHs.

The bulk of the measurements were made using the backscatter (BS) method, and follow-up measurements were performed on selected specimens using the through-transmitted energy (TTE) and flat bottom hole (FBH) techniques. Examples of through-transmission beam maps acquired for use with the TTE method were shown in figure 44. In the BS and TTE methods, a FQ reference block was used. For the FBH method, a powdered nickel alloy block (R88) was used because of anticipated difficulties in drilling small holes into FQ. The BS method was used to measure the attenuation of the nickel block, and it was found to have negligible attenuation (< 0.002 Nepers/cm) below 20 MHz.

The three methods listed in table 10 were selected, in part, because they serve as useful tools for exploring how microstructure affects inspections. The BS method is the traditional measurement technique and is by far the simplest to use. It is also believed to be the technique most sensitive to the effects of wave front distortion, because the entire beam interacts with the reflector in a phase-sensitive manner. In the TTE method, phase variations in the beam are entirely ignored in the analysis and one obtains a direct measurement of the energy-loss contribution that is expected to be present in all ultrasonic measurements. The FBH method is perhaps of greatest interest in an industrial setting, since it yields an attenuation value that is appropriate for describing echoes from small scatterers. Since the maximal echo from a small defect is seen

when the peak pressure field illuminates the defect, the FBH method is likely most sensitive to beam disruption, i.e., to the development of hot spots in the lateral beam profile.

Technical details of the signal analysis procedures used to deduce the attenuation for each measurement procedure can be found in references 24 through 26. Here, a brief general synopsis will be provided. To begin, a thought experiment will be discussed, which forms the basis for the measurement procedures. Consider two blocks of material, which have identical densities and average velocities and differ only in one respect, namely, that the first has zero attenuation and the second does not. By definition, in the specimen with  $\alpha=0$ , the pressure amplitude of a propagating plane wave would not change with distance. In the other specimen, it was assumed that the pressure would drop by a factor of  $\exp(-\alpha z)$  after propagating a total distance of  $z$ . Similarly, if identical reflectors are placed at the same depth,  $z$ , in the two materials and ensonify both using the same transducer, then it is assumed that the echoes differ by a factor of  $\exp(-2\alpha z)$ ; or more precisely, that their spectral magnitudes at frequency  $f$  differ by  $\exp[-2\alpha(f) z]$ . Thus, the attenuation of the second block can be deduced by measuring the ratio of spectral magnitudes for corresponding signals in the two blocks and setting the ratio equal to  $\exp[-2\alpha(f) z]$ .

Unfortunately, nonattenuating reference blocks with the same density and average sound speed as the titanium specimens under investigation were not available. Instead, a FQ or powdered nickel reference block was substituted. Because the densities and sound speeds are not the same, attenuation will not be the only source of echo differences in the titanium and reference blocks. Diffraction and interface phenomena will also introduce differences, and these must be handled. To handle diffraction, the water paths in the BS and FBH methods are adjusted so that

$$Z_{0R} + \left[ \frac{v_{1R}}{v_0} \right] Z_{1R} = Z_{0S} + \left[ \frac{v_{1S}}{v_0} \right] Z_{1S} \quad (1)$$

is satisfied, where:

- $v_0$  = speed of sound in water
- $v_{1R}$  = speed of sound in reference block
- $v_{1S}$  = speed of sound in specimen block (titanium)
- $Z_{0R}$  = one-way water path for reference block
- $Z_{0S}$  = one-way water path for specimen block (titanium)
- $Z_{1R}$  = one-way solid path for reference block
- $Z_{1S}$  = one-way solid path for specimen block (titanium)

When the measurement water paths are adjusted so that equation 1 holds, the effects of beam diffraction (at the location of the back surface or FBH reflectors) are nearly identical for the two blocks. This is strictly true only for homogeneous media in the so-called paraxial limit, but it was assumed that it is also a good approximation for pulse-echo attenuation measurements in the titanium specimens. Beam diffraction is not a factor in the TTE method, since focusing or spreading, per se, does not alter the energy carried by a sonic pulse. Thus, in the TTE method,

the same water paths are used for both the reference and titanium blocks, with the transmitter water path typically being 2-5 cm and the receiver water path typically being a few millimeters.

By virtue of the inspection geometry, it has now been arranged for diffraction effects to approximately cancel for each of the three measurement methods. The next step is to measure the corresponding pulse/echo or through-transmitted signals in the two blocks, and then to compute the ratio of the appropriate signal attribute listed in table 10. Then ask why does this ratio differ from unity. Part of the difference arises from the differing interface transmission and reflection coefficients of the titanium and reference blocks, and the signal ratio is corrected for this effect, using the standard plane wave formulas [26]. Similarly, if the inspection water paths are appreciably different, a correction for the effects of water attenuation are made, using the known temperature-dependent attenuation coefficients of pure water<sup>26,27</sup>. After these corrections, any remaining departure in the signal ratio from unity is attributed to attenuation in the titanium block. In particular, for the corrected ratio:

$$(\text{Titanium signal attribute})/(\text{Reference signal attribute}) = \exp(-\alpha z) \quad (2)$$

where  $z$  is the total travel path through the titanium. It remains then only to solve equation 2 for  $\alpha$ .

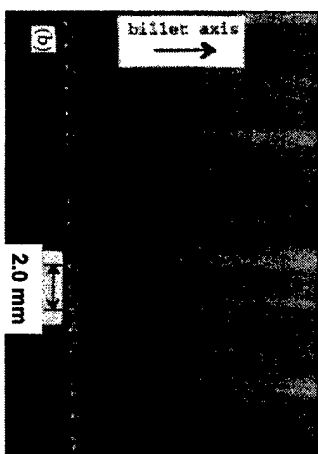
Note that for each of the three measurement methods, two general data analysis approaches can be used:

- A frequency domain approach that leads to a deduced attenuation as a function of frequency within the bandwidth of the probe; or
- A time domain approach that leads to the deduction of a single, frequency-averaged attenuation value.

In the first approach the attributes appearing in the ratio of equation 2 are the amplitudes of the Fourier spectra at a frequency of interest. In the second approach, the ratio quantities are usually chosen to be the peak-to-peak or rectified peak voltages of the sonic signals. In practice, it is usually found that the attenuation value deduced in the time domain approach approximately equals the frequency domain attenuation evaluated at the center frequency of the received broadband signal. The majority of the results reported in this work were deduced using the frequency domain approach.

In engine titanium, the detailed microstructure varies from point-to-point in a specimen, and the large-scale component (macrostructure) is not small compared to a sound wavelength at typical inspection frequencies. As a consequence, beams passing through different portions of the specimen are affected differently, leading to different echoes from nominally identical reflectors. This effect is clearly seen when a transducer is scanned over a flat specimen to acquire a C-scan image of the back-surface echo amplitude. In thinner billet specimens, the pattern of high and low back-surface amplitudes often resembles the physical structure of the columnar macrograins, as shown in figure 46.

Photograph of Large-Scale Microstructure



C-scan Image of BS Echo Amplitude  
(Red = high amplitude)

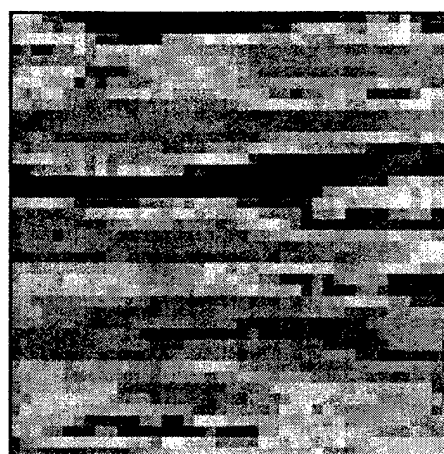


FIGURE 46. RESEMBLANCE OF COLUMNAR MICROSTRUCTURE (LEFT) AND BACK-SURFACE ECHO AMPLITUDE PATTERN (RIGHT) IN Ti-17 BILLET SPECIMEN C1 (The C-scan image was formed by scanning a 1" by 1" region using a 5-MHz F/8-focused transducer)

Because of such signal variations, it would be very misleading to only perform an attenuation measurement at a single location in a given specimen. Instead, for the BS method, the transducer is scanned over the specimen acquiring BS echoes at many (typically  $> 100$ ) locations, and then calculates an average attenuation value and a standard deviation. Similarly, for the FBH method, each titanium or reference specimen contains nine FBHs, and echoes are acquired from each of them. For the TTE method, the measurements are more time consuming owing to the need to scan the receiver, and data is normally collected only for a few transmitter positions (e.g., one at which a large BS echo is observed and one where a small BS echo is observed). Experience shows that details of the emerging beam pattern vary greatly with transmitter position, but that the energy carried by the pulse does not. Thus, positional averaging is not required when the TTE method is used. The opposite is true for the BS method, where the spectrum of the back-surface reflection can vary greatly as the transducer is scanned. An extreme example is illustrated in figure 47, where the specimen is the Ti 6-4 enlarged grain plate, as discussed earlier in section 5.2.2. The coarse macrostructure results in very large BS echo fluctuations, leading to large point-to-point differences in measured  $\alpha$ -vs- $f$  curves. Although the averaged  $\alpha$ -vs- $f$  curve displays a systematic trend, the standard deviation of the individual measurements about their mean is quite large. When graphs such as that of figure 47 are presented, the error bars extend one standard deviation on either side of the mean and, hence, typically enclose about 68% of the individual-site measurements.

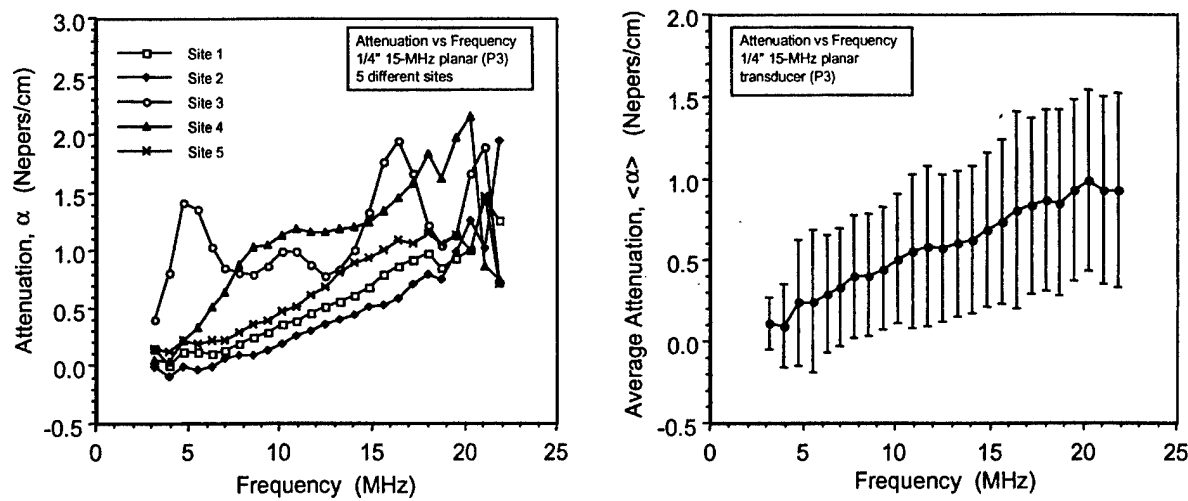


FIGURE 47. USE OF THE BS ECHO METHOD TO MEASURE ATTENUATION IN THE Ti 6-4 ENLARGED GRAIN PLATE (Left: deduced attenuation at five randomly selected sites. Right: average and standard deviation of the BS attenuation for an automated scan over several hundred sites. A 0.25" diameter planar transducer was used.)

When attenuation data is acquired at many sites on a specimen and averaged, as is done for the BS and FBH methods, there are two averaging schemes that can be used to determine a mean, denoted by  $\langle \alpha \rangle$ , and a standard deviation, denoted by  $\sigma$ .

- Calculate an  $\alpha$  value in Nepers/cm or db/inch at each measurement site and then compute  $\langle \alpha \rangle$  and  $\sigma$  from these or
- First average the signal attributes themselves over position to obtain a mean and standard deviation, and then compute an  $\alpha$  value and uncertainty from these by insertion into equation 2.

The basic difference is that the quantities being averaged are cited in dB units in the first case, and in non-dB units (e.g., volts) in the second. The choice of the averaging scheme used influences the quoted attenuation value and, thus, must be taken into account when measured values at different facilities are compared. For that reason, a brief example will be given to illustrate the difference.

Suppose that the BS echo method is applied to a 1/2" thick titanium specimen and observe echoes at three locations, which are 1, 2, and 3 dB below the corresponding FQ echo (after corrections for water attenuation and interface losses). In the first method, the attenuation values at the three sites would be calculated as 1, 2, and 3 dB/inch, respectively, and these would simply be averaged to obtain  $\langle \alpha \rangle = 2$  dB/inch. In the second method, the three signals would be described as having amplitudes of 0.89125, 0.79433, and 0.70795, respectively, relative to a unit amplitude in FQ. This leads to an average amplitude of 0.79784 in titanium, i.e., 1.96 dB below the FQ amplitude. Thus, the average attenuation would be cited as 2.00 dB/inch, using the first averaging method, and as 1.96 dB/inch, using the second method. Similarly, the  $\pm 1 \sigma$  error bars

describing the variation of the measured attenuation values about their mean would differ slightly (extending from 1.184 to 2.816 dB/inch in method 1 and from 1.183 to 2.818 dB/inch for method 2).

Arguments can be made in favor of each averaging scheme. As a general rule, method 1 was usually used by ISU personnel, and method 2 was used by GEAE personnel. In practice, the difference in average attenuation values for the two schemes was almost always less than 5% (with method 1 yielding the higher value) and was much smaller than the standard deviation of the  $\alpha$  values about their mean. Unless otherwise stated in a given table or figure, averaging method 1 should be assumed.

### 5.3.5.2 Specimen-to-Specimen Variations in Attenuation for a Fixed Measurement Geometry.

As will be demonstrated later, in some cases an alteration in the measurement procedure, such as changing the focal properties of the transducer, can significantly affect the value of the measured attenuation. Thus, if one is interested in surveying the manner in which attenuation varies within the class of engine titanium specimens, it is necessary to fix the details of the measurement procedure, and then to apply the procedure systematically to a representative set of specimens. Such systematic measurements are the chief topic of this section. Our goals are to determine typical values of attenuation for engine titanium specimens at the inspection frequencies of greatest interest to the ETC (5-15 MHz) and to discover the major trends in the data.

One such study was performed by applying the traditional BS method to the 14 billet and forging specimens denoted A-N in figure 34. Measurements were made in the radial, axial, and hoop directions using a 10-MHz, 0.25" diameter planar transducer in immersion. Measurement particulars for a typical case are listed in table 11. Owing to the different sizes of the specimens, there were naturally some differences in scan area and reference block thickness.

TABLE 11. INSPECTION PARAMETERS FOR THE MEASUREMENT OF BACK-SURFACE ATTENUATION IN SPECIMEN L, A 3" CUBE CUT FROM THE OUTER PORTION OF A Ti-17 BILLET

Transducer	10-MHz, broadband, 0.25" planar. Panametrics model V312, Serial number 58498
Reference block	Fused quartz; 3.008" thick
Water paths	About 5 cm
Region scanned	2.0" x 2.0" in steps of 0.2" (11 x 11=121 transducer position)
Duration of digitized back-surface echoes	2.55 microseconds (256 points at a sampling rate of 100 MHz)
Frequencies at which $\alpha$ was determined	1.95 MHz to 16.02 MHz in steps of 0.78 MHz
Other notes	There was a 10-dB difference in gain settings for acquisition of the BS echoes from the reference block and titanium specimen.

The results of the inspection described in the above table are summarized in figure 48. The left panel displays the measured BS echo attenuation for Ti-17 billet specimen L when the sound

beam propagated parallel to the billet axis. Both the average and standard deviation of the measured attenuation values are shown as functions of frequency within the probe's useable bandwidth.  $\langle\alpha\rangle$  is seen to rise with frequency, at a rate slightly faster than linear, reaching about 3.5 dB/inch at 15 MHz. In the right-hand panel of the same figure, the average attenuations for the three propagation directions are compared. The mean attenuations in the radial and hoop directions were quite similar and somewhat below the axial value for frequencies above 5 MHz. As in all billet specimens examined, the columnar macrograins of specimen L were elongated in the axial direction and the measured attenuation was greatest for propagation parallel to those macrograins.

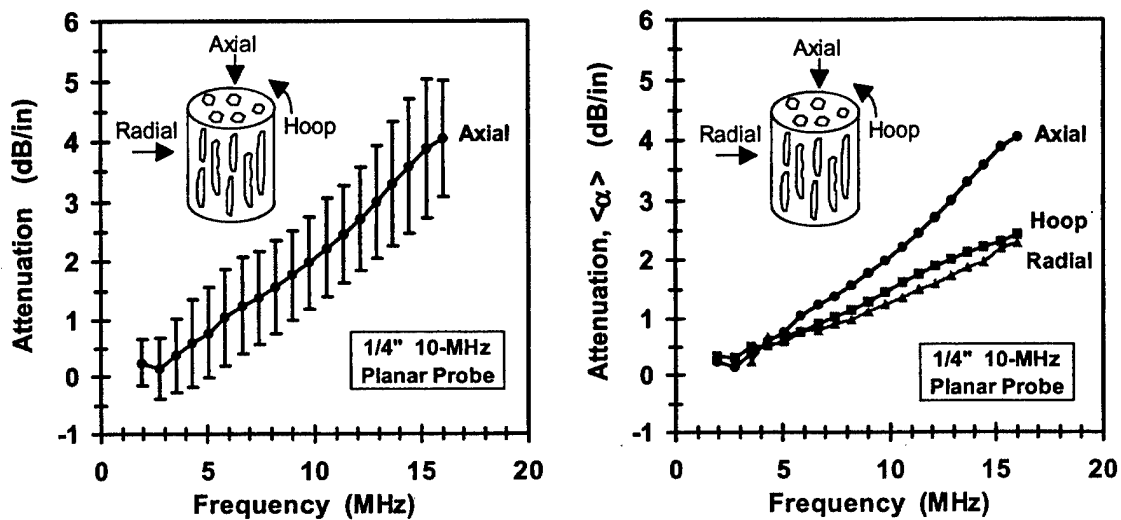


FIGURE 48. MEASURED ATTENUATION OF Ti-17 BILLET SPECIMEN L USING THE BS METHOD

A summary of the position-averaged attenuations for scans of specimens A-N is provided in figure 49. Measured values at both 5 and 10 MHz are indicated. Note that if the rise of mean attenuation with frequency were linear, the value at 10 MHz would be twice that at 5 MHz, and if quadratic, the values would differ by a factor of four.

The following points summarize the measurements of BS echo attenuation in specimens A-N:

- Measured average attenuation rose with frequency, at a rate that was typically faster than linear but slower than quadratic.
- Attenuation values ranged over about one order of magnitude among the suite of specimens: from 0.2 to 2 dB/inch at 5 MHz and from 0.6 to 6 dB/inch at 10 MHz.
- Attenuation tended to be higher in Ti 6-4 material than in Ti-17. The one exception occurred for Ti 6-4 forging specimen G that was inspected only in the radial direction. This specimen had a finer macrostructure relative to the other specimens, and the beam propagated perpendicular to the flow lines.

- d. There was a strong dependence on beam propagation direction. In billets, measured attenuation was always highest for axial propagation. In general, for both billets and forgings,  $\langle \alpha \rangle$  tended to be highest when the beam propagated parallel to the local macrograin elongation direction.
- e. Significant fluctuations in the strength of the back-surface echo were seen during scanning, particularly for axial propagation in billets. For a given specimen and propagation direction, it was not unusual for the minimum and maximum BS echoes to differ by a factor of three or more in peak-to-peak amplitude.
- f. Concurrent with the attenuation measurements, backscattered noise data was being gathered, as will be discussed later in section 5.3.9. An inverse relationship between measured attenuation and measured noise-FOM was seen: in a given specimen the propagation direction for which the measured attenuation was highest was the direction for which the backscattered noise was lowest, and vice versa.

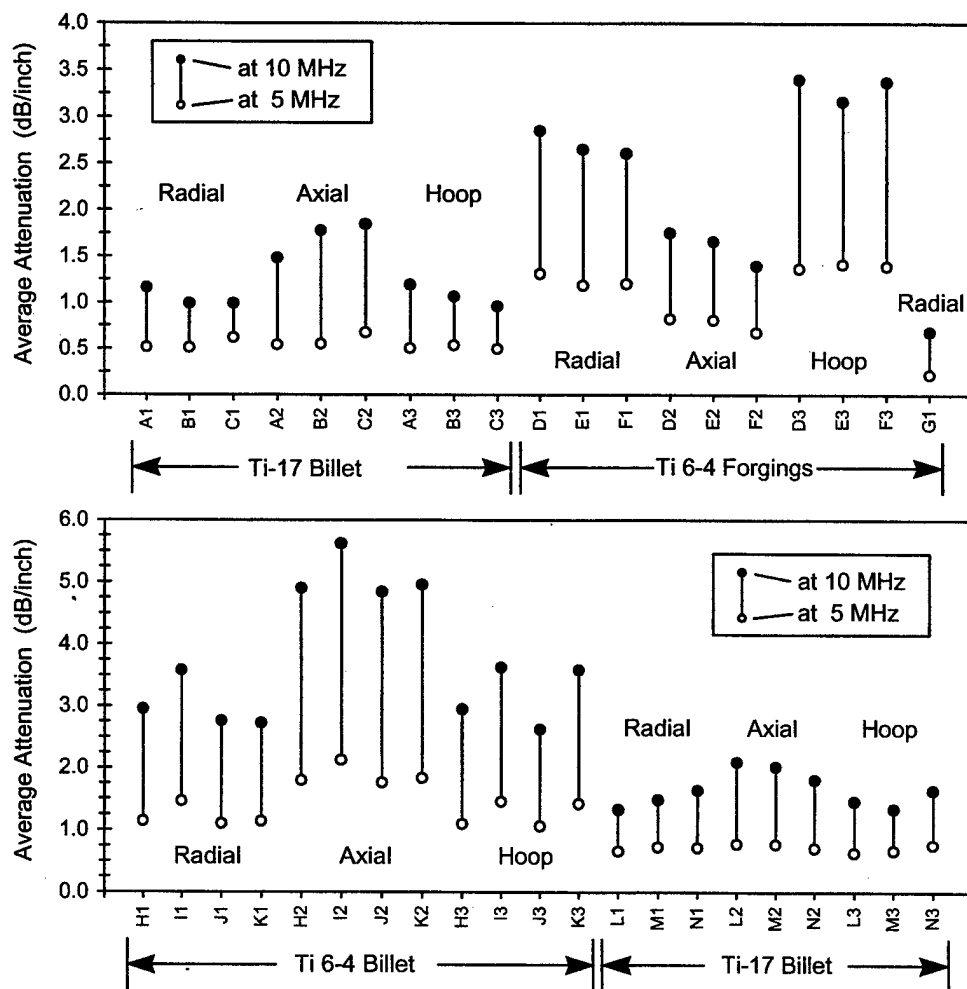


FIGURE 49. MEASURED ATTENUATIONS OF SPECIMENS A-N AT 5 AND 10 MHz, AS DEDUCED BY COMPARING BS ECHOES IN TITANIUM AND FQ BLOCKS

In these measurements only modest differences were seen in the attenuations of specimens cut from different locations on the same billet or forging. However, in most cases the sound propagation path through the specimen was several inches and the measured attenuation was, in effect, an average over that length. A more dramatic dependence of attenuation on position was seen in follow-up studies using thinner coupons. Recall that in section 5.3.3, sound velocity measurements were described on 1" thick coupons removed from six locations in a 6" diameter Ti 6-4 billet (three each from high- and low-noise regions). Attenuation measurements for radial sound propagation were also performed on those coupons, and the results are summarized in figure 50. Among the suite of coupons, the average attenuation is seen to vary by a factor of about 2.5. Thus, point-to-point variations of the effective attenuation within a given billet or forging can be substantial, even if the propagation direction is fixed.

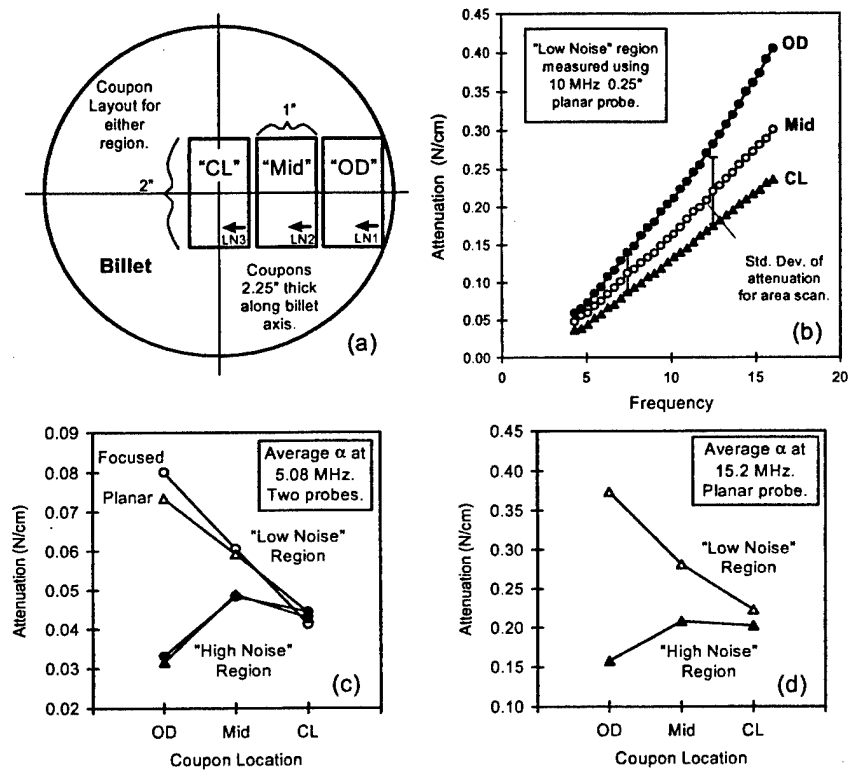


FIGURE 50. BS ECHO ATTENUATION FOR SIX COUPONS FROM A Ti 6-4 BILLET, AS MEASURED USING TWO PROBES: 10-MHz, 0.25" PLANAR AND 5-MHz, 0.75", F=6" FOCUSED ON THE BACK SURFACE (a) COUPON LAYOUT (b)  $\langle \alpha \rangle$ -VS-F CURVES FOR THE THREE COUPONS FROM THE LOW-NOISE REGION, USING THE PLANAR TRANSDUCER (c) AND (d) AVERAGE ATTENUATIONS AT 5.1 MHz AND 15.2 MHz, RESPECTIVELY, FOR ALL SIX COUPONS

### 5.3.6 Dependence of Deduced Attenuation on Details of the Measurement Method.

The BS attenuation measurements described in the previous section were the first to be performed. In the course of carrying out those measurements, it became clear that changes in the details of the measurement procedure, such as the choice of transducer, could have a significant

impact on the deduced attenuation value. Other puzzling aspects of the early data were the large back-surface echo fluctuations that were seen in many specimens and the inverse relationship between attenuation and backscattered noise. These phenomena lead to broadening the scope of the measurements. For a limited number of specimens, additional experiments were performed to study the dependence of deduced attenuation on the choice measurement method and its details. Some of the specimens used in this second round of measurements were members of the original A-N set. Others were newly fabricated specimens which became available. In rough chronological order of performance, the second round of measurements consisted of:

- Method 1—Measurements of BS attenuation using multiple transducers.
- Method 2—Through-transmission beam-mapping experiments with multiple transducers, with associated determination of the TTE (energy) attenuation.
- Method 3—Measurements of FBH attenuation using multiple transducers.

The discussion of the results of these experiments, in sections 5.3.6.1 through 5.3.6.3, will follow this same order. Each section contains a brief description of the method, a discussion of the results, and a summary of the principal findings. Note that when focused transducers were used, the water path was chosen to focus the beam at the specimen back surface (for the BS or TTE method) or at the depth of the holes (for the FBH method). When planar transducers were used, the reference block water path was chosen at a convenient round value, typically between 2 and 5 cm, and the titanium water path was then chosen in accordance with equation 1.

#### 5.3.6.1 Method 1: BS Attenuation Using Multiple Transducers.

Using two or more transducers, selected specimens were scanned to determine the average and standard deviation of the back-surface attenuation for each probe. In selected cases, the entry angle was varied to determine the effects of beam misalignment on the measurement. Specimens were then exchanged and duplicate attenuation measurements completed at other facilities within the ETC team.

For each of the three measurement methods pictured in figure 45 (i.e., BS, TTE, and FBH), the analysis assumes that the sonic beam is normally incident on the reference block and titanium specimen. The TTE and FBH methods are not expected to be particularly sensitive to minor errors in beam alignment. The BS method, however, was found to be very sensitive to beam alignment, particularly when planar transducers were used with the thicker specimens. Alignment errors of several tenths of a degree were found to produce noticeable upward shifts in the  $\alpha$ -vs- $f$  curves. Examples are shown in figure 51. In figure 51(a), deduced  $\alpha$ -vs- $f$  curves are shown for three scans of a Ti-17 billet specimen using a planar transducer. In two of the trials conducted by different investigators on different days, efforts were made to carefully align the incident sound beam normal to the entry surfaces of the fused quartz and titanium blocks and similar results were obtained. In the third trial, the beam was intentionally misaligned by tilting it 0.5 degrees from normal prior to the scan of the titanium specimen. The measurement error due to the 0.5-degree tilt seen to be quite large, indicating the need to carefully adjust the probe angles. A similar measurement error was seen when a focused transducer was misaligned by 0.5 degrees (figure 51(b)), but the size of the error was not as large as in the planar probe case.

In the experiments summarized by figure 51, the beam was always aligned properly for the reference block measurement. The tilting of the beam incident on titanium in selected measurement trials reduced the average strength of the titanium echoes relative to their fused-quartz counterparts, resulting in a higher-deduced titanium attenuation. If the situation had been reversed, with the misalignments set solely for the fused-quartz block, a lower titanium attenuation would have been deduced.

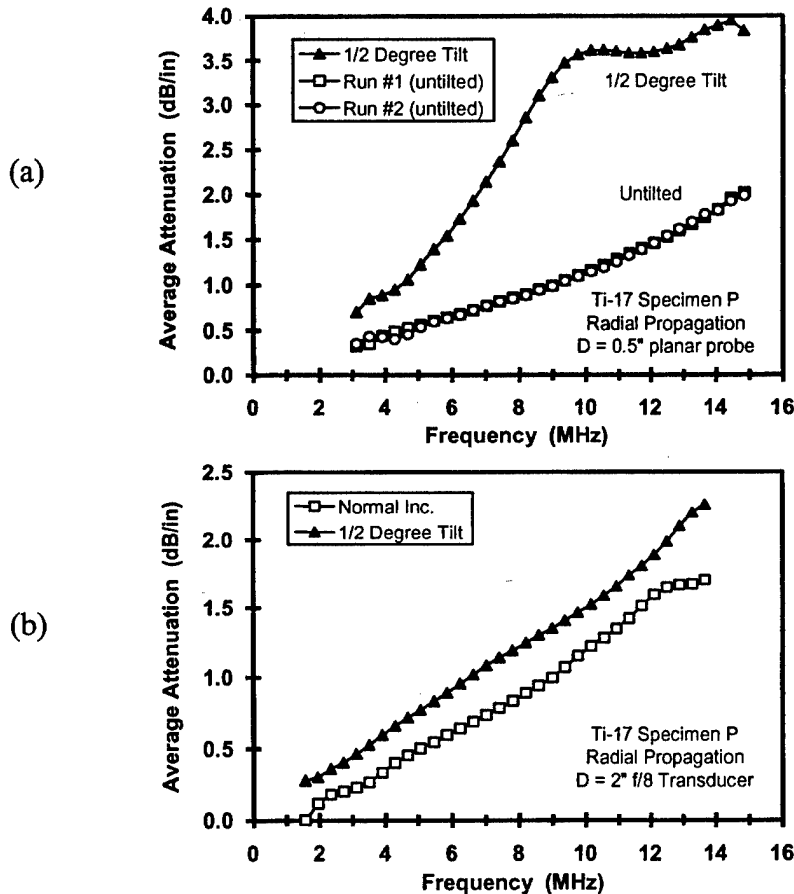


FIGURE 51. EFFECTS OF BEAM MISALIGNMENT ON THE MEASURED BS ATTENUATION OF Ti-17 BILLET SPECIMEN P FOR RADIAL PROPAGATION

(a) RESULTS OF THREE TRIALS USING A 10-MHz, 0.5" PLANAR PROBE  
 (b) RESULTS OF TWO SIMILAR TRIALS USING A LARGE FOCUSED TRANSDUCER

It was verified that close agreement in BS attenuation values could be obtained by teams at different facilities if they used similar transducers, inspection water paths, data averaging methods, and scanned similar regions on the same specimen. An example of the level of agreement is shown in figure 52. Teams at ISU and GEAE made similar attenuation measurements on the same billet specimen. The average attenuation value and the standard deviation about that average are shown in the figure for area scans over similar regions. The two transducers used had the same nominal properties (10-MHz, 0.5" diameter planar) but their ultrasonic pulses had different bandwidths.

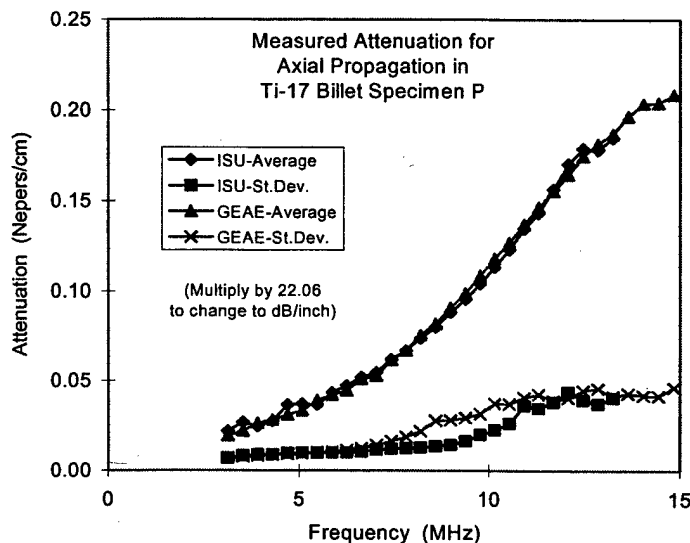


FIGURE 52. ATTENUATION OF Ti-17 BILLET SPECIMEN P (AXIAL PROPAGATION) AS DEDUCED FROM BACK-SURFACE ECHOES AT ISU AND GEAE

Careful beam alignment was the primary requirement for reproducible attenuation measurements. One method of achieving normal-incidence alignment is to place a thin plate atop the specimen, and then to adjust the beam angles to peak-up the collection of echoes arising from reverberations in the plate. It was noted that using metal plates containing large-scale microstructure could result in inaccurate alignment, evidently due to beam steering caused by the metal texture. Thus, powdered-metal or glass alignment plates should be used. Deduced attenuation values were also found to be somewhat sensitive to the thickness of the water gap beneath the back surface of the specimen. Thus, it is recommended that the specimen should be supported by its edges to produce a water gap of at least a few millimeters below its bottom (reflecting) surface. This insures that any reverberations within the bottom water layer can be gated out from the direct BS echo and, hence, do not contribute to the measured attenuation.

With reasonable care exercised during setup and alignment, the dependence of deduced  $\alpha$ -vs- $f$  curves on the focal characteristics of the transducer could be documented. In some cases, the probe dependence was far from subtle. For example, the enlarged grain plate discussed earlier was scanned using three 15-MHz probes: 1/2" diameter planar; 1/4" diameter planar; 1/2" diameter,  $F=3.8"$  focused. Each probe was scanned over the specimen, and the attenuation at each scan point was deduced by comparing the measured BS echo to that from a fused-quartz plate of similar thickness. Very large differences were seen in the deduced attenuation curves (figure 53). In this case, the greater the beam diameter, the greater the average  $\alpha$  value. A tentative explanation for this behavior was developed [28 and 29] based on the coarse macrostructure of the specimen and the assumption that the sound speed was constant within each macrograin. For a smaller diameter beam, there is a greater likelihood that at any given probe position, the beam is entirely within one macrograin. In that case, the sound speed is the same along all beam ray paths, and the wave fronts propagate undistorted. If the beam cross-section spans two or more macrograins, however, different portions of the beam would travel at different speeds, leading to a distortion of the wave fronts. Thus, the probe dependence of the

EGB attenuation could be understood if one assumed that phase distortions were the major contributor. This will be discussed more fully later in the report in section 5.3.7.

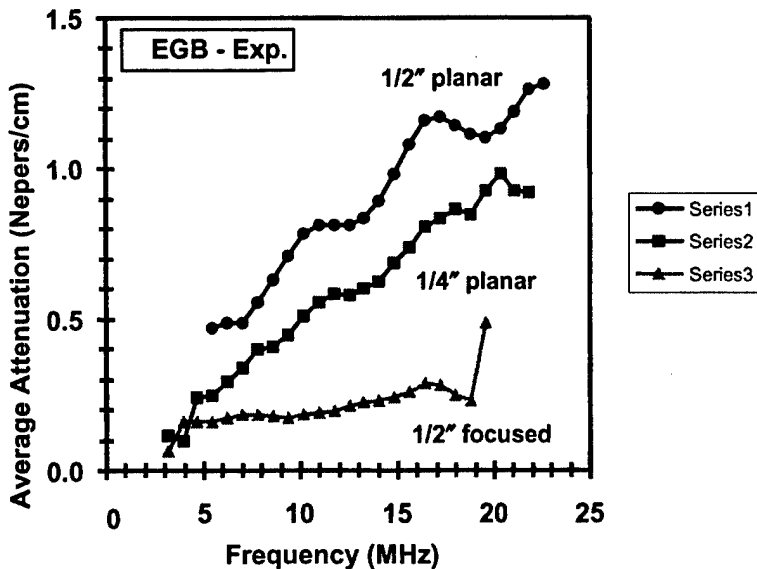
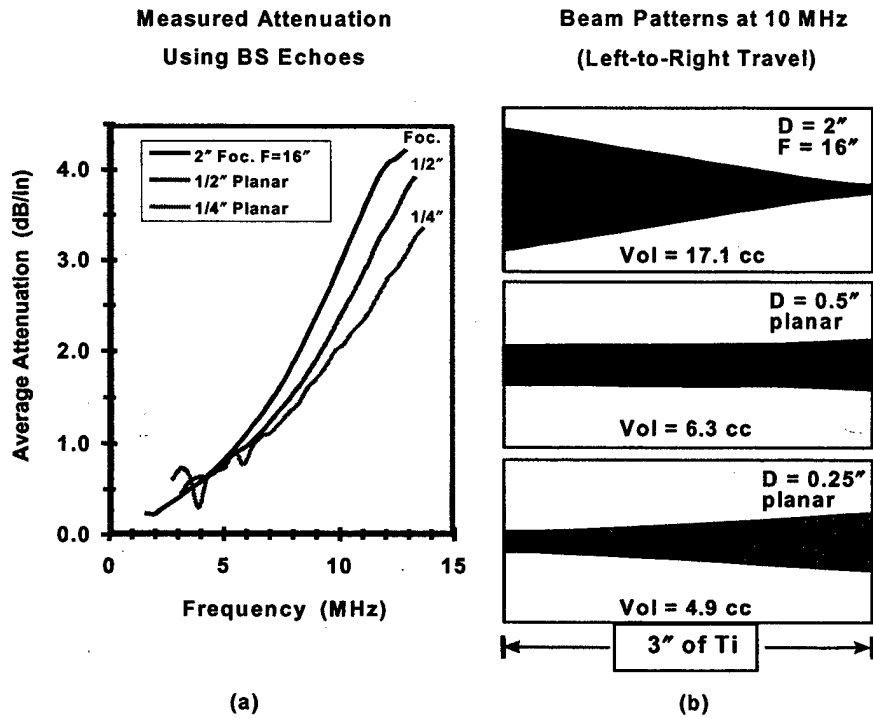


FIGURE 53. AVERAGE BS ATTENUATION OF THE Ti 6-4 ENLARGED GRAIN PLATE AS MEASURED USING THREE 15-MHz BROADBAND TRANSDUCERS

A similar but less dramatic dependence of apparent attenuation on beam size was found for axial propagation in some billet specimens. For example, figure 54(a) displays the measured  $\alpha$ -vs- $f$  curves for a Ti-17 billet specimen using three 10-MHz transducers. For each probe, a simple Gaussian beam model was then used to estimate the incident beam diameter as a function of depth, with the result pictured in figure 54(b). The beam volumes within the 3" cube are indicated, and one sees that the measured  $\alpha$  values at the higher frequencies ( $> 7$  MHz) have the same ordering as the volumes. In this case, owing to the thickness of the specimen and the large diameter of the focused transducer, the beam volume and measured  $\langle\alpha\rangle$  were largest for the focused probe. In contrast, in the examination of the 0.25" thick enlarged grain plate, the focused probe had the smallest beam volume and smallest  $\langle\alpha\rangle$ . However, the same basic trend was seen for both specimens, indicating that measured attenuation can be sensitive to the amount of volume averaging being done by the beam as it propagates. The increase of average BS attenuation with beam volume was more a general tendency rather than an absolute rule. Examples were seen in which large diameter focused transducers yielded smaller  $\langle\alpha\rangle$  values than 0.25" and 0.5" planar probes. It was also noticed that the BS attenuation value obtained with a focused probe was sensitive to the water path used. Figure 55 compares attenuation values for the same Ti-17 billet specimen using the 2" diameter focused transducer and two water paths: one for which the beam was focused on the back surface, and beyond the back surface. Two measurement trials were made for each water path to demonstrate the reproducibility of the measurements. The effect on  $\langle\alpha\rangle$  of defocusing the beam is seen to be significant, particularly at the higher frequencies. For planar probe measurements, the dependence of BS attenuation on water path was found to be much weaker.



**FIGURE 54. EFFECT OF BEAM SIZE ON ATTENUATION OF BACK-SURFACE ECHOES**

(a) AVERAGE  $\alpha$  FOR AXIAL PROPAGATION IN A Ti-17 BILLET SPECIMEN AS MEASURED USING THREE 10-MHz BROADBAND TRANSDUCERS

(b) ESTIMATES OF BEAM PROFILES WITHIN THE 3" THICK SPECIMEN FOR THE THREE TRANSDUCERS

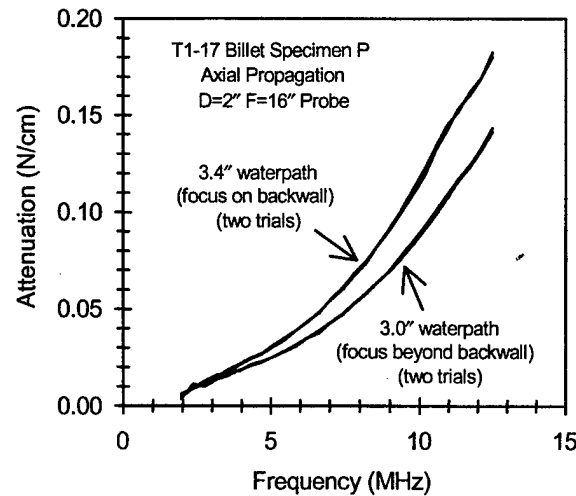


**FIGURE 55. EFFECT OF WATER PATH CHOICE ON MEASURED BS ATTENUATION USING A FOCUSED TRANSDUCER**

For the majority of the cases examined using multiple transducers, the dependence of the BS attenuation on probe properties was smaller than the dependence on inspection direction. This is

illustrated in figure 56(a) and (b) for Ti-17 and Ti 6-4 billet specimens, respectively. Measurements were made for radial and axial sound propagation using three 10-MHz broadband transducers: 0.25" and 0.50" diameter planar; and 0.75" diameter,  $F=12"$  focused. Both the back-surface echo and through-transmitted energy methods were used. For the BS method, the  $\pm 1$  standard deviation error bars are indicated for the focused probe. The probe-to-probe differences, which become more evident at higher frequencies, are less than a third of the average separation of the  $\alpha$ -vs- $f$  curves for radial and axial propagation. In this case, the focused probe had a relatively small diameter (0.75") and the beam volume mismatch with the planar transducers was not as large as in figures 54 and 55 (where the focused probe diameter was 2"). In some cases, the 0.75" focused probe gave rise to larger  $\langle \alpha \rangle$  values than the planar probes and in other cases to smaller values. Note in figure 56 that the dependence of measured attenuation on probe choice was larger for axial propagation than for radial propagation in these two specimens. That also appeared to be the general rule for other billet specimens.

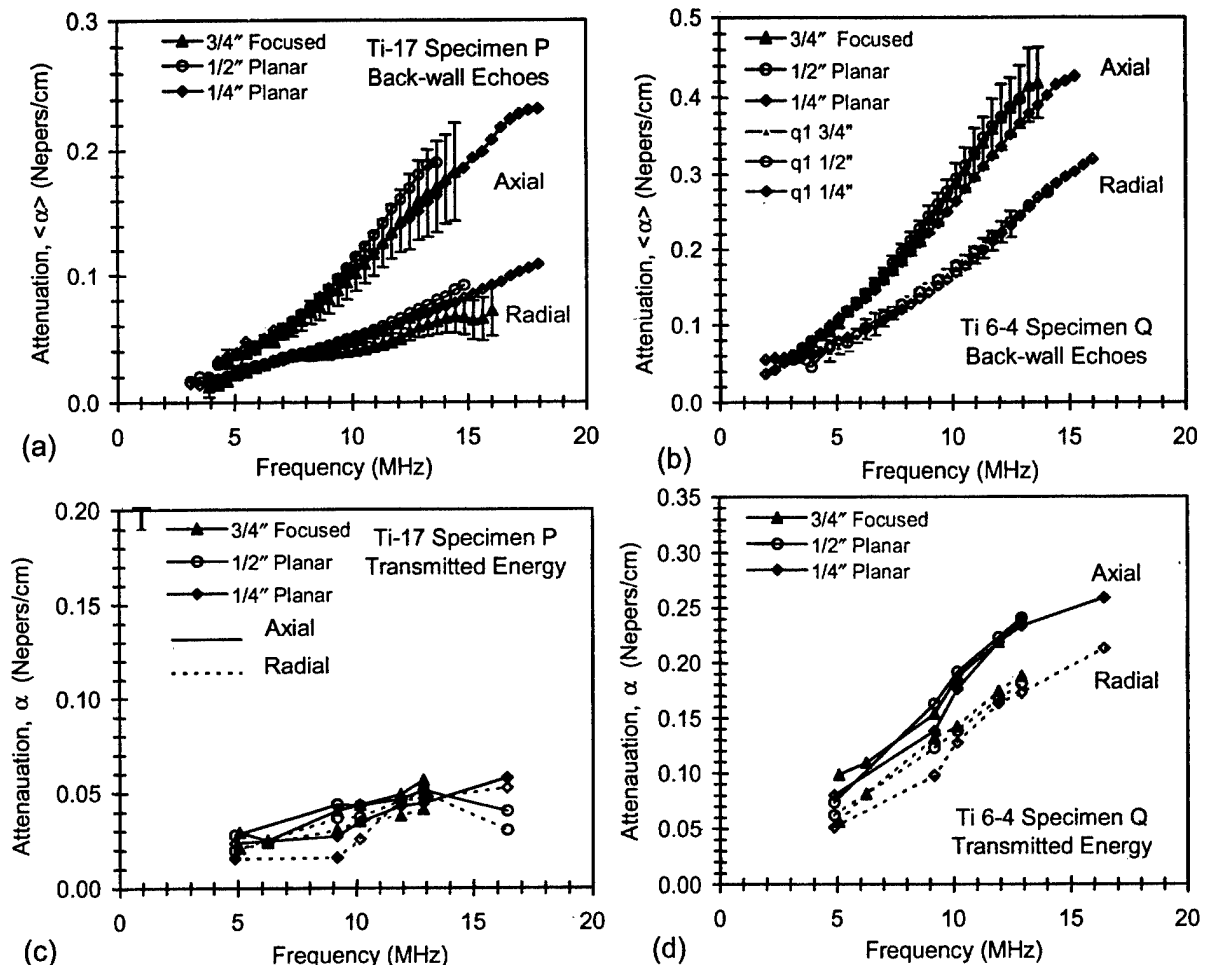


FIGURE 56. AVERAGE ATTENUATIONS OF Ti-17 BILLET SPECIMEN P ((a) AND (c) PANELS) AND Ti 6-4 BILLET SPECIMEN Q ((b) AND (d) PANELS)  
 (a) AND (b) ATTENUATION DEDUCED FROM BS ECHOES (c) AND (d) ATTENUATION DEDUCED USING THE TTE MEASUREMENT PROCEDURE FOR ONE FIXED LOCATION OF EACH (TRANSMITTING) PROBE

In measurements comparing planar and focused transducers, back-surface echo fluctuations were generally smaller for the focused probes (when focused on the back surface), leading to smaller standard deviations in the deduced attenuation. This effect, which appears to be more pronounced at lower frequencies, is illustrated in figure 57. The distribution of back-surface echo strengths is shown for axial propagation in a 3" thick Ti-17 billet specimen using three 10 MHz transducers: one focused on the back surface (3/4" diameter,  $F=12"$ ) and two planar (1/4" and 1/2" diameters). Signal strengths at various frequencies are shown relative to an ideal, fine-grained specimen with the same density and sound speed but negligible attenuation. For the ideal specimen, the probability functions would resemble narrow spikes (Delta functions) centered at 0 dB. One sees that the standard deviation is consistently smaller for the focused probe. The explanation for this behavior is not fully known. If it is assumed that wave front distortion at the back surface is a major cause of the BS echo fluctuations, it can be argued that the effects of such distortion on signal strength will likely be smaller for focused beams than for planar ones. Focused beams have smaller cross-sectional areas, limiting the maximum phase change that can occur across the ensonified portion of the back surface and, hence, limiting signal reduction due to phase cancellation upon reflection. This is the reason why BS echoes from focused beams are less sensitive to beam tilt than similar echoes from planar probes. It likely also applies to phase cancellation effects arising from the microstructure.

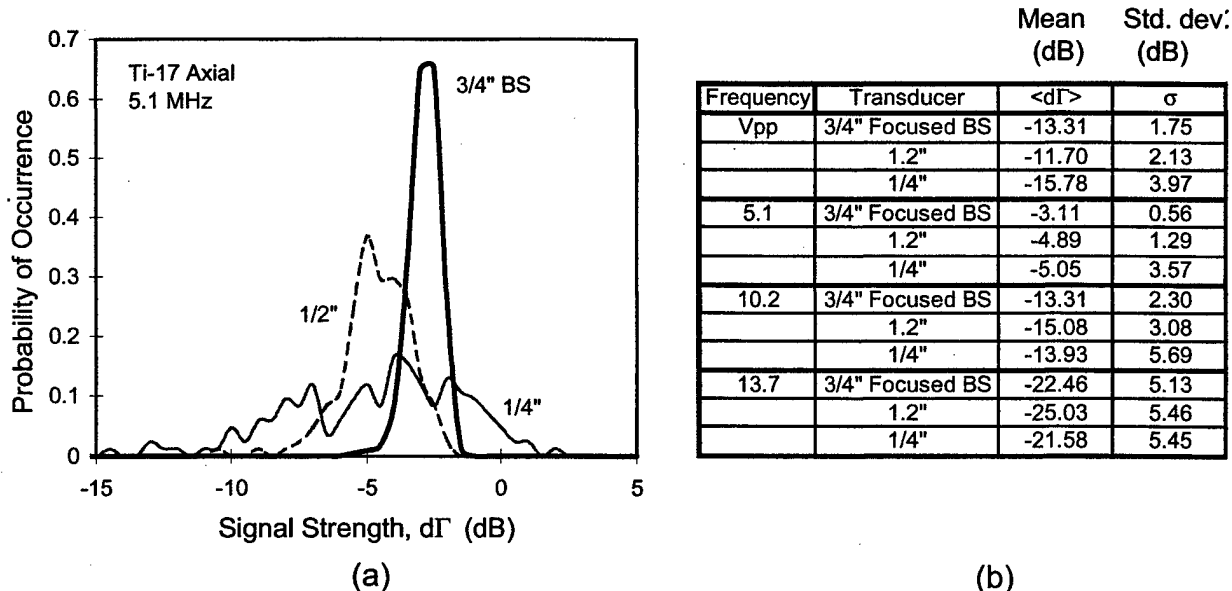


FIGURE 57. MEASURED FLUCTUATIONS OF BACK-SURFACE ECHOES FOR AXIAL PROPAGATION IN A Ti-17 BILLET SPECIMEN (a) VARIABILITY IN THE 5-MHz SPECTRAL COMPONENT OF THE BS ECHO (b) SUMMARY OF THE MEANS AND STANDARD DEVIATIONS OF MEASURED PEAK-TO-PEAK VOLTAGES (VPP) AND SPECTRAL AMPLITUDES AT 5.1, 10.2, AND 13.7 MHz

Current billet inspection practice uses 5-MHz transducers with radially inward beam propagation. For that scenario, little difference was generally found between average BS attenuation values measured with planar and focused transducers, although echo fluctuations were smaller for the latter. An example was shown earlier in figure 50(c). The dependence of

BS echo attenuation on transducer choice, documented in this section, increases with frequency and is more severe for propagation parallel to the macrograins or flow lines. Thus, it is likely to be more of a factor in forging inspections than in billet inspections.

The principal findings for method 1 (BS echoes) are as follows.

- a. Deduced  $\alpha$ -vs- $f$  curves were found to be quite sensitive to probe alignment (beam tilt), particularly for planar probe measurements where a misalignment of 0.5 degrees for a 3" thick specimen could lead to a doubling of the deduced attenuation value. However, reproducible attenuation curves could be obtained by exercising reasonable care during setup.
- b. Measured BS  $\alpha$  values depended on the transducer used, with probe-to-probe differences increasing with frequency. Below 5 MHz, such differences tended to be small. For most specimens, the differences at higher frequencies were modest, i.e., <15% at 15 MHz. Larger differences were seen for the enlarged grain plate and for axial propagation in some billet specimens.
- c. In some situations where there were appreciable probe-to-probe attenuation differences, there appeared to be a correlation between the measured attenuation and the volume of the incident beam within the specimen. The correlation was strongest for the Ti 6-4 enlarged grain block.
- d. In the billet and forging specimens, the dependence of deduced attenuation on transducer choice was generally not as large as the dependence on propagation direction.
- e. When  $\alpha$  -vs- $f$  curves obtained with focused and planar transducers were compared, in most cases, the focused transducer yielded a slightly higher average attenuation value but a smaller standard deviation about that average. Thus, BS echoes tended to fluctuate less in focused probe scanning experiments, so long as the beam was focused on the back surface.

#### 5.3.6.2 Method 2: Through-Transmission Beam-Mapping Experiments With Multiple Transducers.

Using a small diameter receiver, maps were made of the sonic fields transmitted through fused quartz and titanium blocks for several choices of the (fixed) transmitting probe. In the TTE method pictured in figure 45, a small receiver is scanned to map the sound beam that emerges into water after traveling through a titanium or reference block. At ISU, the receiver was a small diameter (~0.5 mm) piezoelectric crystal mounted on a narrow rod. Due to resonant ringing in the crystal and its mount, the frequency spectrum of a received broadband signal contained a series of peaks at isolated frequencies (e.g., at 4.9, 9.2, 10.2, 12.9, and 16.0 MHz), and ISU results are reported only for such resonant frequencies where receiver sensitivity was enhanced. At GEAE, the receiver was usually a standard planar transducer whose face was masked with sound absorbent material except for a small circular passage near its center.

By comparing amplitude and phase C-scan images of either transmitted peak voltage or fixed-frequency spectral components for fused quartz and titanium blocks, the distortions produced by the titanium microstructure could be seen. In addition, the relative amounts of energy carried by different beams could be determined by integrating the square of the magnitude of the through-transmitted response over the cross section of each beam. In doing this, one assumes that the receiver is small enough that the measured response is directly proportional to the arriving pressure.

Some examples of C-scan images obtained using the TTE method were shown earlier in figure 44(a) and (b). A larger set of images, showing both amplitude and phase profiles at 9.2 MHz for FQ and Ti-17 blocks, appears in figures 58 and 59. In this case, a 0.25" diameter planar transducer served as the receiver, and the beams emerging from Ti-17 specimen L were mapped at locations where both strong and weak BS echoes were seen. This was done for beam propagation in the radial, axial, and hoop directions. Amplitudes have been corrected for interface transmission losses, so all seven images in figure 58 would appear nearly identical if the Ti-17 specimen had a very fine isotropic microstructure. To make the images, the point receiver was scanned over a 1.25" by 1.25" area using a 0.025" step size. Note that color images appear in the electronic copy of this report; true gray-scale images appear in reference 24. Relative to the FQ images in figures 58 and 59, some level of beam amplitude or phase distortion is present in each Ti-17 image, with the degree of distortion clearly greatest for axial propagation. Interestingly, when images at all frequencies are visually compared, one sees no obvious overall differences in the degree of distortion at strong and weak echo sites. However, as will be shown later in this section, nonvisual comparisons indicate that a greater amount of phase cancellation is occurring at the weak echo sites.

The measured energy attenuation of billet specimen L is shown as a function of frequency in figure 60 for propagation in the radial and axial directions. Results for hoop propagation are similar to those for radial propagation. Note that the BS measurements used both 0.25" and 0.50"-diameter planar probes, while the TTE measurements used only the 0.25" planar probe and were made at sites where both strong and weak BS echoes were seen. Notice that the  $\alpha$ -vs- $f$  curves for the TTE method are nearly identical at strong and weak BS echo sites. Also notice that for the measurement frequencies beyond 5 MHz, the energy attenuation is significantly smaller than the BS echo attenuation, especially for axial propagation. The same relationship between TTE and BS attenuation is seen in figure 56(a) and (b). For two billet specimens (Ti-17 P, and Ti 6-4 Q) that figure compares TTE and BS measurements made using three transducers. For both alloys, the measured energy attenuations are seen to be approximately independent of the transducer used and are substantially lower than the BS echo attenuations at the higher frequencies. For Ti-17 specimens L and P, there was no clear dependence of the energy attenuation on the propagation direction. However, for Ti 6-4 specimen Q, the TTE attenuation was noticeably larger for axial propagation.

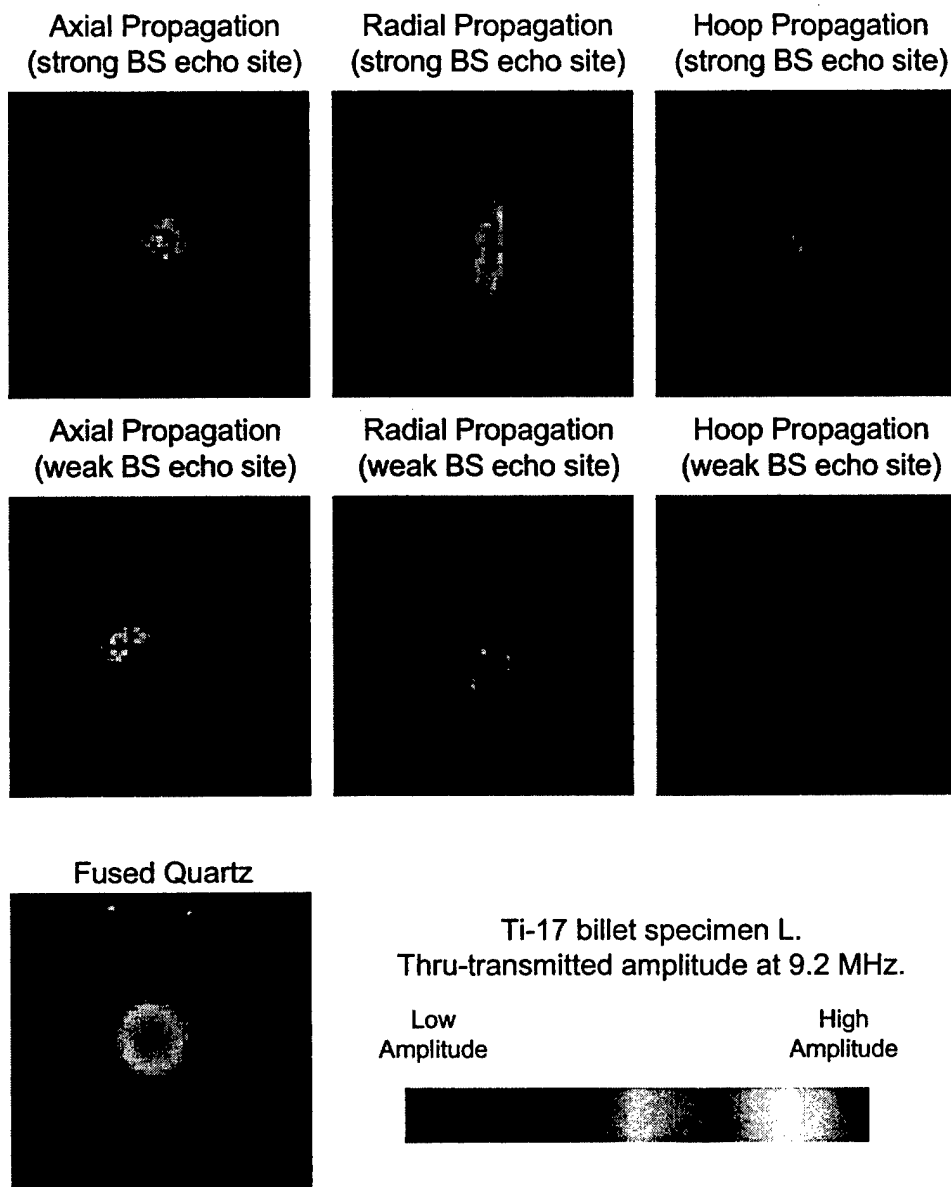


FIGURE 58. THROUGH-TRANSMISSION C-SCAN AMPLITUDE IMAGES OF THE BEAM FROM A 10-MHz, 0.25" DIAMETER PLANAR PROBE AFTER PASSAGE THROUGH 3" THICK BLOCKS OF Ti-17 (BILLET SPECIMEN L) AND FUSED QUARTZ

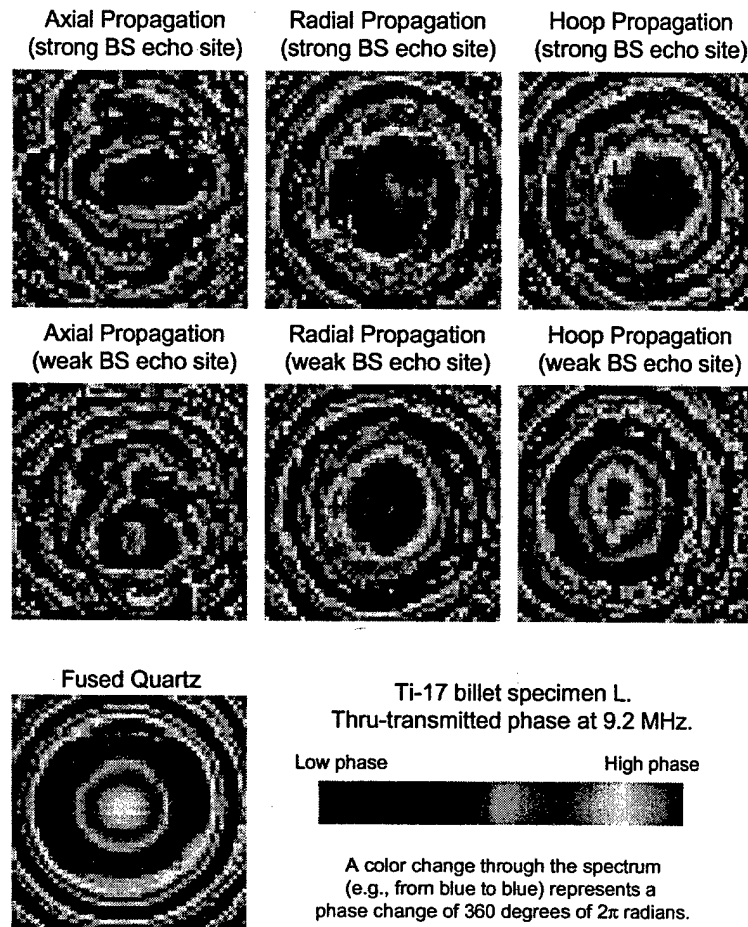


FIGURE 59. C-SCAN IMAGES OF THROUGH-TRANSMITTED PHASE AT 9.2 MHz FOR THE INSPECTION DESCRIBED IN FIGURE 58

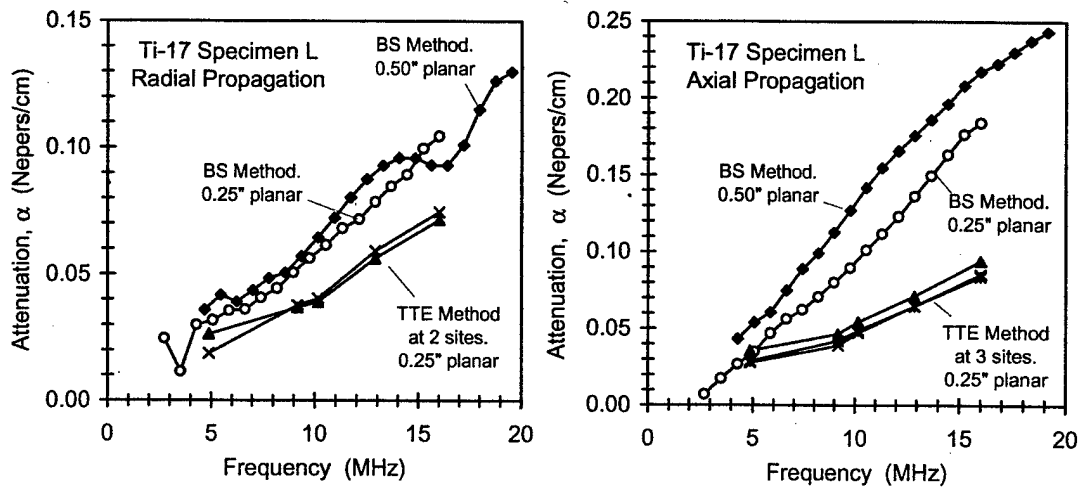


FIGURE 60. COMPARISON OF MEASURED TTE ATTENUATION AND AVERAGE BS ATTENUATION FOR RADIAL AND AXIAL PROPAGATION IN Ti-17 BILLET SPECIMEN L

In summary, the TTE technique provides a rather direct measure of the total energy lost by a beam during travel. The TTE attenuation is found to be relatively independent of the choice of measurement site and to be substantially lower than the measured BS attenuation at frequencies beyond about 5 MHz. This indicates that some combination of beam distortion effects must be responsible for both the extra portion of the back-surface attenuation that is not associated with energy loss and for the large BS echo fluctuation. When C-scan maps of transmitted beams are analyzed to determine the energy-loss attenuation, only the signal amplitudes are used [24]. Later a separate analysis (the so-called Fraction F study) will be described, which makes use of both the amplitude and phase data acquired during the TTE measurements.

The principal findings from method 2 (through transmitted energy) are as follows.

- a. For all of the titanium specimens studied, obvious distortions of the transmitted amplitude and phase profiles were seen. The level of distortion increased with frequency. In some cases, particularly for planar transducers, the amplitude pattern was seen to fragment into multiple hot spots.
- b. For billets, beam distortion was most severe for axial propagation.
- c. For a given specimen and propagation direction, there was little if any difference in transmitted energy at sites where strong and weak back-surface echoes were seen. Thus, variations in beam energy are not responsible for the fluctuations of back-surface echoes with position.
- d. The deduced energy attenuation was approximately independent of the probe used in the measurement.
- e. The energy attenuation tended to be higher for Ti 6-4 billet material than for Ti-17.
- f. At frequencies above 5 MHz, there were clear differences between the attenuation values deduced by the TTE and BS methods, with the former being consistently smaller. Beyond 10 MHz, the TTE (energy loss) attenuation was typically less than half of the BS attenuation, indicating that the latter contained a large contribution from beam distortion effects.

#### 5.3.6.3 Method 3: Measurements of FBH Attenuation Using Multiple Transducers.

Because of its simplicity, the BS method of figure 45 would be the preferred attenuation measurement method in practice. However, most defects in titanium billets are small, isolated voids or inclusions, and the FBH geometry shown in the same figure would appear to offer a more trustworthy approach for determining an attenuation value that is appropriate for echoes from small defects. Because beam distortion effects can affect different types of ultrasonic signals differently, there is no guarantee that the BS and FBH methods would yield similar results, even if the same transducer were used for both.

In the final method, 3 by 3 arrays of #1 FBHs were drilled into a low-attenuation, powdered nickel reference block. Similar arrays of holes were also drilled into selected faces of titanium

alloy blocks, as indicated in table 12. In all cases, the holes were drilled 0.25" deep into nominally 3" thick specimens, resulting in a metal travel path of approximately 2.75" from the sound entry surface to the FBH reflectors. In all cases, the 3 by 3 arrays had a spacing of 0.50" between adjacent holes, allowing the holes to be resolved with both planar and focused transducers. By comparing peak FBH echoes in titanium and nickel, attenuation-vs-frequency curves were deduced for titanium using planar and focused transducers. The results were then compared with attenuation values deduced from back-surface echoes.

TABLE 12. FLAT-BOTTOMED HOLE ATTENUATION SPECIMENS

Specimen Designation	Source Material	Faces Into Which FBH's Were Drilled	Approximate Specimen Dimensions	Specimen Serial Number
Ni	Powdered Nickel alloy (R88)	One 6" x 3" face. (FBH's were positioned on one-half of the face, leaving the other half unaltered for $\nu$ and $\alpha$ measurements.)	6" x 3" x 3"	none
L	Ti-17 billet	Axial, radial, and hoop faces.	3" x 3" x 3"	052094-1Ti-17B, OD
H	Ti 6-4 billet	Radial face only.	3" x 3" x 3""	022594-1Ti-6-4 B, OD
U	Ti 6-4 forging	Axial and radial faces.	3" x 3" x 3"	060394-1Ti-6-4 F, RIM

To begin, the relevant properties of the nickel reference block were measured. From the mass (7.383 kg) and physical dimensions of the block (6.001" by 3.000" by 3.000"), the density was estimated at 8.34 gm/cc. By measuring the arrival times of the first three back-surface echoes, using a 10-MHz, 0.25" planar probe in immersion, the longitudinal sound speed was estimated at 0.600 cm/ $\mu$ s (for travel parallel to the FBH drilling direction). The ultrasonic attenuation for the same propagation direction was determined by comparing back-surface echoes in nickel to those in a 3" thick fused-quartz specimen. Two 10-MHz transducers were used: 0.25" planar and a 2" diameter, F=16" focused probe. The measured nickel attenuation in the 5-15 MHz range was found to be approximately independent of frequency and very small. A small positive value ( $\langle\alpha\rangle = 0.002$  Nepers/cm = 0.04 dB/in) was obtained with the planar transducer, and a small negative value ( $\langle\alpha\rangle = -0.002$  Nepers/cm = -0.04 dB/in) was obtained with the focused probe. It was concluded that the attenuation of the nickel specimen was negligible ( $< 0.002$  Nepers/cm) within the frequency range of interest, and in subsequent analyses, it was assumed to be identically zero.

Attention was then shifted to the three titanium engine specimens. Specimen L was extensively studied because FBH echo measurements could be made in all three propagation directions. For each propagation direction, C-scan images of the holes were made using the same 10-MHz planar and focused transducers used for the Ni block  $\alpha$  measurements. These were compared with similar images of the FBHs in nickel. Attenuation-vs-frequency curves for titanium were then determined by comparing the spectra of the nine-peak FBH echoes in titanium to those in

nickel. For the nickel reference specimen, the water paths were 4.8 and 10.1 cm for the planar and focused probe measurements, respectively, with the latter chosen to maximize the peak-to-peak voltages of the FBH echoes. Water paths for the titanium specimens were then determined using equation 1 to insure that the average effects of beam focusing/diffraction at the FBH plane were the same as for nickel.

Selected C-scan images of gated peak-to-peak voltage (GPV) are displayed in figure 61 for Ti-17 billet specimen L. Three quantities, denoted  $\langle V \rangle$ ,  $\sigma$ , and  $D$  were tabulated for each image.  $\langle V \rangle$  is the average of the nine maximum GPV values (one per hole), corrected for interface losses and water attenuation, and normalized to 100 for nickel. Thus, a value of  $\langle V \rangle = 100$  for Ti-17 would indicate no reduction in GPV due to attenuation, and a small value  $\langle V \rangle$  indicates a large ultrasonic attenuation.  $\sigma$  is the standard deviation of the nine maximum GPV values, expressed as a percentage of the mean, and serves to quantify the level of signal fluctuation.  $D$  is the average diameter in mils of the FBH images at the -6 dB level (50% of maximum GPV value). By comparing  $\sigma$  values, it is shown that signal fluctuations are much larger for the planar probe inspection than for the focused-probe inspection. As noted earlier, the same is generally true for fluctuations of back-surface echoes. There is also obvious evidence of beam steering in the axial inspection when the planar probe is used. Although the nine FBHs are arranged in a regular array with 0.5" spacings, their images clearly are not.

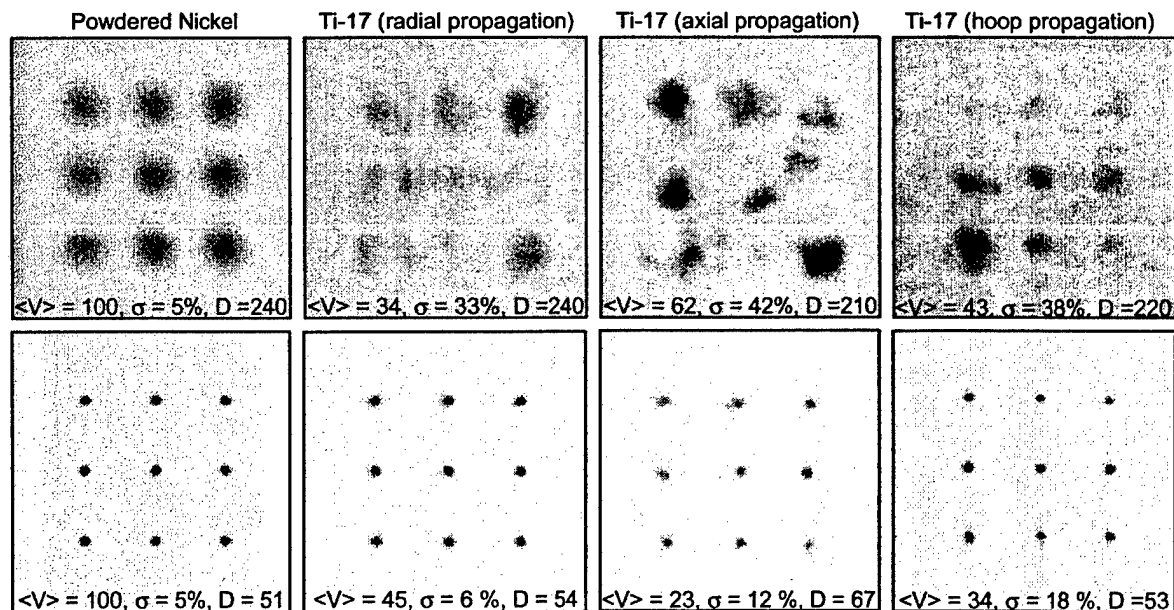


FIGURE 61. C-SCAN IMAGES OF PEAK-TO-PEAK VOLTAGE FOR PLANAR-PROBE (UPPER ROW) AND FOCUSED-PROBE (LOWER ROW) SCANS OF FLAT-BOTTOMED HOLE ARRAYS IN NICKEL AND Ti-17 BILLET SPECIMEN L

It is interesting to note that the inspection direction for which the FBH attenuation is lowest (or highest) depends upon the transducer used. For example, when the planar probe is used, the average FBH echo tends to be stronger for axial rather than radial propagation, indicating lower attenuation for axial propagation. However, the opposite is true when the focused probe is used.

For the focused-probe inspection, the average image diameter (at the focal plane) is larger for Ti-17 than for nickel, indicating that the titanium microstructure acts to defocus the beam. The degree of defocusing is largest for axial propagation. For axial propagation using the small planar probe, however, the average image diameter is smaller for Ti-17, suggesting that the columnar microstructure acts to guide the sound beam somewhat, thus reducing lateral diffraction.

For the focused-probe inspection, average attenuation-vs-frequency curves are displayed in figure 62 for each propagation direction in specimen L. These were deduced by comparing the spectra of the peak FBH echoes in Ti-17 and nickel. The rate of rise with frequency, intermediate between linear and quadratic, is typical of that seen when the BS and TTE methods are applied to engine alloy specimens. Similar curves were obtained when the planar probe was used, although their relative ordering was reversed: for the planar-probe inspection  $\langle\alpha\rangle$  was largest for radial propagation and smallest for axial propagation.

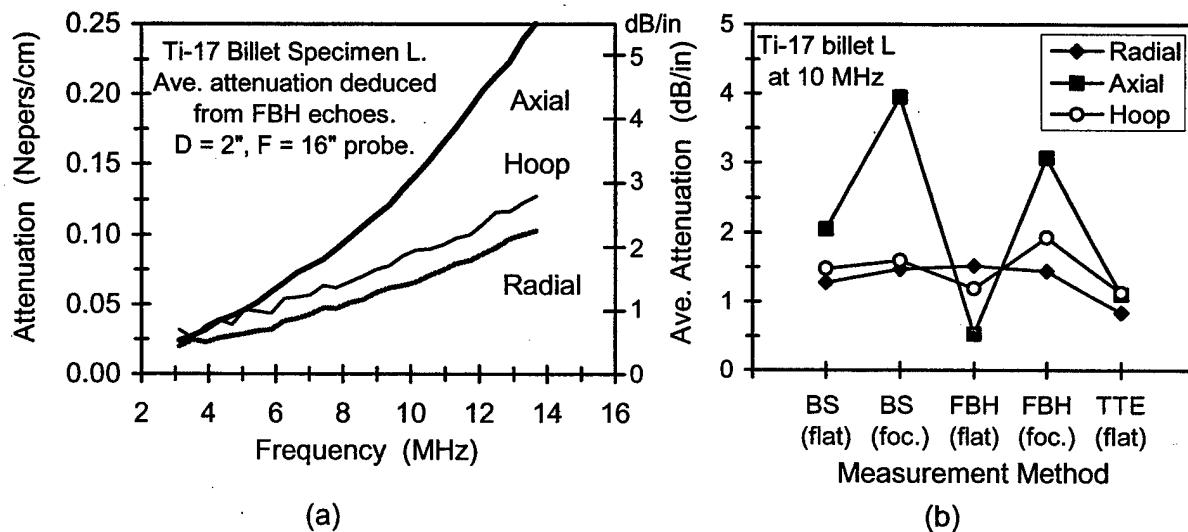


FIGURE 62. (a) AVERAGE ATTENUATION OF Ti-17 BILLET SPECIMEN L AS DEDUCED BY ANALYZING FBH ECHOES USING A D=2", F=16" FOCUSED TRANSDUCER AND (b) COMPARISON OF AVERAGE ATTENUATION VALUES DEDUCED USING THE BS, FBH, AND TTE METHODS WITH PLANAR (FLAT) AND FOCUSED PROBES

Attenuation values deduced from these FBH measurements were then compared to values deduced using the back-surface and through-transmitted-energy methods. BS and TTE attenuation measurements using the same 0.25" planar transducer had been carried out before the FBHs were drilled. BS echo measurements, using the D=2", F=16" focused probe (focused on the back surface), were performed with the FBHs in place by scanning along four line segments in between the rows of holes. The average  $\alpha$  values at 10 MHz deduced using the three measurement methods are compared in figure 62(b). Note that for radial and hoop propagation the different methods yield roughly similar results, but large differences are seen for axial propagation.

FBH attenuation measurements were also carried out on the two Ti 6-4 specimens listed in table 12. The emphasis was on comparing attenuation values and signal fluctuation levels of FBH and BS echoes when the large focused transducer ( $D=2"$ ,  $F=16"$ ) was used. As before, the sonic beam was focused either at the depth of the FBHs or on the back surface region between the holes. Results are summarized in table 13. In each case, only modest differences were seen in the average attenuation coefficients deduced using the FBH and BS methods. This is perhaps not unexpected, since energy loss rather than beam distortion tends to dominate the attenuation process in Ti 6-4 material. Note, however, that signal fluctuations (as measured by the standard deviation  $\sigma$  of the attenuation measurements about their mean) were considerably larger for FBH echoes than for back-surface echoes. This was also the case for Ti-17 specimen L.

TABLE 13. ATTENUATION COEFFICIENTS OF Ti 6-4 SPECIMENS DEDUCED BY ANALYZING FBH AND BACK-SURFACE ECHOES

Specimen	Sound Propagation Direction	Attenuation Deduced From Peak FBH Echoes $\langle\alpha\rangle \pm \sigma$ (dB/inch)		Attenuation Deduced From BS Echoes $\langle\alpha\rangle \pm \sigma$ (dB/inch)	
		5.1 MHZ	10.2 MHZ	5.1 MHz	10.2 MHz
H (Ti 6-4 billet)	Radial	$1.28 \pm 0.44$	$3.08 \pm 0.27$	$1.14 \pm 0.06$	$2.96 \pm 0.13$
U (Ti 6-4 forging)	Radial	$0.65 \pm 0.27$	$1.54 \pm 0.29$	$0.57 \pm 0.06$	$1.48 \pm 0.15$
U (Ti 6-4 forging)	Axial	$0.39 \pm 0.14$	$0.80 \pm 0.07$	$0.31 \pm 0.04$	$0.87 \pm 0.06$

From the limited number of FBH measurements, it was concluded that back-surface attenuation is not always a reliable indicator of the effective attenuation of echoes from small flaws. The differences between back-surface and small-flaw attenuations are expected to be most noticeable when beam-distortion effects are a major contributor to signal attenuation, i.e., when (1) the sonic beam propagates parallel to the macrograin elongation direction in billets (or along flow lines in forgings), (2) higher inspection frequencies are used (i.e.,  $> 5$  MHz), (3) Ti-17 material (rather than Ti 6-4) is being inspected, and (4) the sonic beam is either unfocused or not focused at the depth of the reflector(s).

The principal findings for method 3 (FBH measurements) are as follows.

- For most of the cases studied, the average attenuation values deduced by FBH and BS methods were reasonably similar (when the same transducer was used in each method). However, significant differences were seen in one case where the sonic beam propagated along the macrograin elongation direction. Thus, back-surface attenuation is not always a reliable indicator of the effective attenuation of echoes from small flaws.
- For focused-probe measurements, the titanium microstructure acts to defocus the sonic beam resulting in larger FBH images. In addition, signal fluctuations tended to be larger for peak FBH echoes than for back-surface echoes (under similar focusing conditions).
- When attenuation is deduced from FBH echoes, the high attenuation direction can depend upon the transducer used in the measurements.

### 5.3.7 Beam Disruption, Wave Front Distortion, and Beam Steering: Implications for Signal Reduction.

The TTE measurements described earlier were designed to directly measure the sonic energy transmitted through a specimen and, hence, to remove the effects of beam distortion from the attenuation measurement. The fact that the BS and FBH measurement methods yield attenuation values significantly higher than TTE demonstrates that beam distortion effects are playing a key role in reducing echo amplitudes. As discussed earlier, the distortion effects have been conceptually classified into three categories: beam steering, beam disruption, and wave front distortion. These effects presumably arise because of point-to-point velocity variations in the titanium microstructure. Separate sound rays traveling along nearby paths can travel at different velocities, leading to phase differences. In addition, reflection and refraction of sound at the boundaries of macrograins having different crystalline orientations can cause portions of the beam to channel within macrograins, leading to further distortions. In practice, all three classes of distortion are probably always present to some extent and their effects on ultrasonic signals tend to mix together. Nonetheless, it is informative to conceive of and carry out experiments designed to study their relative importance.

The relative contributions of the three-beam distortion effects will certainly depend on the circumstances of the measurement. The low average attenuation values seen for FBH echoes with planar transducers indicate that amplitude hot spots resulting from beam disruption play a major role in that case. On the other hand, the large fluctuations in BS echoes seen in scanning experiments can be understood if one assumes phase alteration phenomena (distortion or tilting of wave fronts) are the controlling factor.

Because of the simplicity of the measurement, BS echoes are the most practical vehicles for studying ultrasonic attenuation. In this section, four additional follow-up studies of BS echo attenuation in engine titanium alloys will be discussed. In order of presentation these are:

- a. Phase variation study (or Fraction F study): Analysis of the amplitudes and phases of through-transmitted beams emerging from locations where strong and weak back-surface echoes are seen.
- b. EGB study: Measurement and analysis of BS echoes in the Ti 6-4 enlarged grain block.
- c. Beam tilt study: BS attenuation measurements using tilted beams to investigate beam steering in a Ti-17 billet specimen.
- d. Block slicing study: BS attenuation measurements on Ti-17 and Ti 6-4 billet specimens before and after slicing, to determine if attenuations in successive material layers add in the expected fashion.

As will be shown, these studies all indicate that microstructure-induced alterations in the shapes of wave fronts are the major contributor to the excess BS attenuation that does not result from beam energy loss. Again, the format of section 5.3.6 will be followed: each section contains a brief description of the experimental method, a discussion of the results, and a summary of the principal findings.

### 5.3.7.1 Study 1: Phase Variation Study (or Fraction F Study).

In this study, maps were made of the amplitude and phase profiles of sonic beams emerging from a fused-quartz block and from locations in a Ti-17 block where strong and weak back-surface echoes were seen. From the profiles, a dimensionless fraction "F" was computed which estimates the reduction in back-surface echo strength due to phase cancellation effects alone. (A small value of F indicates large-phase cancellations.)

Recall that one interesting finding of the TTE measurements was the similarity in energy attenuation values at sites producing weak and strong back-surface echoes. At both types of sites, the total energy carried by the pulse and transmitted through the specimen was about the same. Thus, the fluctuations in BS echo strength, typically seen during scanning experiments, were not being accompanied by similar fluctuations in pulse energy. This leads to the question of what is responsible for the BS echo fluctuations? One clue can be found in an analysis of the phase information carried by the through-transmitted pulse. To better understand the analysis, a brief discussion of Auld's electromechanical reciprocity relation is in order. That general relationship allows one to relate the electrical voltage signal appearing on an oscilloscope (say, during an ultrasonic pulse/echo inspection) to details of the incident and scattered sonic fields in the vicinity of the reflector. When Auld's theorem is applied to the echo from a back surface, one finds that the echo's spectral magnitude at frequency  $f$ , denoted here by  $|S(f)|$ , can be approximately written<sup>30</sup> as:

$$|S(f)| = \left| C \iint P^2(f, x, y) dx dy \right| \quad (3)$$

Here  $C$  is a constant of proportionality that depends on such things as the transducer efficiency and the reflection and transmission coefficients of the specimen, and  $P(f, x, y)$  denotes the spectral component of the incident pressure field at location  $(x, y)$  on the back surface. The integration is over the back surface itself. Be aware that  $P(f, x, y)$  is a complex quantity which carries both phase and amplitude information. It should be asked, "How large a role do the sonic pressure phases play in determining the strength of the back-surface echo?" According to equation 3, the largest signal will be produced when the phases are the same at all points on the back surface, i.e., when the incident wave fronts are planar and parallel to the back surface. In that case, the phase of the integrand is the same at all points in the integration plane, and the absolute value sign on the right-hand side of equation 3 can be moved inside the integral. Of course, the wave fronts will not generally be planar, even for the beam from a planar transducer propagating in an ideal medium such as fused quartz, since diffraction will act to curve the wave fronts. The fractional reduction in back-surface echo strength (at frequency  $f$ ), due to phase variation over the back surface, is obtained by dividing equation 3 by its maximum (constant phase) value:

$$F = \frac{\left| \iint P^2(f, x, y) dx dy \right|}{\left| \iint P^2(f, x, y) dx dy \right|_{\text{max}}} \quad (4)$$

$F$  then is a dimensionless, frequency-dependent fraction that measures the reduction in the strength of a back-surface echo that is attributable to phase variations (i.e., to wave front curvature, tilting, or other distortion). Note that in this ratio the phases contribute to the

numerator but not to the denominator, and the denominator itself is proportional to the total energy carried by the incident pulse. As an example of the size of  $F$ , consider the case of a beam from an ideal 0.25" diameter planar probe propagating first through 1.3" of water and then through 3" of fused quartz to reach the back surface. This is typical of the reference geometry for some TTE attenuation measurements. The fraction  $F$  for this ideal piston probe case can be calculated using ultrasonic beam models, and one finds that  $F=0.17$ , 0.33, and 0.48 at frequencies of 5, 10, and 15 MHz respectively. Thus, at 10 MHz, wave front distortions associated with ordinary diffraction have caused a 67% reduction in the strength of the back-surface echo. As the frequency is reduced, the beam becomes wider and there is a greater discrepancy in the phases of points in the center and lateral sides of the beam, leading to larger phase cancellations, smaller values of  $F$  and greater reductions in the BS echo.

The through-transmission beam mapping data has been used for Ti-17 billet specimen L to estimate the value of  $F$  at sites where strong and weak back-surface echoes were seen. For this specimen, such data was gathered for all three propagation directions using a 0.25" diameter, 10-MHz planar probe. For the radial and hoop directions, measurements were made at two sites on the specimen: one where a strong back-surface echo was seen and one where a weak echo was seen. For axial propagation, an additional weak echo site was studied. Two measurement trials were conducted for the FQ block. In evaluating  $F$ , three minor approximations were made:

- a. Ideally,  $F$  should have been evaluated at the back surface, but the evaluation was made on a parallel plane in water a few millimeters beyond the back surface.
- b. It was assumed that the small diameter receiver functioned as a true point receiver, i.e., that the received signal is directly proportional to the incident pressure at the receiver location.
- c. The double integral in equation 4 was replaced by a summation over the grid points in the receiver scan plan.

The results for the fused quartz and Ti-17 specimens are shown in figure 63. Notice that at strong echo sites, the value of  $F$  tends to be much larger than at weak echo sites. This indicates that wave front distortions (phase aberrations) caused by the titanium microstructure are responsible for the large differences in BS echo strengths. At weak echo sites, it was found that sufficient sound energy is available to produce a large echo but larger than average phase cancellations are occurring. Measured  $F$  values for the FQ block are seen to be near the ideal values expected for the beam from a perfect piston transducer of the same diameter, propagating through fused quartz. It is interesting to note that for some strong echo sites, the  $F$  value in titanium is larger than that in fused quartz, indicating that in those cases, the microstructure has acted to flatten the wave fronts in the high-pressure portion of the beam and, hence, to actually enhance the echo. In general, two types of wave front distortion could be responsible for producing weak BS echoes. These can be loosely defined as wrinkling and tilting. In the latter, the wave front may be reasonably flat, but it is tilted relative to the back surface—this can occur if the beam is being steered by the microstructure toward nonnormal incidence. Evidence for such beam steering will be discussed in section 5.3.7.3.

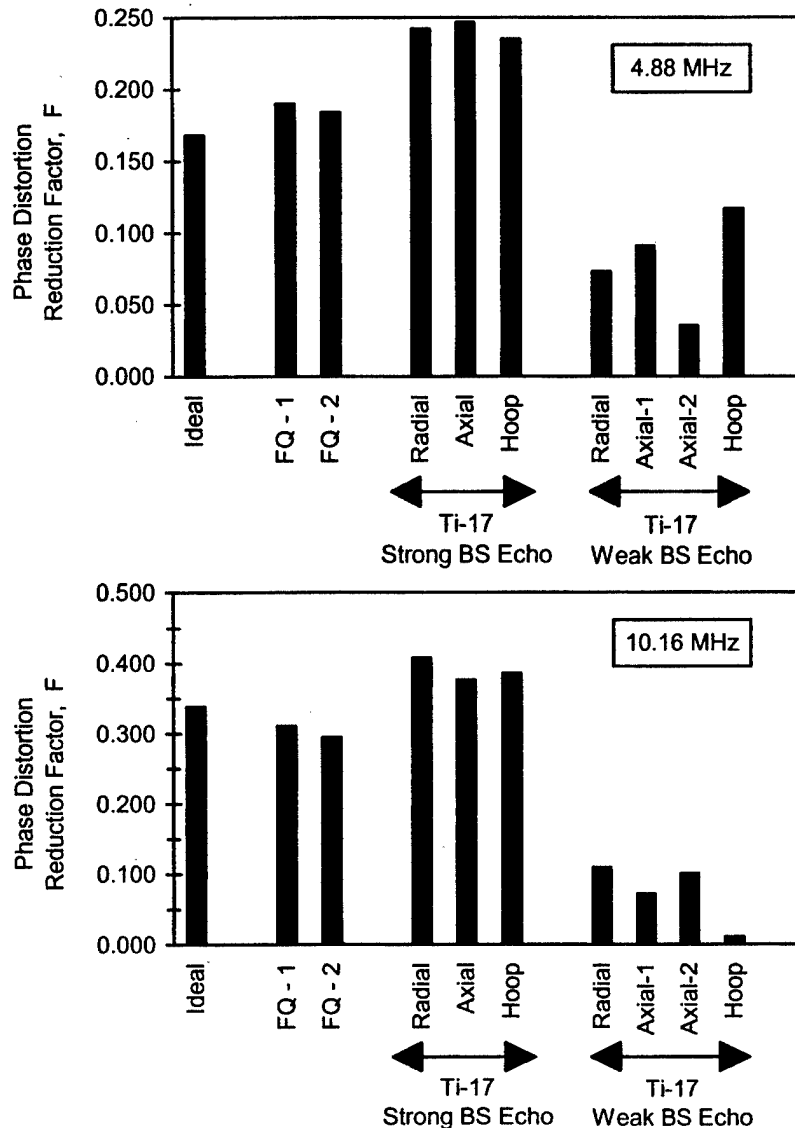


FIGURE 63. VALUES OF THE FRACTION  $F$  FOR BEAMS TRANSMITTED THROUGH A 3" FUSED-QUARTZ BLOCK AND Ti-17 BILLET SPECIMEN L (A small value of  $F$  indicates large phase cancellations upon reflection. A 0.25", 10-MHz planar transducer was used and results are shown for two frequencies.)

The principal findings (Fraction F Study) are as follows.

- For the fused-quartz beam, measured  $F$  values (using a 1/4" planar transmitting transducer) were close to those predicted by ISU models for an ideal piston probe. This lends confidence to the measurement and analysis procedure.
- $F$  values were similar for the FQ beam and the strong echo titanium beam but slightly larger for the latter. For propagation in FQ, the phase cancellations measured by  $F$  arise from the curving of the wave fronts due to beam diffraction. At strong echo locations in

titanium, the microstructure has evidently acted to flatten the wave fronts in the high-pressure portion of the beam, reducing the amount of phase cancellation at the back surface and, hence, enhancing the echo.

- c. For all three propagation directions,  $F$  values were much larger at strong echo locations in titanium than at weak echo locations. This indicates that phase variations (wave front distortion or tilting), rather than amplitude variations (disruption), are responsible for the large differences seen in back-surface echoes when planar probes are used.

### 5.3.7.2 Study 2: Enlarged Grain Block Studies.

The enlarged grain block (EGB) described in section 5.2.2 was used for the second study of beam distortion effects. Using a tightly focused 15-MHz probe, a scan was made to measure the arrival time of the back-surface echo (and hence, the sound speed) as a function of position. Using multiple transducers, additional scans were then made of the block to measure the average attenuation and fluctuations of the back-surface echo amplitude. Comparisons were then made to the predictions of a simple ray model for back-surface echo response.

Because of velocity variations from point-to-point in a given specimen, different portions of a sound beam can travel at different speeds, causing wave fronts to become tilted or otherwise distorted, as illustrated in figure 64. Different parts of the wave front then strike the back surface at slightly different times, resulting in phase cancellations which alter the back-surface echo. The usual effect is to weaken the echo, but as was seen in the fraction  $F$  analysis, it is possible at isolated sites for the microstructure to flatten the arriving wave front, leading to an enhanced echo. Because of its extremely coarse structure, the enlarged grain block offers an excellent vehicle for studying these effects. By using beams of different diameters, it can be arranged for the beam to be confined within one macrograin (no beam distortion due to velocity variations) or to span several macrograins (severe distortion expected). In addition, the sound velocity through the plate thickness is known as a function of position in the EGB, by virtue of the time-of-flight C-scan measurements described in section 5.2.2.

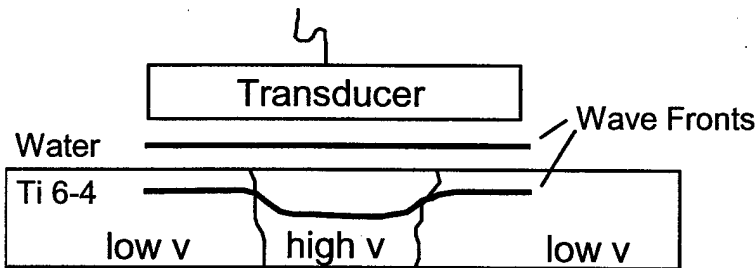


FIGURE 64. A DOWNWARD PROPAGATING WAVE FRONT FROM A PLANAR TRANSDUCER BECOMES DEFORMED WHEN IT ENTERS A METAL SPECIMEN HAVING DIFFERENT SOUND VELOCITIES IN THREE REGIONS

Earlier, figure 53 displayed measured  $\langle\alpha\rangle$ -vs- $f$  curves for BS echoes in the EGB resulting from automated C-scans of the block using three 15-MHz transducers (1/4" planar; 1/2" planar, and 1/2" F/7 focused). Recall that the three transducers yielded quite different average attenuation

values, with  $\langle \alpha \rangle$  growing with beam size. It appears that very little of those measured attenuation values arose from energy loss effects. It was found that when the focused beam was confined within a single macrograin or similar constant velocity region, the measured attenuation was quite low. This is demonstrated in figure 65. There, the 15-MHz focused transducer has been scanned along the line indicated in the leftmost panel. At each probe position, the local  $\alpha$ -vs- $f$  curve was deduced by comparing the observed back-surface echo to one seen in a fused-quartz block of similar thickness. The measured attenuation at 10.2 MHz is displayed as a function of position in the rightmost panel. Notice that there are a number of valleys in the  $\alpha$ -vs-position curve where the measured attenuation is very small. Their locations correspond to plateau regions seen in the BS amplitude and velocity maps of the EGB. The most obvious such valley occupies the range  $1.5 \text{ cm} < y < 2.5 \text{ cm}$  in figure 65(b). There the scan line is cutting across one of the more obvious plateau features, most likely indicating the presence of either a single large macrograin or several smaller macrograins with similar crystalline orientations. In such plateau regions, the measured attenuation tends to be low at all frequencies in the transducer's bandwidth, varying between small positive and negative values [28]. The measurements are, in fact, consistent with  $\alpha=0$  to within the estimated experimental uncertainty.

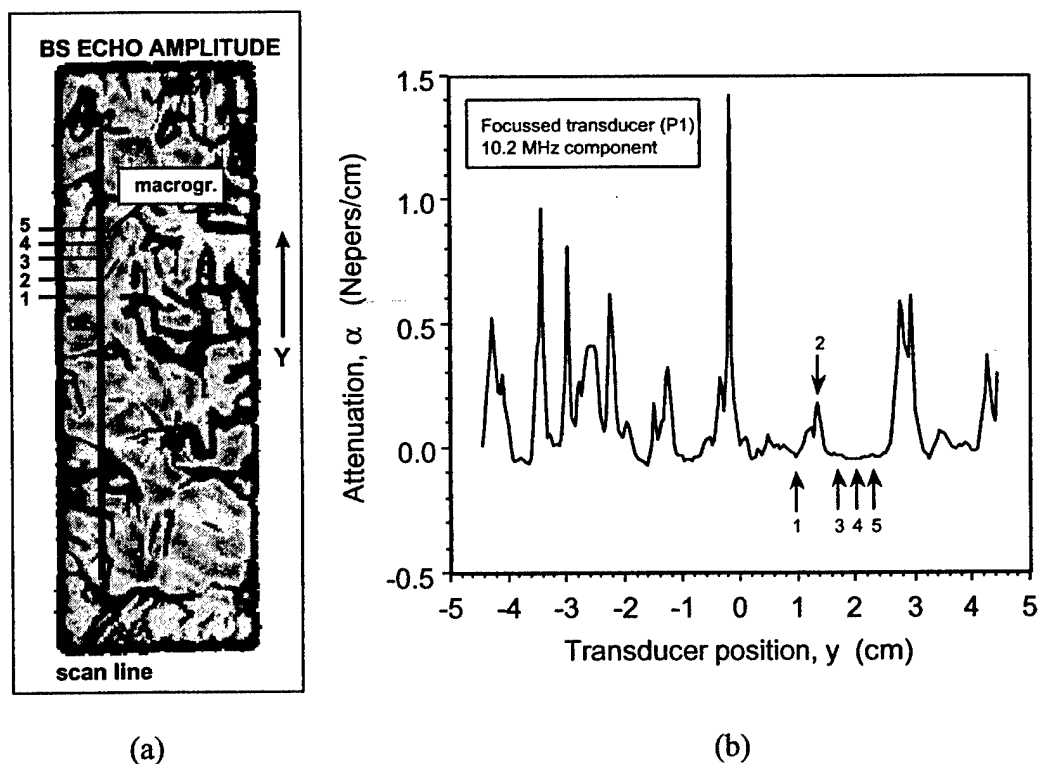
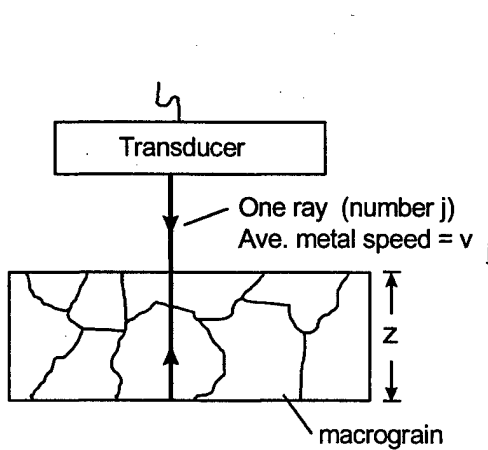


FIGURE 65. (a) C-SCAN IMAGE OF THE MEASURED BACK-SURFACE ECHO AMPLITUDE FOR A SCAN OF THE ENLARGED GRAIN BLOCK USING A 15-MHz, 0.5", F/7 TRANSDUCER AND (b) MEASURED ATTENUATION AT 10.2 MHz AS A FUNCTION OF POSITION FOR THE SCAN LINE INDICATED AT LEFT

Thus, it is concluded that the energy attenuation arising from sound absorption and scattering within a single macrograin must be very small compared to the average BS attenuation values

deduced from the automated scans of the block with the three transducers. It then follows that virtually all of the average BS attenuations shown in figure 53 must be arising from beam distortion effects. For those measurements, a simple ray model was used to estimate the contribution of wave front distortion effects to the measured BS attenuation. A full discussion of those model calculations can be found in reference 28, while only a brief summary will be given here.

The ray model calculations use as inputs the measured EGB sound velocities through the plate thickness. Thus, the aim is to predict BS attenuation from knowledge of the spatial distribution of sound velocities, and the diameter of the sonic beam of each transducer. The basic elements of the ray model for calculating the back-surface response at a fixed transducer position are indicated in figure 66. The model inputs are the average sound velocities along different rays. Outputs are the spectral components of the back-surface echo, relative to a fused-quartz reference, and hence, the effective attenuation for the back-surface echo.



- Partition beam into many rays traveling to back surface and back.
- Consider one frequency (f) at a time.
- Each ray makes a contribution based on its amplitude & phase.

$$A e^{i\theta_j}$$

- The phase depends on the frequency and on the ray's average sound speed.

$$\theta_j = 2\pi \frac{f}{v_j} (2z)$$

- Sum the contributions from all rays to get the BS echo response.

FIGURE 66. THE RAY MODEL FOR BACK-SURFACE ECHO RESPONSE

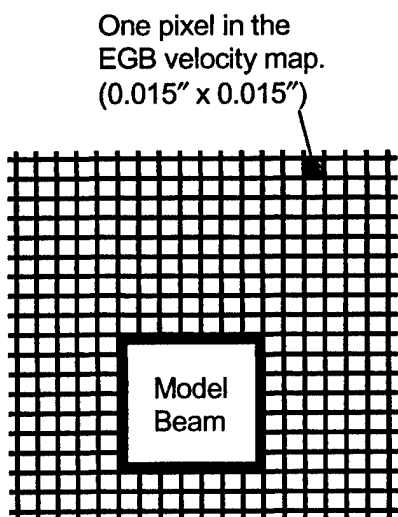
The sound beam is partitioned into a set of (parallel) rays, which for simplicity, are assumed:

- To have small but equal cross-sectional areas; and
- To travel directly downward to the back surface and directly upward to the transducer upon reflection.

Each ray makes a contribution to the observed back-surface echo based on its returning amplitude and phase. All amplitudes are assumed to be the same, but the phases depend on the average speed through the plate, which can be different for each ray. By summing the complex contributions from all rays, the back-surface response can be obtained at a frequency of interest. The response from the fused quartz back surface is calculated in the same fashion. In that case

the velocity is the same for all rays, so the rays return in phase producing a large response. By comparing the predicted responses for titanium and fused quartz, the effective attenuation of titanium can be deduced, just as is done in the actual measurement.

The steps involved in using the ray model to predict the average value and standard deviation of the BS attenuation seen in C-scans is summarized in figure 67. In the calculation, the known plate velocities are used, which have been measured (using a focused transducer) for a fine rectangular grid of points or pixels. The analysis is greatly simplified by replacing each round transducer beam by a square beam of about the same area that contains an integral number of pixels. The assumed beam diameters were 0.25" and 0.50" for the planar probes and 0.050" for the focused probe (the minimum diameter in the focal zone at the center frequency). The dimensions of the equivalent square beams are indicated in figure 67. In the simulation, the square beam is scanned over the block, moving one pixel at a time in each scan direction. At each beam location, it was determined which pixels have been ensonified, read their velocities from the stored velocity data, and then calculate the BS echo response and effective attenuation using the ray model. From the collection of predicted attenuation values at all probe locations in the scan plan, the mean attenuation and standard deviation can be calculated.



1. Use measured velocities as model inputs.
2. Use one ray per measurement pixel.
3. Each probe has a circular beam.  
Deform this into a square of the same area.  
Round off to an integer number of pixels.

	No. of pixels	rounded
1/2" planar	29.5 x 29.5	30 x 30
1/4" planar	14.8 x 14.8	15 x 15
1/2" focused	2.9 x 2.9	3 x 3

4. Scan model beam over EGB.
5. At each beam location, determine:
  - which pixels are ensonified
  - the pixel velocities (look-up table)
  - the BS echo response at selected frequencies
  - the effective attenuation of the BS echo

FIGURE 67. USE OF THE RAY MODEL TO PREDICT BACK-SURFACE ATTENUATION IN THE ENLARGED GRAIN BLOCK

The ray model predictions of back-surface echo attenuation in the EGB are compared with the experiment in figure 68. The upper panels compare predicted mean attenuations and standard deviations for the scan using the 1/4" diameter planar transducer. The lower panels compare the predicted and measured average attenuations for the three transducers. The similarity between measurement and prediction is striking, considering the simplicity of the model used. Both the average back-surface response and the fluctuations about the average are well predicted by the

model. For the two planar transducers, the model even reproduces the minor periodic oscillations that are superimposed on the linear rise of attenuation with frequency. These oscillations are thought to arise from interference effects related to the double-humped nature of the measured velocity distribution in the EGB [28].

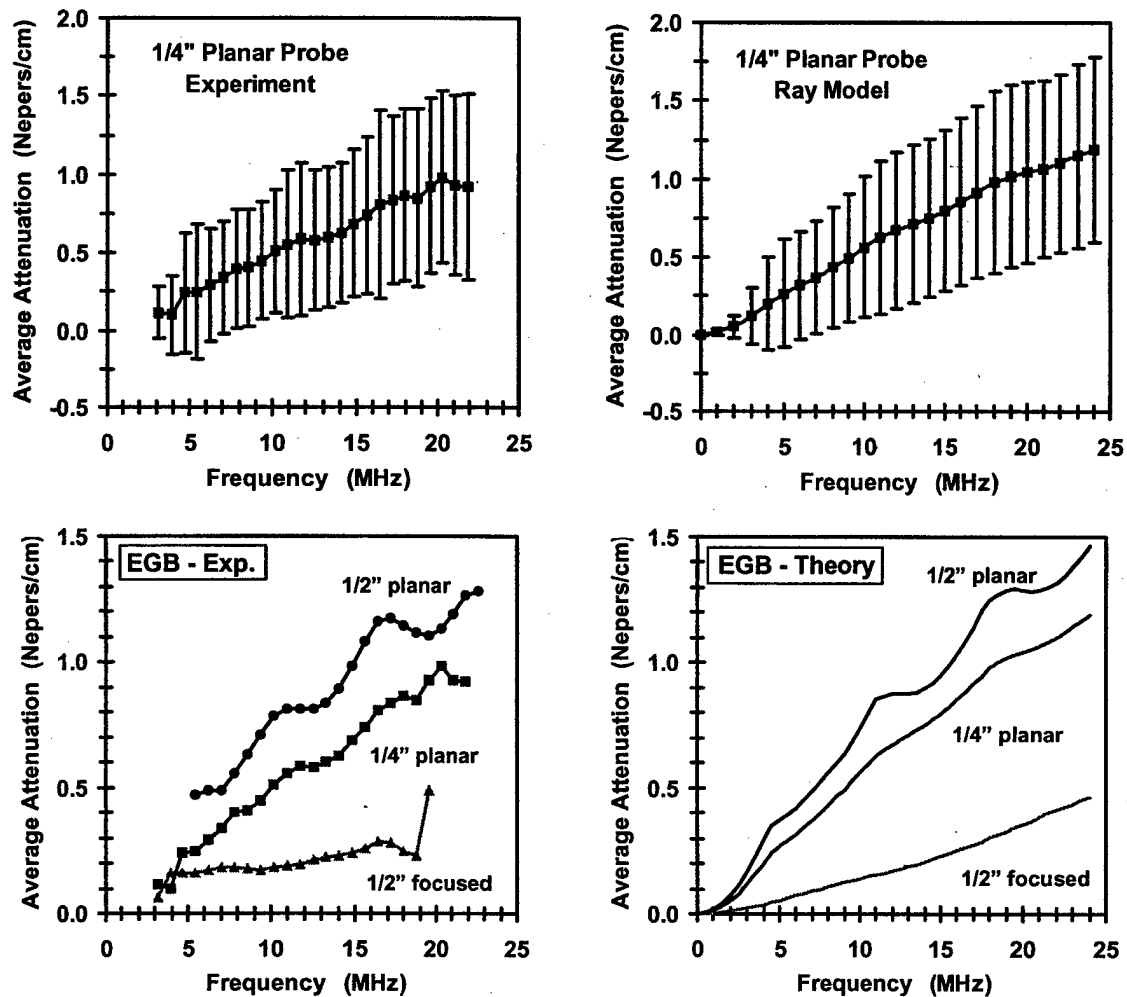


FIGURE 68. COMPARISON OF MEASURED (LEFT) AND PREDICTED (RIGHT) BS ATTENUATIONS FOR THE ENLARGED GRAIN BLOCK

(Top: average and standard deviation of  $\alpha$  when the 0.25" diameter, 15-MHz probe was scanned over the specimen. Bottom: average attenuations for three scans using different 15-MHz broadband transducers.)

Note that the model calculations assume that energy attenuation is absent, and that all observed attenuation is a consequence of wave front alterations. Since model and measurement are in good agreement, one concludes that, on the scale of figure 68, little energy attenuation is present. This is consistent with the earlier experimental finding that the measured attenuation was small when the beam was confined to a single macrograin.

The principal findings (enlarged grain block studies) are as follows.

- a. When the sonic beam is confined within a single macrograin, the measured attenuation is very small compared to the average attenuation measured in scanning experiments. To within experimental uncertainty, the single macrograin attenuation is consistent with  $\alpha=0$ .
- b. The average back-surface attenuation and signal fluctuations seen in scanning experiments can be accurately predicted if
  - The spatial distribution of sound velocities within the block is known; and
  - One assumes that all of the observed signal attenuation and fluctuation arises from wave front distortion.

#### 5.3.7.3 Study 3: Beam Tilt Study.

The wave front modifications responsible for reducing back-surface echoes can be conceptually divided into two categories:

- Wave front tilt, in which the wave front generally maintains its expected shape, but is tilted relative to the back surface (i.e., the beam energy flow is not perpendicular to the back surface); and
- Pure distortion, in which energy flow is normal to the back surface, but the wave front is crinkled or otherwise distorted.

For beams propagating through coarse microstructures, both effects are expected to be present to some degree. The wave front tilt is expected to be enhanced in situations where there is noticeable steering of the beam's center of intensity by the microstructure. Recall that evidence of beam steering was seen earlier (in C-scan images of FBH arrays) for axial sound propagation in billet specimens. When such steering occurs, does it lead to a significant reduction in back-surface echo strength? That question is addressed in this section.

To investigate the effect of beam steering on ultrasonic response, measurements were made for axial propagation in a Ti-17 billet specimen where the effect would likely be largest. Scans were made to measure the BS echo attenuation in two ways using various transducers:

- with the incident beam angles adjusted for normal incidence (the standard method)
- with the beam angles manually adjusted at each probe position to maximize the amplitude of the back-surface echo

The reasoning behind the beam tilt experiment was as follows. For the sake of argument, suppose that in a normal-incident inspection of a flat specimen, the metal microstructure acts to steer the sound beam. In particular, assume that the beam reflected from the back surface arrives at the transducer with its center of intensity displaced laterally from the center of the transducer.

Then one might expect that minor probe angle changes could be made to bring the centers of the beam and transducer face into alignment, increasing the strength of the back-surface echo. (From the wave front point of view, the probe angle changes remove the tilt between the average wave front tangent plane and the back surface, thus minimizing phase cancellation at the back surface.) Thus, if beam steering was acting to appreciably reduce BS echoes, it would be expected to be able to significantly increase those echoes by small counterbalancing changes in the probe angles.

The experiment to test this hypothesis itself is straightforward. First, measure the BS echoes at a grid of sites on a specimen, always keeping the incident beam normal to the entry surface. Then repeat the measurements, making minor manual adjustments in the two probe tilt angles at each site to maximize the peak-to-peak voltage of the BS echo. The attenuation value at each site is then deduced in the usual way by comparison to fused quartz.

This experiment was performed on Ti-17 billet specimen P using three 10-MHz probes (two planar and one focused on the back surface). Axial propagation was chosen since the contribution of beam distortion to BS attenuation was believed to be largest for that propagation direction. For each trial, measurements were made at 49 sites within a 1.2" by 1.2" region. The angular adjustments required to peak up a given BS echo were small: never more than 0.8 degrees and usually less than 0.5 degrees. The adjustments seemed to be fairly random in magnitude and sign, rather than being correlated at nearby scan positions. Consequently, as indicated in table 14, the mean transducer angles obtained by averaging the peak angles found in the manual scan were close to the fixed angles ( $0^\circ$ ) used for the automated normal-incidence scan.

TABLE 14. ANGLE ADJUSTMENT STATISTICS (IN WATER) FOR THE BEAM TILT STUDY

Transducer	Average Magnitude of Angular Adjustment for Either Probe Angle	Average Value of Probe Angle 1 ( $0^\circ$ =normal inc.)	Average Value of Probe Angle 2 ( $0^\circ$ =normal inc.)
1/4" planar	0.33°	+ 0.014°	- 0.070°
1/2" planar	0.10°	- 0.024°	- 0.056°
2", F=16" focused on BS	0.16°	- 0.052°	- 0.022°

For two of the transducers, figure 69 compares average back surface attenuation values as functions of frequency for the normal-incidence and optimized-angle scans. The chart at the bottom of the figure tabulates mean attenuations and fluctuation levels at two frequencies for all three transducers. For the 0.25" diameter planar probe, one sees that the minor adjustments to the tilt angles produced a large increase in the average strength of the back-surface echo and a large decrease in the level of fluctuations about that average. More modest changes were seen for the other two probes. Note that even after optimizing the incident angles, the mean BS attenuation still exceeds the energy loss attenuation, estimated by the TTE method to be about 0.035 N/cm (0.77 dB/inch) at 10 MHz.

The percentage reductions in measured average attenuation values obtained by the manual angle adjustments are listed in table 15 at 5 and 10 MHz for all three probes. In the beam tilting experiment, one basically locates a nearby optimum path for a strong back-surface echo and compares it to the typical path (normal-incidence entry into the metal). Because the center of rotation is near the scanning bridge and not at the transducer face itself, tilting the probe also causes a small lateral shift in the beam. Thus, some of the measured signal increase may simply be due to the fact that one can usually increase a BS echo amplitude somewhat by scanning laterally (without changing the approach angles) and retaining the largest echo. The experiment cannot distinguish unambiguously between the different types of beam distortion effects discussed earlier (steering, disruption, wave front distortion). However, the experiment is expected to detect an attenuation change if beam steering is present and is a major contributor to the deduced attenuation. Thus, the results of the experiment are consistent with the notion that beam steering can be responsible for a significant portion of the measured attenuation, particularly in cases where a small planar probe is used.

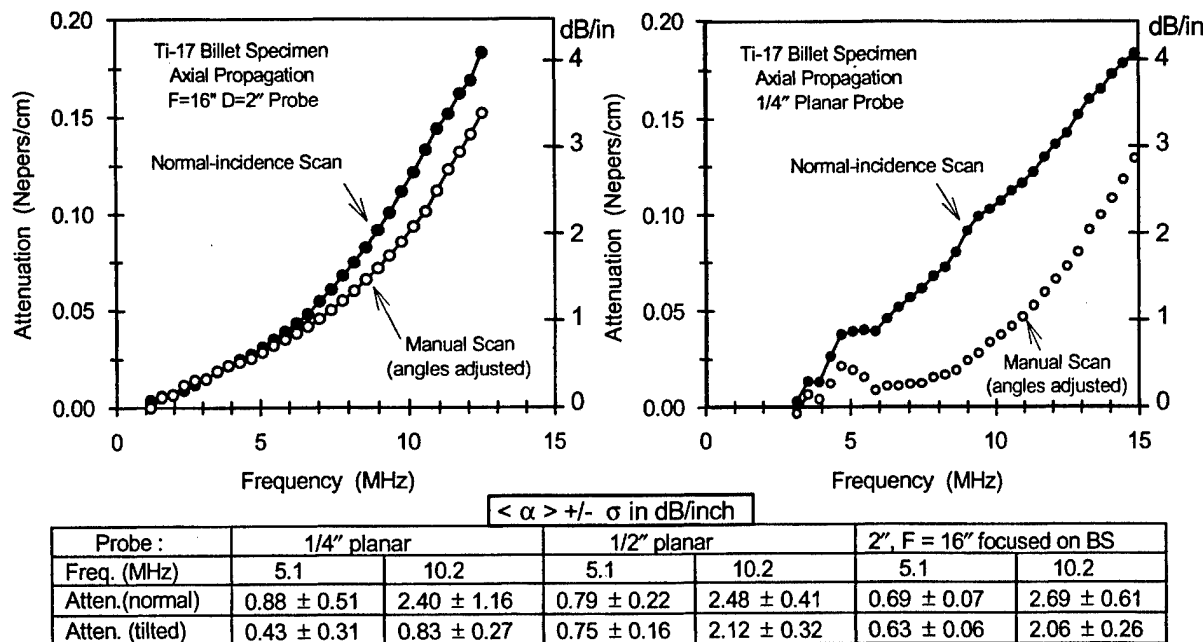


FIGURE 69. AVERAGE ATTENUATION OF BACK-SURFACE ECHOES FOR NORMAL-INCIDENCE AND OPTIMIZED-ANGLE SCANS OF Ti-17 BILLET SPECIMEN P USING FOCUSED (LEFT) AND PLANAR (RIGHT) PROBES

TABLE 15. PERCENTAGE REDUCTION IN APPARENT Ti-17 BACK-SURFACE ATTENUATION ACHIEVED BY ADJUSTING PROBE TILT ANGLES

Transducer	Reduction in $\langle \alpha \rangle$ at 5.1 MHz	Reduction in $\langle \alpha \rangle$ at 10.2 MHz
1/4" planar	51%	65%
1/2" planar	5%	14%
2", F=16" focused on BS	9%	23%

There are some aspects of the beam-tilt experiment that are puzzling. These concern the relative sizes of the attenuation changes for the two planar probes. For a 3" thick specimen, a 0.5-degree tilt in water causes the beam in titanium to be tilted by about 2 degrees (on average), producing a lateral displacement of  $3'' \times \tan(2^\circ) = 0.105''$  by the time the beam reaches the back surface. Such a shift is about equal to the radius of the smallest transducer used, and this shift may be doubled for the full return path to the transducer plane (depending upon how the beam energy meanders back to the front surface). The effect of such a shift on the BS echo amplitude will depend on the magnitude of the shift, the diameter of the transducer, and the amplitude and phase profiles of the reflected beam that strikes the transducer. It is interesting to note that even though the 0.25" probe has the smallest diameter element, and the smallest beam profile on the entry surface, it is (at the center frequency) expected to have the largest beam profile on the back surface. Thus, the measurements are not in the high-frequency geometrical limit, and simple geometrical notions should not be relied on to decide how a certain amount of beam steering is likely to effect measured echoes.

One way to get a handle on the likely effect of beam steering on BS echoes is to make corresponding measurements using the 3" thick FQ reference block, with the same probes and water paths used for the beam tilting experiments. To this end, normal-incidence FQ back-surface echoes were recorded, as were FQ echoes obtained after rotating each probe by 0.5° and 1.0° in water. The spectra of the various fused quartz, back-surface echoes were then computed and are compared in table 16. As one might expect, the probe tilts have the smallest effect for the large focused probe. The effect of the rotations on the planar probe echoes is more dramatic, with the greatest changes occurring for the 1/2" diameter probe. Thus, it is expected that back-surface echoes from the 1/2" planar probe should be the most sensitive beam steering. Given this fact, if beam steering is occurring in the Ti-17 specimen and can be corrected by angle optimization (as is the hypothesis), why isn't a large change seen in apparent attenuation for the 1/2" probe when angle-optimization is used? Why is the observed change largest for the 1/4" probe? Until these questions are answered, perhaps by future experiments, it cannot be definitely said that beam steering is playing a large role in reducing back-surface echoes in titanium.

TABLE 16. PERCENTAGE REDUCTION IN THE 5- AND 10-MHz SPECTRAL COMPONENTS OF THE FUSED-QUARTZ, BACK-SURFACE ECHO RESULTING FROM TILTING THE TRANSDUCER AWAY FROM NORMAL INCIDENCE

Transducer	0.5° Tilt in Water		1.0° Tilt in Water	
	5.1 MHz	10.2 MHz	5.1 MHz	10.2 MHz
1/4" planar	8%	28%	29%	75%
1/2" planar	32%	78%	79%	96%
2", F=16" focused on BS	3%	4%	17%	21%

The principal findings (beam tilt study) are as follows.

- Above 5 MHz, the average BS echo amplitude could often be significantly increased by small changes in the probe angles, resulting in a corresponding reduction in the measured attenuation. The  $\langle \alpha \rangle$  reduction was particular large (65% at 10 MHz) for a 0.25"

diameter planar probe. Much more modest reductions were seen for a 0.5" diameter planar probe and a 2" diameter focused probe.

- b. These results suggest that wave front tilting, due to beam steering, may be a significant contributor to BS echo attenuation for propagation along macrograins or flow lines. However the results are not definitive and are open to other interpretations.

#### 5.3.7.4 Study 4: Slicing Study.

In this work, attenuation-vs-frequency curves are deduced by comparing the spectra of corresponding titanium and fused-quartz echoes with similar travel paths. When this is done, it is generally assumed that signal strength depends upon propagation distance  $z$  through a factor of the form  $\exp(-\alpha z)$ . In this study, the  $\exp(-\alpha z)$  rule is tested by repeatedly measuring  $\alpha$ -vs- $f$  curves for a given specimen using different sound travel paths. Two ways of changing the travel path were used: (1) using back-surface reverberation echoes in the original specimen and (2) physically slicing the specimen, measuring the (direct) BS attenuations of the original specimen and each slice. Both methods were applied to Ti-17 and Ti 6-4 billet specimens, using a 0.25" diameter planar transducer.

The earlier fraction F, EGB, and beam tilt studies all indicate that sonic phase distortions (i.e., wave front wrinkling or tilting) occur and can greatly affect the strength of ultrasonic echoes. This has an important implication for the depth dependence of ultrasonic signals. When energy loss is primarily responsible for signal attenuation, it is reasonable to assume that the decrease of signal strength with propagation distance ( $z$ ) is governed by the factor  $\exp(-\alpha z)$ . Under this assumption, signal reductions, expressed in dB units, add for propagation through successive layers of material. For example, suppose there are two slabs of similar material with relatively uniform microstructures, one 1" thick and the other 2" thick. If an average attenuative signal loss (say, for BS echoes relative to fused quartz) of 5 dB is measured in the 1" slab, then, based on the  $\exp(-\alpha z)$  rule, a loss of  $5 + 5 = 10$  dB would be lost for a similar measurement using the 2" slab. This will likely be the case if energy loss effects dominate the attenuation process. But for engine titanium, it is known that the contribution of beam distortion effects to the measured attenuation can be as large or larger than the contribution from energy loss, particularly at higher frequencies for propagation along macrograins. The effect of beam distortion on signal attenuation may partially saturate after the beam has traveled a certain distance and becomes sufficiently distorted. In that case, the overall attenuation will not obey the  $\exp(-\alpha z)$  rule.

When deducing  $\alpha$ -vs- $f$  curves using any of the measurement methods (BS, TTE, or FBH), one would follow the traditional approach of assuming that the  $\exp(-\alpha z)$  rule holds. Is this valid? A straightforward method for testing the  $\exp(-\alpha z)$  rule is to assume that the rule holds and to compare deduced  $\alpha$ -vs- $f$  curves obtained using travel paths of different lengths. If the same  $\alpha$ -vs- $f$  curve is obtained when using different travel paths (in relatively homogeneous material), then it could be safely assumed that the rule is valid. For BS echoes there are two simple methods of varying the measurement path. They are shown in figure 70 and referred to as the reverberation and slicing methods, respectively. In the first method, one begins with the usual geometry for the BS method, but uses ray paths for which sound reverberates within the fused quartz and titanium blocks. Thus, for a specimen of thickness  $Z$ , one can measure  $\alpha$  over a

round-trip solid path of  $2nZ$  ( $n=1, 2, 3, \dots$ ) by using the  $n$ -th back-surface echo (denoted here by  $BS_n$ ). The second method is more direct but destructive. One first measures the attenuation using the standard BS method, cuts the specimen into two or more slices (for which FQ blocks of comparable thickness are available), and finally applies the BS method to each slice.

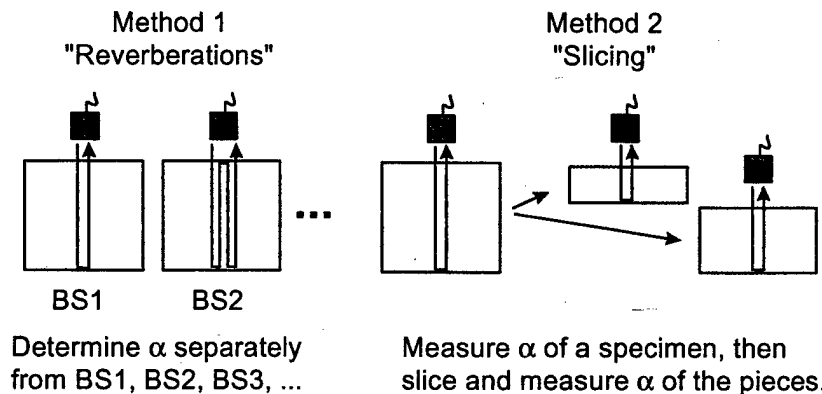


FIGURE 70. TWO METHODS OF VARYING THE METAL TRAVEL DISTANCE USED FOR ATTENUATION MEASUREMENTS

Both methods of varying the measurement path were applied to two cases of interest: [29]

- Axial sound propagation in a Ti-17 billet specimen (where beam distortion effects were known to be significant); and
- Radial sound propagation in a Ti 6-4 billet specimen (where the measured back-surface attenuation was believed to be dominated by energy loss).

Each specimen was originally about 3" thick (before slicing), and the reverberation method was used first. For the Ti-17 specimen, BS1, BS2, and BS3 echoes were analyzed in turn, corresponding to round trip metal travel distances of about 6", 12", and 18", respectively. For the Ti 6-4 specimen, the BS3 echo was found to be only slightly stronger than the competing grain and electronic noise, so only the BS1 and BS2 echoes were analyzed. The measurements were made using a 0.25" diameter, 10-MHz planar probe and a water path of 2.5" for the fused-quartz reference block. The water paths for the titanium blocks were chosen such that the average effect of diffraction was the same as for fused quartz, i.e., by using a generalization of equation 1 for reverberation echoes. In every case, the probe was scanned over a 1.0" by 1.0" area with a step size of 0.1" in each direction, resulting in attenuation measurements at 121 sites. Two such measurement trials were conducted in each case to check the work, since later measurements in the 3" geometry (after slicing) would not be possible. Excellent agreement was generally seen for the two trials, and their results were averaged to obtain the final values reported. The average attenuation-vs-frequency curves deduced from the back-surface reverberation echoes are shown in figure 71. For both titanium alloys, the measured average attenuation coefficient is seen to drop as the travel path is increased, indicating that the  $\exp(-\alpha z)$  rule does not hold. The drop increases with frequency and is much more severe for Ti-17 than for Ti 6-4. The energy loss attenuations measured by the TTE method are shown for comparison on the same figure. One sees that, as the sound travel path increases, the attenuation measured

by the BS reverberation method approaches the energy loss value. If one assumes that both energy loss and beam distortion effects contribute to the overall attenuation of back-surface echoes, this indicates that the contribution of beam distortion alone (expressed in dB/inch or Nepers/cm units) decreases as the sound path becomes greater.

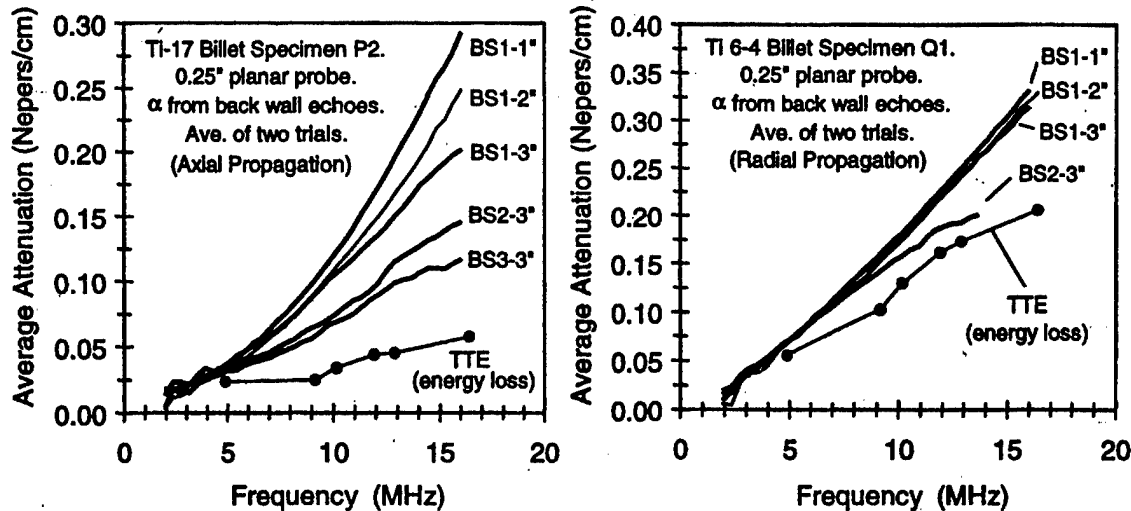


FIGURE 71. EFFECT OF METAL TRAVEL DISTANCE ON MEASURED ATTENUATION  
(Deduced average attenuation coefficients of back-surface echoes are shown for different choices of the specimen thickness (1", 2", or 3") and the echo reverberation (BS1, BS2, or BS3) within that thickness.)

After the reverberation measurements were concluded, each specimen was cut into two slices approximately 1" and 2" thick, respectively, since FQ reference blocks with those thicknesses were available. The attenuations of the slices were then deduced in the standard way by analyzing the BS1 echoes. Again, the 0.25" diameter planar probe was used with the same scan plan and same 2.5" water path in FQ, and two measurement trials were conducted and averaged. The results are shown in figure 71. For both specimens, the deduced mean attenuation coefficient is again seen to depend on travel path, and the dependence is most severe for the Ti-17 case. Because the microstructures of the two slices may be different, it is not necessary that the  $\alpha$ -vs- $f$  curves for the two slices be identical if the  $\exp(-\alpha z)$  rule holds. However, if the rule did hold, the sum of the total attenuations (in dB's) for the 1" and 2" slices would be expected to approximately equal that for the 3" slice (adjusted for the loss of metal during cutting and milling). For Ti-17, for example, the total average attenuations of BS echoes in the 1", 2", and 3" slices are 11.3, 18.8, and 24.3 dB respectively at 14.8 MHz, and the first two clearly do not add to the third.

In summary, the results indicate that the usual  $\exp(-\alpha z)$  attenuation rule does not hold for engine titanium alloys, although it is reasonably accurate at lower frequencies ( $\leq 5$  MHz). The rule is likely most in error in situations where beam distortion effects contribute strongly to measured attenuation, i.e., for propagation parallel to the macrograin elongation direction. When the  $\exp(-\alpha z)$  rule is not accurate, the deduced attenuation coefficient (in dB/inch or Nepers/cm) will depend upon the total metal travel path used in the measurement and will decrease as the travel

path is increased. Thus, when measuring attenuation for the purpose of determining distance-amplitude corrections for planned inspections, it is recommended that one use sonic travel paths similar to those to be encountered in the actual billet or forging inspection.

The principal findings (slicing study) are as follows.

- a. The usual  $\exp(-\alpha z)$  rule does not always hold in engine titanium alloys. Thus, if there is a measured 5-dB signal loss when traversing 1 inch of material, one cannot assume 10 dB of loss when traversing 2 inches of similar material.
- b. The measured average attenuation  $\langle\alpha\rangle$  (in Nepers/cm or dB/inch) depends on the travel path used in the measurement. As the travel path increases, the value of  $\langle\alpha\rangle$  drops, approaching the energy-loss (TTE) value. Thus, the contribution of beam distortion to the measured attenuation appears to saturate.
- c. The dependence of the attenuation coefficient on the measurement distance increases with frequency. For frequencies in the 5-15 MHz range, the dependence was quite large for axial propagation in Ti-17 but rather modest for radial propagation in a Ti 6-4.

#### 5.3.8 Attenuation Summary.

Ultrasonic attenuation measurements were performed on rectangular coupons cut from representative Ti-17 and Ti 6-4 billet and forging specimens. Three measurements techniques were used, referred to as the BS (back surface), TTE (through-transmitted energy), and FBH (flat-bottomed hole) methods, respectively. In each case, the effective attenuation-vs-frequency curve of the titanium coupon was deduced by comparing signals from titanium to similar signals from a low-attenuation reference block (fused quartz or powdered nickel alloy) of similar thickness.

A series of measurements were performed to measure the attenuations of 12 coupons in three propagation directions (radial, axial, and hoop) using the traditional BS method and the same 10-MHz planar transducer. The following points were noted:

- a. Measured average attenuation rose with frequency, at a rate that was typically faster than linear but slower than quadratic.
- b. Attenuation values ranged over about one order of magnitude among the suite of specimens: from 0.2 to 2 dB/inch at 5 MHz and from 0.6 to 6 dB/inch at 10 MHz.
- c. Attenuation tended to be higher in Ti 6-4 material than in Ti-17.
- d. There was a strong dependence on beam propagation direction. The attenuation tended to be highest when the beam propagated parallel to the local macrograin elongation direction in billets or along flow lines in forgings.
- e. Significant fluctuations in the strength of the back-surface echo were seen during scanning, particularly for axial propagation in billets.

In a related set of measurements, 1" thick coupons were removed from six locations in a 6" diameter Ti 6-4 billet (three each from high- and low-noise regions), and attenuations for radial propagation were deduced using the BS method. Among this suite of coupons, the average attenuation was seen to vary by a factor of about 2.5. This suggests that point-to-point variations of the effective attenuation within a given component can be substantial, even if the propagation direction is fixed.

For selected engine titanium specimens, the sonic beam transmitted through the specimen was mapped, and the relative energy carried by the beam was computed. The sonic beam maps revealed substantial distortions of the amplitude and phase profiles, evidently caused by velocity variations associated with the coarse titanium macrostructure. The phase distortions were found to be primarily responsible for the large variations in back-surface echoes seen during scanning experiments. Moreover, comparisons of attenuation values obtained using the BS and TTE methods found that the attenuation of back-surface echoes could be significantly higher than that expected from energy loss alone. Thus, two different sources of effective signal attenuation in titanium were identified: energy loss (due to the absorption and scattering of sound) and beam distortion (which included amplitude distortions, wave front distortions, and beam steering).

The relative sizes of the energy loss and beam distortion contributions to overall signal attenuation could be judged by comparing the measured BS and TTE attenuation values. Those measurements indicate that beam distortion is most likely to be a major contributor when:

- the beam propagates parallel to the macrograin elongation direction (axially in billets or along flow lines in forgings),
- the inspection frequency is high (i.e., above 5 MHz),
- Ti-17 material is inspected rather than Ti 6-4.

When distortion effects were a major contributor to the measured attenuation, a number of interesting phenomena were documented:

- a. Measured BS attenuation values depended on the transducer used, with probe-to-probe differences increasing with frequency. For focused-probe measurements, changing the water path, and hence the degree of focus at the back surface, could also significantly change the measured attenuation value.
- b. When  $\alpha$  -vs- $f$  curves obtained with focused and planar transducers were compared, in most cases the focused transducer yielded a higher average attenuation value but smaller signal fluctuations about that average.
- c. The attenuation deduced from back-surface echoes was not always a reliable indicator of the attenuation appropriate for echoes from small defects (i.e., #1 FBHs). This was especially true for unfocused beams (or, by extension, beams focused in front of or beyond the reflector).

- d. A small change in the beam-tilt angle could partially compensate for beam-steering effects, and, on average, significantly increase the strength of the back-surface echo. Again, this was most pronounced for unfocused beams.
- e. The effects of beam distortion on measured attenuation appeared to saturate with distance, and the dependence of total signal attenuation on depth did not follow the usual  $\exp(-\alpha z)$  rule. Thus, if the attenuative signal loss was 10 dB when traveling through 1 inch of material, it would not be 20 dB in traveling through 2 inches of similar material, but rather some value less than 20 dB. As a consequence, the deduced attenuation value depended on the metal travel path used in the measurement.

In current billet inspection procedures, 5-MHz transducers are used and the sonic beam travels radially inward, perpendicular to the columnar macrograins. Thus, the effects of beam distortion on signal attenuation are generally modest. Even so, the most trustworthy attenuation measurements would be made by using transducers and sound travel paths similar to those used in the actual inspection and to use FBH echoes rather than surface echoes when possible. Beam distortion effects can be expected to be more severe for higher-frequency billet inspections and for forging inspections in general since there the inspecting beam will not always be perpendicular to the metal flow lines.

It would be very helpful to have a fairly general first-order model which predicts the effect of microstructure on sound echoes, i.e., a model which predicts the average signal strength expected in a given circumstance and the size of the expected signal fluctuations about that average. For example, there is an analogous model for backscattered grain noise, which is addressed in a companion part of the ETC program. That model relates grain noise characteristics to details of the measurement system and to a microstructural component, the noise FOM, which is a property of the specimen alone. Moreover, a process for measuring the FOM has been developed. Once the FOM of a specimen has been measured, the model can be used to predict grain noise levels and related information for various inspection scenarios. A similar model is required for the effect of microstructure on echoes from defects and surfaces, together with procedures for measuring the microstructural components, which come into play. It is reasonable to suppose that the contribution of beam distortion to ultrasonic attenuation and signal fluctuation levels can be estimated given sufficient information about velocity inhomogeneities in the specimen under study. It was demonstrated that this is indeed the case for one Ti 6-4 specimen (the so-called enlarged grain block). However, the simple ray model used in that demonstration required detailed velocity-vs-position data that is unlikely to be available for practical inspections. In a more general model, the detailed velocity inputs will presumably be replaced by a small number of measurable parameters determined by the specimen microstructure. Such a model has not yet been developed, although some preliminary investigations into possible model-building approaches are underway [25, 31, and 32]. Recent measurements of FBH signal fluctuations in titanium alloys, performed after the conclusion of the ETC program, are summarized by Margetan, Wasan, and Thompson [32]. That reference discusses the manner in which fluctuations and apparent attenuation of FBH echoes depend on beam focusing.

### 5.3.9 Longitudinal Wave Backscattered Noise Measurements.

In ultrasonic pulse/echo inspections of engine titanium specimens, backscattered microstructural noise is present and can hinder the detection of echoes from small or weakly scattering defects. This noise arises from the scattering of sound by the boundaries of the metal grains and macrograins. In a given measurement, the absolute size of the grain noise echoes will depend on the microstructure of the specimen under study, as well as on details of the inspection system being used. Models of inspection processes have been developed which treat both effects and attempts to predict the absolute noise level seen during an inspection. A brief summary of those noise models appears in appendix B. In the models, the microstructural information is contained in frequency-dependent factors referred to as the FOMs for noise severity. The larger the FOM value, the larger the level of backscattered noise. From knowledge of the FOM and various inspection system parameters, statistical characteristics of the backscattered noise can be predicted. Because the microstructure of most engine titanium specimens is neither uniform nor isotropic, the FOM will generally depend upon the beam propagation direction, and for a fixed propagation direction, the FOM may also vary somewhat from region to region in the specimen.

Figure 72 displays one example of the dependence of backscattered noise on position within a billet. In this case the specimen is a 6" diameter Ti 6-4 billet. The inspection was done using a 1" diameter, 5-MHz bicylindrically focused multizone transducer designed to focus about 1.5" deep in such a billet. The time gate for noise acquisition was 4.0 microseconds long, centered 1 inch deep in the metal. Red coloration represents high-noise voltage and blue/violet represents low-noise voltage. The dark blue feature in the shape of a triangle arises from a mask placed on the outside of the billet to aid in orientation. The boxes identify regions from which coupons were removed for further study. Note that repetitive banding pattern can be seen in the C-scan image of the backscattered noise. It is not unusual for the average noise amplitudes in the high- and low-noise regions of a billet to differ by a factor of two or three.

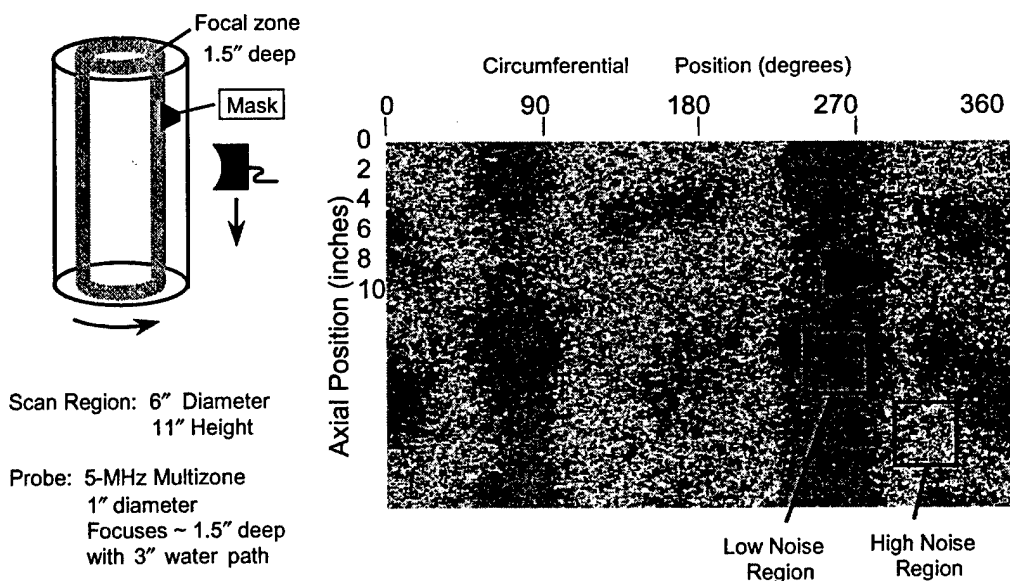


FIGURE 72. C-SCAN IMAGE OF GATED-PEAK NOISE SHOWING THE NOISE BANDING PATTERN OF A 6" DIAMETER Ti 6-4 BILLET

This section covers backscattered noise measurements aimed at deducing the average value of the noise-FOM within a coupon (typically a 3" cube) cut from a billet or forging. This was done so that the average inherent noisiness of different engine titanium specimens could be quantitatively compared, and also to obtain the FOM values required for model calculations of noise levels and S/N ratios pursued under other ETC tasks.

In addition to the measurement of FOM values for representative billet and forging specimens, other noise survey results will be reported that were compiled to gain insight into the manner in which inspection system choices affect noise levels and to help guide model development efforts. These include investigations into:

- Relative sizes of different measures of the noise (rms noise versus gated peak noise);
- Manner in which gated-peak noise characteristics depend on the duration of the time gate;
- Degree to which certain fixed-arrival-time noise distributions are Gaussian.

The emphasis here is on investigating the general characteristics of the backscattered noise in a suite of engine titanium specimens. Other measurements made specifically to test noise model predictions are discussed in appendix B.

Before beginning, it was noted that the manner in which backscattered noise depends upon sound penetration depth (or upon arrival time) is dictated in part by the normalization procedure adopted. For example, in a focused-probe measurement, if one normalizes the noise at a given depth by the strength of an echo from a FBH at the same depth, one generally finds the smallest noise level at the focal plane of the transducer. On the other hand, if the noise at all depths is normalized by the same fixed signal, such as a back-surface echo from a fused-quartz block, then one generally finds the greatest noise level at the focal plane as shown in figure 73. Throughout this section, when noise-vs-depth curves are shown, the reported noise quantities are either unnormalized or normalized using fixed reference echoes. FBH normalization is not used.

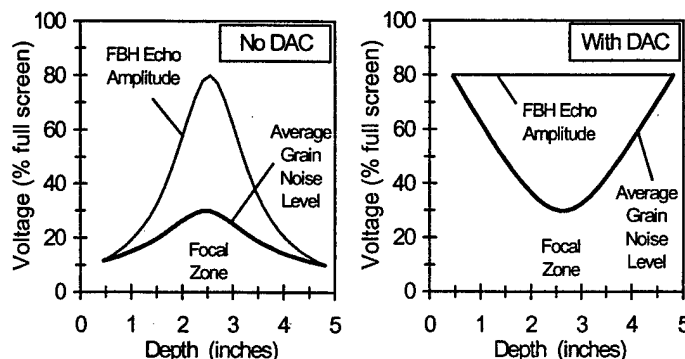


FIGURE 73. TYPICAL DEPENDENCE OF GRAIN NOISE ON DEPTH IN A FOCUSED PROBE INSPECTION OF A BILLET WHEN NO DISTANCE-AMPLITUDE CORRECTION IS USED (LEFT) AND WHEN A DISTANCE-AMPLITUDE CORRECTION BASED ON THE STRENGTH OF A FHB ECHO IS USED (RIGHT)

As shown in figure 74, a normal-incidence, immersion setup is used for backscattered noise measurement and subsequent FOM determination. A focused transducer is generally used, which has gone through a characterization process to determine its effective diameter and geometrical focal length in water. Focused transducers are preferred because the unnormalized backscattered noise level from the focal zone is large and, thus, more likely to dwarf the electronic noise present in the measurement system. Electronic noise will always be present at some level and, hence, contribute to the measured noise and deduced FOM values. If the electronic noise level is a significant fraction of the microstructural noise, the deduced FOM values will be significantly in error.

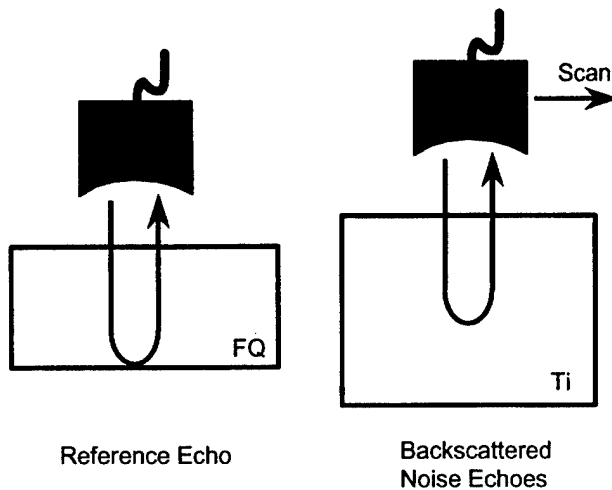


FIGURE 74. INSPECTION SETUP FOR ACQUIRING REFERENCE AND NOISE A-SCANS

Before noise measurements begin, a reference echo from the back surface of a fused-quartz block is acquired and stored. This echo contains information about the duration and frequency content of the incident sound pulse produced by the measurement equipment, and it is used to deduce a system efficiency factor which describes the conversion of electrical energy to sound. The single reference echo is usually acquired with the beam focused on the back surface of the fused-quartz block. After acquisition of the reference echo, the transducer is scanned in a rectangular grid above the metal specimen to acquire noise echoes. The constant water path is chosen such that the beam focus is in the interior of the specimen, well away from the front and back surfaces. At each transducer position, the radio frequencies (RF) noise signal (A-scan) is repeatedly digitized and averaged to lessen the effect of electronic noise and the resulting averaged signal is then stored. At the conclusion of the scan, the stored A-scans are analyzed using the independent-scatterer noise model to extract the FOM as a function of frequency. The complete analysis procedure is described in other references [33 and 34]. Briefly, at each discrete time instant, the average voltage of all the stored RF grain-noise signals is calculated, and this average is subtracted from each signal to approximately remove the instrumentation background voltage. Using an FFT algorithm, the frequency spectrum of each modified noise signal was calculated on some time interval  $[t_a, t_b]$ . The FOM at each discrete frequency is then deduced from the root-mean-squared average of the noise spectral amplitudes at that frequency, normalized by the reference signal spectrum. The smoothness of the FOM-vs-frequency data will depend upon the number of statistically independent noise signals used in the analysis.

Generally, several hundred transducer positions are used, spaced as widely apart as is possible, subject to the constraint that the beam not interact appreciably with the lateral sides of the specimen.

In theory, the choice of the FFT time interval  $[t_a, t_b]$  for FOM determination is arbitrary, but generally, an interval is chosen that encloses the noise scattered from the focal zone. The noise echoes are generally strongest there, and the beam models used in the FOM extraction procedure are most accurate near the focal zone. Note that when specifying time intervals,  $t=0$  is always chosen at the center of the front-surface echo from the metal specimen and time is then proportional to the sound penetration depth.

For a typical FOM measurement, table 17 summarizes the key inspection particulars. Here the specimen, designated H, is a 3" cube from the outer portion of a 9.25" diameter Ti 6-4 billet. In this case, 361 noise A-scans were acquired through each of three orthogonal faces so that the FOM could be deduced for sound propagation in the radial, axial, and hoop directions.

TABLE 17. TYPICAL SETUP AND ANALYSIS PARAMETERS FOR  
NOISE-FOM MEASUREMENT  
(These apply specifically to measurements of Ti 6-4 billet specimen H.)

Transducer	5-MHz broadband, 3/4" diameter, F=6" PTF Panametrics model A3359, Serial No. 133271 Characterized using echoes from a small spherical reflector scanned along the beam's symmetry axis: <ul style="list-style-type: none"> <li>Effective diameter = 1.88 cm = 0.74 inch</li> <li>Geometrical Focal length = 19.94 cm = 7.85 inches</li> </ul>
Reference reflector	Back-surface echo from a 2.54 cm = 1.002" thick fused-quartz block
Water paths	For reference signal: 9.71 cm (3.82") For noise echoes: 3.00 cm (1.18")
Water temperature	Range: 69.1°F to 69.6°F
Region scanned	1.8" x 1.8" in steps of 0.10" (19 x 19 = 361 transducer positions)
Duration of digitized RF noise signals	Typically 22 microseconds (from about 3 to 23 $\mu$ s after the front-surface echo). Sampling rate = 100 MHz
Time interval for FFT analysis of noise	$[t_a, t_b] = [7.44 \mu\text{s}, 12.55 \mu\text{s}]$ (an interval of 5.11 $\mu\text{s}$ centered in the focal zone)
Frequencies at which FOM determinations were made	2.14 MHz to 8.98 MHz in steps of 0.195 MHz
Other notes	There was a 30 dB difference in gain settings for the reference and noise signals.

Although it is not required for FOM determination, it is convenient to calculate and display the average grain noise level as a function of time (or depth). In figure 75, the absolute root-mean-

square (rms) noise level is displayed in volts versus time for each of the specimen H measurement trials. The rms noise level [33 and 34], at a given observation time, has been computed by taking the square root of the average of the squares of the 361 noise voltages observed at that time instant (one such voltage for each transducer position). When only a few hundred noise signals are used, rms noise versus time curves generally display rapid (fine-scale) variations, and these were largely removed by data smoothing to more clearly reveal the large-scale structure.

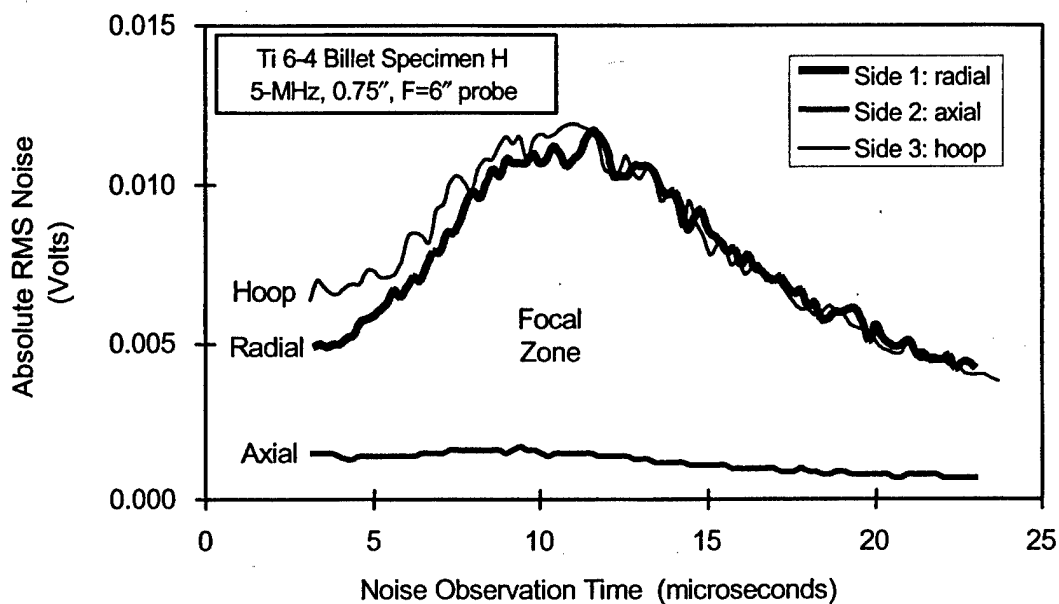


FIGURE 75. ABSOLUTE rms NOISE LEVELS MEASURED FOR RADIAL, AXIAL, AND HOOP PROPAGATION IN Ti 6-4 BILLET SPECIMEN H  
(The measurements used a 5-MHz, F/8 focused transducer.)

Each of the curves in figure 75 is seen to have a single broad peak centered near 10 microseconds, i.e., near to the round trip travel time from the front surface of the specimen to the focal zone. If the microstructure were independent of depth for each propagation direction, all of the curves would be expected to have very similar shapes. However, shape variations are often seen, indicating some degree of FOM variation with depth. Notice that the noise levels are much higher for radial and hoop propagation than for axial propagation. This was the case for all of the Ti 6-4 and Ti-17 billet specimens studied.

Figure 76 shows the deduced FOM values for specimen H, as functions of frequency within the useable bandwidth of the 5-MHz focused transducer. The deduced FOM value depends on the assumed attenuation of the specimen, and the results are shown for two choices of the ultrasonic attenuation.

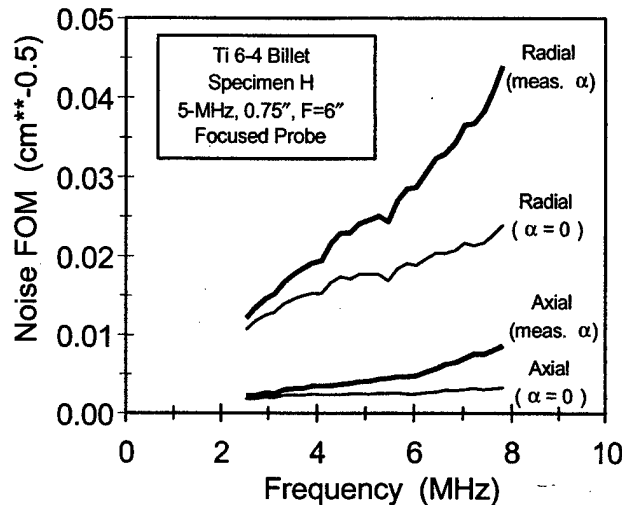


FIGURE 76. FREQUENCY-DEPENDENT FOM VALUES DEDUCED FOR RADIAL AND AXIAL PROPAGATION IN Ti 6-4 BILLET SPECIMEN H  
(Results for hoop propagation, not shown, are similar to the radial case.)

The FOM extraction procedure requires knowledge of the energy-loss attenuation ( $\alpha$ ) as a function of frequency. The attenuation measured from back-surface echoes includes contributions from both energy loss and beam distortion effects, and thus serves as an upper limit to the energy-loss attenuation. In many engine titanium specimens, it is expected that the attenuation arising from beam distortion exceeds that arising from energy loss. For this reason, the FOM extraction calculations were performed twice for each (specimen, side) combination: once using the measured attenuation as the model input, and once using an assumed attenuation of zero at all frequencies. These two attenuation choices should bracket the energy-loss attenuation, and the differences in the FOM values for the two choices will quantify the maximum FOM uncertainty that arises from the uncertainty in attenuation.

Notice that at the higher frequencies in figure 76, there is a substantial difference between the FOM values deduced assuming  $\alpha=0$  and those deduced assuming the measured attenuation. When the assumed attenuation is large, one expects the intensity of the sonic beam to drop rapidly with penetration depth. Then, because the incident beam strength is small, the FOM value in the model must be made large in order to account for the observed noise level. According to the noise model, the FOM value deduced assuming  $\alpha=0$  (at some given frequency), and the FOM value deduced assuming some nonzero value of  $\alpha$  are approximately related by

$$FOM(\alpha) = e^{2\alpha z} FOM(\alpha = 0); z = v_{1S} \frac{t_a + t_b}{2} \quad (5)$$

where  $v_{1S}$  is the speed of sound in the metal and  $[t_a, t_b]$  is the time interval on which the backscattered noise is analyzed. Strictly speaking, the above equation holds only in the limit where the duration of the time interval is small. Nonetheless, it provides a useful rule of thumb for estimating the effect of material attenuation on the deduced FOM value.

Note in figure 76 that the FOM values tend to rise with frequency. This behavior is typical of the billet and forging specimens studied. From theoretical considerations, the FOM value is expected to approach zero at zero frequency, which is usually the case. However, in low-noise cases (such as axial propagation in billets), the extrapolated FOM value at zero frequency is nonzero. This is believed to result from the existence of the noise floor provided by the residual electronic noise. When the backscattered noise is small, the equipment gain settings are at or near their maximum values, and the residual electronic noise level can contribute appreciably to the measured noise. This effect tends to elevate the deduced FOM values, particularly at low frequencies, where the microstructural noise is small.

During FOM survey work, the majority of the measurements were made using the 5-MHz transducer identified in table 17. For a limited number of specimens, follow-up measurements were also made using a 15-MHz focused probe. In those cases, good agreement was generally observed between the two sets of deduced FOM values in the frequency range where the bandwidths of the two transducers overlapped. Results are shown for one such case in figure 77. For the FOM measurement of this billet coupon, the energy loss attenuation was assumed to be one-half of the measured back-surface attenuation. Since the FOM is, by definition, a property of the specimen alone, its measured value should be independent of the measurement details. This was found to be approximately true in practice, as illustrated by figure 77.

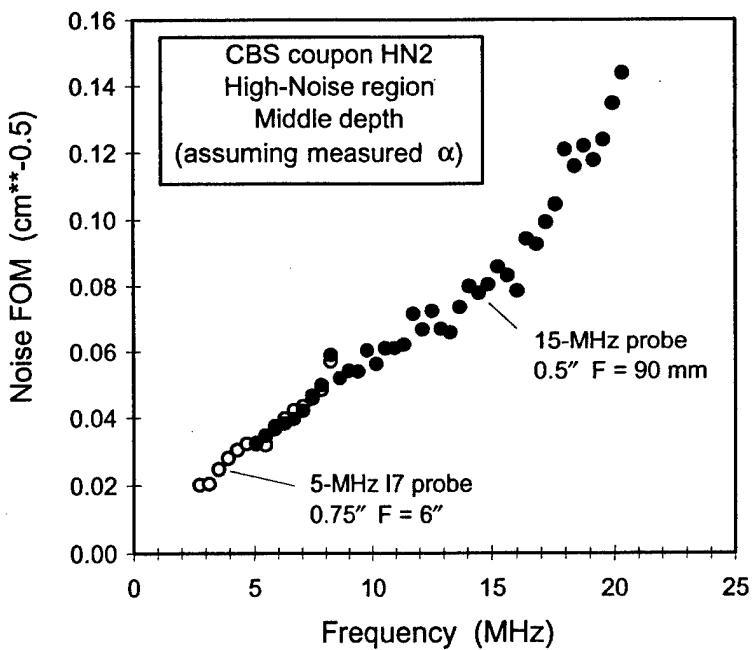


FIGURE 77. FOM VALUES DEDUCED FOR A Ti 6-4 BILLET SPECIMEN USING BOTH 5- AND 15-MHz FOCUSED PROBES

For the 14 specimens denoted A-N, figure 78 summarizes the results of the backscattered noise measurements. All of the measurements were performed in a similar manner using the 5-MHz focused probe identified in table 17. For each specimen and sound propagation direction, the figure displays the measured FOM value at 5 MHz, in the standard units used by the noise models [34]. For each case, a range of values is shown. The upper value assumes that the

energy-loss attenuation is the value measured using back-surface echoes. The lower value assumes that energy-loss attenuation is negligible. The actual FOM value will lie between these two extremes. The average noise level observed in a given measurement is directly proportional to the specimen's FOM value. Thus, figure 78 provides a snapshot of the relative noisiness of the various specimens studied. It can be directly compared to the earlier companion figure summarizing measured ultrasonic attenuations for the same specimens (figure 49).

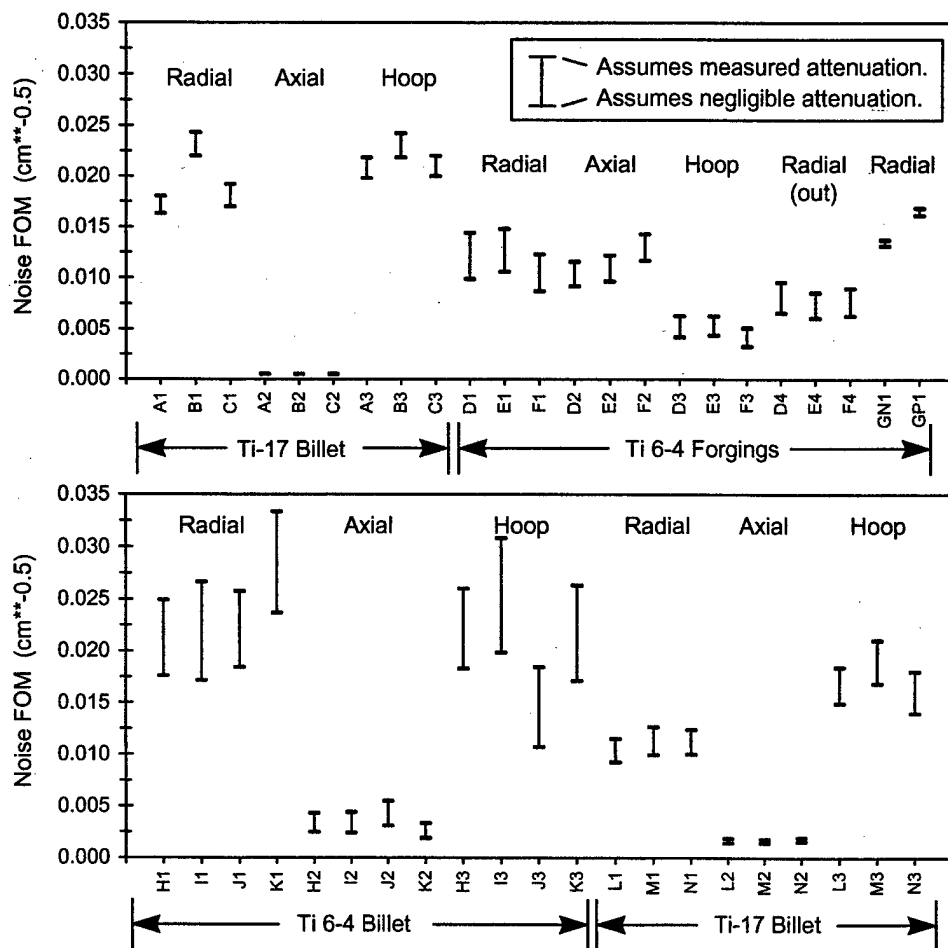


FIGURE 78. MEASURED FOM VALUES AT 5-MHz FOR 14 SPECIMENS,  
DEDUCED BY ANALYZING BACKSCATTERED NOISE A-SCANS  
ACQUIRED WITH A 5-MHz, F/8 TRANSDUCER

(The notation  $x_i$  on the abscissa scale indicates specimen  $x$ , sound propagation direction  $i$   
( $i=1, 2, 3, 4$  for radially inward, axial, hoop, radially outward, respectively).)

### 5.3.10 Summary of Backscattered Noise FOM Results.

The following points summarize the major findings of the backscattered noise survey:

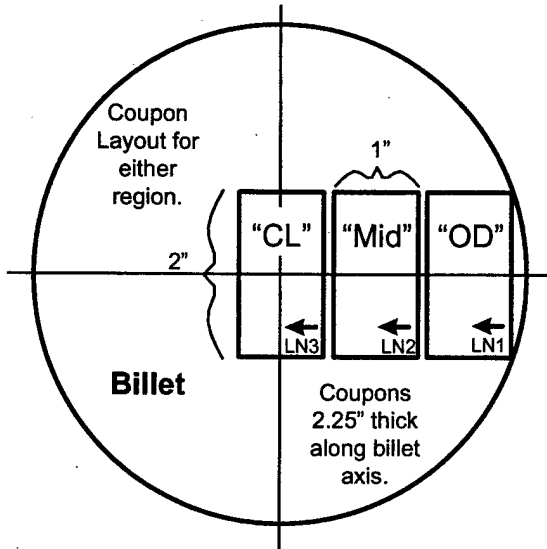
- Measured noise-FOM values tended to increase with frequency in an approximately linear manner. In some cases, the rate of increase was greater than linear; in others it was

less than linear. If one approximates the FOM-vs-frequency curve as a power law,  $FOM=Cf^P$ , then in the majority of cases the power  $P$  was between 0.5 and 1.5.

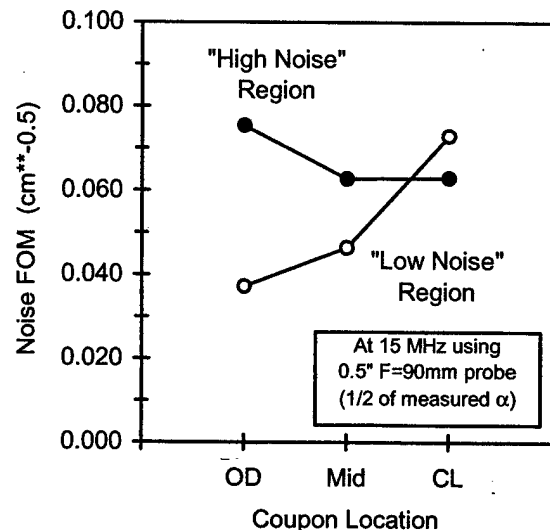
- b. The measured FOM values at a given frequency varied by about a factor of 20 within the set of specimens.
- c. For billets, the noise level was strongly dependent on propagation direction. The FOM for axial propagation was typically an order of magnitude lower than those for radial and hoop propagation.
- d. For forgings, the dependence of FOM on propagation direction was also significant, but not as severe as for billets.
- e. For both billets and forgings, the largest noise levels were seen when the beam traveled perpendicular to the elongation direction of the columnar macrograins or flow lines. Conversely, the smallest noise levels were seen when beam propagation was parallel to those microstructural features.
- f. The high-noise direction was generally the low attenuation direction, and the low noise direction was generally the high attenuation direction.

The last point above is intuitively surprising. The measured attenuation describes the loss of signal strength due to (1) the absorption and scattering of sound waves and (2) various beam-distortion effects. The sizes of backscattered grain noise echoes are one measure of the amount of beam energy lost to scattering as a sound beam propagates. Thus, one might expect the attenuation to be largest for the propagation direction in which the backscattered noise level is largest. This was not the case for the billet and forging specimens' studies. Again, this suggests that a large fraction of the measured attenuation arises from distortion effects, and that these effects are largest when the beam propagates along macrograins or flow lines.

In addition to the strong dependence on propagation direction, the FOM value was observed to vary with position within a given billet. These variations were most clearly seen when measurements were made on a series of smaller coupons removed from adjacent sites. For example, figure 79 displays the dependence of FOM on radial depth in one 6" diameter Ti 6-4 billet. In this case, coupons were removed at three depths from two sites on the billet, one site where the noise level near the OD was high and one site where it was low. These sites were indicated on the C-scan image of noise banding shown earlier in figure 72. The FOM results shown in figure 79(b) assume that the energy-loss attenuation is one-half of the measured back-surface attenuation. One sees that the FOM values for radial propagation vary by about a factor of two with position. It is also worth noting that the high- and low-noise sites switch as the radial depth increases; at the center of the billet, the higher noise site is the one for which the noise near the OD is lower.



(a)



(b)

FIGURE 79. DEPENDENCE OF NOISE ON RADIAL DEPTH AT HIGH- AND LOW-NOISE SITES ON A 6" DIAMETER Ti 6-4 BILLET (CBS BILLET COUPONS)

(a) COUPON LOCATION AND GEOMETRY (b) MEASURED FOM VALUES FOR RADIAL PROPAGATION

Measured velocity and attenuation values for these six coupons were shown earlier in figures 42(d) and 50, respectively. Again, one observes an inverse relationship between attenuation and FOM; the coupons with the highest attenuations tend to have the lowest FOMs and vice versa.

Systematic variations of FOM with depth were also seen in a similar study of a Ti-17 billet where small coupons at three depths were removed and studied. Since the ETC Phase I emphasis was on billet properties, no similar small-coupon studies of property variations in forgings were made. However it is likely that in forgings, as in billets, velocity, attenuation, and noise FOM vary systematically with depth for a fixed propagation direction.

### 5.3.11 Characteristics of Fixed-Time and Gated-Peak Noise Distributions.

In a typical inspection where the transducer is scanned above a component, the details of the backscattered noise A-scan vary rapidly with transducer position. Useful statistical measures of the noise A-scans can be defined in several ways. For example, the rms noise level, illustrated earlier in figure 75, provides a simple means for describing the depth dependence of the noise. In industrial settings, one often measures the peak-to-peak or rectified peak voltage within some preset time gate of interest. Measures of these gated-peak noise (GPN) voltages then play a role in the setting of flaw detection thresholds.

Attributes of the noise A-scans can be thought of as random variables governed by probability distributions (i.e., probability density functions). Two such attributes and their associated

distributions are described in table 18. Note that the fixed-time distribution  $p(v)$  will depend upon the noise arrival time, and the gated-peak distribution  $P(V_{pp})$  will depend upon the starting and ending times of the gate. The precise definition of  $p(v)$  is as follows:

$p(v)\Delta v$  = probability that the RF noise voltage (seen at some fixed sound arrival time) is between  $v$  and  $v + \Delta v$ .

TABLE 18. PROBABILITY DISTRIBUTIONS OF TWO NOISE ATTRIBUTES OF INTEREST

Noise Attribute	Meaning	Properties	Probability Density Function
$v(t)$ or $v$ for short	RF noise voltage observed at some fixed observation time, $t$ .	Can be positive or negative. Has mean of zero.	$p(v)$
$V_{pp}(t_a, t_b)$ or $V_{pp}$	The maximal peak-to-peak voltage of the portion of the noise signal that lies in the time gate bounded by $t_a$ , and $t_b$ .	Nonnegative	$P(V_{pp})$

$P(V_{pp})$  has a similar meaning for the GPN in some time gate of interest. Examples of fixed-time and gated-peak noise probability distributions are shown in the next two figures.

Figure 80 shows measured RF voltage distributions,  $p(v)$ , for two cases: a Ti 6-4 billet inspection and a Ti 6-4 forging inspection. In each case, the backscattered noise from the focal zone of the 5-MHz transducer was examined. For the billet case,  $p(v)$  was found to be nearly Gaussian about  $v=0$ . For the forging, however, the measured distribution was obviously non-Gaussian. When deviations from Gaussian behavior are seen, they generally follow the pattern of figure 80(b): there is a greater probability of observing both extreme voltages and voltages near zero than the Gaussian would predict. Note that the rms noise level introduced earlier is just the width (standard deviation) of the  $p(v)$  distribution. When moving away from the focal zone, the rms noise level drops, and hence, the distributions shown in figure 78 become narrower. They also tend to become more Gaussian in appearance.

Examples of gated-peak noise distributions,  $P(V_{pp})$ , measured using the 5-MHz, F/8-focused transducer, are shown in figure 81 for two specimens. These distributions depend upon the time gate endpoints, and the results are shown for three choices of the gate. Only a few hundred A-scans were examined in each case, so the measured distributions are not very smooth. However, the major trends are evident. As the gate is enlarged, the mean of the distribution shifts to the right because a wider gate affords a better opportunity to observe larger peak noise voltages. In one of the cases shown, the GPN distribution is seen to narrow as the gate is enlarged; in the other case, the distribution becomes broader.

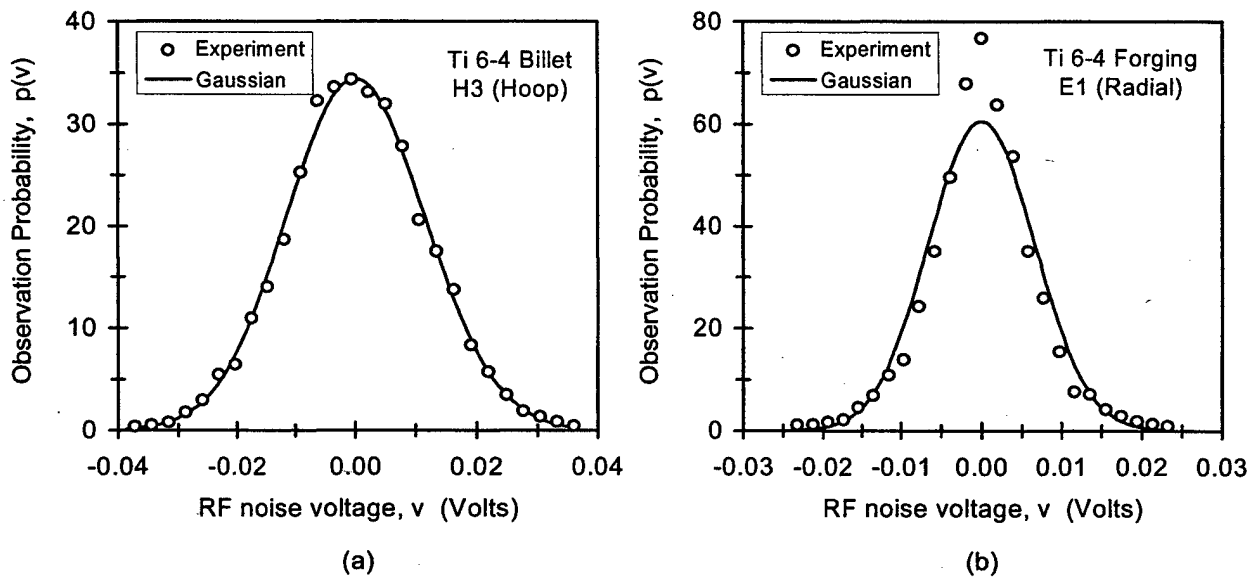


FIGURE 80. RF NOISE VOLTAGE DISTRIBUTIONS FOR BACKSCATTERED NOISE FROM THE FOCAL ZONE OF A 5-MHz, 3/4", F=6" TRANSDUCER (GAUSSIAN FUNCTIONS ARE SHOWN FOR COMPARISON) (a) Ti 6-4 BILLET SPECIMEN H AND (b) Ti 6-4 FORGING SPECIMEN E

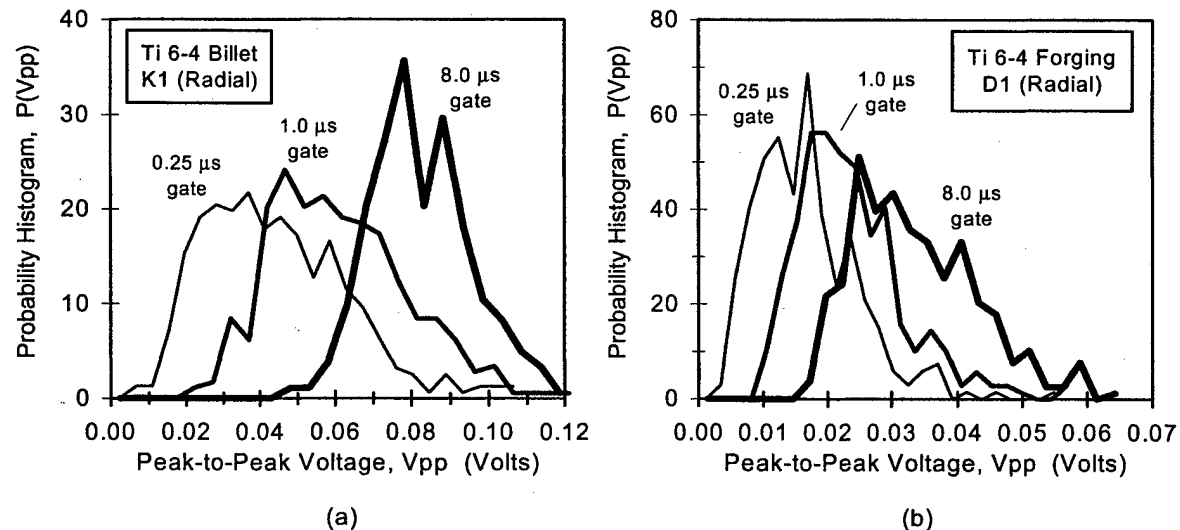


FIGURE 81. GATED-PEAK NOISE DISTRIBUTIONS FOR THREE TIME GATES HAVING DIFFERENT DURATIONS BUT THE SAME CENTER TIME (a) Ti 6-4 BILLET SPECIMEN K, RADIAL INSPECTION AND (b) Ti 6-4 FORGING SPECIMEN D, RADIAL INSPECTION

As discussed in appendix B, the fixed-time and gated-peak noise distributions play important roles in the noise models. In particular,  $P(V_{pp})$  is predicted from  $p(v)$ , which, in turn, is predicted from knowledge of the measurement system and the specimen properties (velocity, attenuation,

and noise FOM). Thus, an understanding of the general relationship between RF noise voltage ( $v$ ) and gated-peak noise voltage ( $V_{pp}$ ) was crucial for model development.

To support the modeling efforts, the noise A-scans originally acquired to determine the FOM values of specimens A-N were re-examined. Various statistical measures of these A-scans were computed (including rms noise levels and moments of the fixed-time and gated-peak noise distributions), and their relationships to one another were studied. That work is described in detail in reference 35 and two of the principal conclusions are summarized below.

One key finding was the close relationship between rms noise and average gated-peak noise (i.e., between the width of  $p(v)$  and the mean of  $P(V_{pp})$ ). That relationship is demonstrated in figure 82. Figure 82(a) displays the dependence of the average gated-peak noise voltage on the choice of gate center time for forging specimen F. Results are shown for two choices of gate duration, and the rms noise level is shown for comparison. Note the very similar depth dependencies of the rms noise and average gated-peak noise (denoted by  $\langle V_{pp} \rangle$ ). When unnormalized, both noise measures peak in the focal zone, with the value of the  $\langle V_{pp} \rangle$  dependent on the duration of the gate. Figure 82(b) further illustrates the relationship between average gated-peak noise and average rms noise for time gates centered in the focal zone. Specimens A-N were examined, and the results are shown for three choices of the gate duration. For a given duration, there is one plotted point in figure 82(b) for each specimen/side combination. Note the near proportionality between the average gated peak noise and the rms noise level (averaged over the duration of the time gate). The constant of proportionality depended on the gate duration, but it was relatively independent of the specimen studied or the inspection direction. This finding gave credence to the notion that  $P(V_{pp})$  attributes could be predicted from knowledge of  $p(v)$ .

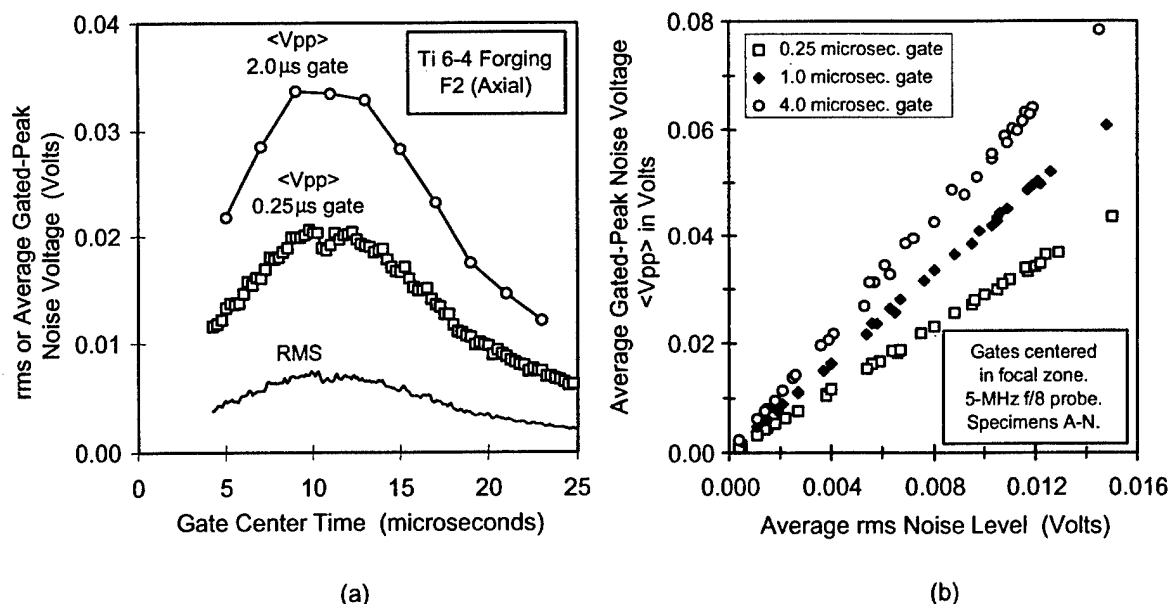


FIGURE 82. RELATIONSHIP BETWEEN GATED-PEAK NOISE AND rms NOISE IN 5-MHz FOCUSED INSPECTIONS

A second key finding of the noise survey concerns the degree to which fixed-time RF noise voltage distributions are Gaussian for typical inspections of engine titanium alloys. As discussed in appendix B, two models for predicting gated-peak noise distributions were developed. The so-called second-generation model assumes that all  $p(v)$  distributions are Gaussian for localized regions when the microstructure is relatively uniform. The third-generation model, on the other hand, allows  $p(v)$  to be non-Gaussian. The second-generation model is much easier to implement, because it requires only the lowest order microstructural factor (FOM), which can be measured in a straightforward manner. The third-generation model requires both FOM and a higher-order factor (FOM') which is much harder to measure in practice.

From general statistical arguments, the fixed-time noise distribution is expected to be nearly Gaussian if a sufficient number of scatterers (grain boundaries) contribute appreciably to the RF noise voltage at the observation time in question. Thus, whether or not  $p(v)$  is Gaussian will depend upon the density of scatterers and the volume of the incident ultrasonic pulse. Since the pulse volume is smallest in the focal zone,  $p(v)$  is least likely to be Gaussian in the focal zone of a tightly focused transducer.

How Gaussian are the fixed-time RF noise distributions for typical 5-MHz inspections? The stored noise A-scans for the 5-MHz, F/8, focused probe inspections of specimens A-N were re-examined to answer this question. In particular, the second and fourth moments of the RF noise voltages in the vicinity of the focal zone were examined to extract a dimensionless parameter M, which describes the shape of the  $p(v)$  distribution near the focus. The precise meaning of M is discussed in reference 35 and need not be concerned here. It is sufficient to know that  $p(v)$  is very Gaussian-like for  $1/M < 0.1$ , not too far from Gaussian for  $0.1 < 1/M < 0.2$ , and noticeably non-Gaussian for  $1/M > 0.2$ .

Figure 83 shows the measured values of the parameter M in the focal zone for 5-MHz inspections of the 14 specimens listed in figure 34. The letters A-N, GN, and GP designate the specimens, and the numbers 1-4 designate inspection directions (1,2,3,4=radially inward, axial, hoop, radially outward, respectively). All measurements were made with a 5-MHz F/8 transducer except for cases GN15 and GP15 which used a 15-MHz, 0.5" F=90 mm probe. For axial inspections of billet specimens, the backscattered noise levels were too small, relative to electronic noise levels, to permit trustworthy determinations of M. However, M could be readily determined for radial and hoop inspections of the billet specimens and was generally found to be in or near the Gaussian regime. This indicates that it should be possible to use the second-generation noise model of appendix B, suitably modified to treat noise banding, to accurately predict noise properties for typical 5-MHz titanium billet inspections.

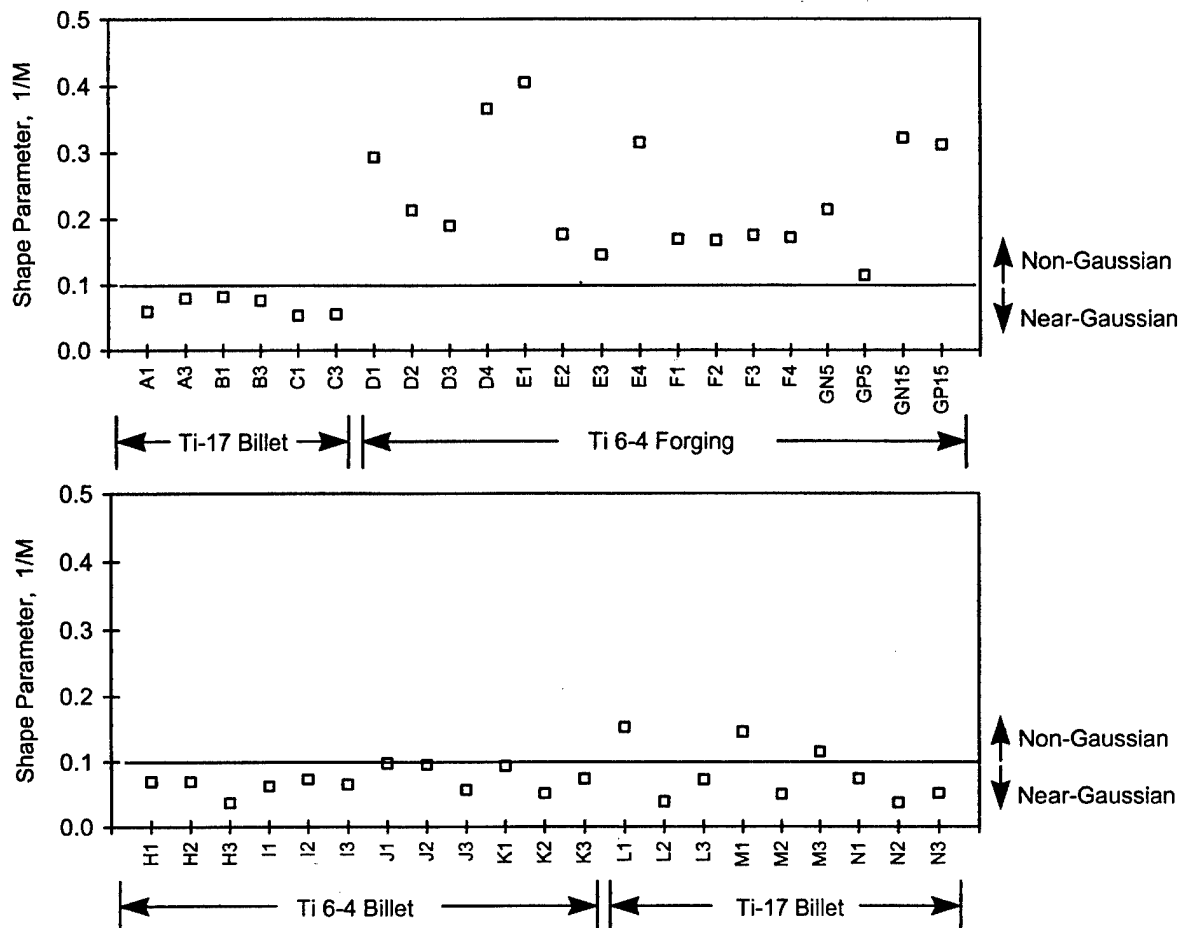


FIGURE 83. VALUE OF THE SHAPE PARAMETER M OBTAINED BY FITTING A K-DISTRIBUTION TO THE MEASURED RF NOISE VOLTAGE DISTRIBUTION  $p(v)$  NEAR THE FOCAL ZONE. THE  $p(v)$  DISTRIBUTION IS NEARLY GAUSSIAN WHEN M IS LARGE (i.e.,  $1/M$  NEAR OR BELOW 0.1).

The situation is different, however, for the forging specimens studied. Non-Gaussian RF noise voltage distributions were seen in the majority of cases for the 5-MHz focused inspection and for two additional 15-MHz focused inspections. Some of this non-Gaussian behavior is likely due to the fact that the forging specimens were larger (typically 6" cubes), emphasizing the variations of microstructure with position. An overall non-Gaussian distribution can be obtained by mixing two or more Gaussian distributions with different widths (i.e., different rms noise levels). But a portion of the non-Gaussian behavior likely arises because only a small number of dominant scatterers typically occupy the pulse volume. Such behavior is demonstrated in figure 84, where  $1/M$  is displayed as a function of noise arrival time for 15-MHz inspections of two regions of a forging specimen. In this case, the backscattered noise was relatively independent of position in each region, so distribution mixing was not a factor. One sees that  $1/M$  varies systematically with time (or depth). There is Gaussian behavior away from the focal zone, but non-Gaussian behavior in the focal zone. This behavior is quite understandable since the volume of the ultrasonic pulse shrinks as the focal zone is approached.

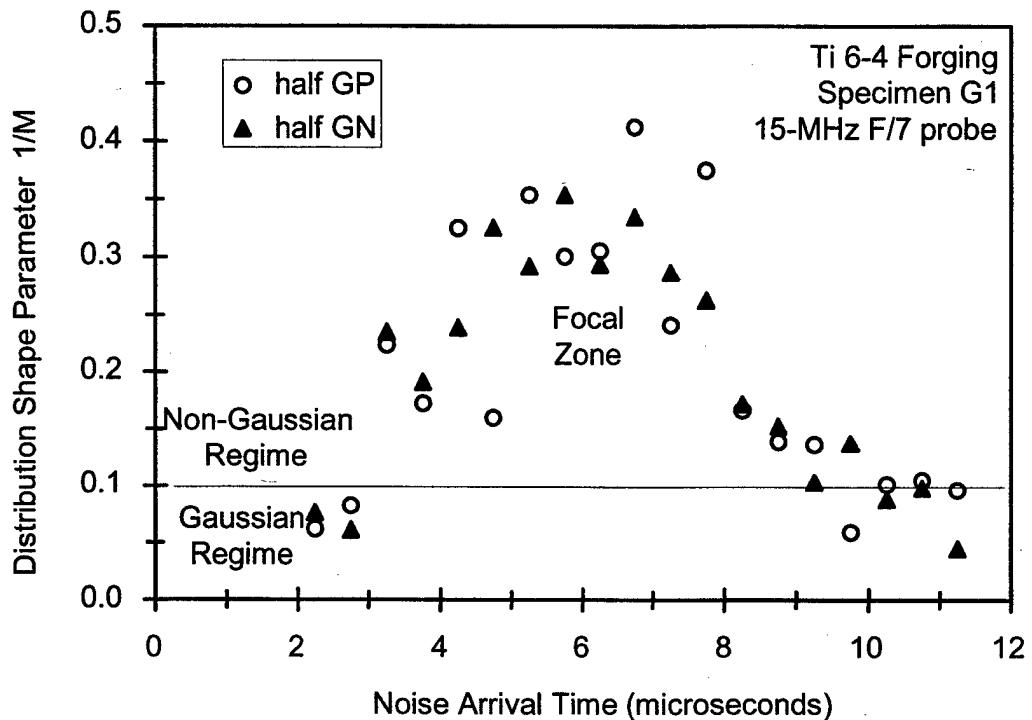


FIGURE 84. NOISE DISTRIBUTION SHAPE PARAMETERS FOR 15-MHz FOCUSED-PROBE INSPECTIONS OF THE P AND N HALVES OF Ti 6-4 FORGING SPECIMEN G AS FUNCTIONS OF THE NOISE ARRIVAL TIME

In summary, the noise-attribute survey suggests that the second-generation noise model is likely to be sufficient for simulating typical 5-MHz billet inspections. However, the third-generation model is probably required for accurate predictions of gated-peak noise distributions in forgings and for billet inspections at higher frequencies. Note that when non-Gaussian behavior is present, the second-generation noise model is still of some use. The close relationship between rms noise and average gated-peak noise (figure 82) suggests that the second-generation model can still make accurate predictions of average gated-peak noise. However, other attributes of GPN distributions, such as standard deviations or the tail locations, will not be well predicted by the second-generation model when non-Gaussian behavior occurs.

### 5.3.12 Noise Distribution Summary: Implications for Inspections.

Backscattered noise survey measurements were carried out on 14 billet and forging specimens using a 5-MHz F/8-focused transducer. Follow-up measurements with a 15-MHz F/7 probe were made on selected specimens. The contribution of the microstructure to the noise is contained in a factor known as the FOM; the larger the FOM, the greater the observed noise. FOM values were measured as a functions of frequency for sound propagation in the radial, axial, and hoop directions of the coupons. It was found that:

- For a fixed specimen and inspection direction, the FOM rose with frequency in an approximately linear fashion;

- b. For a given specimen, the FOM was strongly dependent on inspection direction with a weaker but significant dependence on depth or lateral position (e.g., noise banding);
- c. The highest noise levels were seen when the sound beam propagated perpendicular to the long dimension of the columnar macrograins (billets) or flow lines (forgings);
- d. In billets there was typically an order of magnitude difference in the FOM values for the low-noise (axial) and high-noise (radial, hoop) directions.

Attenuation deduced from back-surface echoes, e.g., the propagation direction for which the noise level was the lowest, was the direction for which the measured attenuation was the highest. This suggests that a large fraction of the measured attenuation arises from beam distortion effects, and that these effects are largest when the beam propagates along macrograins or flow lines.

In addition to the FOM survey work, backscattered noise A-scans in billets and forgings were examined to determine the degree to which certain distributions of RF noise voltages were Gaussian. That work indicates that the second-generation noise model of appendix B (which has been distributed to ETC members as a software package) is likely to be reasonably accurate for typical 5-MHz radial inspections of billets. However, the third-generation model still under active development is likely to be required for forging inspections and for billet inspections at higher frequencies.

## 6. SUMMARY AND CONCLUSIONS.

Because of the key role that titanium alloys play in the integrity of critical rotating engine components for jet engine applications, they are typically ultrasonically inspected several times during the production process. However, titanium is an ultrasonically noisy material that can lead to false indications or missed flaws. In an effort to understand the relationship between microstructure and detectability, the Engine Titanium Consortium completed an extensive study of the fundamental properties of titanium materials. The ability to detect hard alpha inclusions depends primarily on (1) the relative ultrasonic impedances of hard alpha material and unflawed host metal and (2) the crystalline microstructure of the host. The first determines the size of an ultrasonic echo from a hard alpha defect, and the second determines the size of competing noise echoes scattered from grain boundaries. Titanium alloys representative of those used in the manufacture of aircraft engines were identified for this study and appropriate amounts of the material procured. The materials chosen were Titanium 6-4 (Ti-6 wt.% Al-4 wt.% V) and Titanium 17 (Ti-5 wt.% Al-2 wt.% Sn-2 wt.% Zr-4 wt.% Cr-4 wt.% Mo), which provide examples of alpha-stabilized and beta-stabilized alpha-beta alloys respectively. Material procured from industrial participants, and from their suppliers, was used to prepare samples with known defect conditions. The parent materials were also studied to provide baseline information on NDE characteristics. Key accomplishments and findings include the following:

- Synthetic hard alpha (SHA) material, essentially Ti-N-O alloys, can be manufactured by either powder metallurgical or arc-melting techniques. Batches of such SHA material with nitrogen contents ranging from 1.5 to 16.2 wt.% were made for basic property measurements and for insertion as defects into HIPped test specimens.

- The ultrasonic reflectance of a hard alpha inclusion in a titanium alloy host depends on the difference in impedance (product of sound velocity and density) between the two materials. For each 1 wt.% increase in nitrogen content, the longitudinal sound speed of SHA increases by about 3% and the density increases by 1%. The reflectance of hard alpha in a Ti alloy host rises approximately linearly from zero at 0 wt.% N to 0.14 at 10 wt.% N.
- Uncracked, cylindrically shaped SHA inclusions in Ti alloy host material could be imaged and detected with compositions as low as 1.5 wt.% N. The signal-to-noise ratio for such inclusions rose linearly as the nitrogen content was increased.
- Titanium alloys are ultrasonically anisotropic within a single metal grain or within a colony of aligned grains. A plate of Ti 6-4 alloy with very large alpha-grain colonies was produced to study this anisotropy. The minimum longitudinal sound velocity (0.6063 cm/ $\mu$ s) was measured in a colony whose hexagonal symmetry axis was perpendicular to the direction of sound propagation. The maximum sound velocity (0.6712 cm/ $\mu$ s) was measured for propagation parallel to the symmetry axis. The anisotropy in longitudinal sound velocity in Ti 6-4 was roughly twice that reported for pure titanium.
- The above study of velocity anisotropy in the enlarged grain block suggests that uncracked hard alpha inclusions with compositions less than 3 wt.% N might not be detectable if present in a region of large alpha colonies. Based on the measured velocities, the ultrasonic reflectance at the boundary between two alpha-titanium colonies can be as high 0.051. This value exceeds the typical reflectance of uncracked hard alpha inclusions with less than 3 wt.% N (see bullet 2 above). Thus signals from such inclusions could be masked by ultrasonic grain-boundary echoes.
- Ultrasonic property measurements were carried out on rectangular coupons cut from representative Ti-17 and Ti 6-4 billets and forgings. Longitudinal wave velocity, attenuation, and backscattered noise figure-of-merit (FOM) were systematically measured for the radial, axial, and hoop propagation directions in 14 coupons labeled A-N. Additional measurements using these and a dozen other specimens were then made to further investigate the effects of titanium microstructure on ultrasonic (UT) inspections.
- For a given coupon, all measured properties showed a dependence on propagation direction. As shown in table 19, this dependence was generally greatest for backscattered noise, less (but still large) for attenuation, and smallest for velocity. There were also large noise and attenuation differences between coupons from different sources.
- Smaller coupons cut from six different locations in a single Ti 6-4 billet revealed that for a fixed inspection direction (radially inward) the ultrasonic properties varied systematically with radial depth and angular position. The variations were 1.5% for velocity, 200% for grain noise FOM, and 250% for attenuation.
- Attenuation and backscattered noise depended strongly on frequency (f) while velocity did not. If the dependence on frequency is approximated as a power function,  $cf^p$ , then

for attenuation,  $p$  typically ranged from 1 to 2 and for noise FOM,  $p$  typically ranged from 0.5 to 1.5.

- Attenuation and backscattered noise exhibited opposite dependencies on propagation direction within a given coupon. Attenuation was highest and noise FOM was lowest when sound propagated parallel to macrograin elongation (billets) or flow lines (forgings). Conversely, attenuation was lowest and noise highest for propagation perpendicular to macrograins or flow lines.
- Beam mapping measurements revealed that the titanium microstructure could cause significant distortion of the sonic amplitude and phase profiles. These distortions were worse for propagation along macrograins and worse at higher frequencies. They affected all types of ultrasonic measurements.
- When beam distortions were large, there were significant fluctuations in the ultrasonic signal amplitudes of nominally identical reflectors. In addition, different methods for measuring attenuation yielded different results. For example, the average attenuation of back-surface echoes was larger than that expected due to energy loss alone and different from the attenuation deduced from FBH echoes.
- In current billet inspection procedures, 5-MHz transducers are used and the sonic beam travels radially inward, perpendicular to the columnar macrograins. Thus, the effects of beam distortion on the inspection are generally modest. However, beam distortion effects may significantly degrade inspections at higher frequencies, particularly Ti forging inspections at locations where the sound beam is not perpendicular to the flow lines.
- Some models for predicting backscattered noise attributes assume Gaussian noise statistics at each fixed observation time. The noise measurements indicate that these models should be applicable to 5-MHz titanium billet inspections. One such model was in fact used for detection reliability studies by the ETC POD subtask.

TABLE 19. VARIABILITY OF MEASURED ULTRASONIC PROPERTIES IN COUPONS A-N

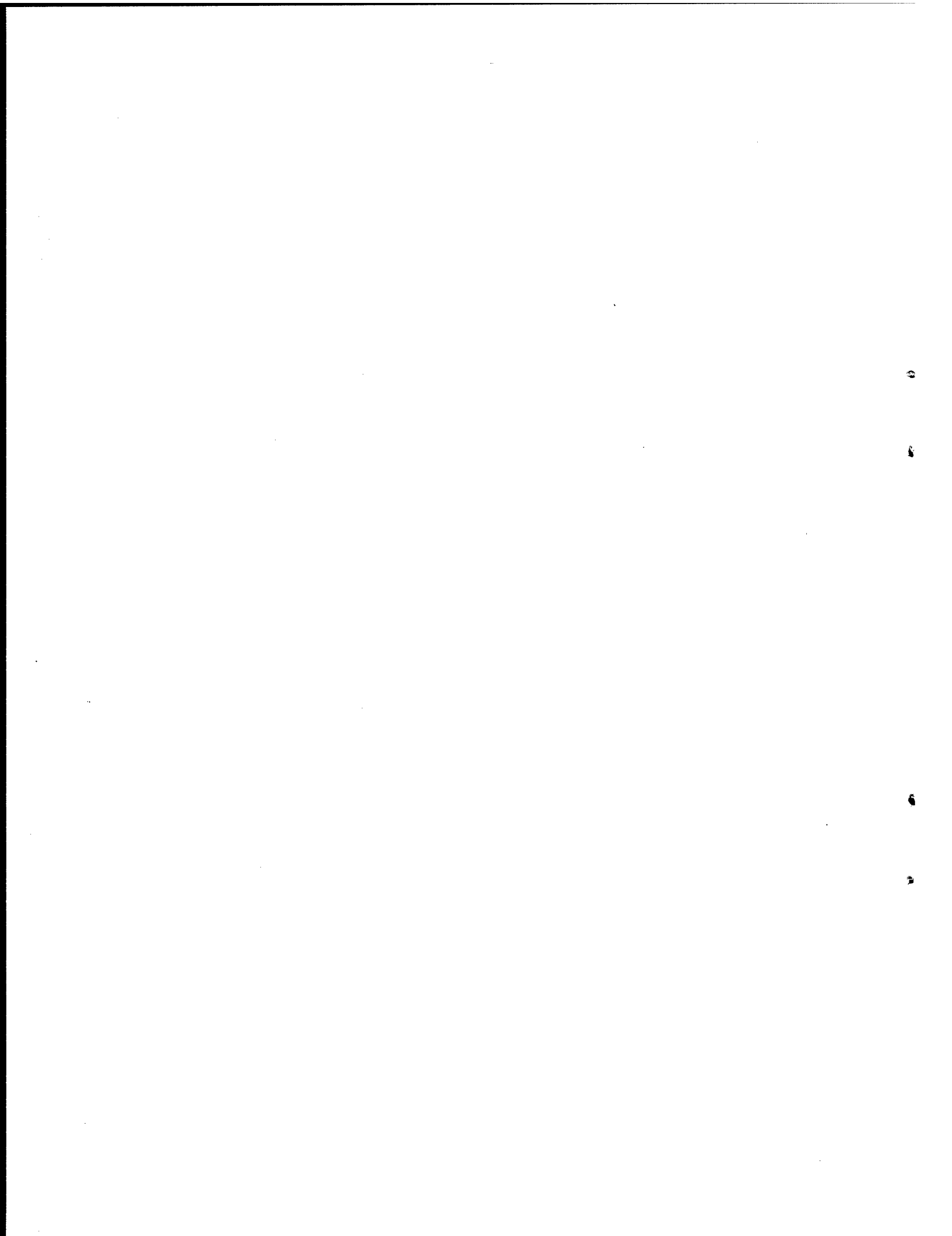
	Fixed Coupon Dependence on Direction	Range of Values Within Suite of 14 Specimens
Velocity at 5 or 10 MHz	Up to 1%	0.604 cm/ $\mu$ s $\pm$ 0.7% (Ti-17) 0.621 cm/ $\mu$ s $\pm$ 0.7% (Ti 6-4)
Attenuation at 5 MHz	Up to factor of 3	0.2 to 2 dB/inch
Noise FOM at 5 MHz	Up to factor of 20	0.001 to 0.035 cm <sup>-0.5</sup>

## 7. REFERENCES.

1. W.P. Conrardy, "Titanium-6Al-4V Low Density Inclusion Problem," TM-MAA-66-20, Air Force Materials Laboratory, Wright-Patterson Air Force Base, OH, 1966.
2. J.F. Wildey, "Focus on Mechanical Failures: Mechanism and Detection," Vibration Institute, Willowbrook, IL, 1991, pp. 3-12.
3. M. Gigliotti, L. Perocchi, and R. Gilmore, "Metallurgical and Materials Transactions A," Vol. 25A, November 1994, pp. 2321-2329.
4. J.L. Murray, "Phase Diagrams of Binary Titanium Alloys," ASM International, Metals Park, OH, 1987.
5. E.M. Grala, "Characterization of Alpha Segregation Defects in Ti-6Al-4V Alloy," AFML-TR-68-304, Air Force Materials Laboratory, Wright-Patterson Air Force Base, OH, 1968.
6. F.W. Wood, "Elimination of Low-Density Inclusions in Titanium Alloy Ingots," AFML-TR-69-47, Air Force Materials Laboratory, Wright-Patterson Air Force Base, OH, 1969.
7. F.J. Vicki, "Titanium Science and Technology," Plenum Press, New York, 1973, pp. 733-741.
8. E. Nieters, R. Gilmore, D. Copley, and P. Howard, "Review of Progress in Quantitative Nondestructive Evaluation," Vol. 14, Plenum Press, NY, 1995, pp. 2137-2144.
9. J.E. Allison, P.A. Russo, S.R. Seagle, and J.C. Williams, "Titanium Science and Technology," Deutsche Gesellschaft für Metallkunde E.V., Oberursel, 1984, pp. 909-916.
10. F.R. Billman and F. F. Rudolph, "Titanium Science and Technology," Plenum Press, New York, 1973, pp. 693-705.
11. B. Ginty, P. Hallam, C. Hammond, G. Jackson, and C. Robb, "Titanium '80 Science and Technology," *The Metallurgical Society of AIME*, Warrendale, PA, 1980, pp. 2095-2103.
12. H. Takatori, "Sixth World Conference on Titanium, Les Éditions de Physique," Cedex, France, 1988, pp. 773-778.
13. L. Stone and H. Margolin, "Transactions Metals Branch AIME," 1953, 197, pp. 1498-1502.
14. E.P. Papadakis, "Physical Acoustics," Vol. 11, Academic Press, New York, 1975, pp. 151-211.
15. F.J. Margetan, Kim Han, and R.B. Thompson, "Density and Ultrasonic Velocity Measurements for Synthetic Hard Alpha Titanium Specimens," Report ISU/ETC-1, ISU Center for NDE, Ames, IA, April 1994.

16. B. Derby, et al., *Journal of Materials Science*, Vol. 18, No. 8, 1983, p. 2345.
17. R.D. Weglein, "Ultrasonics Symposium Proceedings," Vol. 2, IEEE, Piscataway, NJ, 1988, P.1045.
18. R.B. Thompson, et al., "Ultrasonics Symposium Proceedings," Vol. 2, IEEE, Piscataway, NJ, 1989, p. 1117.
19. O. Buck, et al., "Metallurgical Transactions A," Vol. 20A, No. 4, 1989, p. 627.
20. G.C. Ojard, et al., in "Ultrasonic Characterization and Mechanics of Interfaces," Vol. 177, ASME, New York, NY, 1993, p. 183.
21. N. Hsu and H. Conrad, "Scripta METALLURGICA," 1971, 5, pp. 905-908.
22. E. S. Fisher and C. J. Renken, "Single Crystal Elastic Moduli and the hcp—bcc Transformation in Ti, Zr, and Hf," *Physical Review*, 135, A482-A494, 1964.
23. Robert S. Gilmore, GE Research and Development Center, Schenectady, NY, private communication.
24. P.D. Panetta, F.J. Margetan, I. Yalda, and R.B. Thompson, "Ultrasonic Attenuation Measurements in Jet-Engine Titanium Alloys," in *Review of Progress in QNDE*, Vol. 15B, D.O. Thompson and D.E. Chimenti, eds., Plenum, New York, 1996, p. 1735.
25. P.D. Panetta, F.J. Margetan, I. Yalda, and R.B. Thompson, "Observation and Interpretation of Microstructurally Induced Fluctuations of Back-Surface Signals and Ultrasonic Attenuation in Titanium Alloys," *ibid.*, Vol. 16B, 1997, p. 1547.
26. F.J. Margetan, R.B. Thompson, I. Yalda-Mooshabad, and Y.K. Han, "Detectability of Small Flaws in Advanced Engine Alloys," ISU Center for NDE, July 1993. See section III.B.5 for a discussion of attenuation measurements.
27. J.M.M Pinkerton, "A Pulse Method for the Measurement of Ultrasonic Absorption in Liquids: Results for Water," *Nature* 160, 1947, p. 128.
28. F.J. Margetan, I. Yalda, P.D. Panetta, K. Han, and R.B. Thompson, "A Study of the Relationship Between Velocity Variations and Measured Ultrasonic Attenuation in the Ti 6-4 Enlarged Grain Block," Report ISU/ETC-9, Center for Nondestructive Evaluation at Iowa State University.
29. F.J. Margetan, P.D. Panetta, and R.B. Thompson, "Ultrasonic Signal Attenuation in Engine Titanium Alloys," in *Review of Progress in QNDE*, Vol. 17, D.O. Thompson and D.E. Chimenti, eds., Plenum, New York, in preparation.
30. A. Minachi, F.J. Margetan, and D.K. Hsu, "Delamination Sizing in Composite Materials Using the Gauss-Hermite Beam Model," *Ultrasonics*, Vol. 31, No. 4, 1993, p. 237.

31. F.J. Margetan, H. Wasan, and R.B. Thompson, "An Experimental Study of Microstructure-Induced Ultrasonic Signal Fluctuations in Jet-Engine Titanium Alloys," *Review of Progress in QNDE*, 19, D. O. Thompson and D. E. Chimenti, eds., AIP, N.Y., 2000, pp. 1433-1440.
32. S. Ahmed, R. Roberts, and F. Margetan, "Ultrasonic Beam Fluctuation and Flaw Signal Variance in Inhomogeneous Media," *Review of Progress in QNDE*, 19, D.O. Thompson and D. E. Chimenti, eds., AIP, N. Y., 2000, pp. 985-992.
33. F.J. Margetan, R.B. Thompson, I. Yalda-Mooshabad, and Y.K. Han, "Detectability of Small Flaws in Advanced Engine Alloys," ISU Center for NDE, July 1993.
34. F.J. Margetan, R.B. Thompson, and I. Yalda-Mooshabad, "Backscattered Microstructural Noise in Ultrasonic Toneburst Inspections," *Journal of Nondestructive Evaluation*, Vol. 13, September 1994, pp. 111-136.
35. I. Yalda, F.J. Margetan, K.Y. Han, and R.B. Thompson, "Survey of Ultrasonic Grain Noise Characteristics in Jet Engine Titanium," *Review of Progress in QNDE*, 15, D.O. Thompson and D.E. Chimenti, eds., Plenum Press, N.Y., 1996, pp. 1487-1494.



## APPENDIX A—ULTRASONIC TEST SPECIMENS

The ETC Fundamental Studies Team was responsible for manufacturing several dozen ultrasonic test specimens in addition to those listed earlier in section 5.1. These are briefly summarized in the tables A-1 through A-6. In addition to the stamped or etched serial numbers, the tables list (in square brackets) the shorthand designations that are used for selected specimens within the text of section 5.3, e.g., A for specimen BC8535A.

There are six major categories of ultrasonic specimens, each summarized in a separate table. The ultrasonic property blocks (table A-1) were primarily used for basic measurements of velocity, attenuation and backscattered grain noise. Rectangular blocks containing arrays of flat-bottomed hole (FBH) defects (table A-2) or synthetic hard alpha defects (tables A-3 and A-4) were primarily used by the ETC Inspection Reliability Task Group to validate ultrasonic models and methodologies used in making probability of detection estimates A-1. Chord specimens, each containing FBHs located beneath a cylindrically curved entry surface (table A-5), were designed to assess defect detectability in billets for various transducer designs. Finally, there were several miscellaneous specimens (table A-6). Chief among these in importance are the Enlarged Grain Block discussed in sections 5.2 and 5.3 of this report, and the Random Defect Block whose design and use are described in the final report of the ETC Inspection Reliability Task Force [A-1].

In addition to the ultrasonic test specimens described in tables A-1 to A-6, the ETC Fundamental Studies Group was responsible for the manufacture of approximately 40 eddy-current test specimens, principally Ti 6-4 specimens containing notches to simulate surface-breaking cracks. Descriptions of these specimens and their uses can be found in the final report of the ETC Eddy-Current Inservice Inspection Group A-2.

TABLE A-1. RECTANGULAR BLOCKS FROM BILLETS AND FORGINGS USED FOR  
BASIC ULTRASONIC PROPERTY MEASUREMENTS

Material	Specimen Description	Serial Numbers
Ti-17 billet	Three-blocks of (average) thickness 1.3" cut from three different radial locations in a 9" diameter Ti-17 billet.	BC8535A (near center) [A] BC8535B (near OD) [B] BC8535C (intermediate) [C]
Ti 6-4 forging	Three 6" cubes cut from different angular positions (but similar radial positions) in a large ring forging.	940106 NA [D] 940106 NB [E] 940106 NC [F]
Ti 6-4 billet	Four 3" cubes cut from different positions in a 9.25" diameter billet. Two specimens were cut from the center of the billet at different axial positions. Two were cut from the OD region at different axial and angular positions.  A 3 x 3 array of #1 FBHs was later drilled into one face of specimen H (for radially-inward propagation).	022594-1 (OD) [H] 022594-2 (center) [I] 022594-3 (OD) [J] 022594-4 (center) [K] (022594-2 was subsequently sliced into two pieces of thickness 1" and 2", respectively, and re-designated as Q for additional attenuation measurements.)
Ti-17 billet	Three 3" cubes cut from different positions in a 7" diameter billet. One cube centered on the billet axis; two cubes having one face near the OD. 3 x 3 arrays of #1 FBHs were later drilled into three orthogonal faces of specimen L.	052094-1 (near OD) [L] 052094-2 (near OD) [M] 052094-3 (near center) [N]
Ti 6-4 forging	Three 3" cubes cut from different locations in a large forged disk: one from aft rim; one from forward rim; one from web. 3 x 3 arrays of #1 FBHs were later drilled into two faces of specimen U (for axial and radial sound propagation).	060394-1 (aft rim) [U] 060394-2 (forward rim) 060394-3 (web)
Ti-17 billet	Eight 3" cubes cut from different locations in a 13"-diameter billet. Specimens 1-4 are from the same baloney slice of the billet: two specimens from the OD region, one from the center of the billet, and one from midradius. Specimens 5-8 are at corresponding positions in a different baloney slice that has been rotated 45-degrees with respect to the first.	012795-1 (near OD) 012795-2 (near center) [P] 012795-3 (midradius) 012795-4 (near OD) 012795-5 (near OD) 012795-6 (near center) 012795-7 (midradius) 012795-8 (near OD) (Specimen P was subsequently sliced into two pieces of thickness 1" and 2", respectively, for additional attenuation measurements.)
Powdered Ni alloy (R88)	6" x 3" x 3" block with 3 x 3 array of #1 FBH's drilled 0.25" deep into one face. Served as a low-attenuation reference block for FBH echo measurements in blocks H, L, and U above.	(none)

TABLE A-2. RECTANGULAR BLOCKS FROM TITANIUM FORGINGS CONTAINING ARRAYS OF FLAT BOTTOMED HOLES

Material	Specimen Description	Serial Numbers
Ti 6-4	Block with 16 each #1, #2, #3, and #4 FBHs at 1" depth, oriented for normal-incidence longitudinal inspection. [GE block manufactured prior to ETC.]	901004-1L [Denoted as specimen G]
Ti 6-4	Block with 8 each #1, #2, #3, and #4 FBHs at 1" depth, oriented for normal-incidence longitudinal inspection.	F931213-1.5L
Ti 6-4	Block with 8 each #1, #2, #3, and #4 FBHs at 2" depth, oriented for normal-incidence longitudinal inspection.	F931213-2.5L
Ti 6-4	Block with 8 each #1, #2, #3, and #4 FBHs at 1" depth, oriented for 45-degree angle-beam inspection.	F931213-1.5S
Ti 6-4	Block with 8 each #1, #2, #3, and #4 FBHs at 2" depth, oriented for 45-degree angle-beam inspection.	F931213-2.5S
Ti-17	Block with 8 each #1, #2, #3, and #4 FBHs at 1" depth, oriented for normal-incidence longitudinal inspection.	F950508-1.5L
Ti-17	Block with 8 each #1, #2, #3, and #4 FBHs at 2" depth, oriented for normal-incidence longitudinal inspection.	F950508-2.5L
Ti-17	Block with 8 each #1, #2, #3, and #4 FBHs at 1" depth, oriented for 45-degree angle-beam inspection.	F950508-1.5S
Ti-17	Block with 8 each #1, #2, #3, and #4 FBHs at 2" depth, oriented for 45-degree angle-beam inspection.	F950508-2.5S

TABLE A-3. RECTANGULAR BLOCKS FROM TITANIUM FORGINGS CONTAINING ARRAYS OF CYLINDRICAL SYNTHETIC HARD ALPHA INCLUSIONS

Material	Specimen Description	Serial Numbers
Ti 6-4	Block with 8 each #2, #3, #4, and #5 FBH size cylindrical hard alpha inclusions of 1.6 wt.% nitrogen concentration at 1" and 2" depth. Inclusions oriented for normal-incidence longitudinal inspection.	S940119-1.6N
Ti 6-4	Block with 8 each #2, #3, #4, and #5 FBH size cylindrical hard alpha inclusions of 2.6 wt.% nitrogen concentration at 1" and 2" depth. Inclusions oriented for normal-incidence longitudinal inspection.	S940128-2.6N
Ti 6-4	Block with 8 each #2, #3, #4, and #5 FBH size cylindrical hard alpha inclusions of 5.9 wt.% nitrogen concentration at 1" and 2" depth. Inclusions oriented for normal-incidence longitudinal inspection.	S940217-5.9N
Ti 6-4	Block with 8 each #2, #3, #4, and #5 FBH size cylindrical hard alpha inclusions of 1.5 wt.% nitrogen concentration at 1" and 2" depth. Inclusions oriented for 45-degree angle-beam inspection.	SA940513-1.5N
Ti 6-4	Block with 8 each #2, #3, #4, and #5 FBH size cylindrical hard alpha inclusions of 2.8 wt.% nitrogen concentration at 1" and 2" depth. Inclusions oriented for 45-degree angle-beam inspection.	SA940512-2.8N
Ti 6-4	Block with 8 each #2, #3, #4, and #5 FBH size cylindrical hard alpha inclusions of 5.2 wt.% nitrogen concentration at 1" and 2" depth. Inclusions oriented for 45-degree angle-beam inspection.	SA940314-5.2N
Ti-17	Block with 8 each #2, #3, #4, and #5 FBH size cylindrical hard alpha inclusions of 1.5 wt.% nitrogen concentration at 1" and 2" depth. Inclusions oriented for normal-incidence longitudinal inspection.	S950316-1.5N

TABLE A-3. RECTANGULAR BLOCKS FROM TITANIUM FORGINGS CONTAINING ARRAYS OF CYLINDRICAL SYNTHETIC HARD ALPHA INCLUSIONS (Continued)

Material	Specimen Description	Serial Numbers
Ti-17	Block with 8 each #2, #3, #4, and #5 FBH size cylindrical hard alpha inclusions of 2.8 wt.% nitrogen concentration at 1" and 2" depth. Inclusions oriented for normal-incidence longitudinal inspection.	S941202-2.8N
Ti-17	Block with 8 each #2, #3, #4, and #5 FBH size cylindrical hard alpha inclusions of 5.2 wt.% nitrogen concentration at 1" and 2" depth. Inclusions oriented for normal-incidence longitudinal inspection.	S950320-5.2N
Ti-17	Block with 8 each #2, #3, #4, and #5 FBH size cylindrical hard alpha inclusions of 1.5 wt.% nitrogen concentration at 1" and 2" depth. Inclusions oriented for 45-degree angle-beam inspection.	SA950321-1.5N
Ti-17	Block with 8 each #2, #3, #4, and #5 FBH size cylindrical hard alpha inclusions of 2.8 wt.% nitrogen concentration at 1" and 2" depth. Inclusions oriented for 45-degree angle-beam inspection.	SA941201-2.8N
Ti-17	Block with 8 each #2, #3, #4, and #5 FBH size cylindrical hard alpha inclusions of 5.2 wt.% nitrogen concentration at 1" and 2" depth. Inclusions oriented for 45-degree angle-beam inspection.	SA950317-5.2N

TABLE A-4. RECTANGULAR BLOCKS FROM TITANIUM FORGINGS CONTAINING ARRAYS OF SPHERICAL SYNTHETIC HARD ALPHA INCLUSIONS

Material	Specimen Description	Serial Numbers
Ti 6-4	6" x 6" x 3" block containing four spherical hard alpha inclusions 0.063" diameter and 2.7 wt.% nitrogen located 1" deep.	SPH950921A
Ti 6-4	Larger block containing 32 spherical hard alpha inclusions of various sizes and N contents.	SPH950921B

TABLE A-5. CYLINDRICAL CHORD BLOCKS FROM TITANIUM BILLETS  
CONTAINING FLAT-BOTTOMED HOLE DEFECTS

Material	Specimen Description	Serial Numbers
Ti 6-4 billet	One set of 5 chord blocks of 7.0" diameter billet containing 5 each #1 FBH at metal travel depths of 0.5", 1.2", 2.0", 2.8", and 3.5".	954247B1A XXX where XXX = 0.5, 1.2, etc.
Ti-17 billet	One set of 5 chord blocks of 7.0" diameter billet containing 5 each #1 FBH at metal travel depths of 0.5", 1.2", 2.0", 2.8", and 3.5".	973784T2A2 XXX where XXX = 0.5, 1.2, etc.
Ti-17 billet	One set of 8 chord blocks of 10.0" diameter billet containing 5 each #1 FBH at metal travel depths of 0.5", 1.35", 2.25", 3.15", 4.05", 4.5", 4.95", and 5.5".	954447T2A XXX where XXX = 0.5, 1.35, etc.
Ti-17 billet	One set of 8 chord blocks of 13.0" diameter billet containing 5 each #2 FBH at metal travel depths of 0.5", 1.5", 2.5", 3.5", 4.5", 5.5", 6.5", and 7.0".	963304B2 XXX where XXX = 0.5, 1.5, etc.
Ti 6-4 billet	One set of 8 chord blocks of 13.0" diameter billet containing 5 each #2 FBH at metal travel depths of 0.5", 1.5", 2.5", 3.5", 4.5", 5.5", 6.5", and 7.0".	98395 XXX where XXX = 0.5, 1.5, etc.

TABLE A-6. MISCELLANEOUS ULTRASONIC SPECIMENS

Material	Specimen Description	Serial Numbers
Ti 6-4 forging	Enlarged Grain Block. 0.25" x 1.5" x 4.5" rectangular plate containing large macrograins.	(none)
Ti 6-4 billet	Random Defect Block. 10" diameter billet segment containing approximately 70 synthetic hard alpha inclusions of various sizes, shapes, and nitrogen contents.	
Ti 6-4	High-Impedance Inclusion Specimen. One cylinder (1.5" diameter by 3" high, cut from a large Ti 6-4 forged ring) containing a single defect at its center. Defect is a 0.0308" diameter by 0.0154" thick ellipsoid of titanium-molybdenum alloy oriented at 30 degrees tilt from normal. Defect has an approximately 15% impedance mismatch with the host metal.	950111B
Ti 6-4	High-Impedance Inclusion Block. One block (4.75" x 3.75" x 1.00" cut from a large Ti 6-4 forged ring) containing a single defect at its center. Defect is a 0.0298" diameter by 0.0154" thick ellipsoid of titanium-molybdenum alloy tilted 30° from normal. Defect has an approximately 15% impedance mismatch with the host metal.	950111A
Ti 6-4	Five specimens for low-cycle fatigue testing containing subsurface hard alpha defects below a peened surface.	LCF-1, LCF-2, LCF-3, LCF-4, LCF-5

The specimens listed in this appendix are occasionally being used in ongoing research projects, and generally reside either at the ISU Center for NDE, General Electric, Pratt & Whitney, or Honeywell. When not in active use, any given specimen is available for loan for bone fide research purposes. Loan arrangements can be made by contacting:

Lisa Brasche  
 Center for Nondestructive Evaluation  
 Iowa State University  
 1915 Scholl Road  
 Ames, IA 50011  
 Phone: (515) 294-8152  
 E-mail: lbrasche@cnnde.iastate.edu

REFERENCES.

- A-1. R. H. Burk, et al., "A Methodology for the Assessment of the Capability of Inspection Systems for Detection of Subsurface Flaws in Aircraft Turbine Engine Components," Report by the ETC Inspection Reliability Task Force, in press.
- A-2. R. Stephan, et al., "Inservice Inspection: Development of Portable Eddy Current Inspection Tools for Engine Overhaul Applications," Report by the ETC Eddy-Current Inservice Inspection Task Force, in press.

## APPENDIX B—DEVELOPMENT, TESTING, AND USE OF BACKSCATTERED NOISE MODELS

### B.1 INTRODUCTION.

In ultrasonic inspections of metal components, defect detection can be limited by backscattered grain noise from the metal microstructure. The absolute level of the grain noise observed in a given inspection depends on the metal microstructure and on details of the inspection system, such as the focal properties of the transducer, the duration and spectral content of the incident sonic pulse, and the receiver amplification settings. Under the sponsorship of the ETC, models were developed to predict attributes of the backscattered microstructural noise seen in pulse/echo inspections of titanium billets. These models simultaneously treat the effects of the measurement system and the metal microstructure, and are consequently capable of predicting absolute noise quantities.

Here the noise models are briefly reviewed, with an emphasis on the modeling assumptions, the overall approach, and practical applications. Readers interested in the detailed mathematical development of the models should consult the listed references B-1, B-2, B-3, B-4, B-5, B-6, B-7, B-8, B-9, and B-10. The accuracy and utility of the models are then demonstrated by comparing their predictions to the results of selected validation experiments performed at Iowa State University (ISU), General Electric (GE), and Pratt and Whitney (P&W). In general, it was found that the dependence of the observed gated-peak noise on details of the inspection procedure (transducer focal properties, sonic pulse volume, gate duration, gate location) is well predicted by the models.

### B.2 MODEL ASSUMPTIONS AND DEVELOPMENT CHRONOLOGY.

The grain noise models are based on three principal assumptions [B-4]: (1) that multiple scattering events can be neglected; (2) that the total noise signal is an incoherent superposition of the direct echoes from the individual metal grains illuminated by the incident sonic pulse; and (3) that the microstructure is spatially uniform in some region under investigation.

In chronological order of development, the noise models can be partitioned into three categories, as shown in table B-1. Each model version predicts some measure of the absolute backscattered noise from knowledge of (1) the measurement system particulars and (2) certain frequency-dependent factors known as figures-of-merit (FOM), which are solely determined by the metal microstructure. The first two generations use only the lowest-order microstructural quantity, denoted by FOM, while the third-generation model makes use of a higher-order quantity denoted by FOM. More will be said about these inputs a bit later. Each of the three model versions comes in two flavors: broadband (BB) and simplified tone-burst (STB), either of which can be used to model common pulse/echo inspections using broadband pulses. For the BB treatment, the full model formalism is used and transducer radiation patterns are accurately calculated using the Gauss-Hermite beam model. In the STB treatment a number of approximations are invoked, including the simpler Gaussian beam model, to permit very rapid calculations, although with some loss of accuracy.

TABLE B-1. THE THREE VERSIONS OF THE INDEPENDENT-SCATTERER NOISE MODEL

Model Version	Noise Measures Predicted	Microstructure Inputs
First Generation	rms noise level; rms noise spectral components	FOM
Second Generation	Gated-peak noise distributions	FOM
Third Generation	Gated-peak noise distributions	FOM + FOM'

The backscattered noise seen in a given inspection can be quantified in a variety of ways. One practice commonly used at ISU is to measure the so-called root-mean-squared (rms) noise level [B-1]. The rms noise level serves as a convenient means of quantifying the depth or time dependence of the noise, and it was the focus of the first-generation noise model. However, it is not generally used in industrial applications. In industry, it is more common to measure peak-to-peak noise voltages within some preset time window and to use information pertaining to the distribution of these voltages to set thresholds for flaw detection. The desire to predict gated-peak noise (GPN) probability distributions drove the development of the second- and third-generation noise models.

### B.3 NOISE MODEL INPUTS.

The noise models are designed to predict characteristics of the absolute grain noise (in volts) that would be seen on an oscilloscope or similar device during a scanning experiment. Model inputs are of two types: those pertaining to the measurement apparatus and those pertaining to the metal specimen.

The measurement system inputs include the transducer focal properties, the inspection water path, scan plan, equipment gain settings, time gate, and a reference echo. The latter is usually an echo from the front or back surface of a fused-quartz block, and it serves to encode the amplitude, duration, and frequency content of the incident sonic pulse. Certain material properties (density, sound speed, and attenuation) of water and the reference block are also required. Backscattered noise characteristics are particularly sensitive to the transducer focal properties and accurate knowledge of the effective element diameter(s) and geometrical focal length(s) are consequently required for accurate noise predictions. Moreover, for commercially available transducers, the notations stamped on the case by the manufacturer are not always a reliable indicator of the true focal properties. For this reason, beam-mapping methods for experimentally determining the effective diameters and focal lengths of a given transducer were developed for the ETC. The probe characterization method for spherically focused, circular-element probes is described by Margetan, et al. [B-11] and Yalda, et al. [B-12] discusses the characterization of noncircular, bi-cylindrically focused probes.

The metal specimen inputs consist of the geometry of the specimen, the metal density, the sound speed, attenuation, and FOM values for the inspection mode of interest (in this case, longitudinal sound). The specimen geometry determines the surface curvature and tilt at the sound entry point and, hence, affects the beam profile within the metal. Note that attenuation and FOM depend strongly on frequency, while sound speed does not. Thus, attenuation and FOM must be specifically input as functions of frequency.

The microstructural inputs (FOMs) are determined by the variations of local elastic constants from point-to-point within the metal. One way of expressing the FOMs is to relate them to the density of grains and the single-grain far-field scattering amplitudes [B-10]. Alternatively, they can be expressed in terms of two-point correlation coefficients for elastic constants [B-5]. It is possible to calculate the FOMs directly from detailed knowledge of the microstructure (i.e., from grain size, shape, and orientation distributions and single-grain elastic constants). This was demonstrated in reference B-5 for single-phase, equiaxed microstructures. In practical engine titanium inspections, however, such detailed microstructural information is not usually available and an alternative method for deducing FOM values is required. For engine alloys, it was chosen to measure FOM values by analyzing backscattered noise data, as discussed earlier in section 5.3.9.

#### B.4 NOISE MODEL OUTPUTS.

The first-generation noise model predicts only root-mean-squared noise values. The primary output is the rms-noise-voltage-vs-time curve that would be seen in a scanning experiment. The precise meaning of the rms noise voltage is as follows [B-1 and B-5]. Consider some fixed-time instant at which grain noise can be seen, say 5.00 microseconds after the appearance of the front-surface echo. The noise voltage observed at that time will naturally vary as the transducer is scanned, sometimes taking on positive values and sometimes negative ones. The rms noise voltage is obtained by squaring the voltages seen at that fixed-time instant for all transducer positions in the scan pattern, averaging those voltages, and then taking the square root of the average. Note that the averaging process is over lateral position (transducer location) and not over time. In addition to the rms noise voltage, rms averages of the spectral components of noise A-scans can also be predicted using the first-generation noise model [B-3 and B-4].

The second- and third-generation noise models each predict gated-peak-noise probability distributions, i.e., the probability that a measurement of the GPN voltage in a specified time window will yield a value between  $V$  and  $V+\Delta V$ . From such distribution functions, other quantities, such as the average GPN voltage or the standard deviation of the GPN voltages, can be easily obtained.

Regardless of whether one uses rms or gated-peak quantities, the manner in which the noise level depends upon sound penetration depth (or upon arrival time) is dictated, in part, by the normalization procedure adopted. For example in a focused-probe measurement, if one normalizes the noise at a given depth by the strength of an echo from a FBH at the same depth, one generally finds the smallest noise level at the focal plane of the transducer. On the other hand, if the noise at all depths is normalized by the same fixed signal, such as a back-surface echo from a fused-quartz block, then one generally finds the greatest noise level at the focal plane. This behavior is illustrated in figure B-1.

The basic noise models predict absolute noise characteristics, relative to the fixed input reference signal, and hence, these raw predicted noise levels are largest in the focal zone. However, distance-amplitude correction (DAC) factors can be determined by direct measurements on FBH standards or by using models to predict echo amplitudes for FBHs at various depths, then DAC adjusted noise characteristics can be calculated. Model predictions using both types of

normalization (fixed gain; DAC) are included in this chapter, and it will be carefully pointed out as to which normalization scheme is being used in each instance.

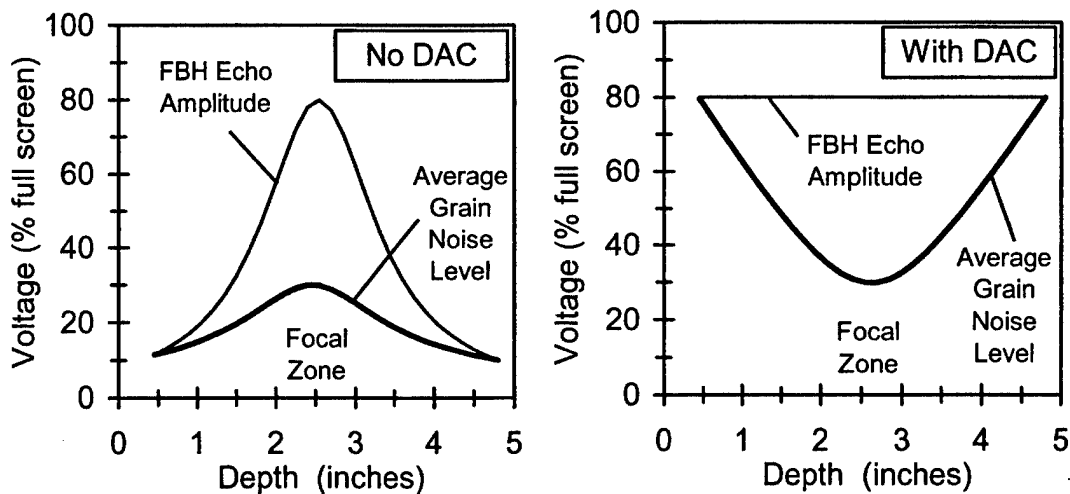


FIGURE B-1. TYPICAL DEPENDENCE OF GRAIN NOISE ON DEPTH IN A FOCUSED PROBE INSPECTION OF A BILLET, WITH (RIGHT) AND WITHOUT (LEFT) DISTANCE-AMPLITUDE CORRECTION (DAC)

#### B.5 FIRST-GENERATION NOISE MODEL.

The major elements of the STB and BB versions of the first-generation noise model were largely completed before the ETC program began [B-1 through B-5]. Some enhancements were added to handle cylindrical geometries at normal and oblique incidence and to allow for DAC corrections. The first-generation model is the basis for the FOM extraction procedure described in section 5.3.9. In addition, the predicted rms-noise-vs-time curve is a key ingredient in the calculation of GPN distributions by the second- and third-generation models. It was therefore prudent to verify that the model was capable of making reasonably accurate predictions of noise properties in the Ti 6-4 and Ti-17 alloys of interest to the consortium.

A series of tests were conducted at ISU, in which

- a. The necessary material properties of a titanium specimen were measured (including its FOM-vs-frequency curve).
- b. Using one or more well-characterized transducers, a suitable reference echo was acquired, and the titanium specimen was then scanned to obtain several hundred digitized noise echoes (A-scans) from its interior.
- c. The measured noise echoes were analyzed to determine the absolute rms-noise-vs-time curve for each transducer.
- d. These curves were compared with model predictions.

The results of one such comparison are shown in figure B-2, with the noise arrival time measured relative to the front surface echo. The specimen was a rectangular prism cut from the outer circumference of a 9" diameter Ti-17 billet. Noise measurements were made using three transducers, two focused and one planar, with the direction of sound propagation being radially inward relative to the original billet. In this case no FBH normalization (DAC correction) has been applied, and the measured rms noise levels are largest where the beams are narrowest. As discussed in section 5.3, different methods of measuring the ultrasonic attenuation of engine alloy material yield different results, leading to some uncertainty in the attenuation. Since the attenuation must be known before the FOM can be determined, this also leads to some uncertainty in the FOM-vs-frequency curve. In figure B-2 predicted rms noise level curves for this Ti-17 specimen are shown for two choices of metal properties: the first using the attenuation deduced from back-surface echoes as measured with a planar transducer; and the second assuming the metal attenuation is negligible. The true attenuation appropriate for noise measurements is expected to lie between these extremes. The two choices lead to slightly different predicted rms-noise-vs-time curves, but, overall, the model predictions are seen to be in good agreement with the experiment.

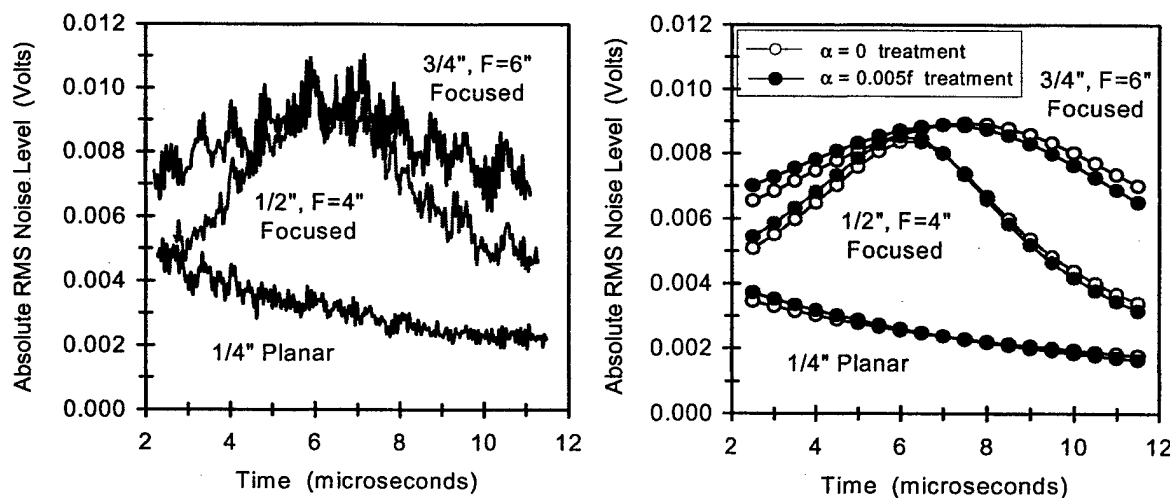


FIGURE B-2. MEASURED (LEFT) AND PREDICTED (RIGHT) ABSOLUTE rms GRAIN NOISE LEVELS FOR THREE INSPECTIONS OF Ti-17 BILLET SPECIMEN A1 USING DIFFERENT TRANSDUCERS

Other examples comparing measured and predicted rms noise curves for titanium alloys can be found in references B-4, B-5, and B-7. For radial inspection using planar and focused transducers with center frequencies in the range 5-15 MHz, the first-generation noise model generally performed well, so long as the microstructure was relatively uniform within the region scanned. All current noise models, as tested, assume that the FOM value does not vary with scan position. However, the models could be easily extended to handle varying FOM, such as that responsible for the noise banding commonly seen in billet inspections.

## B.6 SECOND-GENERATION NOISE MODEL.

The development of noise models for predicting gated-peak noise (GPN) probability distributions was guided by two questions:

1. Under what circumstances can GPN distributions be accurately predicted from knowledge of the rms-noise-vs-time curve?
2. What additional higher-moment information is required for such predictions when the rms noise level alone is not sufficient?

The answer to question number 1 leads to the second-generation noise model, while the answer to question number 2 leads to the third-generation model.

The answers to the two questions hinge on the interrelationships between three probability distributions. When a transducer is scanned above a metal component, the detailed appearance of the backscattered noise A-scan changes. Certain quantities describing A-scan attributes can be thought of as random variables governed by probability distributions. Three such random variables and their associated probability density functions are pictured in figure B-3 and described more fully in table B-2.

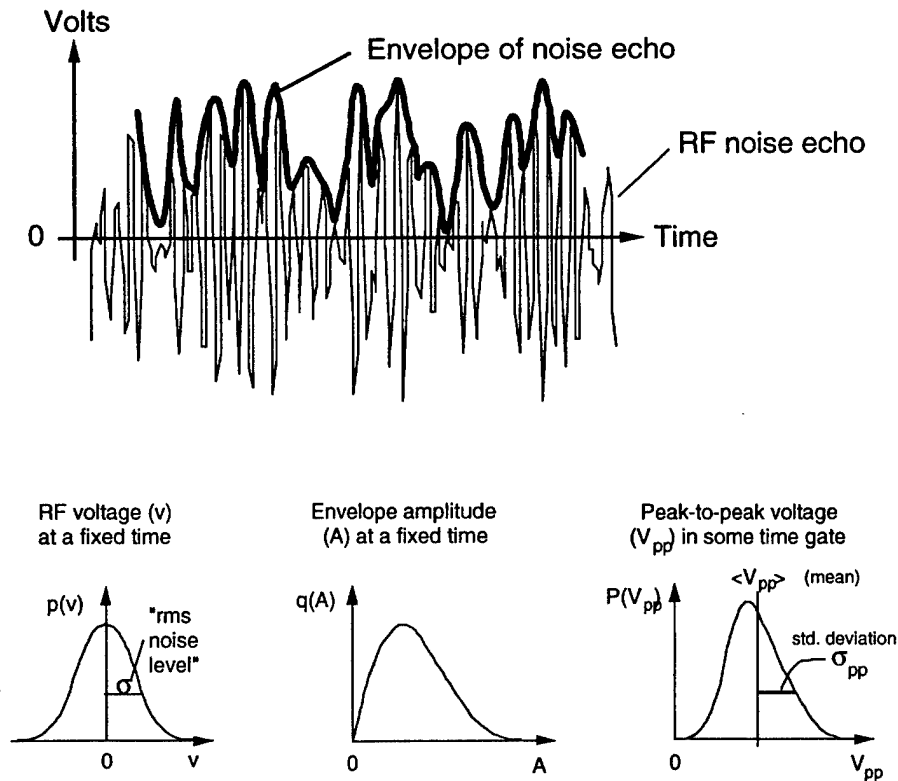


FIGURE B-3. SCHEMATIC REPRESENTATIONS OF A TYPICAL RF NOISE A-SCAN AND ITS ENVELOPE FUNCTION (TOP) AND THREE NOISE DISTRIBUTIONS OF INTEREST (BOTTOM)

TABLE B-2. THREE NOISE ATTRIBUTES OF INTEREST, AND THEIR PROBABILITY DISTRIBUTIONS

Noise Attribute Name	Meaning	Properties	Probability Density Function Name
$v(t)$ or $v$ for short	RF noise voltage observed at some fixed observation time $t$ .	Can be positive or negative. Has mean of zero.	$p(v)$
$A(t)$ or $A$ for short	The amplitude at fixed time $t$ of the envelope function which passes through the peaks of the rectified noise A-scan.	Nonnegative	$q(A)$
$V_{pp}(t_a, t_b)$ or $V_{pp}$	The maximal peak-to-peak voltage of the portion of the noise signal that lies in the time gate bounded by $t_a$ , and $t_b$ .	Nonnegative	$P(V_{pp})$

In the language of table B-2, the rms noise level predicted by the first-generation model is simply the width or standard deviation of the probability distribution  $p(v)$ .

The probability density functions listed in table B-2 are all related. It turns out that if  $p(v)$  is known, then  $q(A)$  can be determined and vice versa. Moreover,  $P(V_{pp})$  can be estimated from  $q(A)$  if some reasonable approximations are adopted, as discussed in references B-8 and B-9. The primary assumption has to do with the time correlation of noise voltages. For any given A-scan, the envelope amplitudes at nearby times are well correlated and those at distant times are uncorrelated. To determine  $P(V_{pp})$  from  $q(A)$ , the time gate is partitioned into subintervals having a duration of about that of the incident pulse. Then it is assumed that within a given subinterval, the envelope voltages are perfectly correlated and that amplitudes in different subintervals are completely uncorrelated. In mathematical terms, a smooth correlation-vs-time-separation curve is being approximated by a step function of width  $\Delta t$ , the so-called time correlation length. With this approximation, the prediction of the largest peak-to-peak voltage in the gate is reduced to the prediction of the largest envelope amplitude in a collection of independent subintervals spanning the gate. Thus, as outlined in reference B-8, the gated-peak noise distribution  $P(V_{pp})$  can be determined if one knows  $q(A)$  or  $p(v)$  at each time instant in the gate.

The second-generation noise model results when one assumes that  $p(v)$  is a Gaussian function with zero mean at each observation time  $t$ , or, equivalently, that  $q(A)$  is a Rayleigh distribution. In that case,  $p(v)$  is completely specified by its width, namely the rms noise level, which is predicted by the first-generation model. This assumption is not without merit. The Central Limit Theorem of statistics implies that  $p(v)$  is expected to be Gaussian if many, i.e., 10 or more, scatterers (grain boundaries) contribute appreciably to the RF noise voltage seen at time  $t$  for a typical transducer position. This will occur if the sonic pulse volume is large compared to the

effective volumes of the metal grains. Moreover, as reported earlier in section 5.3.11, survey measurements were conducted to determine the degree to which  $p(v)$  was Gaussian in the focal zone where the pulse volume is smallest. It was found that  $p(v)$  was generally quite Gaussian for radial inspections of billet material using focused 5-MHz, 0.75" F/8 transducers. Non-Gaussian behavior was seen in some cases for focused 15-MHz inspections, and for some larger forging specimens at lower frequencies. For the large forging specimens, with dimensions of 6" by 6", the FOM values varied noticeably with position, and part of the observed non-Gaussian behavior can be attributed to the mixing of distributions that arises when scanning a nonuniform microstructure. The effects of distribution mixing could be easily incorporated into the second-generation noise model in cases where the position-dependence of the FOM was known.

To summarize, in the second-generation noise model, the distribution of RF noise voltages seen at any sound arrival time in a scanning experiment is assumed to be Gaussian. Strictly speaking, this need only be true when scanning over a region where the microstructure is uniform. Then, gated-peak noise distributions for arbitrary time gates are predicted by a two-step approach: (1) the first-generation model is used to predict the absolute rms-noise-vs-time curve for the inspection in question and (2) the formalism of reference B-8 is used to predict the gated-peak noise distribution from knowledge of the rms-noise-vs-time curve.

Tests of step 2 were conducted to gauge its accuracy, using both engine titanium specimens and a stainless steel one. The latter specimen had a simple single-phase microstructure, and the grains were sufficiently small (mean diameter of 100 microns) that Gaussian noise behavior was expected. Measured and predicted gated-peak noise distributions are compared for the stainless steel specimen (SS) and a Ti 6-4 billet specimen (K1) in figure B-4 for a few choices of the time gate duration. In each case the time gate was centered at the beam focus and the gate duration is indicated. The experimental distributions were obtained by binning 990 measured voltages for specimen SS and 361 voltages for specimen K1. Other examples can be found in reference B-8. In general, the second-generation model was found to accurately predict the means and widths of gated-peak noise distributions when the Gaussian assumption held.

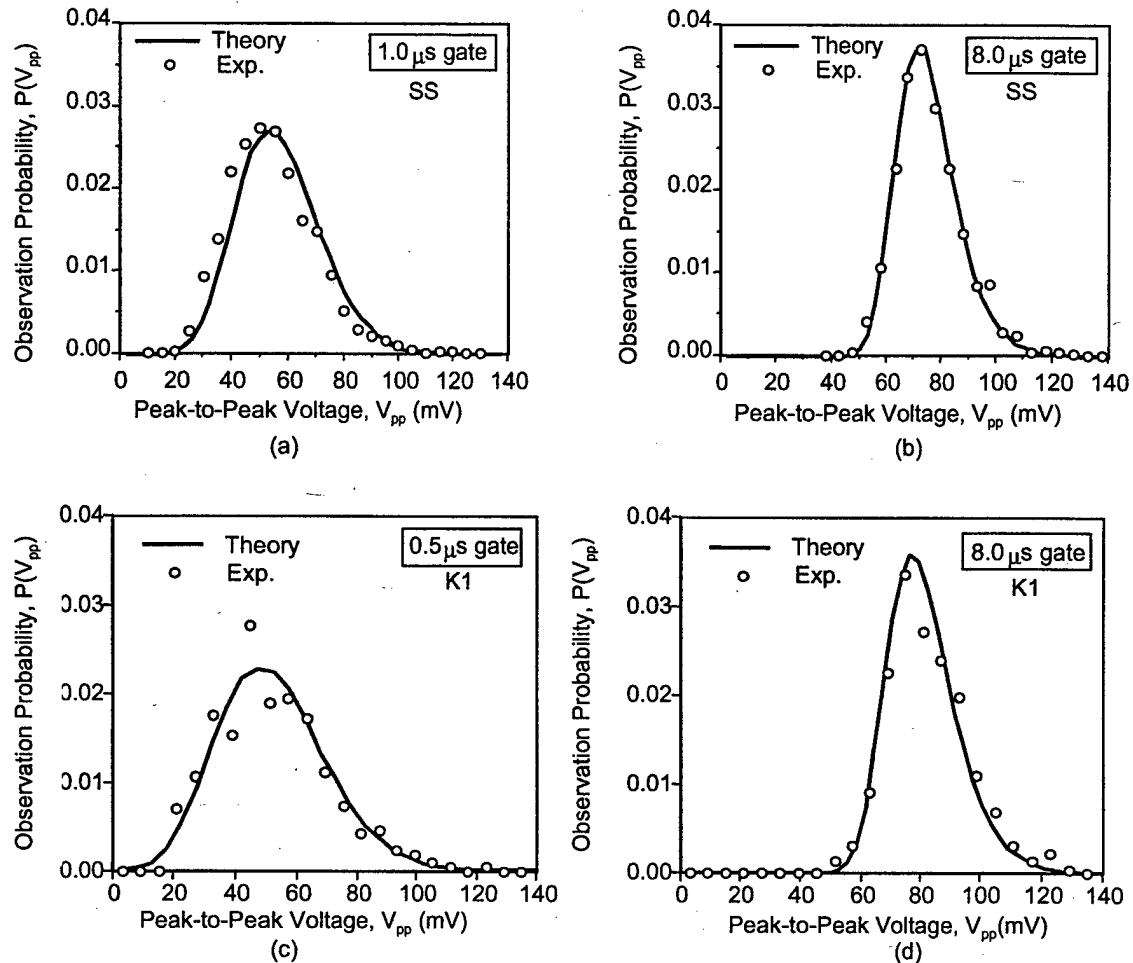


FIGURE B-4. MEASURED AND PREDICTED DISTRIBUTIONS OF GATED PEAK-TO-PEAK GRAIN NOISE VOLTAGES SEEN IN PULSE/ECHO INSPECTIONS WITH A 5-MHz, 0.75" DIAMETER, F=6" (F/8)-FOCUSED TRANSDUCER. (a) AND (b) RESULTS FOR A STAINLESS STEEL CASTING SPECIMEN DENOTED BY SS. (c) AND (d) RESULTS FOR RADIALLY-INWARD INSPECTION OF A Ti 6-4 BILLET SPECIMEN K1.

### B.7 THIRD-GENERATION NOISE MODEL.

The second-generation model, with future software modifications to handle spatially-varying microstructure, is believed to be sufficient for simulating 5-MHz multizone billet inspections. However, for forging inspections and higher-frequency billet inspections, the Gaussian approximation for  $p(v)$  may not be adequate because relatively few scatterers contribute to the backscattered noise.

In the third-generation model,  $p(v)$  is allowed to be non-Gaussian. In particular,  $p(v)$  is allowed to be a member of a two-parameter family of distributions known as K-distributions. The K-distribution is an exact solution to a certain two-dimensional random walk problem and, consequently, has some desirable mathematical properties. It includes the Gaussian as a limiting case and has been used by a number of researchers to model radar and sonic noise [B-8].

Recall that in the second-generation model,  $p(v)$  is completely determined by the rms noise level or, equivalently, by its second central moment denoted here by  $\langle v^2 \rangle$  [ $\langle v^2(t) \rangle$  is the square of the rms noise level at time  $t$ ]. In an analogous manner, the K-distribution version of  $p(v)$  is completely specified by its first two nonzero central moments, namely  $\langle v^2 \rangle$  and  $\langle v^4 \rangle$ . In the first- and second-generation models,  $\langle v^2 \rangle$  can be expressed in terms of the measurement system particulars and the microstructure (i.e., FOM). In the third-generation model, an additional relationship is formulated, which expresses  $\langle v^4 \rangle$  in terms of the measurement system and the microstructure [B-10]. This introduces a higher-order microstructural quantity, FOM'.

Here is an outline of the manner in which the third-generation noise model would be used in practice to predict gated-peak noise distributions:

1. For a specimen of interest, backscattered noise waveforms would be measured and subsequently analyzed to extract FOM and FOM'.
2. For any planned inspection, knowledge of FOM, FOM', and the measurement system particulars would be used to predict  $\langle v^2 \rangle$  and  $\langle v^4 \rangle$ , the moments of the RF voltage distribution  $p(v)$  at each time instant in a time gate of interest.
3. From  $\langle v^2 \rangle$  and  $\langle v^4 \rangle$ , the K-distribution approximation to  $p(v)$  would be determined.
4. From knowledge of  $p(v)$  at each time in the gate, the gated-peak noise distribution would be predicted, using the same technique employed for the second-generation model.

Tests were performed to compare the second- and third-generation models in situations where the second-generation model was known to be inaccurate because  $p(v)$  was clearly non-Gaussian. In particular, using measured values of  $\langle v(t)^2 \rangle$  and  $\langle v(t)^4 \rangle$  for engine titanium specimens, steps 3 and 4 above were performed, and the predicted GPN distributions were compared with experiment. Then using only the measured  $\langle v(t)^2 \rangle$  values, the second-generation model formalism was used to predict GPN distributions, which could also be compared with experiment. Results of one such test are shown in figure B-5. In this case, the time gate was centered at the beam focus, and results are shown for four choices of the gate duration. The experimental distributions were obtained by binning 305 measured voltages. Predictions were made using both the second-generation noise model (Gaussian) and the third-generation model (K-Distribution). For this inspection, the second-generation model predicts distributions that are much too narrow. In general, when the number of scatterers in the beam volume was small, it was found that the use of  $\langle v(t)^4 \rangle$  information significantly improved the accuracy of predicted GPN distributions.

A procedure for measuring the FOM of a given specimen by analyzing backscattered noise has long been available and was routinely used on the billet and forging specimens studied as part of the ETC Fundamental Studies Task. The practical use of the third-generation noise hinges on the ability to develop a robust procedure to similarly measure FOM'. In that endeavor, it has been less successful to date. A model expression was developed that related  $\langle v(t)^4 \rangle$  to (1) details of the measurement system; and (2) the specimen microstructure through the factors FOM and FOM'. A procedure to measure FOM' by using this model expression to analyze measured noise

data was then formulated. However, in trials using synthetic noise data, the extracted FOM' values were often found to be inaccurate.

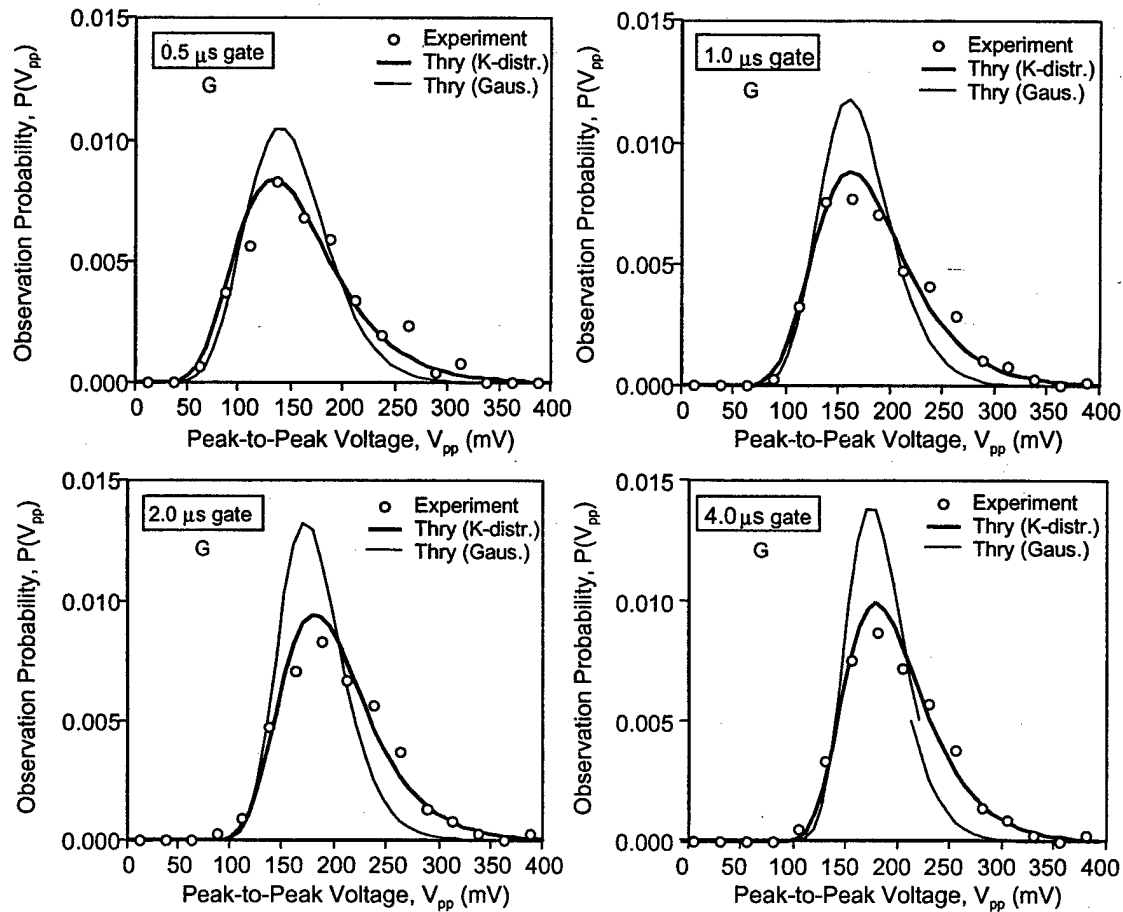


FIGURE B-5. MEASURED AND PREDICTED DISTRIBUTIONS OF GATED-PEAK GRAIN NOISE VOLTAGES FOR A 15-MHz, F/7 FOCUSED-PROBE INSPECTION OF Ti 6-4 FORGING SPECIMEN G

The results of one such trial are summarized in figure B-6. Monte-Carlo methods were used to generate synthetic noise echoes that were then input into the FOM/FOM' measurement procedure. In each trial, 500 ensembles of titanium microstructure were generated by filling a volume with randomly centered, randomly oriented titanium grains. The backscattered RF noise signal (A-scan) from each ensemble was then calculated by summing the echoes from the individual grains when a model pulse ensonified the ensemble. The model pulse was a 15-MHz toneburst of about 1 microsecond duration from a hypothetical focused probe. This process produced 500 synthetic noise signals (one per ensemble) that were then input to the proposed FOM/FOM' measurement procedure. The measured values of FOM and FOM' at 15 MHz were then compared with the known exact values, which depended on the distribution of grain sizes and, hence, on the density of grains assumed in the simulation. Results are shown in figure B-6 for three trials each at three different grain densities. The correct value is indicated by the horizontal line, and the result of each analysis trial is indicated by a plotted point with error bars.

The assumed density of grains in grains/cc is indicated by  $N$ . As can be seen, very good results were obtained for the lower order parameter FOM. The results for FOM' were less satisfactory. The deduction of the FOM' value is based on the analysis of the non-Gaussian behavior observed when the sonic pulse encloses a relatively small number of grains. Thus, to accurately estimate FOM', one needs an experimental situation where the beam ensonifies the proper number of grains: enough grains that statistical arguments still apply but not so many that Gaussian behavior dominates. It seems hard to strike the proper balance with the current formulation of the third-generation model. When the number of grains in the beam is too small, certain statistical assumptions in the model may be breaking down, causing the deduced value of FOM' to be inaccurate. When the number of grains is too large, Gaussian behavior dominates and the uncertainty in the measured FOM value is large.

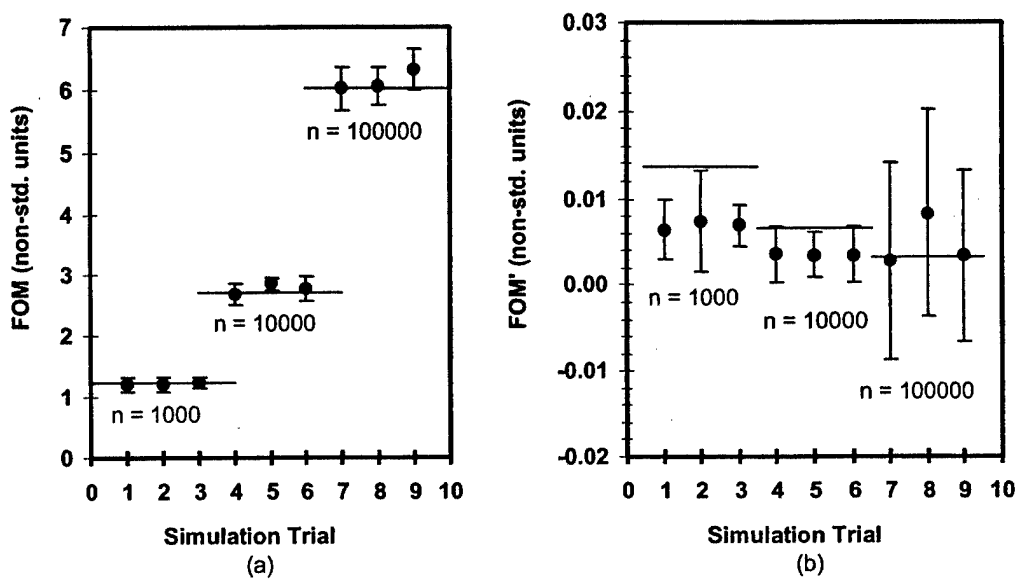


FIGURE B-6. TESTING OF THE FOM (a) AND FOM' (b) EXTRACTION PROCEDURE USING SYNTHETIC NOISE DATA

#### B.8 PRACTICAL USES OF THE NOISE MODELS: PREDICTIONS OF RELATIVE NOISE CHARACTERISTICS.

As has been demonstrated, accurate prediction of absolute noise levels is possible but requires detailed knowledge of the metal microstructure that enters through the frequency-dependent FOM factors. For a typical industrial inspection of a billet or forging, such FOM information is not generally available, although it could be deduced by analyzing backscattered noise waveforms from regions where the microstructure is spatially uniform. FOM values have been measured in this way for cubes cut from representative engine alloy specimens and a wide spread of values was found as documented earlier in figure 76. In the absence of specific FOM information about the specimen being inspected, how can the noise models be used? One approach is to use the models to predict how changes in the inspection procedure or component geometry will affect the backscattered noise from the microstructure at hand. This subsection will demonstrate such predictions of relative noise properties.

In the previously discussed work done to validate noise model predictions, the measurements were made at the Iowa State University Center for Nondestructive Evaluation research facility with greater attention paid to certain details than is common in industrial settings. For example, auxiliary beam mapping experiments were carried out to characterize the radiation pattern of all transducers used, RF noise waveforms were repeatedly digitized and averaged to remove the contribution from electronic noise and fairly small regions of metal having relatively uniform microstructures were scanned when noise waveforms were acquired. For the model tests that will now be described, all of the experimental data were gathered by industrial members of the Consortium using their own equipment and measurement methods. This allowed the Consortium to better assess the practical use of the noise models in typical industrial settings.

Gated-peak noise is of primary interest to the industrial ETC members, and several model studies were undertaken to compare predicted and measured values of average GPN voltages. Three of the studies are described below. They deal with the effect upon the measured noise of changes in (1) the focusing scheme (data supplied by David Copley and Pat Howard, GE); (2) the volume of the incident ultrasonic pulse (Pat Howard and Robert Gilmore, GE); and (3) the duration and location of the time gate (Jeff Umbach, Pratt & Whitney). The second-generation noise model was used throughout and predictions were made using both the full broadband (BB) and simplified toneburst (STB) model treatments. For each specimen studied, one necessary model input was the FOM-vs-frequency curve, which was presumed to be unknown. The FOM-vs-frequency curve was estimated as follows: (1) based on the results of the earlier survey experiments, it was assumed that the FOM was directly proportional to frequency and (2) the constant of proportionality for each specimen was chosen so that some single predicted noise attribute (generally an average overall noise level) matched experiment. With the FOM thus fixed, the predicted dependence of the backscattered noise on the varying inspection feature was then compared with experiment. Full descriptions of the modeling work can be found in reference B-10. Some of the chief results are summarized below.

Results of the first model study are summarized in figure B-7. The left panel displays the experimental findings of Copley and Howard [B-13] who compared the relative merits of two focusing schemes for inspecting 10" diameter cylindrical billets. In the conventional (CV) inspection, a single 5-MHz cylindrically focused transducer was used, and in the multizone (MZ) inspection, six separate 5-MHz bi-cylindrically focused transducers were used, each designed to focus sound within a different depth zone. Both inspections were carried out on a 10.25" diameter Ti 6-4 calibration standard with FBH's located at various depths. The peak amplitude of each FBH echo was measured, as was the average gated-peak noise voltage in an 8-microsecond-wide time gate centered on the FBH echo. The measured noise, normalized by the echo from a #2 FBH, is shown as a function of radial depth in figure B-7(a). Similarly, normalized model predictions are shown in figure B-7(b) for both the BB and STB model treatments. For the intermediate depths, the reduction in the N/S ratio achieved by the multizone system is seen to be predicted with good accuracy. The two major shortcomings of the model predictions are (1) the model curves rise somewhat more slowly with depth than do their experimental counterparts and (2) the predicted advantage of MZ over CV is too small for the deepest holes. These problems could be rectified by modifying two of the model inputs, namely (1) by assuming that the microstructural FOM increases with depth and (2) by assuming that the

effective focal length of the CV probe is shorter than its nominal value so that its beam diverges at a faster rate deep in the billet.

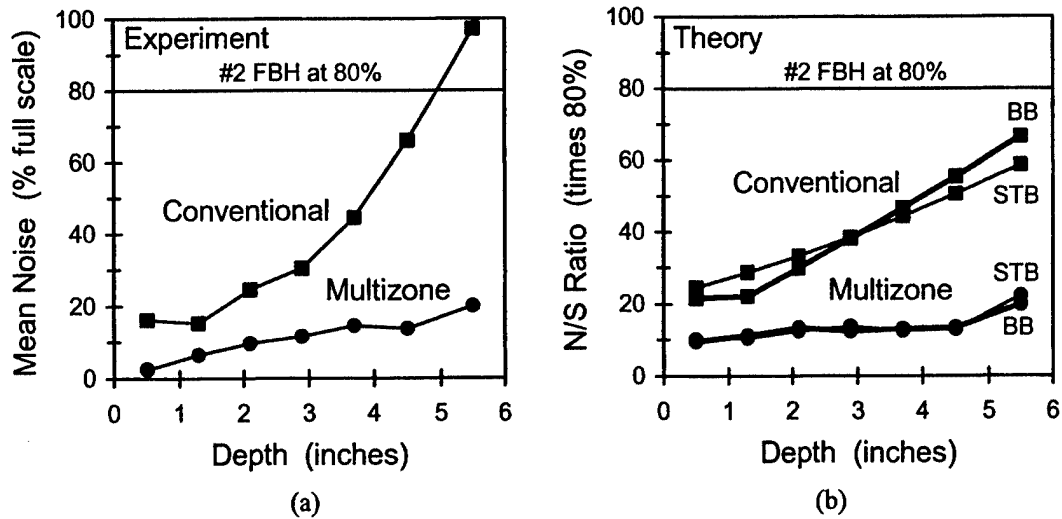


FIGURE B-7. COMPARISON OF THE AVERAGE GATED-PEAK NOISE LEVELS (NORMALIZED BY #2 FBH ECHOES) FOR 5-MHz CONVENTIONAL AND MULTIZONE INSPECTIONS OF A 10.25" Ti 6-4 BILLET CONTAINING FLAT-BOTTOMED HOLES: (a) EXPERIMENT AND (b) MODEL PREDICTIONS

In a second study, the noise model was used to simulate experiments conducted to study the relationship between backscattered noise and the volume of the incident sonic pulse. Howard and Gilmore [B-14] made measurements on three rectangular titanium alloy specimens using nine different circular, spherically focused transducers. The pulse volume of each transducer was determined by measuring (1) the time duration of a back-surface echo and (2) the lateral area of the focal spot (by scanning a #1 FBH and analyzing the resulting C-scan image). Backscattered gated-peak grain noise was then measured for a wide time gate centered at the focal plane, and noise attributes, normalized to the peak echo from a #1 FBH, were plotted versus pulse volume. The results for the average GPN are shown as plotted points in figure B-8(a). Note that since the noise voltages are normalized by FBH echoes, noise/signal ratios (N/S) are actually plotted. The model predictions, shown as curves on the same figure, are seen to reproduce the general trend of the measured data. An analysis of the model formalism indicates that such N/S should be approximately proportional to the square root of pulse volume. In figure B-8(b) the measured data and model predictions have been plotted versus the square root of the pulse volume, and the N/S values have been renormalized such that the nine measurements for each specimen have a mean value of unity. There is then a single predicted curve for each model treatment. The measured data are seen to rise approximately linearly with the square root of volume, as expected, with some scatter about the model predictions.

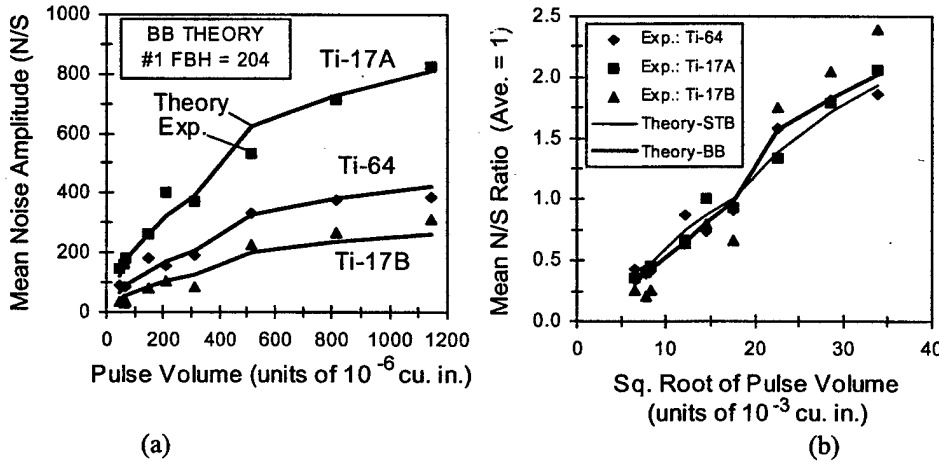


FIGURE B-8. DEPENDENCE OF THE AVERAGE GATED-PEAK NOISE VOLTAGE ON THE VOLUME OF THE INCIDENT ULTRASONIC PULSE (a) EXPERIMENTAL RESULTS OF HOWARD AND GILMORE FOR THREE SPECIMENS (PLOTTED POINTS) AND NOISE MODEL PREDICTIONS USING THE BB FORMALISM (SOLID CURVES) AND (b) RENORMALIZED VALUES OF N/S PLOTTED VERSUS THE SQUARE ROOT OF THE PULSE VOLUME

The third model study was a simulation of Umbach's measurements [B-10] on the dependence of noise on the depth and duration of the time gate. Backscattered grain noise attributes were measured by scanning a spherically focused 15-MHz transducer over one surface of a rectangular specimen cut from a large ring forging. Noise C-scans at various depths revealed that the noise was not spatially uniform (figure B-9(a)), primarily because the curved forging flow lines were not parallel to the entry surface. Because of the sharp sonic focus and the relatively large size of the macrostructural elements, the backscattered noise from the focal zone was found to exhibit the non-Gaussian behavior that occurs when the beam ensonifies a relatively small number of dominant scatterers. In addition, noise measurements made in water alone, with the specimen removed, indicated that a significant amount of residual electronic noise was present when the grain noise was measured. Nonuniform microstructure, non-Gaussian noise behavior, and electronic noise are generally present to some extent in engine titanium inspections. These complicating effects were enhanced in the Umbach data, thus presenting a more challenging test of the model's ability to predict relative noise levels in practical settings.

Umbach measured and stored backscattered RF noise waveforms at 46 by 73 scan positions and various measures of the noise could be calculated from these. The measured root-mean-squared noise level for the full scan region is shown in figure B-9(b), while figure B-9(c) and (d) display the dependence of the mean gated-peak noise voltage on the time gate choice (without FBH normalization). In particular, figure B-9(c) displays measured and predicted average GPN voltage versus gate center for a series of 1-microsecond gates having different center times, while figure B-9(d) displays measured and predicted average GPN voltages for a series of time gates having the same center time but different durations ranging from 0.1 to 5.6 microseconds. The time gates referenced in figures B-9(c) and B-9(d) are indicated in figure B-9(b). Separate results are shown for the full scan region (E) and for the four quadrants (A, B, C, D) so that the

variation due to specimen inhomogeneity can be gauged. The shapes of the predicted rms noise level curves compare well with experiment in the focal zone; however, the measured rms noise is generally higher than predicted at early and late times, presumably due to the presence of electronic noise, which imposes a noise floor. The dependence of the mean gated-peak noise on the gate choice is predicted with reasonable accuracy, given the scatter of the data from one quadrant to the next. Note that figure B-9(c) displays the effect of shifting the time gate center while holding its duration fixed, while figure B-9(d) displays the effect of widening the time gate while leaving its center unchanged. If the non-Gaussian noise behavior is taken into account by using the third-generation model and measured  $\langle v^4 \rangle$  data, the predictions become more accurate on average, as indicated by the dashed curves in figures B9(c) and (d). However, such corrections effectively require knowledge of both microstructural factors (FOM and FOM'), which is unlikely to be available in practice.

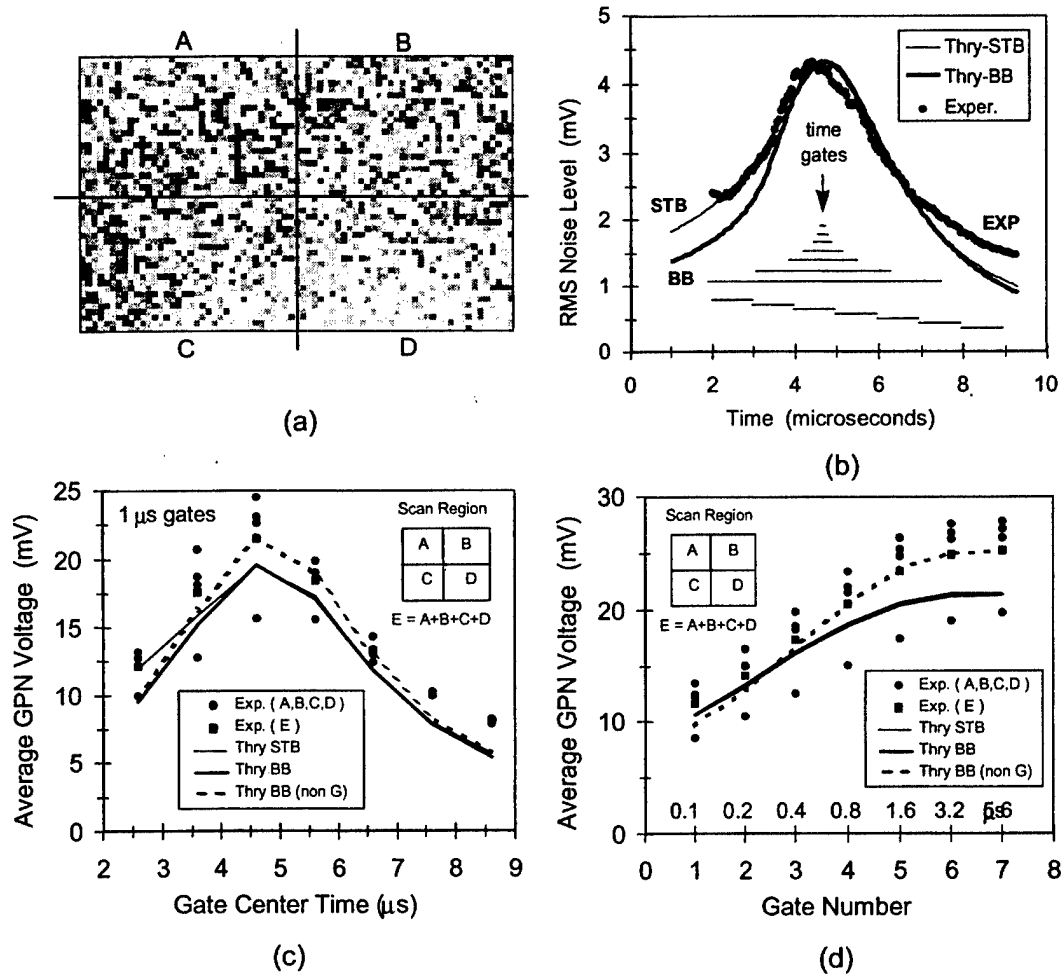


FIGURE B-9. UMBACH'S MEASUREMENTS OF GRAIN NOISE IN A Ti 6-4 FORGING SPECIMEN USING A 15-MHz FOCUSED PROBE (a) C-SCAN IMAGE SHOWING THE GPN VOLTAGE VERSUS POSITION FOR A NARROW TIME GATE CENTERED 0.64" BELOW THE ENTRY SURFACE (b) MEASURED AND PREDICTED RMS NOISE LEVELS FOR THE ENTIRE SCAN REGION, AND (c) AND (d) MEASURED AND PREDICTED AVERAGE GPN VOLTAGE FOR VARIOUS CHOICES OF THE TIME GATE

In summary, by comparing model predictions to measured noise data supplied by industry, it has been demonstrated that, even without detailed FOM information, the noise models can predict with reasonable accuracy the change in average gated-peak noise (or average S/N or N/S ratio) that accompanies a change in the inspection procedure. Three such studies were considered in which the inspection procedure was altered. These involved, respectively (1) replacing a conventional focusing scheme by a multizone scheme in billet inspection, (2) switching spherically focused transducers in forging inspections to change the volume of the incident sonic pulse, and (3) changing the center or duration of the inspection gate for a fixed choice of transducer and water path. In each case the model calculation correctly predicted the direction (increase or decrease) of the associated change in the backscattered grain noise level. In addition, the magnitude of the change was typically predicted to within  $\pm 20\%$  ( $\pm 1.6$  dB). This suggests that the noise models, when combined with suitable flaw signal models, can be a useful design tool for optimizing inspections and assessing inspection reliability.

#### B.9 TIES TO OTHER ETC TASKS.

As opportunities arose, the second-generation noise model was used to support the work of the ETC Inspection Reliability Task (or POD Task). There were two primary studies in which the noise model played an important role. The first dealt with the origin of signal fluctuations from identical scatterers and the second concerned the design of the POD random defect test specimen.

Experimental studies were conducted by the POD group in which a specimen containing multiple FBHs was repeatedly scanned using different choices of inspection parameters (i.e., transducer, scan plan, water path, angle of incidence, etc.). These scans were done for the dual purposes of determining the effects of inspection choices on flaw signal amplitudes, and testing certain signal-prediction models. It was noticed that for a fixed inspection procedure, there were often sizable differences in the amplitudes of echoes from neighboring, nominally identical holes. Two main effects were believed to be responsible for the signal fluctuations: (1) the superimposition of backscattered grain noise on the FBH echoes and (2) the effects of beam distortions arising from local velocity variations within the microstructure. Using the measured FOM of the specimen, the noise model was used to predict GPN distributions for small time gates centered on the FBH echoes. From these distributions, the average expected echo fluctuations due to superimposed grain noise could be estimated. It was found that the combined effects of electronic noise and grain noise accounted for about 80% of the observed fluctuations for small holes (#1 and #2) and about 30% of the fluctuations for the larger holes (#3 and #4). The remainder of the signal fluctuations was presumably caused by beam distortion effects. A fuller discussion can be found in reference B-15.

The second-generation noise model was also extensively used in the design of the POD random defect specimen. This is a 10" diameter Ti-64 billet specimen containing several dozen synthetic hard alpha defects embedded at randomized positions. The billet will be inspected using both conventional and multizone schemes, and the results of the inspections will be compared with model predictions. It was desired that some defects would be detectable with both inspection schemes, some with only one scheme, and some with neither. To choose the sizes, shapes, orientations, locations, and nitrogen contents of the defects, model calculations of flaw signal

amplitudes and competing backscattered noise were made for many hypothetical defects. In this process, the second-generation noise model was used to predict gated-peak noise distributions for various inspection scenarios, using measured FOM data from unflawed billet material as one input. The results of these studies were used to choose the characteristics of the embedded defects. A sample noise model calculation is shown in figure B-10. Note that the DAC referenced in the figure was designed such that echoes from #3 FBHs were independent of depth. To assess the detectability of various flaw candidates, predicted noise voltages were compared with predicted flaw echoes. More details concerning the design of the random defect specimen can be found in the summary report of the POD task [B-16].

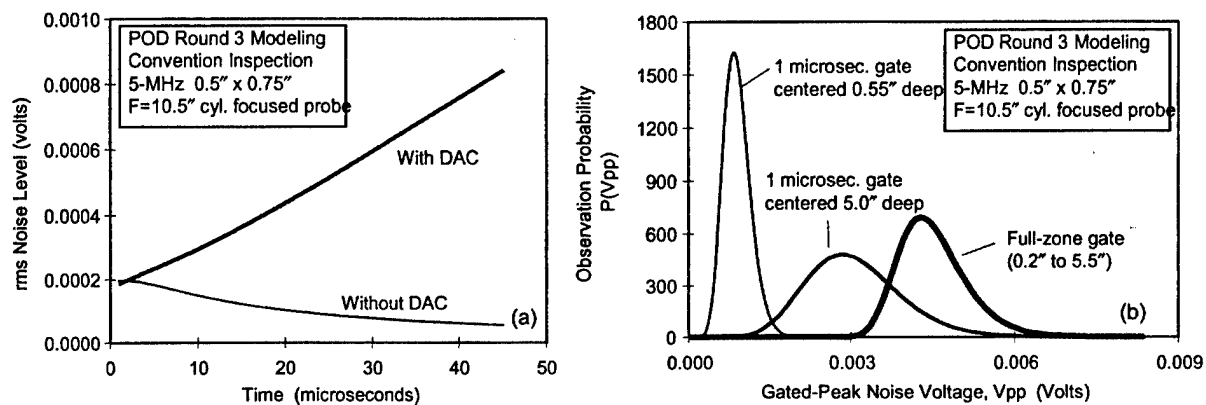


FIGURE B-10. EXAMPLES OF NOISE MODEL CALCULATIONS USED IN THE DESIGN OF THE POD RANDOM DEFECT SPECIMEN (a) CALCULATED rms NOISE LEVELS FOR A CONVENTIONAL INSPECTION OF THE 10.25" BILLET WITH AND WITHOUT DISTANCE-AMPLITUDE CORRECTION AND (b) CALCULATED GATED-PEAK NOISE PROBABILITY DISTRIBUTIONS (WITH DAC) FOR THREE TIME GATES OF INTEREST

#### B.10 SUMMARY.

As part of the overall ETC effort, three interrelated models were developed to predict attributes of the backscattered microstructural noise seen in pulse/echo inspections of billets. The models treat the effects of both the measurement system and the metal microstructure. They are consequently capable of predicting absolute noise voltages if certain microstructural factors (FOMs) are known. Both root-mean-squared and gated-peak noise quantities can be predicted, and model predictions generally compared well to noise measurements made in engine titanium specimens.

The FOM-vs-frequency data required for absolute noise predictions can be measured by properly analyzing noise A-scans gathered using a well-characterized transducer. However, such data is not routinely available during billet inspections. Even when FOM data is not available, it has been demonstrated that the models can be used to make useful predictions of relative noise levels, e.g., to predict the effect upon the average gated-peak noise level of some change in the inspection procedure. This capability, when combined with flaw-signal prediction models, should provide a useful tool for designing optimized inspections. Software for making noise model predictions has been provided to ETC members (i.e., SNCALC1 [B-17] and related code).

## B.11 REFERENCES.

- B-1. Margetan, F.J., T.A. Gray, and R.B. Thompson, "A Technique for Quantitatively Measuring Microstructurally Induced Ultrasonic Noise," *Review of Progress in QNDE*, 10B, D.O. Thompson and D.E. Chimenti, eds., Plenum Press, N.Y., 1991, p. 1721-1728.
- B-2. Margetan, F.J. and R.B. Thompson, "Microstructural Noise in Titanium Alloys and its Influence on the Detectability of Hard-Alpha Inclusions," *Review of Progress in QNDE*, 11, D.O. Thompson and D.E. Chimenti, eds., Plenum Press, N.Y., 1992, p. 1717-1724.
- B-3. F.J. Margetan, R.B. Thompson, and I. Yalda-Mooshabad, "Modeling Ultrasonic Microstructural Noise in Titanium Alloys," *Review of Progress in QNDE*, 12, D.O. Thompson and D.E. Chimenti, eds., Plenum Press, N.Y., 1993, p. 1735-1743.
- B-4. F.J. Margetan, R.B. Thompson, I. Yalda-Mooshabad, and Y.K. Han, "Detectability of Small Flaws in Advanced Engine Alloys," ISU Center for NDE, July 1993. (This 221-page report summarizes three years of Air Force sponsored research on the use of ultrasound to detect defects in titanium engine components, and discusses at great length the BB and STB versions of the first-generation noise model, and a related Monte-Carlo noise model.)
- B-5. Margetan, F.J., R.B. Thompson, and I. Yalda-Mooshabad, "Backscattered Microstructural Noise in Ultrasonic Toneburst Inspections," *Journal of Nondestructive Evaluation*, Vol. 13, Plenum Press, N.Y., 1994, pp. 111-136.
- B-6. Margetan, F.J., I. Yalda-Mooshabad, and R. B. Thompson, "Estimating Ultrasonic Signal-To-Noise Ratios for Inspections of Cylindrical Billets," *Review of Progress in QNDE*, 13, D.O. Thompson and D.E. Chimenti, eds., Plenum Press, N.Y., 1994, p. 1737-1744.
- B-7. Margetan, F.J., K.Y. Han, I. Yalda, Scot Goetsch, and R.B. Thompson, "The Practical Application of Grain Noise Models in Titanium Billets and Forgings," *Review of Progress in QNDE*, 14, D.O. Thompson and D.E. Chimenti, eds., Plenum Press, N.Y., 1995, p. 2129-2136.
- B-8. Margetan, F.J., I. Yalda, and R.B. Thompson, "Predicting Gated-Peak Grain Noise Distributions for Ultrasonic Inspections of Metals," *Review of Progress in QNDE*, 15, D.O. Thompson and D.E. Chimenti, eds., Plenum Press, N.Y., 1996, p. 1509-1516.
- B-9. Margetan, F.J. and R.B. Thompson, "Methods for Estimating Distributions Governing Gated Peak Grain Noise," 23 pages, Report ISU/ETC-3, ISU Center for NDE, Ames, IA, May 1994.
- B-10. Margetan, F.J., I. Yalda, R.B. Thompson, J. Umbach, U. Suh, P.J. Howard, D.C. Copley, and R. Gilmore, "Ultrasonic Grain Noise Modeling: Recent Applications to Engine Titanium Inspections," *Review of Progress in QNDE*, 16, D.O. Thompson and D.E. Chimenti, eds., Plenum Press, N.Y., 1997, p. 1555-1562.

- B-11. Margetan, F.J. and R.B. Thompson, "The Use of Axial Pressure Field Scans to Characterize Spherically-Focused Ultrasonic Transducers, and Results for Three Nominally Identical 5-MHz Probes," 24 pages, Report ISU/ETC-5, ISU Center for NDE, Ames, IA, June 1994.
- B-12. Yalda, I., P.D. Panetta, F.J. Margetan, and R.B. Thompson, "Characteristics of Ultrasonic Focused Transducers Using Axial Scans and C-Scans," Review of Progress in QNDE, 16, D.O. Thompson and D.E. Chimenti, eds., Plenum Press, N. Y., 1997, p. 927-934.
- B-13. Copley D.C. and P.J. Howard, "Operational Performance of a Multizone Billet Inspection System," Review of Progress in QNDE, 15, D.O. Thompson and D.E. Chimenti, eds., Plenum Press, N. Y., 1995, p. 2145.
- B-14. Howard P.J. and R.S. Gilmore, "Ultrasonic Noise and the Volume of the Ultrasonic Pulse," Review of Progress in QNDE, 15, D.O. Thompson and D.E. Chimenti, eds., Plenum Press, N. Y., 1996, p. 1495.
- B-15. Margetan, F.J., P.D. Panetta, I. Yalda, and R.B. Thompson, "The Relationship Between Flaw Signal Fluctuations and Backscattered Grain Noise in a Ti 6-4 Flat-Bottomed Hole Plate," 29 pages, Report ISU/ETC-8, ISU Center for NDE, Ames, IA, June 1995.
- B-16. Burkell, R.H., et al., "A Methodology for the Assessment of the Capability of Inspection Systems for Detection of Subsurface Flaws in Aircraft Turbine Engine Components," Report by the ETC Inspection Reliability Task Force, in press.
- B-17. Margetan, F.J., "User Notes for SNCALC1: Software for Rapid Estimates of rms Noise Levels and Signal-To-Noise Ratios," Report ISU/ETC-2, ISU Center for NDE, Ames, IA.